Measurement-Based Quantum Information Processing with Imperfect Operation

A thesis submitted to Queen's University, Belfast
for the degree of Doctor of Philosophy

by

Mark Simon Tame, BSc MSc

Faculty of Engineering and Physical Sciences
Queen's University, Belfast
August 14, 2007

Abstract

Recently, there has been considerable interest from the quantum information community in a new approach to quantum information processing (QIP) known as the measurement-based (MB) model. The model is based on the use of measurements to manipulate entanglement (quantum correlations) shared between the elements of multipartite quantum systems in order to carry out processing tasks, such as quantum computation (QC). This Thesis addresses the MB model and its practical operation when imperfections are present. The imperfections considered are in the form of intrinsic systematic noise, natural limitations in the structure of the quantum resources and environment-induced decoherence in a variety of experimental setups.

An analysis of basic MB QIP under the effects of intrinsic imperfections in the generation of *cluster state* resources is first provided. It is found that in order to limit the effects of noise, the management of protocols on small clusters processed via just a few measurements is the best strategy. Although this severely restricts the potential uses of the MB model using cluster states, computational algorithms can still be performed. To highlight this, two quantum algorithms that can be implemented using the MB model with minimal resource cluster states are introduced. It is shown how the two-qubit Deutsch's algorithm can be carried out using a linear optical setup. A cluster state implementation of a two-qubit quantum game is also proposed. For the resource state on which a MB protocol is realised, a benefit of using more sophisticated entanglement structures should be the ability to construct compact simulations of quantum algorithms. The impact of natural three-qubit interaction-based resources on the computational power of MB QIP is therefore studied. It is shown that the required features of this unusual entanglement structure can be fully embodied by suitably prepared optical lattice systems. The setup is then used to provide a more compact construction for a Toffoli gate than the standard MB cluster state model. This gate is important for scalability reasons when performing quantum algorithms on registers larger than just two qubits. In the search for compact gate constructions and minimal resource algorithm design, in order to reduce the effects of imperfections, one can also consider the possibility of using higher-dimensional elementary units instead of standard qubits at each lattice site in a cluster state. The effects of environment-induced decoherence in d-dimensional MB QIP are therefore studied. A significant reduction in the performance of cluster state resources for $d > 2$ is found when Markovian decoherence is present. Finally, a novel minimal resource fault-tolerant scheme for the MB model is introduced, based on the use of encoded qubits in an effective cluster state resource. It allows one to protect the quality of the entangled resources and the encoded information within from experimentally relevant sources of decoherence. A proposal for an optical lattice setting is outlined and an experimental test of the scheme using a linear optical setup is described in detail.

List of publications

[1] **M. S. Tame**, M. Paternostro, M. S. Kim and V. Vedral, *"An economical route to one-way quantum computation"*, *Int. J. Quant. Inf.* **4**, 689-703 (2006).

[2] **M. S. Tame**, M. Paternostro, M. S. Kim and V. Vedral, *"Quantum-information processing with noisy cluster states"*, *Phys. Rev. A* **72**, 012319 (2005).

[3] M. Paternostro, **M. S. Tame** and M. S. Kim, *"Hybrid cluster state proposal for a quantum game"*, *New J. Phys.* **7**, 226 (2005).

[4] **M. S. Tame**, M. Paternostro, M. S. Kim and V. Vedral, *"Natural three-qubit interactions in one-way quantum computing"*, *Phys. Rev. A* **73**, 022309 (2006).

[5] **M. S. Tame**, M. Paternostro, C. Hadley, S. Bose and M. S. Kim, *"Decoherence-based exploration of d-dimensional one-way quantum computation"*, *Phys. Rev. A* **74**, 042330 (2006).

[6] M. Paternostro, **M. S. Tame**, G. M. Palma and M. S. Kim, *"Entanglement generation and protection by detuning modulation"*, *Phys. Rev. A* **74**, 052317 (2006).

[7] **M. S. Tame**, R. Prevedel, M. Paternostro, P. Böhi, M. S. Kim and A. Zeilinger, *"Experimental realization of Deutsch's algorithm in a one-way quantum computer"*, *Phys. Rev. Lett.* **98**, 140501 (2007).

[8] **M. S. Tame**, M. Paternostro and M. S. Kim, *"One-way quantum computing in a decoherence-free subspace"*, *New J. Phys.* **9**, 201 (2007).

[9] R. Prevedel, **M. S. Tame**, A. Stefanov, M. Paternostro, M. S. Kim and A. Zeilinger, *"Experimental demonstration of a decoherence-free one-way quantum processor"*, *Phys. Rev. Lett.* **99**, 250503 (2007).

Table of contents

List of figures

Chapter 1

Introduction

1. Introduction

Since its formulation in the early 1920's quantum mechanics has played a fundamental role in our understanding of how Nature behaves on the microscopic scale and smaller. 'Puzzling' and 'non-intuitive' are words that were often used by scientists to describe quantum theory when it was first proposed and these sentiments are still held by researchers in the field of quantum physics today. However, compelling evidence for its correctness has been found over the last century in the form of its predictive power in a wide range of experimental settings. It has been successful in explaining many physical phenomena, such as experiments probing the structure of the atom during the 1930's, nuclear fusion in stars in the late 1930's, the behaviour of elementary particles since the 1940's and superconductors since the 1950's, to name only a few examples. Quantum mechanics is in essence a mathematical framework or *set of rules* that can be applied in order to describe a given physical system. Its use is not always necessary and depends on various factors such as the scale of the system and how well it is isolated from everything else. The behaviour that quantum mechanics predicts can often seem bizarre and even its inventors Einstein, Bohr, Heisenberg and Schrödinger, amongst many others, were never entirely satisfied with its philosophical implications. Despite this, since its conception scientists have used the mathematical framework to predict with great success the outcomes of experiments for many physical systems. Einstein himself recognised that quantum mechanics provided the best model for describing the scientific data available, even though he never accepted the theory as being complete.

Since the 1970's, the ability to investigate the behaviour of single quantum systems has become possible. Scientists have developed the capability to control and manipulate these systems with numerous methods in a range of different experimental setups. The invention of the Laser [1] and its development over the years has played a crucial role in this. Techniques such as trapping single atoms in 'atom traps' [2–8] have allowed atoms to be isolated from the rest of the world and their individual behaviour to be studied by probing with laser light. Devices that enable the transfer of single electrons [9, 10] and photons (quanta of light) [11] have also been demonstrated experimentally with great success. These advances have stimulated theoretical interest in the use of quantum controlled devices for investigating and probing deeper into the intricate features of quantum physics. This interest, together with the development of quantum

mechanics from a new information-theoretic point of view, has led physicists to the possibility of using quantum-based devices for carrying out information processing tasks. Technologies such as quantum computing (QC) and quantum cryptography have also emerged, offering important advantages over their *classical* (non-quantum) counterparts. These advantages include a vast decrease in the *running time*[1] of various mathematical algorithms and significantly higher levels of security for communication. The properties of quantum physics that at first seemed strange and rather curious to its founders are now being exploited in the design of novel schemes for quantum information protocols. The development of quantum information theory has also led to new fundamental insights into quantum physics itself, such as the roles of entanglement (quantum correlations) and measurements in the dynamics of quantum systems, both isolated and in contact with the rest of the world. Apart from the potential advantages quantum information processing (QIP) offers, there are practical reasons why microscopic scale information protocols based on quantum mechanics are needed. In 1965 Moore predicted [13] that the number of transistors per integrated circuit (for minimum component cost) would double every two years. This rate has now been maintained for over 40 years, with the size of the transistors becoming smaller and smaller. There will come a point, within the next decade, when quantum effects in the circuits will be unavoidable[2].

It was first recognised by Benioff [16–18] in the early 1980's that quantum mechanical computational processes could be at least as powerful as classical computational processes. Around the same time, Feynman [19] suggested that computers based on the principles of quantum mechanics could actually overcome the essential difficulties faced when trying to simulate complex quantum systems on classical computers. In 1985, while attempting to derive a stronger version of the Church-Turing thesis[3] from a physical perspective, Deutsch [23] was naturally led to consider computational devices based on the framework of quantum mechanics. This work, together with Benioff's and Feynman's insights, laid the foundations of modern-day quantum computing. In his paper, Deutsch

[1] The running time of an algorithm on a particular input, is the number of primitive operations or 'steps' executed [12].

[2] Novel methods such as extended optical lithography [14] and 3D chip stacking [15] techniques developed by IBM in the last few years could stretch this prediction.

[3] A thesis that addresses the efficiency of algorithmic processes [20–22].

provided a simple example algorithm which indicated that quantum computers could provide computational power that exceeds classical computers for certain tasks. Soon after, several more examples of efficient quantum algorithms were proposed. In 1994, Shor discovered [24] that finding the prime factors of integers and the so-called *discrete logarithm problem* could both be solved more efficiently using a quantum computer. Then in 1995, Grover [25] showed that an unstructured database search could be performed more efficiently than any classical computer if a quantum approach is adopted.

Information protocols using quantum mechanics are not just limited to those of a computational nature. In the late 1960's Wiesner [26] put forward several simple quantum cryptographic schemes, although his work was not formally published until 1983. In 1984, Bennett and Brassard (BB84) [27], building on the earlier work of Wiesner, proposed a protocol that allowed two parties to distribute private encryption keys[4] over a distance. The protocol meant that over a fixed-distance the parties involved never had to compromise the high level of security they would have obtained if they had personally exchanged their keys. Since then, a number of other cryptographic protocols using similar principles have been proposed [30], most notably the scheme introduced by Ekert [31] in 1991 using entangled quantum states. Protocols based on the concept of distributing encryption keys are now commonly known as quantum key distribution (QKD). Many other quantum communication protocols exist. From quantum secret sharing [32] to quantum fingerprinting [33], all are tailored to particular tasks. The use of quantum mechanics in information processing and communication has only begun to make physicists think about how information really is physical. It seems quite reasonable to believe that there are many new and exciting potential applications based on quantum mechanics still waiting to be discovered.

Within only the last few years, a number of different approaches have been used to implement *known* quantum protocols in state-of-the-art experiments. Nuclear magnetic resonance (NMR), ion traps, all-optical and solid state systems have been considered, each having particular strengths and weaknesses [34]. However, quantum technology is still at a very early stage. Advanced demonstrations of

[4]The keys took the form of a one-time pad [28], the only system of public cryptography that has been shown to be unbreakable [29].

quantum algorithms have not gone beyond 7 qubits, a very small number considering the amount required to do practically useful tasks with the algorithms of Shor and Grover. In 1998 Chuang *et al.* [35] achieved a 2-qubit realisation of a simple quantum algorithm (based on Deutsch's 1984 example) using NMR techniques. In quick succession several more experimental demonstrations were performed, such as the hydrogen nuclear spin two-qubit device by Jones and Mosca [36]. In 2001, Vandersypen *et al.* [37] realised a 7 qubit NMR-based device which demonstrated a simple example of Shor's prime factorisation algorithm. Other setups, most notably all-optical, have also achieved considerable success for small computational protocols with photons [38, 39], although their use has been more directly applied to carrying out quantum communication protocols.

Optical experiments have demonstrated that the photon resources required for cryptographic protocols, such as the BB84 and Ekert QKD schemes, can be achieved [40–42] and maintained over a long distance: in optical fibres up to 100 km [43–48] and in free space up to 144 km [49, 50]. The great progress of quantum cryptography is due largely to the minimal quantum resources that the protocols require. As a result it is at the stage where commercial and military products are now being offered by companies such as *MagiQ*, *id Quantique* and *SmartQuantum*. Quantum computing on the other hand requires much larger resources for performing its algorithms and numerous problems still need to be overcome, both at the experimental and theoretical level. From a computational point of view, inventing new and efficient quantum algorithms is hard because many difficult problems arise. The first is our use of intuition in the design process, which is deeply rooted in the classical world. When constructing algorithms to do certain tasks, if we use classical ideas and concepts, then the algorithms will be limited to classical capabilities. One needs to think in a non-intuitive 'quantum mechanical way' during the design process. In addition, the constructed algorithm should be significantly more efficient than any classical one that accomplishes the same task, or at the very least provide new beneficial features. The task performed must also be of direct applicability for a computational problem. All these factors make it a challenging problem for theoreticians to construct new quantum algorithms and protocols.

From an experimental perspective, physically scalable qubit systems need to

be identified and developed. The systems also need to allow universal sets of operations to be implemented and have the ability to initialise and read out the information being processed [51]. Unavoidable errors occur in many places in quantum systems. Effects such as decoherence (environment-induced noise) and the imperfect operation of key components in the setup act to destroy or modify the quantum information in a way that produces undesired protocol outcomes. Various methods are known to counter these problems, such as quantum error correction [52–54]. However, it remains to be seen how these methods can be implemented in practice, given the high demand of control and isolation that even small quantum resources require. Scaling to larger resources in order to perform more computationally useful tasks also increases the quantum system's susceptibility to imperfections. There is still much work to be done before QC can be put to practical use.

Within the last few years, a new way of performing quantum protocols has emerged which utilises entanglement shared between the elements of a multipartite quantum system. The model is based on the precise measurement of parts of highly entangled quantum systems known as cluster states [55, 56]. This special type of measurement-based (MB) model[5] has a *one-way* characteristic in the sense that once measurements are performed, in order to process information encoded within the cluster state, they cannot be undone without regenerating entanglement. This is in stark contrast to the standard circuit model for QC [60–62], where in general a network of quantum gates generates entanglement *during* the operation of a protocol and no measurements are made until the very end. Given a large enough cluster state one can carry out *universal* quantum computing, *i.e.* any quantum logic operation can be performed by making appropriate measurements on the state. In this sense the cluster state is called a *universal resource* [63]. Measurements on an individual part of a multipartite entangled state such as a cluster state cannot increase any entanglement, thus all the entanglement required for a given protocol must be initially present within the state. The MB one-way model for QIP has begun to attract substantial attention recently from the quantum information community, both theoretical [64–69] and experimental [70–81], due to its suitability for realisation in a wide range of experimental setups.

[5]Other types of MB models exist, most notably teleportation-based QIP [57–59].

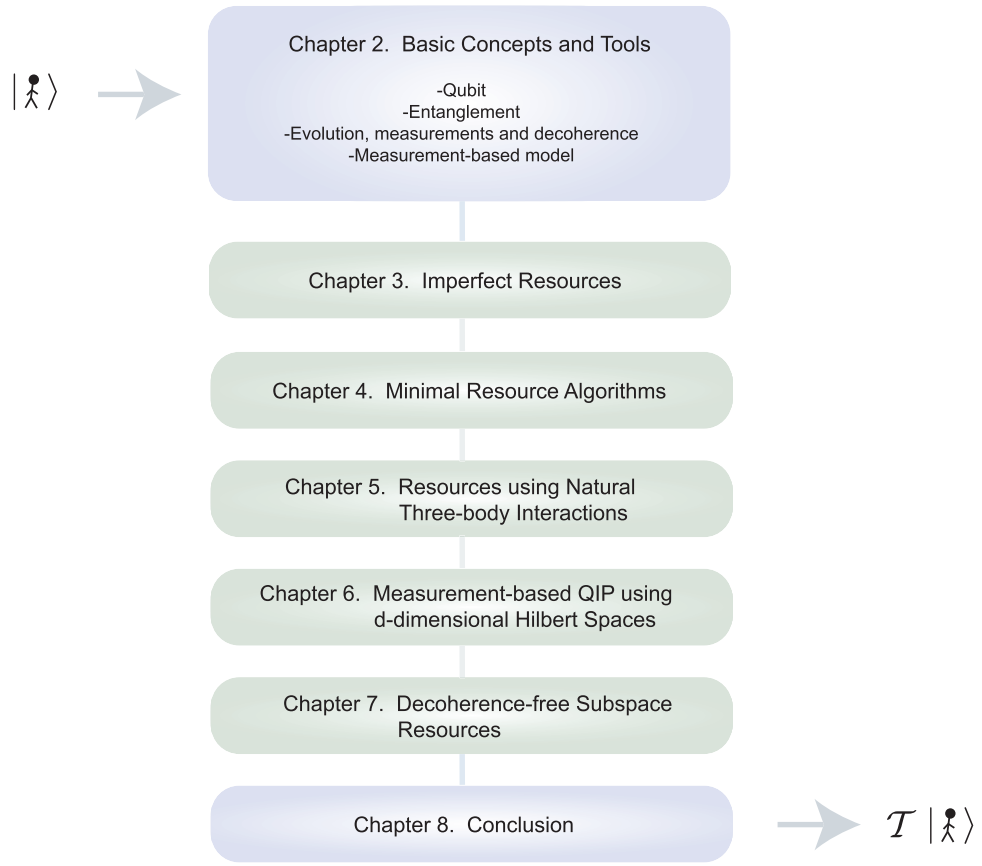

Figure 1.1: Outline of the $\mathcal{T}$hesis.

This Thesis addresses the MB model and its practical implementation in realistic experimental settings. The effects of noise from decoherence and imperfections in the generation of cluster state resources are studied in relation to the performance of quantum protocols being carried out on them. It is found that in order for the model to be most efficient, the use of small minimised resources is the best strategy. From this perspective it is then natural to ask what useful protocols can be implemented and how can they be realised using state-of-the-art technology. The MB model is, however, a more general term given to a wide range of *resources* on which measurements are performed in order to carry out information processing tasks. As such, investigating novel structures for the resources, as is performed in this Thesis, sheds light on the potential advantages this model could have over other QC models. Most importantly of all, though, is how to protect MB quantum resources from decoherence and imperfections while adopting a minimal resource approach. This is an essential topic investigated in

this Thesis.

The outline of the Thesis is as follows (see Fig. 1.1): In Chapter 2 an introduction to the basic tools and concepts of quantum information is given. This sets in place the framework needed for the following Chapters. In Chapter 3 the effects of imperfections in the generation of cluster state resources on the performance of protocols are analysed and discussed. Chapter 4 introduces two algorithms that can be performed using minimal cluster state resources and describes the experimental linear optical setup used to demonstrate them, along with the results obtained. In Chapter 5, the entanglement structure of cluster states is modified in order to show that advantages in terms of compact quantum gate simulations can arise through careful construction of the resources. In Chapter 6, the Hilbert space of each elementary unit of the cluster state is enlarged and it is seen how the encoded quantum information becomes more exposed to decoherence. Finally, in Chapter 7 a novel scheme for protection from decoherence using minimal resources is introduced and its performance is tested in a linear optical setup. Chapter 8 concludes with some final remarks and an outlook for the future of MB QIP. It is assumed throughout that readers have a basic knowledge and experience of quantum mechanics and quantum optics.

Chapter 2

Basic concepts and tools

In this Chapter, the relevant tools and concepts needed for Chapters 3-7 of the Thesis will be introduced. The concept of a qubit will be discussed, along with that of entanglement and the various tools one can use to measure it. The evolution of closed and open quantum systems and the role of decoherence will also be outlined, together with a description of how general measurements can be formalised in quantum mechanics. Finally, the MB one-way model for QIP will be introduced.

2.1 The qubit

From a classical perspective, the fundamental unit of information is the binary digit, or *bit* [82]. One cannot consider physical carriers of information with *less* freedom than being allowed to exist in two states 0 or 1, "yes" or "no", as they would not provide any actual information. Physical carriers of bits can be found everywhere these days, from electrical signals propagating thousands of kilometres in wires connecting computers all around the world, to the small sub-micrometre sized magnetic regions in hard-drives of portable music players. Information processing, or rather, classical information processing, deals with the acquisition, interpretation, storage and communication of bits.

Information processing carried out using physical systems at the quantum level, where quantum mechanics is required to describe how systems behave, introduces a new fundamental unit of information. This is known as the quantum bit, or *qubit* [83]. In order to grasp the concept of what exactly a qubit is, one needs to understand how nature at this level is described by quantum mechanics. A quantum system can be formalised mathematically as a Hilbert space $\mathcal{H}$ (a complex vector space[1]) in which the state of the system is represented by a complex state vector. For every measurable quantity, there is a corresponding Hermitian operator[2] called an observable which is defined on the Hilbert space.

[1]The state of a classical physical system can be defined by a description of all known properties of that system. The set of all possible states forms the "state space", known as the configuration (or phase) space in classical mechanics and is a real vector space. Quantum mechanics describes physical systems with complex amplitudes, hence it uses a complex vector space.

[2]Hermitian operators O satisfy the condition $O = O^\dagger$, where † corresponds to a transpose ^{T}

Quantum mechanics is also a linear theory, in that it allows a physical system to be in a linear superposition of two different states. To see this, consider a photon, the quantised unit of light and a quantum system in itself. We can define a qubit basis for the Hilbert space describing this quantum system using the photon's polarisation degree of freedom. An orthogonal-state basis $\{|0\rangle, |1\rangle\}$ can be chosen[3] (known as the *computational basis*), where the horizontal polarisation state $|H\rangle$ is associated with the logical state $|0\rangle$ and the vertical polarisation state $|V\rangle$ with the logical state $|1\rangle$. This is in direct analogy with the classical bit state basis $\{0, 1\}$. The structure of the Hilbert space in quantum mechanics allows the state of the photon's polarisation qubit[4] $|\psi\rangle$ to be described as being in a linear superposition

$$|\psi\rangle = \alpha\,|0\rangle + \beta\,|1\rangle\,, \tag{2.1}$$

where the arbitrary complex numbers α and β define a fixed phase between the relative terms $|0\rangle$ and $|1\rangle$. Together they satisfy the normalisation condition $|\alpha|^2+|\beta|^2 = 1$. This mathematical condition originates because once the photon's qubit state is measured (see later in this Chapter), $|\alpha|^2$ ($|\beta|^2$) corresponds to the probability that the state of the photon's polarisation will be found to be $|0\rangle$ ($|1\rangle$). Eq. (2.1) can also be written as the complex vector $(\alpha \quad \beta)^T$, where T denotes the transpose. The basis $\{|0\rangle, |1\rangle\}$ chosen here is not special however and other basis states can be used, as long as they form an orthonormal basis: $\{|e_1\rangle := (e_1^1, e_1^2)^T, |e_2\rangle := (e_2^1, e_2^2)^T\}$, where $\langle e_i|e_j\rangle = \sum_k (e_i^k)^* e_j^k = \delta_{ij},\ \forall\ i, j$. For example $\{|+\rangle, |-\rangle\}$ is another possible choice, where $|\pm\rangle = \frac{1}{\sqrt{2}}(|0\rangle \pm |1\rangle)$.

It should now be made clear how different the qubit is to the bit. The state of a bit can be measured without affecting its value, whereas a qubit, upon measurement, is reduced to one of the basis states with its associated probability. One might think that an infinite amount of information could therefore be extracted from an encoded qubit due to the continuous parameters α and β. However, any single measurement of a qubit provides at most one bit of classical informa-

and complex conjugation *. This ensures that the measurement outcomes are represented by real quantities. However, recently it has been noted [84] that one can assign complex numbers to a measurement outcome, so that this condition of hermiticity can be relaxed under certain conditions.

[3] Here we use what is known as the *Dirac notation* $|\ \rangle$ to describe a quantum state [85].

[4] A photon can carry more than a qubit of information depending on which degree of freedom is used.

tion, despite the initial encoded content. One could prepare a large ensemble of identical qubits in a particular state and perform a set of measurements in specific bases on each of them (known as *state tomography* and discussed in more detail in Chapter 4), thereby obtaining a good estimate of the state and hence the continuous values α and β. However, if the qubit's state is unknown and only one copy is provided, then it is impossible, due to the linearity of quantum mechanics, to extract more than one bit of information [86]. This is because once a measurement is made, the state will in almost all cases be changed and we can never reset it, as we do not know what it was originally. We cannot even copy the state in order to carry out state tomography[5].

The most general description of a qubit can be written mathematically as a *density matrix*

$$\rho_{qubit} = \frac{1}{2}(\mathbb{1} + \vec{n} \cdot \vec{\sigma}), \tag{2.2}$$

where $\vec{n} = n(\sin\theta\cos\phi, \sin\theta\sin\phi, \cos\theta)^T$ is a real vector of length n ($0 \leq n \leq 1$), $\vec{\sigma}$ represents the vector of the three Pauli matrices[6] $(\sigma_x, \sigma_y, \sigma_z)^T$ with the angles having the ranges $\theta \in [0, \pi]$ and $\phi \in [0, 2\pi]$. Writing the state of a qubit in matrix form like this, instead of as a vector state $|\psi\rangle$, allows one to describe the physical case when a quantum state has classical statistical properties. In this situation the state is known as a *mixed* quantum state. It can describe a classical *or* quantum bit and also states *in between* that share properties of both. This is useful as it allows us to incorporate the case when quantum states are statistically prepared[7], rather than coherently as in Eq. (2.1). It also allows one to describe quantum states that start out as coherent (or *pure*) and *decohere* (become classically mixed) under the influence of environment-induced noise (discussed later in this Chapter).

[5]This is a consequence of the *no-cloning theorem* [86]: Assume a cloning device C exists and that it can clone the state $|\psi\rangle$, then $C : |\psi\rangle|0\rangle \rightarrow |\psi\rangle|\psi\rangle = (\alpha|0\rangle + \beta|1\rangle)(\alpha|0\rangle + \beta|1\rangle) = \alpha^2|0\rangle|0\rangle + \alpha\beta|0\rangle|1\rangle + \beta\alpha|1\rangle|0\rangle + \alpha^2|1\rangle|1\rangle$. However by the linearity of quantum mechanics $C|\psi\rangle|0\rangle = C(\alpha|0\rangle + \beta|1\rangle)|0\rangle = \alpha|0\rangle|0\rangle + \beta|1\rangle|1\rangle$. There is a contradiction between the initial assumption and the theory of quantum mechanics and hence C cannot exist.

[6]Here $\sigma_x = \begin{pmatrix} 0 & 1 \\ 1 & 0 \end{pmatrix}$, $\sigma_y = \begin{pmatrix} 0 & -i \\ i & 0 \end{pmatrix}$ and $\sigma_z = \begin{pmatrix} 1 & 0 \\ 0 & -1 \end{pmatrix}$.

[7]If a quantum state is prepared as $|0\rangle$ and $|1\rangle$ with (real-valued) probabilities p_0 and p_1 respectively ($p_0 + p_1 = 1$), the state is given by $\rho_{qubit} = \begin{pmatrix} p_0 & 0 \\ 0 & p_1 \end{pmatrix} \equiv p_0|0\rangle\langle 0| + p_1|1\rangle\langle 1|$, where the last identity uses Dirac notation for matrices [85].

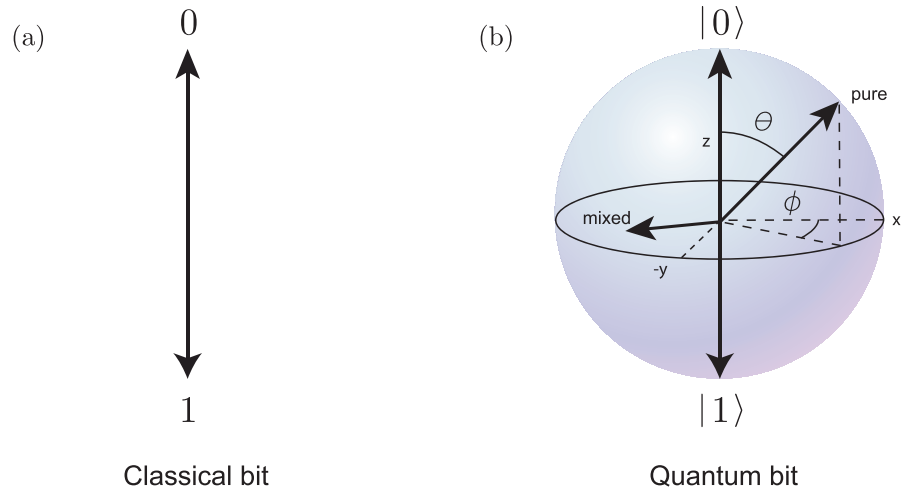

Figure 2.1: **(a)**: Possible states of a classical bit. **(b)**: A quantum bit's allowed states can be described by a Bloch sphere. Each point on (in) the sphere corresponds to a pure (mixed) density matrix ρ of the form given by Eq. (2.2).

A density matrix ρ in general has the following mathematical properties in the Hilbert space $\mathcal{H}$ describing a physical system: **(1)** ρ is a Hermitian operator, $\rho = \rho^\dagger$. **(2)** ρ is a positive semi-definite operator, *i.e.* $\forall\,|\psi\rangle \in \mathcal{H}: \ \langle\psi|\,\rho\,|\psi\rangle \geq 0 \Leftrightarrow \rho \geq 0$. This is equivalent to the statement that for ρ all eigenvalues $\lambda_i \geq 0$. **(3)** $\mathrm{Tr}(\rho) = \sum_i \lambda_i = 1$. **(4)** If ρ is a pure state (as in Eq. (2.1)), then $\rho^2 = \rho$.

A pure state of a qubit can be represented as a point on the surface of a sphere with unit radius ($n = 1$ in Eq. (2.2)), known as the *Bloch* sphere. This is shown in Fig. 2.1 **(b)**. Here the parameterisation $\alpha = \cos\theta/2$ and $\beta = e^{i\phi}\sin\theta/2$ is used. If ρ describes a mixed qubit state, then it corresponds to a point inside the sphere ($0 \leq n < 1$).

2.2 Entanglement in quantum systems

Entanglement is a truly quantum phenomenon with no analogous concept in any classical description of nature. It is perhaps best described in the words of Schrödinger, who first introduced the term [87]:

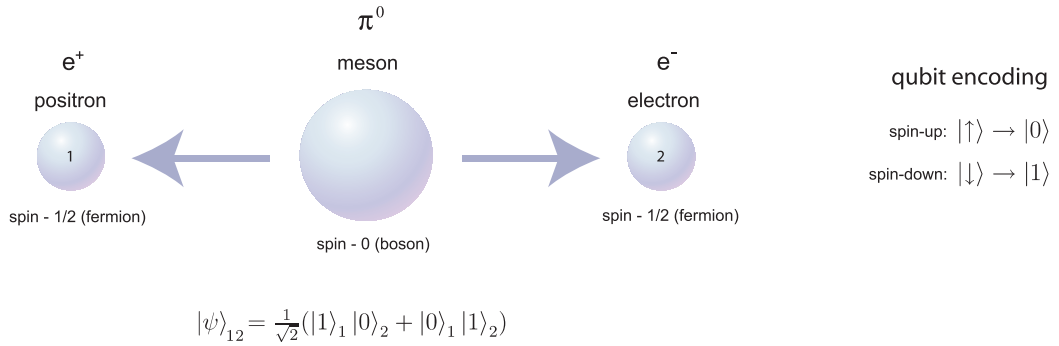

Figure 2.2: When a particle decays into two smaller particles, quantised versions of classical properties such as spin must be conserved in the process. Here, if one particle's spin is measured as "spin-up" the other must be "spin-down" and vice-versa with probability given by $|1/\sqrt{2}|^2 = 1/2$.

> *"When two systems, of which we know the states by their respective representatives, enter into temporary physical interaction due to known forces between them, and when after a time of mutual influence the systems separate again, then they can no longer be described in the same way as before, that is, by endowing each of them with a representative of its own. I would not call that one but rather the characteristic trait of quantum mechanics, the one that enforces its entire departure from classical lines of thought. By the interaction the two representatives have become entangled."*

The "physical interaction", or *entanglement* that Schrödinger describes in the passage above can also result from the splitting of a quantum system into smaller parts. For instance, if a pair of particles is created simultaneously from the decay of a larger particle, then this "splitting" must obey conservation of certain physical properties such as spin or momentum (which are treated as quantised). As a result, the two smaller particles become entangled with each other in these quantum degrees of freedom. An example is shown in Fig. (2.2). In general, when quantum mechanics is relevant for describing how a physical system behaves and that system is made up of a number of parts (for instance particles), an understanding of the role played by entanglement between each part in the system's evolution is important, as it can greatly modify the overall dynamics.

In the example given in Fig. (2.2) the state

$$|\psi\rangle_{12} = \frac{1}{\sqrt{2}}(|1\rangle_1 |0\rangle_2 + |0\rangle_1 |1\rangle_2) \tag{2.3}$$

is defined mathematically in the joint Hilbert space $\mathcal{H}_{12}$, a *direct tensor product* of the two individual Hilbert spaces describing each particle: $\mathcal{H}_{12} = \mathcal{H}_1 \otimes \mathcal{H}_2$. In general, any bipartite pure state defined in a Hilbert space of this form is said to be entangled when it cannot be written as a *separable* state $|\psi\rangle_{12} = |\gamma\rangle_1 |\delta\rangle_2 (\equiv |\gamma\rangle_1 \otimes |\delta\rangle_2)$[8], where $|\gamma\rangle_1$ ($|\delta\rangle_1$) is an arbitrary state vector in $\mathcal{H}_1$ ($\mathcal{H}_2$). For mixed states, the definition of entanglement becomes the following: A mixed state ρ_{12} is entangled (or inseparable) if it cannot be written as a *convex combination* of direct products of density matrices ρ_1^i and ρ_2^i

$$\rho_{12} = \sum_i p_i \rho_1^i \otimes \rho_2^i \tag{2.4}$$

where $0 \leq p_i \leq 1$ and $\sum_i p_i = 1$. The convex restriction limits Eq. (2.4) to mixed states only, as any pure state $\rho \in \mathcal{H}$ can never be expressed as a convex sum (combination) of two other states ρ_a and ρ_b, *i.e.* $\rho \neq \lambda\rho_a + (1-\lambda)\rho_b$, where $0 \leq \lambda \leq 1$ [9].

2.2.1 Entanglement quantification

The definitions given previously for bipartite entangled pure and mixed states provide us with an insight into whether a particular system is entangled or not. However these definitions are by no means constructive. In general it turns out to be a difficult task deciding whether a given state is separable or not [88, 89]. Moreover, how does one *quantify* entanglement?

[8] In many cases throughout this thesis, it will be convenient to suppress the direct tensor product symbol $\otimes$. The notation $|\gamma, \delta\rangle_{12} \equiv |\gamma\rangle_1 |\delta\rangle_2$ may also be used.

[9] To see this, let $\rho = |\psi\rangle\langle\psi|$ and choose a state $|\psi_\perp\rangle \in \mathcal{H}$, where $\langle\psi_\perp|\psi\rangle = 0$. This means $\langle\psi_\perp| \rho |\psi_\perp\rangle = 0 = \lambda \langle\psi_\perp| \rho_a |\psi_\perp\rangle + (1-\lambda) \langle\psi_\perp| \rho_b |\psi_\perp\rangle$. The right hand side is a sum of two nonnegative terms (due to property **(2)** of density matrices) and as the sum vanishes, then both terms must vanish also. If λ is not 0 or 1, then ρ_a and ρ_b must be orthogonal to $|\psi_\perp\rangle$. However, $|\psi_\perp\rangle$ is allowed to be *any* vector orthogonal to $|\psi\rangle$ and therefore $\rho_a = \rho_b = \rho$ is the only possibility. Pure states are thus extremal points of the convex *set* of all $\rho \in \mathcal{H}$.

The way to proceed is to classify all types of operations that can be applied to quantum systems which only *create* or *increase* classical correlations, but not quantum correlations (entanglement). Then one can introduce any quantity that monotonously decreases under such operations as a measure of entanglement[10] [90, 91]. To begin with, the states ρ_{12} in Eq. (2.4) and $|\psi\rangle_{12} = |\gamma\rangle_1 |\delta\rangle_2$ are separable because they can be created by two agents, Alice (who has access only to $\mathcal{H}_1$) and Bob (who has access only to $\mathcal{H}_2$) using local operations[11] and classical communication (LOCC). For example, Alice can prepare the state ρ_1^i with probability $\sqrt{p_i}$ and correspondingly Bob prepares the state ρ_2^i with probability $\sqrt{p_i}$. In general, entangled states are those states in a Hilbert space $\mathcal{H}$ that cannot be created using only LOCC.

Quantities that do not increase under LOCC are an appropriate starting point in quantifying entanglement. Any scalar-valued function derived from a system's state ρ that does not increase under LOCC is called an *entanglement monotone* [90, 91]. A *good* measure of entanglement $E(\rho)$ for a state $\rho \in \mathcal{H}$ should then satisfy at least the following conditions [92]: **(1)** $E(\rho)$ is an entanglement monotone. **(2)** $E(\rho) = 0$ *iff* (if and only if) ρ is separable. **(3)** $0 \leq E(\rho) \leq 1$. At present, there is no widely accepted list of axioms for entanglement measures [93, 94], however it is essential that an entanglement measure is an entanglement monotone. Throughout this Thesis several entanglement measures will be used depending on their suitability for a specific physical context. They are as follows:

1. von Neumann entropy (pure)

For a pure bipartite state $\rho_{12} = |\psi\rangle_{12} \langle\psi|$, the von Neumann entropy of either of the two subsystems provides a good measure of entanglement. It is defined as

[10] As this quantity should never increase under operations which are only creating or increasing classical correlations.

[11] An operation is called *local* if the subsystems of a complete quantum system ρ evolve independently from each other under its action. For a bi-partite system this can be written as a mapping $\mathcal{E}_{local}$ of the form: $\mathcal{E}_{local}(\rho) = \sum_{ij} E_i \otimes F_j \; \rho \; E_i^\dagger \otimes F_j^\dagger$, with $\sum_{ij} E_i^\dagger E_i \otimes F_j^\dagger F_j = \mathbb{1}_{\mathcal{H}_1 \otimes \mathcal{H}_2}$. Note that operations on each subsystem within $\mathcal{E}_{local}$ include any measurements or unitary/non-unitary evolution. $\mathcal{E}_{local}$ can easily be generalised to multi-partite systems.

follows

$$E_{\mathrm{vN}}(\rho_{12}) = -\mathrm{Tr}(\rho_1 \log_2 \rho_1) = -\mathrm{Tr}(\rho_2 \log_2 \rho_2), \tag{2.5}$$

where $\rho_i = \mathrm{Tr}_j(\rho_{12})$, $i \neq j$, *i.e.* a partial trace over one of the subsystems[12]. The state given in Eq. (2.3) gives $E_{\mathrm{vN}}(|\psi_{12}\rangle) = 1$ and is said to hold 1 *ebit* of entanglement [95]. It is called a maximally entangled state, as one can make any bipartite qubit state (pure or mixed) from it using LOCC. A simple way to see why the von Neumann entropy can be considered as an entanglement measure is given as follows: Consider two agents, Alice and Bob who use k maximally entangled states $|\psi\rangle_{12}$ of the form given in Eq. (2.3) with LOCC to prepare n copies of a chosen (partially entangled) bipartite pure state $|\phi\rangle_{12}$. Let k_{min} be the minimum number of $|\psi\rangle_{12}$ needed to do this. Then consider the reverse process where Alice and Bob want to transform n copies of $|\phi\rangle_{12}$ back into k' $|\psi\rangle_{12}$'s, letting k'_{max} be the maximum number of $|\psi\rangle_{12}$ that can be extracted. It can be shown using dense coding techniques that [95, 96]

$$\lim_{n\to\infty} \frac{k_{min}}{n} = \lim_{n\to\infty} \frac{k'_{max}}{n} \equiv S(\rho_1), \tag{2.6}$$

where $S(\rho_1)$ $(= S(\rho_2))$ is the von Neumann entropy $E_{\mathrm{vN}}(\rho_{12})$ for the state $|\phi\rangle_{12}$ defined by Eq. (2.5). As $|\psi\rangle_{12}$ carries the maximal amount of entanglement, k/n ($k_{min} = k'_{max} = k$ in the limit $n \to \infty$) can be regarded as characterising the amount of entanglement carried by $|\phi\rangle_{12}$. In a way, it is what we need to "pay" in $|\psi\rangle_{12}$'s in order to be able to make the state $|\phi\rangle_{12}$. The first term in Eq. (2.6) is known as the entanglement of formation and the second is known as the entanglement of distillation. Eq. (2.6) can be verified for pure bipartite systems of arbitrary dimension [95].

[12]The partial trace of a quantum system allows one to construct a reduced state description of a particular subsystem when all other subsystems are out of reach, *i.e.* they cannot be manipulated/addressed in an experiment. These subsystems may interact with each other and also with many other degrees of freedom surrounding the quantum system. If a general state $\rho \in \mathcal{H}_1 \otimes \mathcal{H}_2$ is given by $\rho = \sum_{i,j,k,l} \rho_{ijkl} |i\rangle |j\rangle \langle k| \langle l| \equiv \sum_{i,j,k,l} \rho_{ijkl} |i\rangle_1 \langle k| \otimes |j\rangle_2 \langle l|$, where the computational basis is used, then the partial trace with respect to $\mathcal{H}_2$ is $\mathrm{Tr}_2 : \rho \mapsto \sum_j \sum_{i,k} \rho_{ijkj} |i\rangle_1 \langle k|$.

2. Entanglement of Formation and Distillation (mixed)

For mixed states there are a number of entanglement measures available, however the situation is much more involved than the pure state case, as both quantum and classical correlations are present in the physical system that the state describes. Two important measures that can be carried over from the pure state case are the entanglement of formation E_F and the entanglement of distillation E_D, however, in general they are not equal. In the mixed state case $E_F(\rho)$ is defined as the infimum of the average entanglement of an ensemble of pure states $\rho_i = |\psi_i\rangle \langle\psi_i|$ that represent ρ [95]

$$E_F(\rho) = \inf \sum_i p_i E_{vN}(\rho_i) \tag{2.7}$$

which reduces to Eq. (2.6) if ρ is pure. Horodecki *et al.* have shown [97] that in the limit $n \to \infty$ maximally entangled states $|\psi\rangle_{12}$ are considered, any good ensemble (mixed state) entanglement measure E satisfies the equality $E_D \leq E \leq E_F$.

3. Concurrence $2 \otimes 2$ (pure and mixed)

Calculating E_F from Eq. (2.7) can be a computationally demanding task due to the necessity of taking the infimum over all possible decompositions of the state ρ. However, for bipartite qubit systems ($2 \otimes 2$), E_F can be calculated analytically as $E_F(\rho) = -x\log_2 x - (1-x)\log_2(1-x)$, with $x = (1 + \sqrt{1 - C^2(\rho)})/2$ [98, 99]. Here the quantity $C(\rho)$ is known as the *concurrence* and is given by

$$C(\rho) = \max\{0, \lambda_1 - \lambda_2 - \lambda_3 - \lambda_4\}, \tag{2.8}$$

where the λ_i's are the square roots of the eigenvalues of the non-Hermitian matrix $\tau = \rho(\sigma_y \otimes \sigma_y)\rho^*(\sigma_y \otimes \sigma_y)$ in decreasing order. Here ρ^* is the complex conjugate of ρ in the computational basis and each λ_i is a non-negative real number. As E_F varies from 0 to 1, $C(\rho)$ is a monotonically increasing function which also varies from 0 to 1, therefore one may take it on its own as a good measure of entanglement. Due to the easiness of finding the λ_i's in Eq. (2.8) for

a given ρ, calculating the concurrence is an efficient method for quantifying the entanglement in pure and mixed bipartite qubit systems.

4. Negativity of partial transposition $2 \otimes 2$ & $2 \otimes 3$ (pure and mixed)

Another measure of entanglement that will be used in this thesis is based on the Peres-Horodecki criterion. This is a necessary [100] and sufficient [101] condition for the presence of entanglement in $2 \otimes 2$ and $2 \otimes 3$ quantum systems. The criterion states that a bipartite density matrix ρ_{12} is entangled if its partial transpose $\rho_{12}^{T_1}$ or $\rho_{12}^{T_2}$ has any negative eigenvalues. More precisely

$$\text{In } \mathbb{C}^2 \otimes \mathbb{C}^2 \text{ or } \mathbb{C}^2 \otimes \mathbb{C}^3 \ \rho \text{ is separable iff } \rho^{T_1} \geq 0. \tag{2.9}$$

An easy way to see the if part of the statement is the following [100]: If ρ is separable, one can write $\rho = \sum_{i=1}^{K} p_i \left|e_i\right\rangle \left|f_i\right\rangle \left\langle e_i\right| \left\langle f_i\right| = \sum_{i=1}^{K} p_i \left|e_i\right\rangle \left\langle e_i\right| \otimes \left|f_i\right\rangle \left\langle f_i\right|$, where $\{\left|e_i\right\rangle\}$ and $\{\left|f_i\right\rangle\}$ correspond to an arbitrary basis in $\mathcal{H}_1$ and $\mathcal{H}_2$ respectively[13]. Next we have $\rho^{T_1} = \sum_{i=1}^{K} p_i (\left|e_i\right\rangle \left\langle e_i\right|)^{T_1} \otimes \left|f_i\right\rangle \left\langle f_i\right| = \sum_{i=1}^{K} p_i \left|e_i^*\right\rangle \left\langle e_i^*\right| \otimes \left|f_i\right\rangle \left\langle f_i\right| = \sum_{i=1}^{K} p_i \left|e_i^*\right\rangle \left|f_i\right\rangle \left\langle e_i^*\right| \left\langle f_i\right| \geq 0$. Recalling property **(2)** of density matrices, one can see that the eigenvalues of this partially transposed matrix are non-negative. The same procedure can be carried out with respect to $\mathcal{H}_2$ and the *if* statement is valid for arbitrary dimensions. In the special cases of $2 \otimes 2$ and $2 \otimes 3$, using a more complex proof [101], one can complete the iff statement. As a result of Eq. (2.9), the negativity of the partial transposition (NPT) is a necessary and sufficient criterion for entangled states. Using the NPT, a good entanglement measure can be defined as [102, 103]

$$E_{NPT}(\rho) = \max\{0, -2 \sum_i \lambda_i^-\}, \tag{2.10}$$

where λ_i^- are the negative eigenvalues of ρ^{T_1}. The factor 2 is introduced so that $0 \leq E_{NPT} \leq 1$. Finally, there is an order relationship between the concurrence ($C(\rho)$) and the NPT ($E_{NPT}(\rho)$) entanglement measures:

$$C(\rho) - 1 + \sqrt{2C^2(\rho) - 2C(\rho) + 1} \leq E_{NPT}(\rho) \leq C(\rho), \tag{2.11}$$

[13]Note that this is not a restricted convex sum and includes pure states also.

where for pure states we have the monotonic relation $E_{NPT}(\rho) = g(C(\rho))$. However one must be careful comparing the entanglement of two different mixed states as $g(C(\rho_1)) - g(C(\rho_2)) \neq E_{NPT}(\rho_1) - E_{NPT}(\rho_2)$. The difference depends on the bounding function of Eq. (2.11) [102, 103].

Multipartite entanglement and higher dimensions

In this section entanglement measures for low-dimensional bipartite quantum systems only have been considered. However, there has been much work carried out recently on the topic of entanglement quantification for higher dimensional systems and multipartite structures (for a review, see Refs. [93, 94]). More details will be given for specific cases when they are introduced later in this Thesis. For the moment, it is important to note that entanglement measures such as the concurrence ($C(\rho)$) and NPT ($E_{NPT}(\rho)$), although basic in the context of multipartite structures and higher dimensions, are useful tools in understanding the role that quantum correlations play in a given system's dynamics. Important information can be obtained just by looking at the behaviour of entanglement in low dimensional subsystems of larger systems. Examples of this will be seen in the next Chapter.

2.3 Evolution, Measurements and Decoherence

2.3.1 Evolution

The time evolution of a *closed* quantum system described by a pure state $|\psi\rangle$ is given by the *Schrödinger equation* [104]

$$i\hbar \frac{d\,|\psi\rangle}{dt} = H\,|\psi\rangle\,. \tag{2.12}$$

Here, $\hbar$ is Planck's constant and H is a Hermitian operator known as the Hamiltonian. The solution to this equation is given by $|\psi(t_2)\rangle = \exp[\frac{-iH(t_2-t_1)}{\hbar}]\,|\psi(t_1)\rangle$ $\equiv U(t_1,t_2)\,|\psi(t_1)\rangle$, where $U(t_1,t_2) = \exp[\frac{-iH(t_2-t_1)}{\hbar}]$ is a unitary operation ($U^\dagger U =$

1). This association can be quite useful in various cases where a continuous time description (corresponding to Schrödinger's equation) can be substituted by a discrete time description using unitary operations, *e.g.* $|\psi'\rangle = U|\psi\rangle$, where $|\psi'\rangle$ corresponds to $|\psi\rangle$ at an arbitrary later time[14]. However, it is important to note that Eq. (2.12) does not represent the evolution of an actual physical process, but the evolution of the probabilities for the outcomes of potential experiments on the quantum system described by $|\psi\rangle$ at a later time [105]. As the Hamiltonian in Eq. (2.12) is Hermitian, it has a spectral decomposition $H = \sum_i E_i|\psi_i\rangle\langle\psi_i|$ with eigenvalues E_i and eigenvectors $|\psi_i\rangle$, usually referred to as the energy eigenstates or stationary states (as they only acquire an overall numerical phase factor during the evolution).

2.3.2 Measurements

As the evolution of a closed quantum system is always unitary and governed by an equation of the form given in Eq. (2.12), accessing information about the physical state of the system must involve an external interaction of some sort, therefore "opening" it in the process. This is exactly what a measurement is. Once a measurement or *observation* is made (in order to extract some information from the system), the dynamics of the system alone cannot be described by unitary evolution. The measuring process *is* the interface between open and closed quantum systems and as we shall see, that of classical and quantum descriptions of nature also [106, 107]. Here, the measurement process, also known as an *intervention* process [108], can be considered to consist of two main parts: The first is the acquisition of information by an apparatus that produces a record of the intervention, most commonly known as the *measurement*. The second is a change of environment in which the quantum system evolves after the measurement. Interventions can be mathematically represented by completely positive maps, as will be introduced and discussed next. However first it is important to provide a motivation as to why this mathematical formalism of

[14] In the case of a time-dependent Hamiltonian : $H(t) = H_0 + \lambda W(t)$, one has $|\psi(t)\rangle = \exp[-\frac{i}{\hbar}\int_{t_1}^{t} H(t')dt']\,|\psi(t_1)\rangle \equiv U(t_1,t)\,|\psi(t_1)\rangle$. Obtaining the form of $U(t_1,t)$ can be quite difficult due to the time dependence in $H(t)$ (and also that $H(t)$'s at different times may not commute), but approximation methods can be exploited. For example, if $\lambda \ll 1$ and $H_0 \sim W(t)$, perturbation theory can be used.

maps is valid.

The measuring process can be described dynamically as follows[15] [108]: First a unitary interaction of the quantum system $|\psi_0\rangle = \sum_s c_s |s\rangle$ with a measuring apparatus in the initial state $|A\rangle$ takes place,

$$\sum_s c_s |s\rangle \otimes |A\rangle \rightarrow \sum_{s,\lambda} c_s U_{s\lambda} |\lambda\rangle . \tag{2.13}$$

This is sometimes referred to as a "premeasurement" [109]. Next a complete basis for the new combined quantum system and apparatus, denoted $\mathcal{C}$ from now on, is given by $\{|\lambda\rangle\} \rightarrow \{|\mu, \xi\rangle\}$, where μ labels a macroscopic subspace and ξ labels microscopic states in that subspace. Each macroscopically distinguishable subspace will correspond to one of the future outcomes of the intervention[16]. Thus after the premeasurement we have[17] $|\psi_1\rangle = \sum_{s,\mu,\xi} c_s U_{s\mu\xi} |\mu, \xi\rangle$. An environment with basis $\{|e_\alpha\rangle\}$ is then introduced, where $|e_\omega\rangle$ is assumed to be the state of the environment straight after the premeasurement. The states $|\mu, \xi\rangle$ with different μ are macroscopic and can interact with different microscopic environments, whereas the states with different ξ within a particular μ are protected. The combined system $\mathcal{C}$ therefore interacts unitarily with the environment resulting in the state $|\psi_2\rangle = \sum_{s,\mu,\xi,\alpha} c_s U_{s\mu\xi} b_{\mu\omega\alpha} |\mu, \xi\rangle \otimes |e_\alpha\rangle$, where the total state of the quantum system, apparatus and environment ρ is still considered pure, $\rho = |\psi_2\rangle\langle\psi_2|$. However, ρ contains environment operators of the form $|e_\alpha\rangle\langle e_\beta|$ which are unknown to an experimentalist performing the measurement and can be considered *unknowable* for all pratical purposes [110]. These degrees of freedom must be traced out of ρ, *i.e.* a partial trace. When this is done, one ends up with a reduced density matrix containing terms of the form $\sum_\alpha b_{\mu\omega\alpha} b^*_{\nu\omega\alpha}$. It can be shown [108] that $\sum_\alpha b_{\mu\omega\alpha} b^*_{\nu\omega\alpha} \simeq \delta_{\mu\nu}$, where the time taken to make this approximation is called the *decoherence time* [111–114] and will be discussed in more detail in the next Section. This *decoherence* is caused by the environment's microscopic degrees of freedom, that are not robust, being

[15] There are numerous interpretations of quantum mechanics, each with its own way of introducing and defining the measurement process. Here for the sake of definiteness and also convenience, a choice is made to follow closely Ref. [108].

[16] The labels μ could for instance be labels printed on various detectors.

[17] A starting mixed state can also be considered in place of Eq. (2.13) [108]. The corresponding details for the next steps follow the similar arguments.

disturbed by the apparatus' macroscopic degrees of freedom. Thus, the reduced density matrix of the quantum system and apparatus becomes block-diagonal and all *statistical predictions* are equivalent to those of an ordinary mixture of pure states $|\psi_\mu\rangle = \sum_{s,\xi} c_s U_{s\mu\xi} |\mu, \xi\rangle$. This mixture of unnormalised density matrices $\rho_\mu = |\psi_\mu\rangle\langle\psi_\mu|$ is that which replaces the original pure state $|\psi_1\rangle$, where the trace of ρ_μ is the probability of obtaining outcome μ.

The last step of the intervention is that part of the combined system $\mathcal{C}$ is discarded. The part that is discarded can depend on the outcome μ and may not even be necessary in some physical cases [108]. Two sets of basis vectors are therefore introduced, $|\mu, \sigma\rangle$ which corresponds to the new system and $|\mu, m\rangle$ which is the part that is discarded (partially traced over/out). The new density matrix in subspace μ is given by $\rho'_\mu = \sum_{s,t} c_s c_t^* \sum_{m,\sigma,\tau} U_{s\mu\sigma m} U^*_{t\mu\tau m} |\mu, \sigma\rangle\langle\mu, \tau|$. Thus, the reduced density matrix for the new system within each μ has elements $\langle\mu, \sigma| \rho'_\mu |\mu, \tau\rangle$ given by

$$(\rho'_\mu)_{\sigma\tau} = \sum_m \left(\sum_{s,t} (A_{\mu m})_{\sigma s} \rho_{st} (A^*_{\mu m})_{\tau t} \right), \tag{2.14}$$

where $\rho_{st} = c_s c_t$ is the system's initial state and the Kraus operators [115] are defined as $(A_{\mu m})_{\sigma s} = U_{s\mu\sigma m}$. Note that the indices s and σ (as well as t and τ for the conjugate operation) correspond to the original system and to the final one respectively. If we omit these indices then Eq. (2.14) becomes

$$\rho \to \rho'_\mu = \sum_m A_{\mu m} \rho A^\dagger_{\mu m}, \tag{2.15}$$

where μ represents the detector that was involved in the intervention, m corresponds to any subsystem discarded and the trace of the unnormalised density matrix ρ'_μ is the probability of obtaining outcome μ, *i.e.* $p_\mu = \mathrm{Tr}(\sum_m A_{\mu m} \rho A^\dagger_{\mu m}) = \mathrm{Tr}(\rho E_\mu)$. Here the positive operators[18] $E_\mu = \sum_m A^\dagger_{\mu m} A_{\mu m}$ have the same dimension as ρ and $\sum_\mu E_\mu = \mathbb{1}$ due to the unitarity of $U_{s\mu\sigma m}$. They are therefore elements of a positive operator valued measure (POVM) [115–118]. Eq. (2.15) describes the most general completely positive map[19] [115, 116, 119]. In the

[18] $\langle\psi| E_\mu |\psi\rangle \geq 0 \ \forall \ |\psi\rangle \in \mathcal{H}$.

[19] A mapping $\$: \rho \to \rho'$ that takes an initial density matrix ρ to a final density matrix ρ' satisfies the following: **(1)** $\$ preserves Hermiticity, **(2)** $\$ is trace preserving, **(3)** $\$ is completely

simple case where no auxiliary part of $\mathcal{C}$ is discarded, one can drop the m subscript and we have $\rho \to \rho_\mu = A_\mu \rho A_\mu^\dagger$ with probability $p_\mu = \mathrm{Tr}(A_\mu \rho A_\mu^\dagger)$ and $(A_\mu)_{\xi s} = U_{s\mu\xi}$. Again we have positive operators $E_\mu = A_\mu^\dagger A_\mu$ and $\sum_\mu E_\mu = \mathbb{1}$. It is also customary to normalise the state such that

$$\rho \to \rho_\mu = \frac{A_\mu \rho A_\mu^\dagger}{\mathrm{Tr}(A_\mu \rho A_\mu^\dagger)}, \tag{2.16}$$

with probability $p_\mu = \mathrm{Tr}(A_\mu \rho A_\mu^\dagger)$ that outcome μ occurs. From Eqs. (2.15) and (2.16) we obtain three possible classes of POVM. The first contains those operators that project the initial quantum state into a *fixed* set of orthogonal states. The second corresponds to those operators that project the state into a fixed set of non-orthogonal states and the third class is that of non-projective operators, *i.e.* the set of possible final states ρ_μ is *not-fixed*, but depends on the input state. Before going into the details of the three types of POVM, it is important to note that from Eq. (2.16), one may also use an even simpler model for the measurement process if ρ describes an initial pure state $|\psi\rangle$. In this case Eq. (2.16) becomes

$$|\psi\rangle \to \frac{A_\mu |\psi\rangle}{\sqrt{\langle\psi| A_\mu^\dagger A_\mu |\psi\rangle}}, \tag{2.17}$$

with $p_\mu = \langle\psi| A_\mu^\dagger A_\mu |\psi\rangle$ as the probability that outcome μ occurs.

1. Projective measurements (orthogonal)

Here all E_μ can be written as the outer product of pairs of orthogonal state vectors and we have $E_\mu = A_\mu^\dagger A_\mu = A_\mu$. For example, for a qubit the POVM $\{E_\mu^{p-o}\} := \{A_1, A_2\}$ is *projective* and *orthogonal* for $A_1 = |+\rangle\langle+|$ and $A_2 = |-\rangle\langle-|$, where $|\pm\rangle = 1/\sqrt{2}(|0\rangle \pm |1\rangle)$. Upon measurement of an arbitrary qubit $|\psi\rangle = \alpha|0\rangle + \beta|1\rangle$ in this projective orthogonal basis, using Eq. (2.16) or Eq. (2.17) one obtains the state $\rho_1 = |+\rangle\langle+|$ with probability $p_1 = (|\alpha + \beta|^2)/2$

positive and **(4)** $ is linear. These four properties keep the final output density matrix as a valid physical description of the system. A *completely positive* map considers a possible extension of ρ to a larger Hilbert space $\mathcal{H} = \mathcal{H}_A \otimes \mathcal{H}_B$, where $_A is completely positive if $_A \otimes \mathbb{1}_B$ is positive on that extension. Requirement **(3)** is necessary, as one can never be sure that there is no system B coupled to A of which we are unaware.

and $\rho_1 = |-\rangle\langle -|$ with probability $p_1 = (|\alpha - \beta|^2)/2$. This type of intervention is called a von Neumann measurement [106], where the POVM becomes a projection-valued measure (PVM). Projective orthogonal measurements will be used extensively in the next Section in order to perform MB QIP using multipartite entangled resources.

2. Projective measurements (non-orthogonal)

Here all E_μ can be written as the outer product of pairs of general state vectors and again we have $E_\mu = A_\mu^\dagger A_\mu = A_\mu$. For example, the qubit POVM $\{E_\mu^{p-no}\} := \{A_1, A_2, A_3\}$ is *projective* and *non-orthogonal*, where $A_1 = |\psi_1\rangle\langle\psi_1|$, $A_2 = |\psi_2\rangle\langle\psi_2|$ and $A_3 = |\psi_3\rangle\langle\psi_3|$, with states $|\psi_1\rangle = \sqrt{2/3}\,|0\rangle$, $|\psi_2\rangle = \sqrt{1/6}\,|0\rangle + \sqrt{1/2}\,|1\rangle$ and $|\psi_3\rangle = -\sqrt{1/6}\,|0\rangle + \sqrt{1/2}\,|1\rangle$ (note these are not the output states after measurement, see Eqs. (2.16) and (2.17)). Neumark's theorem [120, 121] states that any POVM can be considered as an orthogonal measurement in a higher dimensional space. In the above example this is easy to see by considering $\{E_\mu^{p-no}\} \in \mathcal{H}_2$ (a qubit Hilbert space) becomes $\{E_\mu^{p-o}\} \in \mathcal{H}_3$ (a *qutrit* Hilbert space) where we have $\{E_\mu^{p-o}\} := \{|u_1\rangle\langle u_1|, |u_2\rangle\langle u_2|, |u_3\rangle\langle u_3|\}$, with $|u_1\rangle = \sqrt{2/3}\,|0\rangle + \sqrt{1/3}\,|2\rangle$, $|u_2\rangle = \sqrt{1/6}\,|0\rangle + \sqrt{1/2}\,|1\rangle - \sqrt{1/3}\,|2\rangle$ and $|u_3\rangle = -\sqrt{1/6}\,|0\rangle + \sqrt{1/2}\,|1\rangle + \sqrt{1/3}\,|2\rangle$. Therefore if an intervention applies $\{E_\mu^{p-o}\} \in \mathcal{H}_3$ and we trace out the $|2\rangle\langle 2|$ degrees of freedom, corresponding to a discarding of the $m = 2$ subspace (see Eq. (2.14)), then $\{E_\mu^{p-no}\} \in \mathcal{H}_2$ is effectively applied.

3. Non-projective measurements

All the remaining sets of measurements, *i.e.* those sets which contain at least one member that cannot be written as an outer product of state vectors are *non-projective* and we have $\sqrt{E_\mu} = A_\mu = A_\mu^\dagger$, as $\sqrt{E_\mu}$ is Hermitian. For example with a qubit one can have $\{E_\mu^{np}\} := \{\frac{\sqrt{2}}{1+\sqrt{2}}|1\rangle\langle 1|, \frac{\sqrt{2}}{1+\sqrt{2}}\frac{(|0\rangle - |1\rangle)(\langle 0| - \langle 1|)}{2}, \mathbb{1} - E_1 - E_2\}$.

2.3.3 Decoherence

Decoherence was briefly introduced in the last section in order to help describe how measurements of quantum systems can occur. It is now appropriate to discuss in more detail what is meant by decoherence and how one can characterise its different forms. In essence, decoherence can be thought of as the loss of information from a quantum system due to its unitary interaction with an external environment, whose microscopic degrees of freedom we subsequently have no access to (for all practical purposes). Historically, decoherence in the way that has just been described and also mentioned in the last section is known as phase damping [111–114] and will be discussed in more detail next. However many researchers often refer to decoherence as an umbrella term for other types of processes, including various kinds of damping. Here, a description of the dynamics behind *true* decoherence (phase damping) will be given, along with two other physically relevant "decoherence" models of amplitude damping and depolarisation.

Phase Damping

In the last section, the decoherence process was said to occur as a result of an interaction between the macroscopic degrees of freedom of a quantum system and the microscopic degrees of freedom of an environment, which we subsequently trace out. Formally, one can write the process as

$$\begin{aligned} U_{sE}: \quad |0\rangle_s |e_0\rangle_E &\rightarrow \sqrt{1-p}\,|0\rangle_s |e_0\rangle_E + \sqrt{p}\,|0\rangle_s |e_1\rangle_E \\ |1\rangle_s |e_0\rangle_E &\rightarrow \sqrt{1-p}\,|1\rangle_s |e_0\rangle_E + \sqrt{p}\,|1\rangle_s |e_2\rangle_E \,. \end{aligned} \tag{2.18}$$

Here the quantum system s makes no transitions, but the environment *scatters off* it and is kicked into orthogonal states ($\langle e_i|e_j\rangle = \delta_{ij}$) with probabilities depending on the state of the system. By tracing out the environmental degrees of freedom (*i.e.* by a partial trace) one finds that the resulting statistical representation of the system can be described as if the initial state ρ undergoes the

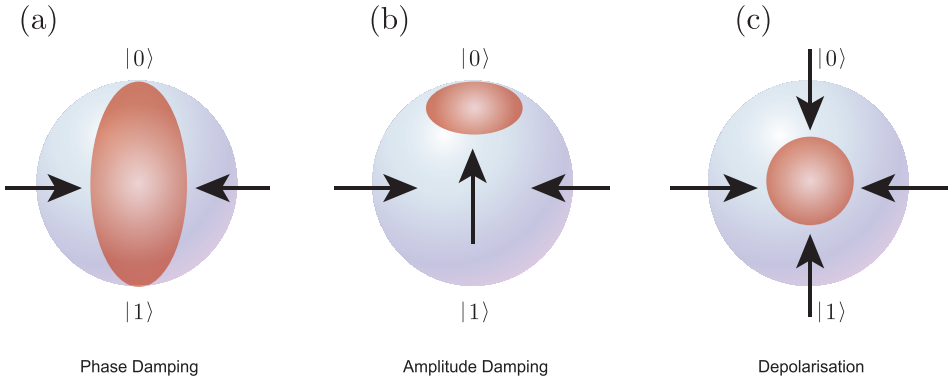

Figure 2.3: The effect of various decoherence processes on the form of the qubit Bloch sphere (see Fig. (2.1) for more details). **(a)**: Phase damping has the effect of squeezing states along the x-y axis of the sphere into the middle. **(b)**: Amplitude damping pushes states up towards $|0\rangle\langle 0|$. **(c)**: Depolarising shrinks states into the totally mixed state $\frac{1}{2}\mathbb{1}$ in the centre.

completely positive map (also known as a channel)

$$\$(\rho) = \rho' \equiv A_0 \rho A_0^\dagger + A_1 \rho A_1^\dagger + A_2 \rho A_2^\dagger, \tag{2.19}$$

where the Kraus operators are given by $A_0 = \sqrt{1-p}\mathbb{1}$, $A_1 = \sqrt{p}|0\rangle\langle 0|$ and $A_2 = \sqrt{p}|1\rangle\langle 1|$. The density matrix describing the state of the system therefore becomes

$$\rho' = \begin{pmatrix} \rho_{00} & (1-p)\rho_{01} \\ (1-p)\rho_{10} & \rho_{11} \end{pmatrix}. \tag{2.20}$$

If the scattering process occurs at a rate Γ (the probability of a scattering event per unit time), then we have that $p = \Gamma \Delta t \ll 1$. The evolution after a time $t = n\Delta t$ is then dictated by the concatenated channel map $\$^n$ and one finds that the off-diagonal elements in Eq. (2.20) become supressed by $(1-p)^n = (1-\Gamma\Delta t)^n$. Using $\lim_{\Delta t \to 0}(1-\Gamma\Delta t)^n = e^{-\Gamma t}$ we have

$$\rho' = \begin{pmatrix} \rho_{00} & e^{-\Gamma t}\rho_{01} \\ e^{-\Gamma t}\rho_{10} & \rho_{11} \end{pmatrix}. \tag{2.21}$$

The effect of this channel on the Bloch sphere of a qubit is given in Fig. 2.3 **(a)**, where one can see that the sphere is squashed along the x-y axis. After a time $t \gg \Gamma^{-1}$ the qubit's state can be described as an incoherent mixture $\rho' = \rho_{00}|0\rangle\langle 0| + \rho_{11}|1\rangle\langle 1|$. This process can be put into a physical context by

considering a particle in a superposition of position eigenstates $1/\sqrt{2}(|x\rangle + |-x\rangle)$ (macroscopic states) interacting with photons which scatter from the particle. One cannot keep track of the (microscopic) states of the photons for all practical purposes and thus they must be traced out in our description of the state of the particle. If the particle is heavy, its state of motion is not affected greatly by the scattered photons and the damping time scale (the time it takes for a significant amount of momentum to be transferred from the particle to the photons) is much longer than the rate of *phase* damping. The decoherence (phase damping) time scale Γ can therefore be seen as the time for a single photon to be scattered by the particle. We will see later in Chapter 3 that this model for phase damping, as described above, is relevant for describing the effect of the environment on atoms in optical lattices, ions in ion traps and many other quantum systems.

Amplitude Damping

Amplitude damping is another physically relevant decoherence process and can be used to describe the decay of an excited state of a two-level atom as a result of spontaneous emission of a photon. In a similar way to the phase damping channel we can write the process as

$$\begin{aligned} U_{sE}: \quad |0\rangle_s |e_0\rangle_E &\rightarrow |0\rangle_s |e_0\rangle_E \\ |1\rangle_s |e_0\rangle_E &\rightarrow \sqrt{1-p}\,|1\rangle_s |e_0\rangle_E + \sqrt{p}\,|0\rangle_s |e_1\rangle_E\,, \end{aligned} \tag{2.22}$$

where $|0\rangle_s$ ($|1\rangle_s$) represents the ground (excited) state of the atom and $|e_0\rangle_E$ ($|e_1\rangle_E$) represents the vacuum (one photon) state of the photon field. By tracing out the environmental degrees of freedom one obtains

$$\$(\rho) = \rho' \equiv A_0 \rho A_0^\dagger + A_1 \rho A_1^\dagger, \tag{2.23}$$

where the Kraus operators are given by $A_0 = |0\rangle\langle 0| + \sqrt{1-p}|1\rangle\langle 1|$ and $A_1 = \sqrt{p}|0\rangle\langle 1|$. The density matrix describing the state of the system therefore becomes

$$\rho' = \begin{pmatrix} \rho_{00} + p\rho_{11} & \sqrt{1-p}\rho_{01} \\ \sqrt{1-p}\rho_{10} & (1-p)\rho_{11} \end{pmatrix}. \tag{2.24}$$

The evolution after a time $t = n\Delta t$ is again dictated by the concatenated channel map $\$^n$ and one finds that the ρ_{11} element of the density matrix becomes $\rho_{11} \rightarrow (1-p)^n\rho_{11}$. Taking the probability of a transition in the time interval Δt as $\Gamma\Delta t$, we have that the probability an atom remains in the excited state $|1\rangle_s$ for a time t becomes $(1-\Gamma\Delta t)^{t/\Delta t}$ (where $n = t/\Delta t$), which gives $\lim_{\Delta t\rightarrow 0}(1-\Gamma\Delta t)^{t/\Delta t} = e^{-\Gamma t}$. The off-diagonal elements follow that of the phase damping channel with half the damping rate. Thus, one finds that Eq. (2.24) becomes

$$\rho' = \begin{pmatrix} \rho_{00} + (1-e^{-\Gamma t})\rho_{11} & e^{-\Gamma t/2}\rho_{01} \\ e^{-\Gamma t/2}\rho_{10} & e^{-\Gamma t}\rho_{11} \end{pmatrix}, \tag{2.25}$$

and the density matrix describes an atom that will inevitably end up in its ground state $|0\rangle_s$. The effect of this channel on the Bloch sphere of a qubit is shown in Fig. 2.3 **(b)**, where the sphere can be seen as being squashed up into the $|0\rangle$ pole. After a time $t \gg \Gamma^{-1}$ the qubit's state description becomes $\rho' = (\rho_{00} + \rho_{11})|0\rangle\langle 0| = |0\rangle\langle 0|$.

Depolarisation

The last decoherence model that will be discussed is depolarisation. It is a model that has some nice symmetry properties and we shall see later in Chapter 7, that in the case of state transfer using measurement-based techniques, this model becomes physically relevant.

The depolarisation process acting on a qubit's state $|\psi\rangle$ can be written as

$$\begin{aligned} U_{sE}: \quad |\psi\rangle_s |e_0\rangle_E \quad \rightarrow \quad & \sqrt{1-p}\,|\psi\rangle_s \otimes |e_0\rangle_E \\ & + \sqrt{\frac{p}{3}}\left[\sigma_x |\psi\rangle_s \otimes |e_1\rangle_E + \sigma_y |\psi\rangle_s \otimes |e_2\rangle_E + \sigma_z |\psi\rangle_s \otimes |e_3\rangle_E\right], \end{aligned} \tag{2.26}$$

where p is the probability an error (a bit flip σ_x, phase flip σ_z or bit and phase flip σ_y) occurs on the qubit, with the environment keeping a record of which type, while $(1-p)$ is the probability that the qubit will remain unchanged. Tracing

out the environmental degrees of freedom one obtains

$$\$(\rho) = \rho' = A_0\rho A_0^\dagger + A_1\rho A_1^\dagger + A_2\rho A_2^\dagger + A_3\rho A_3^\dagger, \tag{2.27}$$

where the Kraus operators are given by $A_0 = \sqrt{1-p}\mathbb{1}$, $A_1 = \sqrt{p/3}\sigma_x$, $A_2 = \sqrt{p/3}\sigma_y$ and $A_3 = \sqrt{p/3}\sigma_z$. The density matrix describing the state of the system therefore becomes

$$\begin{aligned} \rho' &= (1-p)\rho + \frac{p}{3}(\sigma_x\rho\sigma_x + \sigma_y\rho\sigma_y + \sigma_z\rho\sigma_z) \\ &\equiv (1-p)\rho + \frac{p}{2}\mathbb{1}. \end{aligned} \tag{2.28}$$

This type of "decoherence" is also known as *white noise* and results in a uniform shrinking of the qubit Bloch sphere into the centre, as shown in Fig. 2.3 **(c)**.

The master equation

In the previous sections it was shown that it is possible to describe the evolution of a quantum system's state, from pure to mixed, when the system interacted with an environment unitarily and subsequently the environmental degrees of freedom were traced out. The evolution of the *sub*-system (the quantum system) as a result became non-unitary. It is also possible and in some cases desirable to describe a sub-system's non-unitary evolution in terms of a differential equation similar to Schrödinger's equation as given in Eq. (2.12). This is usually only possible if the action of the environment on the sub-system's evolution is considered to be *Markovian* [122], or *local-in-time*[20]. Schrödinger's equation is a first order differential equation and governs the evolution of the combined system and environment ρ_{sE}. However if we know only $\rho_s(t')$ at a given time, then we do not have complete initial information to work out $\rho_s(t'+dt)$, as this depends not only on $\rho_s(t')$ but also on $\rho_s(t)$ at earlier times. The reason why this is so, is because in the combined system, the environment retains a *memory* of $\rho_s(t)$ and can transfer it back to the quantum system at any time t'' later.

[20] A *non-Markovian*, or *non-local-in-time* action of the environment on the sub-system's evolution can also be made into a differential equation [123]. However, the techniques required to do this become quite complex. In addition, the associated system-environment interactions are not of direct relevance to the physical systems considered in this Thesis.

This is known as non-Markovian evolution. An *exact* Markovian description of the seperate dynamics of a quantum system (which is joined to an environment) is therefore impossible. However, in many cases one can obtain a very good approximation using a Markov approach. This depends of course on how local-in-time the environment-system dynamics are, *i.e.* the time it takes for the environment to *forget*[21] the information it gains from the system $(\Delta t)_{mem}$, must be much shorter than the time scale on which we want to model/follow the system's evolution $(\Delta t)_{coarse}$. Finally this time scale $(\Delta t)_{coarse}$ must be much shorter than the actual time scale of the dynamics for which we want to track $(\Delta t)_{track}$, for example the damping time scale of a system. Therefore we must satisfy the hierarchy $(\Delta t)_{track} \gg (\Delta t)_{coarse} \gg (\Delta t)_{mem}$.

The density matrix form of Schrödinger's equation is known as the von Neumann equation and is written as $\dot{\rho_s} = -i[H_s, \rho_s]$ (with $\hbar = 1$ set for convenience), where H_s is the Hamiltonian that generates unitary evolution[22] in the system s. When the system interacts weakly with an environment unitarily and we take a Markov approximation, the system's dynamics alone become non-unitary and we write the evolution as $\dot{\rho}_s = \mathcal{L}[\rho_s]$, where $\mathcal{L}$ is a linear trace-preserving completely positive map known as the *Lindbladian* [124], or Lindblad superoperator. Explicitly one finds [96, 125–127]

$$\dot{\rho}_s = \mathcal{L}[\rho_s] \equiv -i[H_s, \rho_s] + \sum_{\mu>0} \left(L_\mu \rho_s L_\mu^\dagger - \frac{1}{2} L_\mu^\dagger L_\mu \rho_s - \frac{1}{2} \rho_s L_\mu^\dagger L_\mu \right), \qquad (2.29)$$

which is known as Lindblad's equation or the *master equation* (in Lindblad form). Here the terms $L_\mu \rho_s L_\mu^\dagger$ induce possible quantum *jumps* in the system, while the $\frac{1}{2} L_\mu^\dagger L_\mu \rho_s$ and $\frac{1}{2} \rho_s L_\mu^\dagger L_\mu$ terms normalise the case when no jumps occur. The form of the operators L_μ depends on the nature of the system-environment coupling. Eq. (2.29) will be used in Chapter 6, where phase and amplitude damping of harmonic oscillators will be considered. It should be noted however, that the master equation approach described above is not as general as the Kraus operator approach given in the last section and is actually contained within

[21] The *forgetfulness* being related to the correlation time of the environment-system fluctuations.

[22] Which one can solve to find $\rho_s(t) = U(t)\rho_s(0)U(t)^\dagger$, where $U(t) = \mathcal{T}\exp[-i\int_0^t H(t')dt']$. $\mathcal{T}$ is the time-ordering operator, as Hamiltonians at different times do not necessarily commute.

it. This can be seen as follows: Once the time dependence of $\rho_s(t)$ has been determined from the solution of Eq. (2.29), in a particular basis for the system, one can always find a set of time-dependent Kraus operators $\{A_\mu\}$ such that $\rho_s(t) = \sum_\mu A_\mu(t)\rho_s(0)A_\mu^\dagger(t)$. However the reverse is not always true and in general, Kraus operators can be used to describe non-Markovian dynamics [128].

2.4 Resources for Measurement-based quantum processing

2.4.1 The cluster state

A complete characterisation of cluster states is a good starting point in understanding how MB QIP can be performed. Cluster states are a class of pure multipartite entangled states that are contained within a more general class known as graph-states [55]. A cluster state is an entangled state of qubits positioned at specific sites of a lattice structure known as a cluster $\mathcal{C}$ (some examples of this structure are shown in Fig. 2.4) and is denoted by $|\phi_{\{\kappa\}}\rangle_{\mathcal{C}}$. It is formally defined as the eigenstate of the set of Hermitian operators

$$K^{(a)} = \sigma_x^{(a)} \bigotimes_{b\in \mathrm{nghb}(a)\cap\mathcal{C}} \sigma_z^{(b)} \tag{2.30}$$

such that $K^{(a)}|\phi_{\{\kappa\}}\rangle_{\mathcal{C}} = (-1)^{\kappa_a}|\phi_{\{\kappa\}}\rangle_{\mathcal{C}}$ [55, 56, 129, 130]. Here, each $K^{(a)}$ acts on the qubit occupying site $a \in \mathcal{C}$ and on any other qubit occupying a neighboring lattice site $b \in \mathrm{nghb}(a) \cap \mathcal{C}$ (as shown in Fig. (2.4) **(a)** & **(b)**). They are *correlation operators* which form a complete set of $|\mathcal{C}|$ independent and commuting observables for the qubits within $\mathcal{C}$. Thus, a cluster state $|\phi_{\{\kappa\}}\rangle_{\mathcal{C}}$ is completely specified by the set of numbers $\{\kappa\} := \{\kappa_a \in \{0,1\} | \, a \in \mathcal{C}\}$. For example, a different cluster state $|\phi_{\{\kappa'\}}\rangle_{\mathcal{C}}$ belonging to the same physical cluster $\mathcal{C}$ (*i.e.* the same lattice configuration), is completely described by the elements in the set $\{\kappa'\} := \{\kappa'_a \in \{0,1\} | \, a \in \mathcal{C}\}$. All the cluster states of an N qubit cluster $\mathcal{C}_N$ correspond to the $2^{|\mathcal{C}|}$ possible combinations of the elements in $\{\kappa\}$. They are mutually orthogonal and form a basis in the 2^N-dimensional Hilbert space of

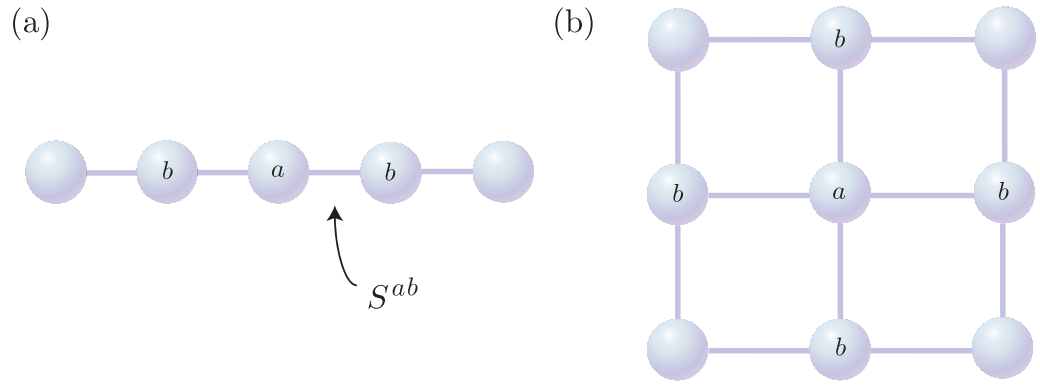

Figure 2.4: Two different types of cluster state with correlation centres a shown together with their neighbours b. **(a)**: A linear or one-dimensional cluster state. **(b)**: A two-dimensional cluster state.

the cluster. These states are also all equivalent under the application of $\sigma_z^{(a)}$ on individual qubits. In this thesis, the simplified notation $|\phi\rangle_{\mathcal{C}} := |\phi_{\{\kappa\}}\rangle_{\mathcal{C}}$ will often be used, where $\{\kappa\} = \{0, \forall a \in \mathcal{C}\}$. This particular cluster state is generated by first preparing the product state $|+\rangle_{\mathcal{C}} = \bigotimes_{a\in\mathcal{C}} |+\rangle_a$ of the qubits at all the sites a of $\mathcal{C}$. Here, $|\pm\rangle_a = (1/\sqrt{2})(|0\rangle \pm |1\rangle)_a$ are the eigenstates of $\sigma_x^{(a)}$ and $|0\rangle_a$ ($|1\rangle_a$) is the eigenstate of $\sigma_z^{(a)}$ corresponding to the $+1$ (-1) eigenvalue. The unitary transformation $S^{(\mathcal{C})} = \prod_{\langle a,b\rangle} S^{ab}$ is then applied to this initial state, where $\langle a, b\rangle := \{a, b \in \mathcal{C} | b - a \in \gamma_d\}$ and $\gamma_1 = \{1\}$, $\gamma_2 = \{(1,0)^T, (0,1)^T\}$, $\gamma_3 = \{(1,0,0)^T, (0,1,0)^T, (0,0,1)^T\}$ for the respective dimension d of the cluster being used. Each operator S^{ab} can be described by a controlled-phase gate denoted as

$$S^{ab} = |0\rangle_a\langle 0| \otimes \mathbb{1}^{(b)} + |1\rangle_a\langle 1| \otimes \sigma_z^{(b)}, \tag{2.31}$$

which shifts the phase of the state $|1\rangle_a |1\rangle_b \rightarrow -|1\rangle_a |1\rangle_b$, leaving all others unchanged. This gate is also known as a controlled-σ_z operation, or CZ. It constitutes an entangling operation between the qubits at sites a and b of the cluster $\mathcal{C}$, as they can no longer be considered as a product state once it has been applied. It is important to note that all S^{ab}'s mutually commute and therefore the time required for the generation of an N-qubit cluster state is independent from N [129, 130]. The state generated by the action of $S^{(\mathcal{C})}$ on $|+\rangle_{\mathcal{C}}$ is given by

$$S^{(\mathcal{C})}|+\rangle_{\mathcal{C}} \equiv \prod_{<a,b>} S^{ab} \bigotimes_{a\in\mathcal{C}} |+\rangle_a = |\phi\rangle_{\mathcal{C}}. \tag{2.32}$$

An Ising type interaction[23] between the qubits in a square lattice will produce a time-evolution operator having the form of $S^{(\mathcal{C})}$.

2.4.2 The one-way quantum computer

Let us assume that we want to carry out a unitary operation U_g associated with a particular quantum gate g which acts on an unknown input state $|\psi_{\text{in}}\rangle$ of n *logical* qubits. The idea behind the MB one-way quantum computer ($\text{QC}_{\mathcal{C}}$) model is to use a cluster of N *physical* qubits in a particular configuration $\mathcal{C}(g)$ to simulate the gate. In order to better understand how the U_g operation on $\mathcal{C}(g)$ takes place, it is convenient to consider the cluster as partitioned into three sections. First, consider an n-qubit input section $\mathcal{C}_I(g)$ which encodes the input logical state $|\psi_{\text{in}}\rangle$. Then a body section $\mathcal{C}_M(g)$ and finally an n-qubit output section $\mathcal{C}_O(g)$ for the read-out of U_g. The three sections have no mutual overlap and taken altogether, they reconstruct the structure of the cluster (*i.e.* $\mathcal{C}_\alpha(g) \cap \mathcal{C}_\beta(g) = \emptyset$, $\cup_\alpha \mathcal{C}_\alpha(g) = \mathcal{C}(g)$, where $\alpha, \beta \in \{I, M, O\}$ and $\alpha \neq \beta$). To begin, $|\psi_{\text{in}}\rangle$ is prepared on the physical cluster qubits in $\mathcal{C}_I(g)$ and the state is denoted as $|\psi_{\text{in}}\rangle_{\mathcal{C}_I(g)}$. It satisfies

$$|\psi_{\text{in}}\rangle_{\mathcal{C}_I(g)} = P^{\mathcal{C}_I(g)}_{Z,\{\mathbf{Z}\}}[\alpha_i] \bigotimes_{j=1}^{n} |+\rangle_j \tag{2.33}$$

where the multi-qubit projector[24] $P^{\mathcal{C}_I(g)}_{Z,\{\mathbf{Z}\}}[\alpha_i] = \sum_{i=1}^{2^n} \alpha_i P^{\mathcal{C}_I(g)}_{Z,\mathbf{z}_i}$, with the single $\mathbf{z}_i$ state projector

$$P^{\mathcal{C}_I(g)}_{Z,\mathbf{z}_i} = \bigotimes_{j=1}^{n} \frac{\mathbb{1} + (-1)^{s_j^{\mathbf{z}_i}} \sigma_z^{[j]}}{2} \tag{2.34}$$

which projects each qubit in $\mathcal{C}_I(g)$ into the state $|s_j^{\mathbf{z}_i}\rangle_j$, with $s_j^{\mathbf{z}_i}$ as the value of the j-th binary digit of the integer $\mathbf{z_i}$ ($\{\mathbf{Z}\} := \{\mathbf{z}_i | i \in 2^n\}$) and $[j]$ correspond-

[23] Here, the Ising interaction is given by $H_I = \hbar \frac{g}{4} \sum_{a,b \in c | b-a \in \gamma_d} \sigma_z^{(a)} \sigma_z^{(b)}$.

[24] A single qubit projector on qubit j can be written as $(P_Z)_j = \frac{\mathbf{1} + (-1)^{s_j} \sigma_z^{(j)}}{2} \equiv \frac{1}{2}(|0\rangle\langle 0| + |1\rangle\langle 1| + (-1)^{s_j}(|0\rangle\langle 0| - |1\rangle\langle 1|))$. If qubit j is in the state $|+\rangle_j$, then the application of $(P_Z)_j |+\rangle_j$ *projects* out $|0\rangle_j$ if $s_j = 0$ and $|1\rangle_j$ if $s_j = 1$. The application of $(P_Z)_j$ can also be thought of as a measurement operation if the value of s_j is left unknown (see Eq. (2.17)), with the interpretation that $|0\rangle_j$ will be obtained with probability $p_0 = 1/2$ ($s_j = 0$) and $|1\rangle_j$ will be obtained with probability $p_1 = 1/2$ ($s_j = 1$).

ing to an operation on logical qubits. It should be made clear that although the multi-qubit projector $P^{\mathcal{C}_I(g)}_{Z,\{\mathbf{z}\}}[\alpha_i]$ is an orthogonal projective measurement operator, it does not correspond to measurements which are performed in reality, but is *fictitiously* introduced in order to relate the logical input state $|\psi_{\text{in}}\rangle$ to any possible state present on the physical input qubits of the cluster [130]. In other words, $\mathcal{C}_I(g)$ is analogous to the input register in the quantum circuit model and $|\psi_{\text{in}}\rangle_{\mathcal{C}_I(g)}$ is an arbitrary superposition of computational states $|\psi_{\text{in}}\rangle_{\mathcal{C}_I(g)} = \sum_{i=1}^{2^n} \alpha_i |\mathbf{z}_i\rangle$, $(\sum_{i=1}^{2^n} |\alpha_i|^2 = 1)$.

After the preparation of $|\psi_{\text{in}}\rangle_{\mathcal{C}_I(g)}$, the cluster is entangled by the operation $S^{\mathcal{C}(g)}$ given in Eq. (2.32). A pattern of measurements $\mathcal{M}^{\mathcal{C}_M(g)}$ is then applied to the *body section* of the cluster $\mathcal{C}_M(g)$. This pattern is specified by a set of vectors $\vec{r}_a$ $(a \in \mathcal{C}_M(g))$ defining the bases in the Bloch sphere of a set of single-qubit orthogonal projective measurements to be performed in $\mathcal{C}_M(g)$ (which are not fictitious). The set of measurement outcomes obtained after $\mathcal{M}^{\mathcal{C}_M(g)}$ is applied are denoted as $\{s\} = \{s_a \in \{0,1\} \mid a \in \mathcal{C}_M(g)\}$. Performing a *measurement pattern* on the body section of a cluster is formally equivalent to applying the projector[25]

$$P^{\mathcal{C}_M(g)}_{\{s\}}(\mathcal{M}) = \bigotimes_{k \in \mathcal{C}_M(g)} \frac{\mathbb{1} + (-1)^{s_k} \vec{r}_k \cdot \vec{\sigma}^{(k)}}{2} \tag{2.35}$$

to the initial state. It is easy to see that $S^{\mathcal{C}(g)}$ and $P^{\mathcal{C}_I(g)}_{Z,\{\mathbf{z}\}}[\alpha_i]$ commute. With $P^{\mathcal{C}_M(g)}_{\{s\}}(\mathcal{M})$ acting only on the body section $\mathcal{C}_M(g)$ of the cluster, the state of the entire cluster $\mathcal{C}(g)$ after this procedure can be written as

$$P^{\mathcal{C}_I(g)}_{Z,\{\mathbf{z}\}}[\alpha_i] \underbrace{P^{\mathcal{C}_M(g)}_{\{s\}}(\mathcal{M}) \underbrace{S^{(\mathcal{C}(g))}|+\rangle_{\mathcal{C}(g)}}_{|\phi\rangle_{\mathcal{C}(g)}}}_{|\psi\rangle_{\mathcal{C}(g)}}. \tag{2.36}$$

We can therefore write $|\psi\rangle_{\mathcal{C}(g)} = |m\rangle_{\mathcal{C}_M(g)} \otimes |\psi\rangle_{\mathcal{C}_I(g) \cup \mathcal{C}_O(g)}$. While the body qubits are now considered to have been *removed* by the set of measurements in $\mathcal{M}^{\mathcal{C}_M(g)}$, Eq. (2.36) still contains degrees of freedom from the unmeasured input section $\mathcal{C}_I(g)$. To eliminate them and obtain just the cluster qubits of $\mathcal{C}_O(g)$, we perform measurements in the σ_x-eigenbasis on each qubit in $\mathcal{C}_I(g)$. That is, we obtain

[25] This generalises P_Z to all single qubit orthogonal projective measurements.

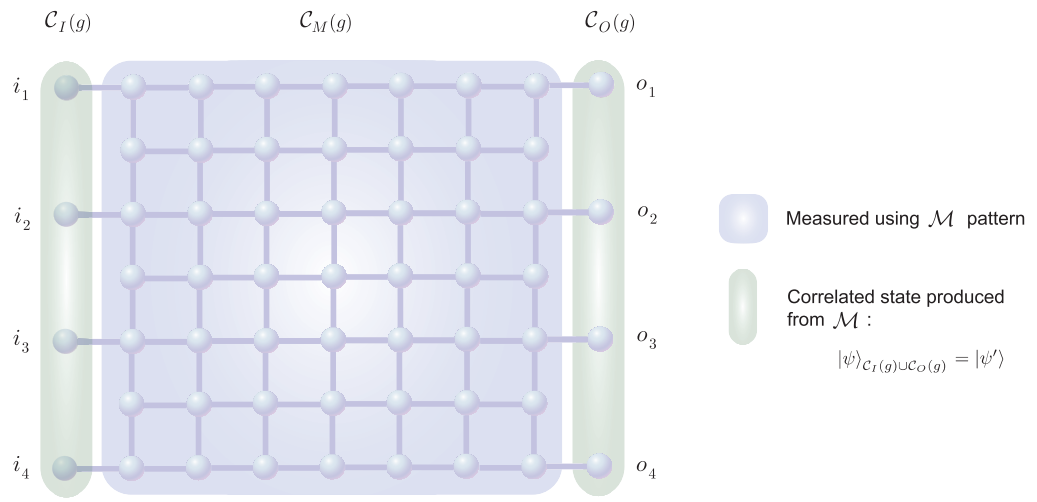

Figure 2.5: Here the measurement pattern $\mathcal{M}$ applied to all the qubits $a \in \mathcal{C}_M(g)$ produces correlations in the state $|\psi\rangle_{\mathcal{C}_I(g)\cup\mathcal{C}_O(g)} = |\psi'\rangle$ such that it satisfies Eq. (2.38) for a chosen U_g. For example, if $\mathcal{M}$ consists of σ_x measurements on all qubits $a \in \mathcal{C}_M(g)$, then the state $|\psi'\rangle$ satisfies Eq. (2.38) with $U_g = \mathsf{SWAP}$, where $\mathsf{SWAP} : |x_1x_2x_3x_4\rangle \rightarrow |x_4x_3x_2x_1\rangle$. This is a multi-qubit swap gate, with $|\psi_{in}\rangle = |\alpha\rangle_{i_1}|\beta\rangle_{i_2}|\gamma\rangle_{i_3}|\delta\rangle_{i_4}$ and $|\psi_{out}\rangle = |\delta\rangle_{o_1}|\gamma\rangle_{o_2}|\beta\rangle_{o_3}|\alpha\rangle_{o_4}$ [129].

the state

$$|m\rangle_{\mathcal{C}_I(g)} \otimes |\psi_{\text{out}}\rangle_{\mathcal{C}_O(g)} = P^{\mathcal{C}_I(g)}_{\{s\}}(X) P^{\mathcal{C}_I(g)}_{Z,\{\mathbf{z}\}}[\alpha_i]|\psi\rangle_{\mathcal{C}_I(g)\cup\mathcal{C}_O(g)}, \tag{2.37}$$

where $P^{\mathcal{C}_I(g)}_{\{s\}}(X) = \otimes_{k\in\mathcal{C}_I(g)} \frac{\mathbf{1}+(-1)^{s_k}\sigma^{(k)}_x}{2}$. A theorem central to the cluster state model [130], states that with a large enough cluster $\mathcal{C}$, by applying an appropriate measurement pattern $\mathcal{M}$ (designed using the correlation operators $K^{(a)}$ of the cluster qubits $a \in \mathcal{C}_M(g)$ [129, 130]), one can manipulate the correlations in the cluster to produce a state $|\psi\rangle_{\mathcal{C}_I(g)\cup\mathcal{C}_O(g)}$, which we will denote as $|\psi'\rangle$ for convenience, that satisfies the set of eigenvalues equations

$$\begin{aligned} \sigma^{\mathcal{C}_I(g),j}_x \left(U_g \sigma^{(j)}_x U^\dagger_g\right)^{\mathcal{C}_O(g)} |\psi'\rangle &= (-1)^{\lambda_{x,j}}|\psi'\rangle, \\ \sigma^{\mathcal{C}_I(g),j}_z \left(U_g \sigma^{(j)}_z U^\dagger_g\right)^{\mathcal{C}_O(g)} |\psi'\rangle &= (-1)^{\lambda_{z,j}}|\psi'\rangle. \end{aligned} \tag{2.38}$$

If Eq. (2.38) is satisfied, then the logical input state $|\psi_{\text{in}}\rangle$ (see Eq. (2.33)) and

the output $|\psi_{\text{out}}\rangle$ are related via

$$|\psi_{\text{out}}\rangle = U_g U_\Sigma |\psi_{\text{in}}\rangle, \tag{2.39}$$

where U_Σ is a *byproduct* operator, dependent on the results of the measurements in $\mathcal{C}_I(g)$ and $\mathcal{C}_M(g)$, acting locally on the logical qubits and given by

$$U_\Sigma = \bigotimes_{j=1}^{n} (\sigma_z^{[j]})^{s_j^x + \lambda_{x,j}} (\sigma_x^{[j]})^{\lambda_{z,j}}. \tag{2.40}$$

Thus, the design of the appropriate measurement pattern $\mathcal{M}$ allows one to effectively simulate the action of the gate g. Fig. 2.5 shows an outline of the entire process, with an interesting example given in the caption.

However, we must counteract the unwanted effect of the byproduct operator which appears in the simulation. If g belongs to the Clifford group[26], the propagation of U_Σ through U_g in Eq. (2.39) leaves U_g unaffected. That is: $U_g U_\Sigma \equiv \tilde{U}_\Sigma U_g$ with $\tilde{U}_\Sigma = U_g U_\Sigma U_g^{-1}$ which remains a product of local Pauli operations on the qubits in $\mathcal{C}_O(g)$. We then just apply the *decoding operator* $\tilde{U}_\Sigma^\dagger$ to the output cluster qubits in order to wash out the effect of the byproduct operator. On the other hand, if g is not in the Clifford group, we obtain $U_g U_\Sigma = U_\Sigma \tilde{U}_g$, while still keeping the local nature of the byproduct operator. In this case, the measurement pattern must be made adaptive in order to account for the propagation effect [130].

2.4.3 Basic building blocks, concatenation and the stabiliser formalism

It is clear that the important elements in the $\text{QC}_\mathcal{C}$ model are the design of the appropriate measurement pattern, along with a complete knowledge of the corresponding decoding operator. The pattern $\mathcal{M}^{\mathcal{C}_M(g)}$ suitable for a gate g on a cluster state $|\phi\rangle_{\mathcal{C}(g)}$ can be found by using a *stabiliser approach*. This means

[26]The Clifford group is the *normaliser* of the Pauli group in that it maps Pauli operators onto Pauli operators under conjugation, *i.e.* if U_Σ is a Pauli operator and U_g is in the Clifford group then the conjugation of U_Σ under U_g is given by $(U_g U_\Sigma U_g^{-1})$ and is also a Pauli operator.

combining the correlation operators $K^{(a)}$ from Eq. (2.30) that define $|\phi\rangle_{\mathcal{C}(g)}$ (by adding, multiplying by a scalar or multiplying together) with the projectors $P_{s_k}^{(k)} = \frac{\mathbf{1}+(-1)^{s_k}\vec{r}_k\cdot\vec{\sigma}^{(k)}}{2}$ (corresponding to possible measurements that could be made on qubits $k \in \mathcal{C}_M$ in the cluster state) to derive valid eigenvalue equations of the form given in Eq. (2.38) for the state $|\psi'\rangle$ that satisfy the desired U_g. It is easy to see that this procedure can become quite complex. Furthermore, the realisation of a given cluster state is a system-dependent issue. A method particularly suited for condensed-matter systems (as well as optical lattices, discussed later in Chapter 3), is the creation of regular cluster configurations from which redundant qubits, not necessary for the computational steps performed are removed through single-qubit measurements in the computational basis $\{|0\rangle, |1\rangle\}$. In ideal conditions, the removals are harmless for the performance of a particular gate simulation. But when (intrinsic or external) decoherence is introduced in the cluster, this is no longer true. One of the key results of the next Chapter will be that the number of measurements performed on the cluster qubits (either within $\mathcal{M}^{\mathcal{C}_M(g)}$ or instrumental to the cluster state generation) should be as small as possible. Thus, tailoring a cluster state using the stabiliser formalism to cleanse it from the redundant qubits may not be the best strategy from this point of view also. Very recent experimental efforts in the all-optical scenario have demonstrated that small clusters of just a few qubits can be efficiently produced within state-of-the-art technology [71, 73–78, 80]. In these cases, the setup is built so that *exactly* the layout needed is produced and no qubit has to be thrown away. Small optical clusters can then be mutually connected by gluing them as suggested in [131] and realised in [74].

Fortunately, an alternative approach to the stabiliser construction of exploitable cluster configurations is possible [132–134] and can be beneficial depending on the quantum protocol one wishes to perform in a given physical setup. Here, the approach uses fundamental configurations or basic building blocks (BBB's). By concatenating them, *i.e.* placing the blocks next to each other such that they *overlap*, any desired layout corresponding to a precise computational task can be constructed and the appropriate decoding operator $\tilde{U}_\Sigma^\dagger$ is naturally retrieved. This concatenation technique gives us the possibility of designing optimal elementary steps on small cluster configurations, each corresponding to one stage of an experiment. However, as the method breaks down a $\mathrm{QC}_\mathcal{C}$ simulation into

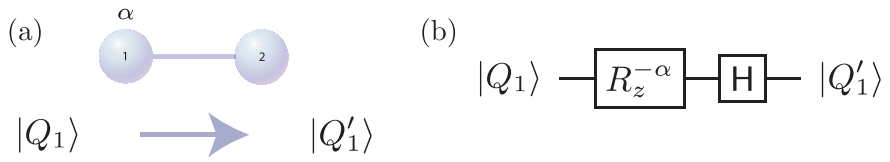

Figure 2.6: **(a)**: The BBB_1 layout. **(b)**: The operation simulated when qubit 1 is measured in the $B_1(\alpha)$ basis and $s_1^{xy(\alpha)} = 0$ is obtained.

elementary gates, it does severely restrict the correlation structure of the cluster [135]. The main advantage of the concatenation technique compared to the stabiliser approach is that it constitutes a useful construction strategy, permiting one to carefully limit the effects of imperfections and design minimal resource algorithms. These applications will be discussed in more detail in the next few Chapters.

To start with, the BBB's will be introduced and their equivalent network circuits will be given. The diagrammatic notation is such that each qubit will be represented by the symbol of a circle. The angle α next to the i-th qubit symbol identifies the basis $B_i(\alpha) := \{|\alpha_+\rangle, |\alpha_-\rangle\}$ in which that qubit is measured. Here, $|\alpha_\pm\rangle = (1/\sqrt{2})(|0\rangle \pm e^{i\alpha}|1\rangle)$ with α the angle from the positive x axis in the x-y plane of the Bloch sphere and $s_i^{xy(\alpha)} \in \{0, 1\}$ is the corresponding measurement outcome. Note that the basis $B_i(\alpha)$ is a restriction of the general measurement basis given in Eq. (2.35). In the configurations shown here, the orientation is irrelevant so long as the topology does not change.

The smallest cluster state one can conceive consists of two qubits and can be used to simulate a unitary operation on one logical qubit $|Q_1\rangle$ encoded on a physical cluster qubit (thus $|\mathcal{C}_I(g)| = 1$), as shown in Fig. 2.6 **(a)**. This configuration will be denoted from now on as BBB_1. The overall operation simulated by BBB_1, when the measurement on qubit 1 gives $s_1^{xy(\alpha)} = 0$ as the outcome, is shown in Fig. 2.6 **(b)**, where $R_z^{-\alpha}$ represents a rotation around the z axis by an angle $-\alpha$ and H denotes a Hadamard gate[27]. Due to the probabilistic nature of the simulation, it is necessary to apply a decoding operator $\tilde{U}_\Sigma^\dagger(s_1^{xy(\alpha)}) = \sigma_x^{s_1^{xy(\alpha)}}$ to qubit 2. Using the same two-qubit cluster layout, with two encoded logical qubits $|Q_1\rangle$ and $|Q_2\rangle$ (*i.e.* here $\mathcal{C}_I(g) \equiv \mathcal{C}_O(g)$, see Fig. 2.7 **(a)**), we simply

[27]Here $R_z^\alpha = \begin{pmatrix} 1 & 0 \\ 0 & e^{i\alpha} \end{pmatrix}$ and $\mathsf{H} = \frac{1}{\sqrt{2}} \begin{pmatrix} 1 & 1 \\ 1 & -1 \end{pmatrix}$.

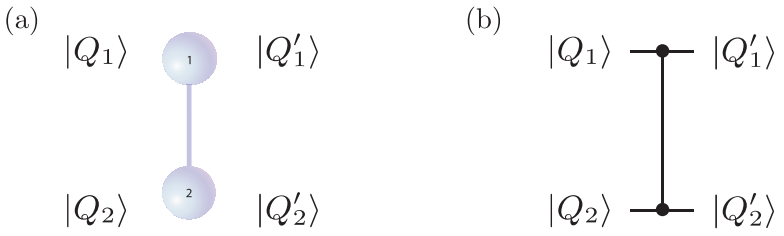

Figure 2.7: The CZ gate simulated by BBB_2 on two logical qubits $|Q_1\rangle$ and $|Q_2\rangle$.

simulate a controlled phase gate (CZ), as indicated in Fig. 2.7 **(b)**. We denote this configuration as BBB_2.

Our set of BBB's is completed by the introduction of BBB_3 shown in Fig. 2.8 **(a)**, where qubits 1 and 3 encode the input states and a measurement is performed on qubit 2 in the $B_2(\alpha)$ basis. This pattern simulates the transformation

$$T_{BBB_3} = \frac{1}{\sqrt{2}} \begin{pmatrix} 1 \pm e^{-i\alpha} & 0 & 0 & 0 \\ 0 & 1 \mp e^{-i\alpha} & 0 & 0 \\ 0 & 0 & 1 \mp e^{-i\alpha} & 0 \\ 0 & 0 & 0 & 1 \pm e^{-i\alpha} \end{pmatrix}, \tag{2.41}$$

where the top (bottom) sign corresponds to $s_2^{xy(\alpha)} = 0$ ($s_2^{xy(\alpha)} = 1$). For $\alpha = \{0, \pi\}$ *i e.* a measurement of the bridging qubit in the $\pm\sigma_x$ eigenbasis ($\{|+\rangle, |-\rangle\}$ for $+\sigma_x$ and $\{|-\rangle, |+\rangle\}$ for $-\sigma_x$), one obtains a non-unitary gate. Of particular interest is when $\alpha = \frac{\pi}{2}$, this is the σ_y eigenbasis ($\{|+_y\rangle, |-_y\rangle\}$, with $|\pm_y\rangle = (1/\sqrt{2})(|0\rangle \pm i\,|1\rangle)$) which corresponds to an operation decomposed as shown in Fig. 2.8 **(b)**. The decoding operator for this specific gate simulation is $\tilde{U}_\Sigma^\dagger = -i\sigma_z^{(1)s_2^{xy(\pi/2)}} \otimes \sigma_z^{(3)s_2^{xy(\pi/2)}}$.

Using this set of BBB's, one can construct more complicated configurations. In order to see this more clearly, the following observation from [130] must be used:

Observation 1. *Consider a quantum circuit g associated with the unitary operator U_g simulated on a cluster $\mathcal{C}(g)$. Let g be comprised of two consecutive circuits g_1 and g_2 on subclusters $\mathcal{C}(g_1)$ and $\mathcal{C}(g_2)$ respectively, i.e. $g = g_2 g_1$ and $\mathcal{C}(g) = \mathcal{C}(g_1) \cup \mathcal{C}(g_2)$, with $\mathcal{C}(g_1) \cap \mathcal{C}(g_2)$ containing one cluster qubit for each logical qubit. These subgates have associated unitary operators U_{g_1} and U_{g_2}. The method of entangling the whole cluster $\mathcal{C}(g)$ and performing the required*

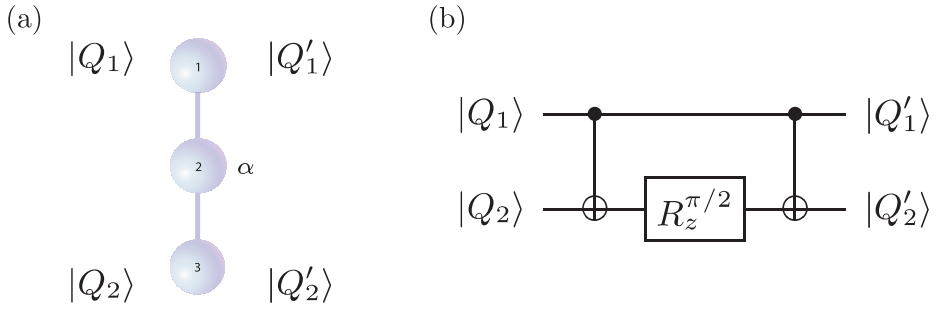

Figure 2.8: (a): The BBB_3 configuration. **(b)**: The equivalent quantum circuit corresponding to the operation simulated by BBB_3 with $\alpha = \pi/2$ and $s_2^{xy(\frac{\pi}{2})} = 0$.

measurements for simulating g, is equivalent to entangling the qubits of $\mathcal{C}(g_1)$, performing the required measurements for g_1, then entangling the qubits of $\mathcal{C}(g_2)$ and performing the required measurements for g_2.

Proof. In the first method, the logical input state $|\psi_{\text{in}}\rangle$ is encoded onto the cluster qubits in the input section $\mathcal{C}_I(g_1)$ of the first subcluster. The entire cluster $\mathcal{C}(g)$ is then entangled and qubits in $\mathcal{C}(g) \setminus \mathcal{C}_O(g_2)$ are measured in the required bases, with the logical output state $|\psi_{\text{out}}\rangle$ present on the cluster qubits of $\mathcal{C}_O(g_2)$.

In the second method, the logical input state $|\psi_{\text{in}}\rangle$ is again encoded onto the cluster qubits in the input section $\mathcal{C}_I(g_1)$ of the first subcluster. The subcluster $\mathcal{C}(g_1)$ is then entangled and qubits in $\mathcal{C}(g_1) \setminus \mathcal{C}_O(g_1)$ are measured in the required bases, with the intermediate logical output state $|\psi'_{\text{out}}\rangle$ present on the cluster qubits of $\mathcal{C}_O(g_1) = \mathcal{C}_I(g_2)$. A similar procedure for the second subcircuit g_2 is carried out and the logical output state $|\psi''_{\text{out}}\rangle$ is present on the cluster qubits of $\mathcal{C}_O(g_2)$.

To show the two methods are equivalent, is to show that $|\psi_{\text{out}}\rangle = |\psi''_{\text{out}}\rangle$. Let P_1 and P_2 be projectors representing the measurements on qubits in $\mathcal{C}(g_1) \setminus \mathcal{C}_O(g_1)$ and $\mathcal{C}(g_2) \setminus \mathcal{C}_O(g_2)$ respectively with $S^{(\mathcal{C}(g_1))} =: S_1$ and $S^{(\mathcal{C}(g_2))} =: S_2$ representing the entanglement operations on subclusters $\mathcal{C}(g_1)$ and $\mathcal{C}(g_2)$ respectively. As P_1 commutes with S_2, we find that

$$P_2 S_2 P_1 S_1 = P_2 P_1 S_2 S_1, \tag{2.42}$$

This mixture of entangling operators and projectors acts on the state $|\psi_{\text{in}}\rangle_{\mathcal{C}_I(g)} \otimes_{a\in\mathcal{C}(g)\setminus\mathcal{C}_I(g)} |+\rangle_a$. As they act equivalently, we have that $|\psi_{\text{out}}\rangle = |\psi''_{\text{out}}\rangle = U_g U_\Sigma |\psi_{\text{in}}\rangle$ and the two methods are equivalent. □

Observation 1 can be extended to an arbitrary number of sub-gates g_i associated with unitary operators U_{g_i} on sub-clusters $\mathcal{C}(g_i)$. These then make up the gate g associated with the operator U_g on the entire cluster $\mathcal{C}(g)$. For each projector P_i there is an associated unitary operator U_{g_i} applied to the logical qubits. However U_{g_i} is not the only operation applied. Due to the fact that there are two possible outcomes for each qubit measured, the gate simulation is probabilistic. It turns out that for all the BBB's in the last section, the actual unitary operation implemented can be written as $U_{g_i} U_\Sigma(s_i)$ ($g_i = BBB_i$, $i = 1, 2, 3$), where $U_\Sigma(s_i)$ is a local byproduct operator dependent on the outcome $s_i := s_j^{xy(\alpha_j)}$ of the measurement performed on the j-th qubit in the $\mathcal{C}(g_i)\setminus\mathcal{C}_O(g_i)$ part of the cluster. In this way the unitary operation U_{g_i} becomes deterministic, as we can always propagate $U_\Sigma(s_i)$ through it, keeping the byproduct operator local. For a large concatenation of subclusters, this propagation procedure can be carried out for U_{g_i} and $U_\Sigma(s_a, s_b, s_c) = \sigma_x^{s_a}\sigma_y^{s_b}\sigma_z^{s_c}$, where $s_a, s_b, s_c \in \{0, 1\}$ are a result of the byproduct operators corresponding to the gates acting before U_{g_i}. However, when U_{g_i} is not in the Clifford group, it will change upon propagation of the byproduct operators through it. For all of the BBB's mentioned before, we find that this only occurs with $R_z^{-\alpha}\sigma_x^{s_a}$ and $R_z^{-\alpha}\sigma_y^{s_b}$. We may write

$$\begin{aligned} R_z^{-\alpha}\sigma_x^{s_a} &= \sigma_x^{s_a} R_z^{-\alpha'}, \\ R_z^{-\alpha}\sigma_y^{s_b} &= \sigma_y^{s_b} R_z^{-\alpha''}, \end{aligned} \tag{2.43}$$

where $\alpha' = (-1)^{s_a}\alpha$ and $\alpha'' = (-1)^{s_b}\alpha$. In other words the measurements must become adaptive, but the resources (in terms of the number of cluster qubits) never change, the byproduct operators always remain local and we can counteract their effect by changing the measurement angle from α to $-\alpha$. Overall, in a large concatenated circuit of BBB's, we end up with the logical input $|\psi_{\text{in}}\rangle$ and output

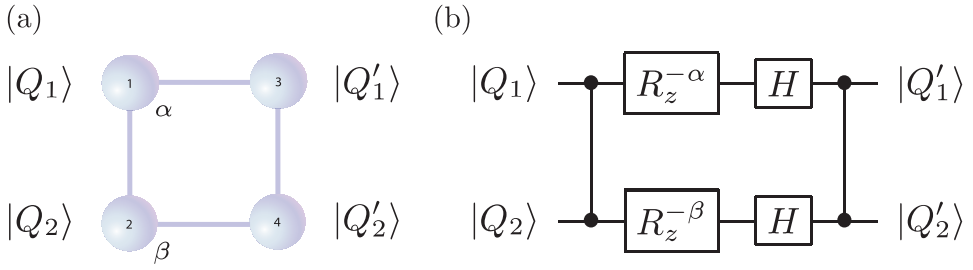

Figure 2.9: The concatenation of two BBB_1's (Fig. 2.6) with two BBB_2's (Fig. 2.7).

$|\psi_{\text{out}}\rangle$ of the unitary simulation $U_g = \prod_{i=|\mathcal{N}|}^{1} U_{g_i}$, related via

$$|\psi_{\text{out}}\rangle = \left(\prod_{i=|\mathcal{N}|}^{1} \tilde{U}_{\Sigma}(s_i) \right) \left(\prod_{i=|\mathcal{N}|}^{1} \tilde{U}_{g_i} \right) |\psi_{\text{in}}\rangle. \tag{2.44}$$

Here, $\mathcal{N}$ is the number of subgates, and the $\tilde{}$ represents the fact that the byproduct operators change on propagation, or the unitary operations of the subclusters become adaptive. A final note to add is that some byproduct operators will have to propagate *further* than others in this scheme. By applying the hermitian conjugate $\tilde{U}^{\dagger}_{\Sigma}(s_a, s_b, s_c) = (\prod_{i=|\mathcal{N}|}^{1} \tilde{U}_{\Sigma}(s_i))^{\dagger}$ of the propagated byproduct operators we will recover the unitary operation desired. The $\tilde{U}^{\dagger}_{\Sigma}(s_a, s_b, s_c)$ are decoding operators and for each logical qubit, they will always be a multiple from the set $\{\mathbb{1}, \sigma_x, \sigma_z, \sigma_y\}$ up to a global phase factor $\in \{1, -1\}$. We therefore recover the cluster state MB model for QC, without the need for the stabiliser formalism and eigenvalue equations of Eq. (2.38). It is now easier to see how to design the cluster configuration which simulates a desired quantum circuit and we are on our way toward the construction of computationally useful *extended* building blocks (EBB's). By concatenating two BBB_1's and two BBB_2's, we produce a two-dimensional square cluster state, also known as a *box cluster*. This cluster configuration has recently been experimentally realised and used in order to perform a two-qubit quantum search algorithm [71, 76, 80] and a two-player quantum game [81]. The physical layout, the measurement pattern and the corresponding equivalent circuit are shown in Fig. 2.9. Next, by concatenating two BBB_1's and a BBB_2, we obtain a simple four-qubit linear cluster. This is particularly interesting because if the single-qubit measurements are performed in the σ_x-eigenbasis, the corresponding equivalent quantum circuit is locally equivalent

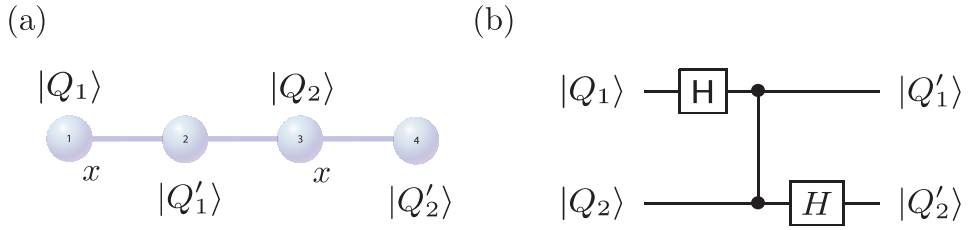

Figure 2.10: The concatenation of two BBB_1's and one BBB_2 with measurements in the $B_1(0)$ and $B_3(0)$ basis.

to a CNOT gate (controlled-σ_x operation) *i.e.* the read-out bases of qubits 2 and 4 are the σ_x eigenbases instead of the usual σ_z ($\{|0\rangle, |1\rangle\}$) [136]. The layout and the measurement pattern are shown in Fig. 2.10. The importance of this cluster configuration will be commented on in the next Chapter, where its role in an economical scheme for cluster state MB QIP is highlighted. For the moment, it is instructive to explicitly compute the byproduct operator corresponding to this gate simulation. The decoding operator needed after the measurement pattern in BBB_1 is given by either $\mathbb{1}$ or σ_x, depending on the outcome of the measurement performed. Thus, including the random action of the byproduct operators, the transformation in Fig. 2.10 can be represented overall by

$$\left(\mathbb{1} \otimes \sigma_x^{s_3^{xy(0)}}\right) (\mathbb{1} \otimes \mathsf{H})\ \mathsf{CZ} \left(\sigma_x^{s_1^{xy(0)}} \otimes \mathbb{1}\right) (\mathsf{H} \otimes \mathbb{1}). \tag{2.45}$$

Note that no rotation operator appears in the above expression because of the choice of $B_1(0)$ and $B_3(0)$ for the measurement pattern. Using the fact that $\mathsf{CZ}(\sigma_x \otimes \mathbb{1}) = (\sigma_x \otimes \sigma_z)\mathsf{CZ}$ and that $\mathsf{H}\ \sigma_z = \sigma_x \mathsf{H}$, the $(\sigma_x^{s_1^{xy(0)}} \otimes \mathbb{1})$ part in Eq. (2.45) can be propagated until we end up with $\tilde{U}_\Sigma\ (\mathbb{1} \otimes \mathsf{H})\ \mathsf{CZ}\ (\mathsf{H} \otimes \mathbb{1})$, where

$$\tilde{U}_\Sigma = \sigma_x^{(2)s_1^{xy(0)}} \otimes \sigma_x^{(4)[s_1^{xy(0)} \oplus s_3^{xy(0)}]}, \tag{2.46}$$

with $\oplus$ as the logical XOR operation. This result is therefore easily demonstrated by a simple argument based on the concatenation technique. Our EBB set is completed by the configuration in Fig. 2.11 **(a)**, *i.e.* the concatenation of one BBB_3 and two BBB_1's. The bases for the measurement pattern are $B_{1\to 3}(\alpha = \pi/2)$ and qubits 1 and 3 encode the input states. The overall transformation is decomposed as shown in Fig. 2.11 **(b)**. Following the lines depicted above, the propagated byproduct operator corresponding to this gate simulation is $\tilde{U}_\Sigma =$

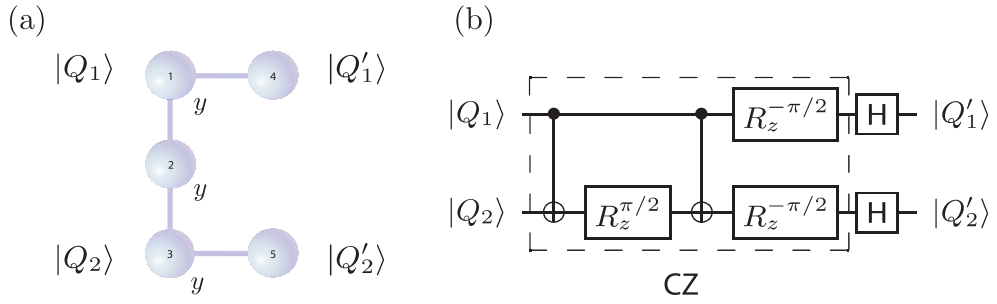

Figure 2.11: **(a)**: The configuration obtained by concatenating two BBB_1's with a BBB_3. The single-qubit measurements are in the $B_{1\to 3}(\pi/2)$ bases. **(b)**: The corresponding equivalent quantum circuit. The boxed part is equivalent to a CZ gate.

$\sigma_x^{(4)s_1^{xy(\pi/2)}\oplus s_2^{xy(\pi/2)}} \otimes \sigma_x^{(5)s_3^{xy(\pi/2)}\oplus s_2^{xy(\pi/2)}}$. We will see in the next Chapter that this EBB plays a central role in the original fifteen qubit CNOT gate simulation discussed in Ref. [130].

2.5 Remarks

In this Chapter, the relevant tools and concepts needed for Chapters 3-7 of the thesis have been introduced. The concept of a qubit was discussed, along with that of entanglement and the various tools one can use to measure it. The evolution of closed and open quantum systems and the role of decoherence was also outlined, together with a description of how general measurements can be formalised in quantum mechanics. Finally, the MB one-way model for QIP was introduced and it was shown how protocols can be performed as a simulation using highly entangled multipartite cluster state as a resource. With these tools now 'at hand', we can begin our investigation into MB QIP with imperfect operation.

Chapter 3

Imperfect resources

This Chapter is concerned with the analysis of basic MB QIP protocols under the effect of intrinsic non-idealities in cluster states. These non-ideal conditions are based on the introduction of randomness in the entangling steps that create the cluster state and are motivated by the unavoidable imperfections faced when creating entanglement using condensed-matter systems. Phase damping is a significant source of decoherence in these systems also and therefore its action on individual qubits in a cluster is studied. Aided by the use of the efficient concatenation method introduced in Chapter 2, that allows one to easily construct a cluster state configuration for a given quantum protocol, quantum state transfer and various fundamental gate simulations through noisy cluster states are addressed. It is found that in order to limit the effects of noise, the management of small clusters processed via just a few measurements is the best strategy. In light of this, an experimentally realisable four-qubit linear cluster state which simulates a CNOT gate is addressed. This study also reinforces recent ideas related to all-optical implementations of MB one-way quantum computers.

3.1 Introduction

The class of cluster states and their related protocols for QC provide an interesting perspective for the realisation of MB QIP tasks. However their realistic operation deserves a deeper analysis and understanding. For example, it is still not clear if the MB model is more robust against the effects of external sources of noise and imperfection than the standard quantum circuit model. Initial studies with regards to this have shown that Markovian noise affecting a cluster state when one-way QC is being carried out on it can be mapped into non-Markovian imperfections in the corresponding quantum circuit being simulated [138]. Thus, one can take advantage of already existing theorems, valid for the quantum circuit model [139], to find proper thresholds for fault-tolerant cluster state computation [137, 138, 140]. A realistic model for imperfect cluster state generation will be introduced in the next Section and an analysis of how this affects both the intrinsic properties of cluster states and the basic ingredients in computation will be given. The consequences of decoherence due to phase damping individually affecting the qubits in one- and two-dimensional configurations will also

be addressed. The analysis of effects resulting from the model for noise on various key QIP protocols will be undertaken using the *concatenation* technique for the construction of compact configurations in the $\mathrm{QC}_{\mathcal{C}}$ model, as introduced in Chapter 2. With this technique, one can bypass the stabiliser formalism approach [130] and quickly construct economical circuit simulations using cluster states. To highlight this, a CNOT simulated on a simple four-qubit linear cluster is introduced and an outline for an all-optical setup where it can be implemented is also given.

3.2 Imperfect Generation of a Cluster State

The key element in generating a cluster state is the ability to perform the controlled gates $S^{ab} = |0\rangle_a\langle 0| \otimes \mathbb{1}^{(b)} + |1\rangle_a\langle 1| \otimes \sigma_z^{(b)}$ on the qubits a and b occupying the sites of a cluster $\mathcal{C}$. However, these operations can be inherently imperfect or not precisely controllable. For example, an optical lattice loaded by neutral atoms is a candidate for the embodiment of a $\mathrm{QC}_{\mathcal{C}}$ [141–144]. In this particular setup, two-qubit interactions are realised through controlled collisions of the atoms loading the optical lattice, using either switching or moving-trap potentials [145, 146]. Several experiments [141, 142] consider a one-dimensional lattice loaded with neutral atoms such as ^{87}Rb containing two selected hyperfine levels $|c_1\rangle$ and $|c_2\rangle$ that embody the qubit degrees of freedom. The state of an atom occupying the j-th site in the lattice, prepared in its internal state $|c_1\rangle$ ($|c_2\rangle$), can be described by an application of the bosonic creation operator $\hat{c}_1^{(j)\dagger}$ ($\hat{c}_2^{(j)\dagger}$) to a fiducial initial atomic state. The Hamiltonian describing the atomic dynamics takes the form of a *two-species* Bose-Hubbard model [144]

$$H_{ol} = \sum_{j=1}^{N}\left[\frac{1}{2}U_1\hat{c}_1^{(j)\dagger}\hat{c}_1^{(j)\dagger}\hat{c}_1^{(j)}\hat{c}_1^{(j)} + \frac{1}{2}U_2\hat{c}_2^{(j)\dagger}\hat{c}_2^{(j)\dagger}\hat{c}_2^{(j)}\hat{c}_2^{(j)} + U_{12}\hat{c}_1^{(j)\dagger}\hat{c}_2^{(j)\dagger}\hat{c}_1^{(j)}\hat{c}_2^{(j)}\right]. \tag{3.1}$$

Here, $U_{1,2}$ (U_{12}) corresponds to the strength of an on-site repulsive force experienced by two atoms of the same (different) *species*. In general, the two-species Bose-Hubbard Hamiltonian would also include a *hopping* term $\sum_{<i,j>}(h_1^{ij}\hat{c}_1^{(i)\dagger}\hat{c}_1^{(j)} +$

$h_2^{ij}\hat{c}_2^{(i)\dagger}\hat{c}_2^{(j)}$), where the $h_{1,2}^{ij}$ correspond to the strength of tunneling between sites i and j for the same species (the summation is extended to all the nearest neighbour sites i, j, denoted by $< i, j >$). The model in Eq. (3.1) assumes $U_{1,2}, U_{12} \gg \max\{h_{1,2}^{ij}, \forall i, j\}$, which corresponds to the Mott-insulator regime [147]. Each term in Eq. (3.1) is responsible for giving dynamical phases $e^{i\phi_{mk}}$ to the joint internal states $|c_m\rangle |c_k\rangle$ $(m, k = 0, 1)$ of two atoms that are made to occupy the same lattice site. To do this, one starts from a Mott-insulator with one atom per lattice site and employs switching or moving-trap potential techniques [145, 146] to selectively address individual atomic species in a lattice-wide fashion. By varying the laser parameters correctly one can induce phases conditioned on the internal states of atoms at adjacent lattice sites a and b to give $|c_m\rangle_a |c_k\rangle_b \rightarrow (-1)^{mk} |c_m\rangle_a |c_k\rangle_b$. However, the U parameters are in general a function of the position in the lattice (*i.e.* they have a spatial profile along the linear lattice) and therefore their values can fluctuate due to instabilities in the intensities of the lasers used in order to create the lattice. Fluctuating U's give rise to a random phase shift $e^{i\theta}$ imposed during the qubit-qubit interaction, which may be different from the $\theta = \pi$ value required to attain a perfect cluster state. Thus, the accuracy of the S^{ab}'s critically depends on the control we have over the strength of the interactions. The initial filling-fraction of the lattice may also influence the performances of the gates and the extent to which entanglement can be spread across the cluster [141, 142, 144]. If the degree of control is not optimal, we face the problem of imperfect (inhomogeneous) interactions throughout the physical lattice. Here, this issue is addressed formally by considering imperfect entangling operations S_D^{ab}'s on the qubits of the cluster. The model consists of controlled-phase gates having the form

$$S_D^{ab} = |0\rangle_a\langle 0| \otimes \mathbb{1}^{(b)} + |1\rangle_a\langle 1| \otimes \left(|0\rangle_b\langle 0| - e^{i\theta_a}|1\rangle_b\langle 1|\right), \tag{3.2}$$

which add the phase θ_a to the desired and optimal π. As in the ideal case, all S_D^{ab}'s mutually commute and the imperfect entangling operation $S_D^{\mathcal{C}} = \prod_{<a,b>} S_D^{ab}$ is unitary (see Eq. (2.32) in Chapter 2).

Let us consider the use of Eq. (3.2) for the generation of a one-dimensional noisy cluster state (a *noisy linear cluster state*). By applying $S_D^{\mathcal{C}}$ to the product state

$|+\rangle_{\mathcal{C}}$ of N qubits in a linear configuration, we find

$$|\phi\rangle_{\mathcal{C}}^{D} = S_{D}^{\mathcal{C}}|+\rangle_{\mathcal{C}} = 2^{-N/2}\sum_{\mathbf{z}_i}\prod_{j=1}^{N-1}(-e^{i\theta_j})^{z_j^i z_{j+1}^i}|\mathbf{z}_i\rangle, \tag{3.3}$$

where z_j^i is the value of the j-th binary digit of the integer $\mathbf{z}_i$ and the summation runs over all the $\mathbf{z}_i$ for $i \in \{0, ..., 2^N - 1\}$.

In order to characterise the effect of this kind of non-ideality, an immediate benchmark is provided by the fidelity[1] between ideal and noisy cluster states. The overlap $f_N = {}_{C_N}\langle\phi|\phi\rangle_{C_N}^{D}$, where $|\phi\rangle_{\mathcal{C}_N}$ is obtained from Eq. (3.3) with $\theta_j = 0, \forall j$, leads to $f_N = 2^{-N}\sum_{\mathbf{z_i}}\prod_{j=1}^{N-1} e^{i\theta_j z_j^i z_{j+1}^i}$. There are 2^N terms in this expression, with the fidelity given by $\mathcal{F}_N = |f_N|^2$. However, the assumption is that the control on the phases introduced by the qubit-qubit interaction is limited. Thus, there is a lack of knowledge about the values of the θ_j's in a noisy cluster state. This means that each of them must be averaged over an appropriate probability distribution. We can set a range $\mathbf{r}_j$ within which each phase can take values from and introduce the probability distribution $p(\theta_j)$. The average overlap $\bar{f}_N$ for the noisy linear cluster state becomes

$$\bar{f}_N = 2^{-N}\sum_{\mathbf{z_i}}\prod_{j=1}^{N-1}\{\int_{|\mathbf{r}_j|} p(\theta_j)e^{i\theta_j}d\theta_j\}^{z_j^i z_{j+1}^i}, \tag{3.4}$$

where $|\mathbf{r}_j|$ is the *width* of the range of variation of θ_j and $p(\theta_j)$ depends on the specific physical model used in the cluster state generation. The nature of the fluctuations of the phases is characterised by the way in which the interactions among the elements of a lattice are realised and thus there is no *universal model*. In Fig. 3.1 **(a)** an example of $\bar{\mathcal{F}}_N$ for a flat $p(\theta_j)$ distribution is provided, for the case of linear clusters of various lengths. A large deviation from the ideal state is found with this qualitative behaviour holding irrespective of the model used for the unwanted phase distribution. The analysis can be extended to two-dimensional cluster states where analogous qualitative results can be found. The

[1]The fidelity $\mathcal{F}(\rho,\sigma) = \mathrm{Tr}(\sigma^{1/2}\rho\sigma^{1/2})$ represents a *distance measure* [128] which quantifies how close two quantum states ρ and σ are to each other. It is symmetric in its inputs $\mathcal{F}(\rho,\sigma) = \mathcal{F}(\sigma,\rho)$ and $0 \leq \mathcal{F} \leq 1$, with equality in the first inequality *iff* ρ and σ are supported on orthogonal subspaces and equality in the second inequality *iff* $\rho = \sigma$. In the case of pure states $\rho = |\phi\rangle\langle\phi|$ and $\sigma = |\psi\rangle\langle\psi|$ we have $\mathcal{F}(\rho,\sigma) = |\langle\phi|\psi\rangle|^2$.

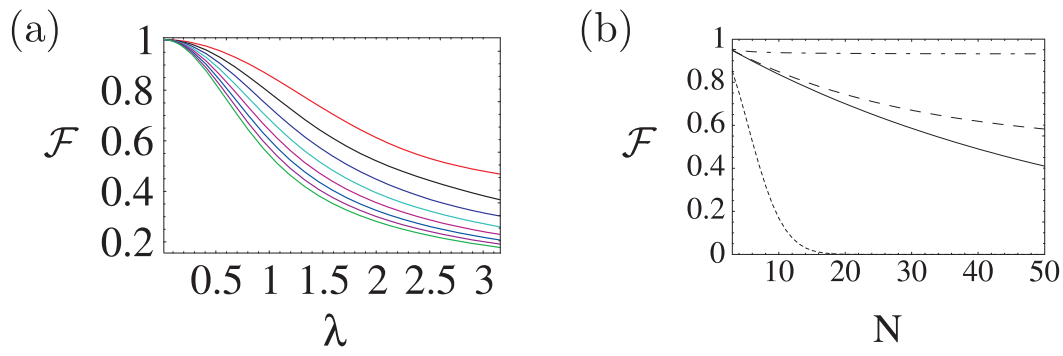

Figure 3.1: **(a)**: $\bar{\mathcal{F}}_N$ against $|\mathbf{r}_j| = \lambda$ for $p(\theta_j) = \lambda^{-1}$. From top to bottom $N = 3 \rightarrow 10$. **(b)**: Phase damping effects on multiqubit entangled states. The curves from top to bottom represent N-qubit W, GHZ, linear cluster and $N \times N$ cluster states. For convenience, the rescaled phase damping time is $\Gamma = 0.062$ (corresponding to $\mathcal{F}_{50}^{C_{lin}} = 0.5$). Similar behaviours are found for different values of Γ.

structure of the quantum correlations has also been observed to be profoundly different from what is found in $|\phi\rangle_{\mathcal{C}_N}$. Genuine multipartite entanglement is shared between the subparties of ideal cluster states, where the entanglement is encoded in the state as a whole [55, 56]. Any reduced bipartite state, obtained by tracing out all the qubits but an arbitrary pair, is separable as it does not violate the necessary and sufficient Peres-Horodecki criterion for separability of a mixed qubit state [100–102]. However the imperfect S_D^{ab}'s alter this result. For example, take a linear cluster of $N = 3$, the ideal state is locally equivalent to a Greenberger-Horne-Zeilinger (GHZ) state $|\psi_{GHZ}\rangle = (1/\sqrt{2})(|000\rangle + |111\rangle)$ and tracing out any one of the qubits should give a separable state of the remaining two qubits [148]. However, two unwanted phases are embedded in the corresponding noisy state $|\phi\rangle_{\mathcal{C}_3}^D$. The partial trace of $|\phi\rangle_{\mathcal{C}_3}^D\langle\phi|$ over the third qubit gives a bipartite state which violates the Peres-Horodecki criterion for $\theta_2 \neq k\pi$ ($k = 0, 1, ..$) and $\forall\, \theta_1 \neq \pi$. This is a characteristic shared by all the two-qubit states obtained by tracing qubits 3 to N in a given $|\phi\rangle_{\mathcal{C}_N}^D$.

In order to quantify the entanglement of the reduced density matrices ρ_{ij} ($i, j \in \{1, ..., N\}$, $i \neq j$), we can use the *concurrence* $C_{ij} \equiv C(\rho_{ij})$ (see Chapter 2). One finds that only nearest-neighbour bipartite entanglement is settled in a symmetric way along an arbitrarily long noisy cluster (*e.g.* $C_{12} = C_{(N-1)N}$, irrespective of N), while any non-nearest neighbour entanglement is absent due

to the randomness, more pronounced in pairs of non-nearest neighbour qubits. In this case the corresponding density matrices depend, in general, on more unwanted phases than those of nearest neighbour ones[2]. The average concurrence obtained by assuming Gaussian fluctuations of each θ_j, around $\theta_j = 0$ and with a standard deviation σ can also been considered. It is found that as σ increases (up to $\sigma = 1$), the fragile quantum correlations of the *body pairs* $(i, i+1)$ with $i \in \{2, ..., N-2\}$ disappear, breaking the quantum channel connecting input qubit 1 to output qubit N. This is due to the fact that the qubits in these pairs (after tracing out the rest) are exposed to more randomness than those in the pairs $(1, 2)$ and $(N-1, N)$. We are left with the entangled mixed states of these *extremal* pairs which can mutually share only classical correlations. By increasing the randomness, even this entanglement will disappear eventually. The analysis can be extended to the case of arbitrary N, despite the difficulties in finding the reduced density matrices of large cluster states [149]. Thus, the multipartite entanglement is reduced to the benefit of bipartite correlations which may be very fragile against fluctuations in the unwanted phases, possibly leading to a complete entanglement-breaking effect.

In addition to studying the imperfect generation of cluster states, it is also interesting to understand the effects of decoherence. This is important for physical realisations, as the accuracy of a logical gate simulated on a cluster state interacting with an environment may be spoiled. Here, decoherence due to individual phase damping affecting each qubit in the cluster is considered, a model which is relevant in practical situations of qubits exposed to locally fluctuating potentials. In this case the off-diagonal elements of a single-qubit density matrix ρ^d decay as $e^{-\Gamma}$, with Γ the rescaled phase daming time (see Chapter 2). For a single qubit prepared in $|+\rangle$, the fidelity is $\mathcal{F} = \langle +|\rho^d|+\rangle = \frac{1}{2}(1 + e^{-\Gamma})$. For large clusters of qubits, it is relevant to compare their behaviour under phase damping with other multiqubit states such as the GHZ and W states given by (for $N \geq 3$) $|\psi_{GHZ^N}\rangle = (1/\sqrt{2})(|00...0\rangle + |11...1\rangle)$ and $|\psi_{W^N}\rangle = (1/\sqrt{N}) \sum_{perm} perm(|0...01\rangle)$ respectively. Here $perm(|\phi\rangle)$ corresponds to a binary permutation of the state $|\phi\rangle$. For N-qubit GHZ and W states, the state fidelities are $\mathcal{F}_N^{GHZ} = (1 + e^{-\Gamma N})/2$ and $\mathcal{F}_N^W = (1 + (N-1)e^{-2\Gamma})/N$, while for N-qubit ($N \geq 2$) linear cluster states $\mathcal{F}_N^{C_{lin}} = 2^{-N} \sum_{h=0}^{N} B(N, h) e^{-\Gamma h}$, with the binomial coefficient $B(N, h)$. The ex-

[2]Note that at $\theta_j = \pi\,(\forall j)$ no entanglement is found, as in this case $S_D^{ij} \equiv \mathbb{1}^{ij}$.

pression for an $N \times N$ cluster is found for $N \to N^2$. These functions are plotted against N and shown in Fig. 3.1 **(b)**, where one can see that when state fidelity is used as a benchmark, linear cluster states are quite fragile against individual phase damping.

3.3 Information flow across a noisy linear cluster

From the previous Section one can see that MB QIP protocols should be strongly affected by imperfections in the initial entanglement created between the qubits in a cluster. Here, a broader picture of the effect of this noise model on various key QIP protocols is given. We can now start the analysis of the performances of one-way protocols for QIP with *noisy cluster states*. While Section 3.4 will be dedicated to the basic computational steps, here a communication issue represented by the transfer of quantum information through a cluster state is considered. We can then determine the reliability of state transmission along a quantum channel represented by a linear cluster. Quantum state transfer has recently received considerable attention in the context of limited-resource QIP [150–153]. Here, the approach will be to use a quantum resource provided by the multipartite entanglement in a cluster state and conditioned dynamics given by measurements.

The idea behind the realisation of information flow through a cluster state is simple. In the one-way model, seen from the original stabiliser viewpoint, any set of single-qubit measurements performed on the qubits belonging to $\mathcal{C}_M(g)$, together with the measurements in the σ_x-eigenbasis of the qubits in $\mathcal{C}_I(g)$ (see Section 2.4.2), processes the encoded input state and at the same time, transfers it to the $\mathcal{C}_O(g)$ section. Thus, one can naively think about simulating the identity gate $g = \mathbb{1}$ using an appropriate linear cluster state, where the transfer of the input state to the output section of the cluster occurs naturally. However it is much simpler to think of this information flow in a linear cluster in terms of the concatenation of many BBB_1's. In this case, measuring qubit 1 in the $B_1(0)$ basis, means the encoded state is transferred to 2, while at the same time rotated

by H (see Fig. 2.6 in Chapter 2). Thus, forgetting for the moment the effect of the byproduct operator, by arranging the concatenation of many BBB_1's, *i.e.* a pattern of measurements in the single-qubit σ_x-eigenbasis for all the qubits in $\mathcal{C}_I(g) \cup \mathcal{C}_M(g)$ of a sufficiently long linear cluster, either we realise the information flow we are looking for (when the number of effective Hadamard gates is even) or we simply obtain $|\psi_{\text{out}}\rangle = \mathsf{H}\,|\psi_{\text{in}}\rangle$ which can be corrected once we know the parity of N.

The question raised here is about the efficiency of the transfer process when imperfect resources are used. Ideally the fidelity for information transfer would be equal to unity. However, this is not the case if noisy linear clusters are considered. In order to obtain a full picture of the protocol for information flow, we need to calculate the form of the correct decoding operator arising after the concatenation of many BBB_1's.

3.3.1 Identity and Hadamard gate

We already know that BBB_1 with $B_1(0)$ effectively simulates H on a logical qubit $|\psi_{\text{in}}\rangle$, with $\tilde{U}_\Sigma = \sigma_x^{s_1^{xy(0)}}$. If we now concatenate two BBB_1's to obtain a three-qubit linear cluster, by measuring qubits 1 and 2 we simulate

$$\sigma_x^{s_2^{xy(0)}} \mathsf{H} \sigma_x^{s_1^{xy(0)}} \mathsf{H} = \underbrace{\sigma_x^{s_2^{xy(0)}} \sigma_z^{s_1^{xy(0)}}}_{\tilde{U}_\Sigma} \mathbb{1} \tag{3.5}$$

on the logical qubit $|\psi_{\text{in}}\rangle$. The decoding operator to decode the logical information transferred to and stored on qubit 3 is then given by $\tilde{U}_\Sigma^\dagger = \sigma_z^{s_1^{xy(0)}} \sigma_x^{s_2^{xy(0)}}$. The advantage of using this concatenation technique with respect to the stabiliser formalism will be evident when larger linear clusters are considered.

3.3.2 Information flow

In the concatenation model, for an arbitrarily long odd-N qubit cluster state, the concatenation of $N-1$ BBB_1's results in $\prod_{i=(N-1)}^{1} (\sigma_x^{s_i^x} \mathsf{H})$ applied to the

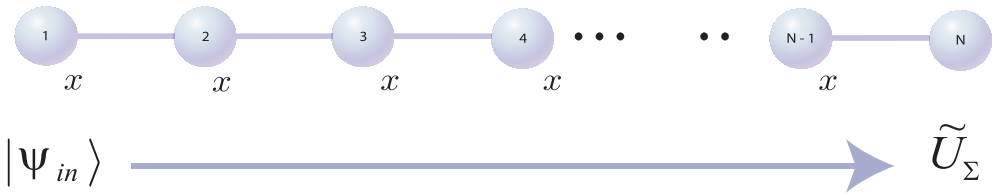

Figure 3.2: Information flow through an N-qubit linear cluster.

input state $|\psi_{\rm in}\rangle$, where $s_i^x = s_i^{xy(0)}$ is set for convenience. Each time the σ_x Pauli matrix corresponding to an even-labelled qubit is propagated through an H, thus being transformed into a σ_z-Pauli matrix, the product $\mathsf{HH} = \mathbb{1}$ is obtained and the σ_x-Pauli matrices of odd-labelled qubits remain unchanged. This results in all the even labels (odd labels) becoming associated with σ_z (σ_x) and we obtain the following structure for the propagated byproduct operator

$$\tilde{U}_{\Sigma} = \sigma_z^{(N)s_1^x \oplus (\sum_{i=2}^{(N-1)/2} s_{2i-1}^x) \mathrm{mod} 2} \sigma_x^{(N)s_2^x \oplus (\sum_{i=2}^{(N-1)/2} s_{2i}^x) \mathrm{mod} 2} . \tag{3.6}$$

So far, we have just dealt with ideal cluster states. The above protocol for the transfer of information encoded in $|\psi_{\rm in}\rangle = a|0\rangle + \sqrt{1-a^2}|1\rangle$ across an N-qubit noisy linear cluster is now considered. The theoretical analysis developed up until now can still be applied to the case of $S^{ab} \rightarrow S_D^{ab}$ *i.e.* the form of the byproduct operator is the same as Eq. (3.6). The measurement pattern for information flow on an encoded noisy linear cluster state can be simulated. Despite the computational challenge represented by the exponentially growing number of different outcome sets (for an N-qubit linear cluster, there are 2^N different sets $\{s_j^x\}$, $j \in \{1, ..., N\}$), it has been possible to explicitly calculate the state transfer fidelity $\mathcal{F}_N(a, \theta_j) = |\langle\psi_{\rm in}|\psi_{out}\rangle|^2$ for each outcome set, up to $N = 9$ qubits. This enables an evaluation of $\tilde{\mathcal{F}}_N(a, \theta_j)$, *i.e.* the state fidelity *averaged* over all the different sets of measurement outcomes, after the application of the relevant decoding operator given by the hermitian conjugate of Eq. (3.6). This quantity gives an estimate of the average performance of the transfer process. It is important to note that this approach is only one of the possibilities available, the other being the postselection of the event corresponding to a favourable outcome configuration. For example, one could choose to discard all the events but the one where $s_j^x = 0$, $\forall j \in \{1, ..., N\}$ as this case corresponds to $\tilde{U}_{\Sigma}^{\dagger} = \mathbb{1}^{(N)}$ and therefore no local adjustment is required after the simulation of the identity

gate.

However, in order to perform a more quantitative investigation and wash out any initial state-dependence, the average state-transfer fidelity for any input state $|\psi_{\rm in}\rangle$ must be considered [150–153]. This can be done by assuming a uniform distribution for a and integrating over the Bloch sphere surface as $\bar{\mathcal{F}}_N(\theta) = (1/4\pi)\int \tilde{\mathcal{F}}_N(a,\theta)d\Sigma$, where $d\Sigma$ is the surface element. The comparison between $\tilde{\mathcal{F}}_N(a,\theta_j)$ and $\bar{\mathcal{F}}_N(\theta)$ reveals an almost uniform behaviour of $\mathcal{F}_N(a,\theta)$ with a. On the other hand, the integration over the Bloch sphere's surface allows one to compare $\bar{\mathcal{F}}_N(\theta)$ with 2/3, the best fidelity achievable by measuring an unknown qubit state along a random direction and then sending the result through a classical channel using classical correlations [154] (see also Bose and Paternostro *et al.* [150–153]). The value 2/3 can therefore be seen as a threshold value for $\bar{\mathcal{F}}_N(\theta)$ that confirms entanglement must have been used in the transfer process along the cluster [155]. The analysis of $N = 3, 5, 7$ and 9-qubit cases in Fig. 3.3 **(a)** reveals that as soon as $\theta \simeq 0.65$, $\bar{\mathcal{F}}_9(0.65) < 2/3$. By increasing θ, all the other transfer fidelities (except the case of $N = 3$) become worse than the classical threshold value and are thus useless for quantum state transfer. The range of usefulness of the cluster channel shown in Fig. 3.3 **(a)** is considerably small if probability distributions attached to the θ_j's are considered. A quantitative addressing of the case for individual Gaussian functions, centered on $\theta_j = 0$ and with increasing standard deviation σ has been performed. In Fig. 3.3 **(b)**, the totally averaged fidelity $\mathcal{F}_{N,\sigma} \propto \int p(\theta,\sigma)\bar{\mathcal{F}}_N(\theta)d\theta$, for a Gaussian $p(\theta,\sigma)$ which retains a parameterisation in N and the standard deviation σ is shown. For $\sigma = 1$, it can be seen that already for $N \geq 4$ the cluster channel becomes less efficient than the best classical strategy for transfer. On the other hand, by reducing the amount of randomness in the noisy cluster state, *i.e.* by reducing the spread of the distribution down to $\sigma = 0.5$, the usefulness of the transfer protocol is restored, but only for cluster channels of just a few qubits ($N < 8$). Thus, the conclusions drawn here from the study of state transfer through linear cluster states coincide with those previously found for the state fidelity in Section 3.2: whenever intrinsic random imperfections are considered within the cluster state model, the dimension of the resource will play a critical role in the efficiency of a QIP protocol carried out on it.

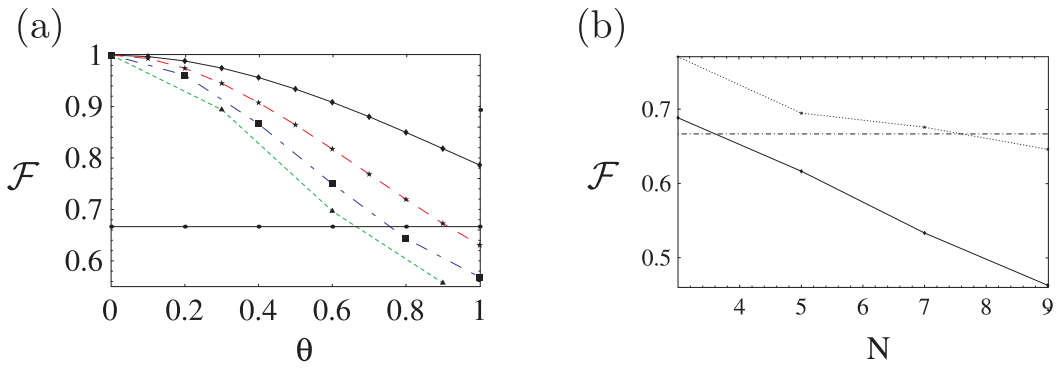

Figure 3.3: **(a)**: Fidelity of information transfer with a averaged over the single-qubit Bloch sphere and all phases $\theta_j = \theta$ $(\forall j)$. From top to bottom curve, we show $N = 3$ (⧫), $N = 5$ (★), $N = 7$ (■) and $N = 9$ (▲). The horizontal line (•) represents the classical threshold 2/3. **(b)**: Fidelity of information transfer with a averaged over the Bloch sphere and θ_j averaged over Gaussian distributions, centered on $\theta_j = 0$, with standard deviation $\sigma = 0.5$ (★, dotted line) and $\sigma = 1$ (⧫, solid line). Again, the classical threshold is shown for comparison (■).

3.4 Computation with noisy cluster states

We are now in a position to investigate the performance of the $\mathrm{QC}_{\mathcal{C}}$ model within the framework of noisy cluster states. In this Section, both single-qubit rotations and two-qubit entangling gates are addressed, paying particular attention to the *paradigm* of this class of gates, the CNOT. The gate fidelity relative to these operations will be thoroughly studied against the effects of unwanted phases introduced by the S_D^{ab}'s.

3.4.1 Arbitrary rotation

The approach used to simulate arbitrary rotations $U_R \in SU(2)$ [130] requires the decomposition of the rotation in terms of the elements of the Euler-angle vector $\mathbf{\Omega} = (\zeta, \nu, \xi)$ as $U_R = R_x^{\zeta} R_z^{\nu} R_x^{\xi}$, where the elementary rotations around the j-axis $(j = x, z)$ are given by $R_j^{\Omega_i} = \exp(-i\Omega_i \sigma_j/2)$. In order to simulate the action of U_R on the input state $|\psi_{\mathrm{in}}\rangle$, we require a five-qubit linear cluster state[3]

[3]It is possible to use just four qubits, however one must allow the operation H to be included in the byproduct operator [71, 76]. Here the standard case of only Pauli operations in the byproduct is considered.

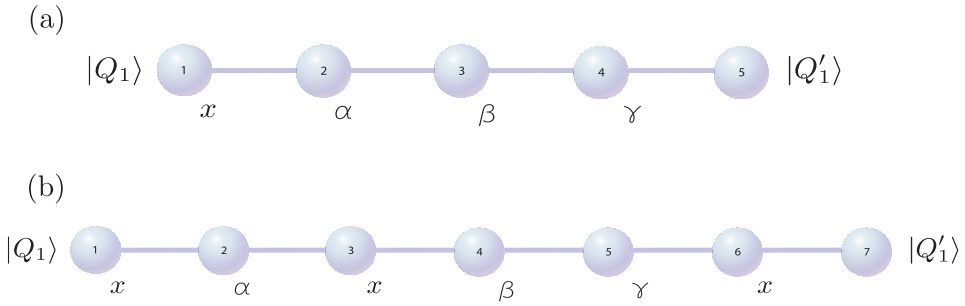

Figure 3.4: **(a)**: The layout for a single-qubit rotation where the input logical state encoded on qubit 1, is rotated by U_R and transfered to qubit 5 after the measurements shown. **(b)**: A modified configuration with two redundant qubits (qubit 3 and 6) which are removed via σ_x measurements.

and the pattern shown in Fig. 3.4 **(a)** [130]. The pattern consists of single-qubit measurements along directions in relation to the Euler angles. These relations can be seen very easily if one pictures Fig. 3.4 **(a)** as a concatenation of four BBB_1's. In this case we have

$$\begin{aligned}
&\sigma_x^{s_4^{xy(\gamma)}} \mathsf{H} R_z^{-\gamma} \sigma_x^{s_3^{xy(\beta)}} \mathsf{H} R_z^{-\beta} \sigma_x^{s_2^{xy(\alpha)}} \mathsf{H} R_z^{-\alpha} \sigma_x^{s_1^{xy(0)}} \mathsf{H} \\
&\equiv \sigma_x^{s_4^{xy(\gamma)}} \sigma_z^{s_3^{xy(\beta)}} \sigma_x^{s_2^{xy(\alpha)}} \sigma_z^{s_1^{xy(0)}} \mathsf{H} R_z^{-\gamma'} \mathsf{H} R_z^{-\beta'} \mathsf{H} R_z^{-\alpha'} \mathsf{H} \\
&\equiv \tilde{U}_\Sigma R_x^{-\gamma'} R_z^{-\beta'} R_x^{-\alpha'}, \qquad (3.7)
\end{aligned}$$

where $\alpha' = (-1)^{s_1^{xy(0)}} \alpha$, $\beta' = (-1)^{s_2^{xy(\alpha)}} \beta$ and $\gamma' = (-1)^{s_1^{xy(0)} \oplus s_3^{xy(\beta)}} \gamma$ with $\tilde{U}_\Sigma^\dagger = \sigma_z^{(5) s_1^{xy(0)} \oplus s_3^{xy(\beta)}} \sigma_x^{(5) s_2^{xy(\alpha)} \oplus s_4^{xy(\gamma)}}$. The measurement bases have now become adaptive, however this does not pose a problem as long as one measures in the order of the qubits in the cluster. Then by redefining the angles for the measurement bases as $\alpha = (-1)^{s_1^{xy(0)}}(-\xi)$, $\beta = (-1)^{s_2^{xy(\alpha)}}(-\nu)$ and $\gamma = (-1)^{s_1^{xy(0)} \oplus s_3^{xy(\beta)}}(-\zeta)$, we can simulate the correct rotation U_R. The procedure is now used to simulate the rotation of the input state $|\psi_{\text{in}}\rangle = a|0\rangle + b|1\rangle$, $(b = \sqrt{1-a^2})$ via a five-qubit noisy linear cluster. The postselection of the measurement results corresponding to the measurement of the tensorial product $|+\rangle_1 |+\rangle_2^\alpha |+\rangle_3^\beta |+\rangle_4^\gamma$ is assumed for convenience. It is easy to write the form of the input state-encoded cluster state

$$a\,|0\rangle_1 \left(|\eta\rangle^D + |\mu\rangle^D\right)_{2,3,4,5} + b\,|1\rangle_1 \left(|\eta\rangle^D - e^{i\theta_1}\,|\mu\rangle^D\right)_{2,3,4,5}, \qquad (3.8)$$

where $|\eta\rangle^D$ ($|\mu\rangle^D$) is the part of the noisy subcluster state which has the first qubit in $|0\rangle$ ($|1\rangle$) and the qubit labels have been explicitly introduced. The

measurement pattern in Fig. 3.4 **(a)** together with the specified assumption about the set of outcomes, leads directly to the final logical state present on qubit 5

$$\begin{aligned}|\psi_{\text{out}}\rangle = \Big[a\left(1+e^{i\xi}+e^{i\nu}-e^{i(\xi+\nu+\theta_2)}\right)+\sqrt{1-a^2}\left(1+e^{i\nu}\right.\\ \left.-e^{i(\xi+\theta_1)}+e^{i(\xi+\nu+\theta_1+\theta_2)}\right)\Big]|+\rangle_5+\Big[a\left(1+e^{i\xi}-e^{i(\nu+\theta_3)}\right.\\ \left.+e^{i(\xi+\nu+\theta_2+\theta_3)}\right)+\sqrt{1-a^2}\left(1-e^{i(\xi+\theta_1)}-e^{i\nu+\theta_3}\right.\\ \left.-e^{i(\xi+\nu+\theta_1+\theta_2+\theta_3)}\right)\Big]e^{i\zeta}(|0\rangle-e^{i\theta_4}|1\rangle)_5.\end{aligned} \tag{3.9}$$

This should be compared to the ideally rotated state $U_R|\psi_{\text{in}}\rangle$. The fidelity $\mathcal{F}_{R5} = |\langle\psi_{\text{out}}|U_R|\psi_{\text{in}}\rangle|^2$, averaged over all possible input states and over individual Gaussian distributions associated with each unwanted θ_j, is shown in Fig. 3.5 **(a)** for different values of the Euler angles (this average benchmark is labelled as $\bar{\mathcal{F}}_{R5}$). The initial state dependences are washed out by assuming a uniform distribution for each value of a, while the Gaussian functions are all centered on $\theta_j = 0$ and have equal standard deviation σ. It is evident that the average gate fidelity has a considerable dependence on the particular rotation one would like to simulate. However, an average over all the rotation angles is meaningless, as the choice of the elements of the vector $\mathbf{\Omega}$ is imposed by the specific computation protocol desired. The general trend, irrespective of the Euler angles, is that the gate fidelity is reduced by the increase of randomness in the system given by the value of σ. The reduction can be considerable even within *moderate* deviations from the ideal values $\theta_j = 0, \forall j$ (see the ■ or the ♦ case in Fig. 3.5 **(a)** for example, which suffer an average fidelity reduction of about 20%, for $\sigma \simeq 0.4$).

The analysis above is however unable to highlight the effect of redundant qubits initially present in the physical configuration of a cluster. These must be *removed* before the effective gate simulation is performed [130]. Such a removal of qubits, not necessary for the simulation of a particular gate, can be achieved by measuring them in the σ_x or σ_z eigenbasis. For the case of measurements in the σ_z eigenbasis, we break any entanglement between that qubit and the rest of the cluster. Whereas for measurements in the σ_x eigenbasis, when pairs of qubits are measured, we obtain a reduced cluster state where the qubits no longer affect the QIP protocol being simulated [130]. This removal is a very important point and the influence of noise on QIP protocols has only been partially clarified by the

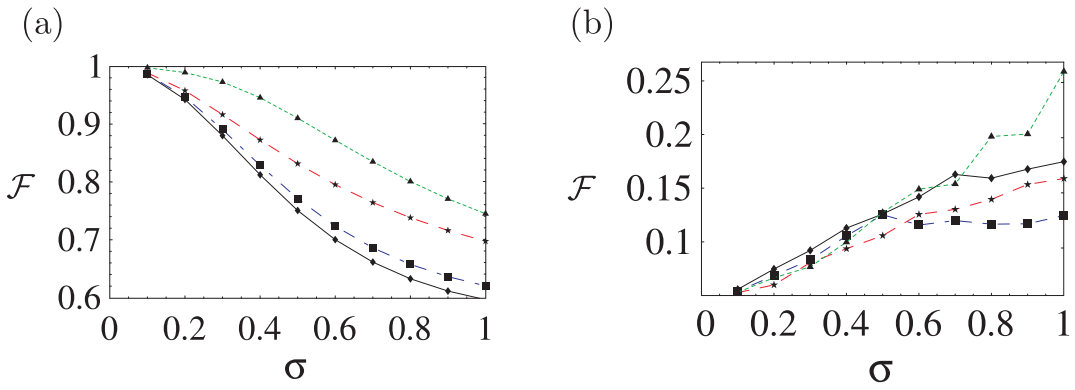

Figure 3.5: **(a)**: The fidelity of one-qubit rotations decomposed using the Euler angles (ζ, ν, ξ), when the model of noise is considered. The fidelity is plotted against a common standard deviation σ on the unwanted phases for various Euler angles. The angles considered are $\zeta = \pi/4$, $\nu = \xi = 0$ (♦, solid line), $\zeta = \nu = \pi/2$, $\xi = 0$ (★, dashed line), $\zeta = 0$, $\nu = \xi = \pi/4$ (■, dot-dashed line) and $\xi = \zeta = 0$, $\nu = \pi$ (▲, dotted line); **(b)**: The difference $\bar{\mathcal{F}}_{R5} - \bar{\mathcal{F}}_{R7}$ between the gate fidelity of the configurations in Figs. 3.4 **(a)** and **(b)**.

study about quantum state transfer in Section 3.3. Indeed, a measurement of a qubit in a state affected by a set of θ_j's, spreads noise throughout the cluster. More precisely, the unwanted phase θ_j which was attached to the $j-$th qubit, eliminated from the cluster by a measurement, is then *inherited* by the surviving qubits surrounding the j-th one. This leaves us with a smaller cluster state which is plagued by a larger number of unwanted phases. This *noise inheritance effect* must obviously be kept to a minimum.

The influence of noise does not depend on the particular angle chosen for the measurement basis and noise inheritance appears after any measurement (belonging to a legitimate measurement pattern) on a cluster state. It thus becomes an intrinsic feature of the inherently noisy cluster state generation that is addressed here. A way to give an explicit account of the inheritance effect is by fictitiously modifying the configuration in Fig. 3.4 **(a)** as shown in Fig. 3.4 **(b)**, where qubits 3 and 6 are considered to be redundant. After their elimination, via measurements in the σ_x-eigenbasis (which do not break the channels between the surviving qubits 2 & 4 and 5 & 7), the physical layout is exactly the five-qubit linear cluster considered in Fig. 3.4 **(a)**. The gate fidelity $\mathcal{F}_{R7}$ after the removal of these qubits and the correction of the resulting cluster state via local operations (as if a Hadamard gate has been performed between qubits 3 & 4 and

6 & 7) has been calculated. Analysing the effects of noise spreading through the measurements, one finds that the average of $\mathcal{F}_{R7}$ over the input states and individual Gaussian distributions ($\bar{\mathcal{F}}_{R7}$) is always smaller than $\bar{\mathcal{F}}_{R5}$. This is shown in Fig. 3.5 **(b)**, where the difference $\bar{\mathcal{F}}_{R5} - \bar{\mathcal{F}}_{R7}$ (always positive) is plotted against σ, for the rotation angles considered in Fig. 3.5 **(a)**. The differences between the two cluster configurations can easily exceed 10% and are larger for increased randomness in the cluster. Their behaviours as the Euler angles are changed, are almost uniform until $\sigma \simeq 0.6$. Then for increased randomness, the specific way in which the inherited phases are distributed within the structure of the cluster state becomes relevant and some discrepancies occur. The message here is that there is a counterintuitive dependence of the gate fidelity on the specific angles of rotation; some rotations are more *exposed* to the noisy cluster state model than others.

3.4.2 CNOT gate

In order to complete the analysis of MB QIP protocols in the $\mathrm{QC}_{\mathcal{C}}$ model with intrinsic noise, the simulation of a CNOT is addressed as the paradigmatic example of an entangling two-qubit gate [128]. The behaviour of the original fifteen qubit proposal [130] under noisy conditions and in the presence of a redundant qubit is first examined. Then, it will be compared with other configurations for CNOT simulation, where the resource requirements can be dramatically reduced down to no more than four qubits.

The input states will be denoted $|Q_1\rangle = a|0\rangle + b|1\rangle$ and $|Q_2\rangle = c|0\rangle + d|1\rangle$ which encode the control and target state respectively. Consider the fifteen-qubit two-dimensional cluster state (the *squashed*-I configuration) whose layout and measurement pattern are shown in Fig. 3.6 **(a)**. Its operation in terms of stabiliser formalism can be found in Ref. [130]. Here, interest is focused on the concatenation technique, which gives an immediate picture of the equivalent quantum gates simulated by this cluster configuration. Using the BBB's and EBB's introduced in Chapter 2, it is straightforward to derive the equivalent quantum circuit as shown in Fig. 3.6 **(b)**. The role played by the EBB introduced in Fig. 2.11, bridging the two otherwise independent subclusters, is crucial

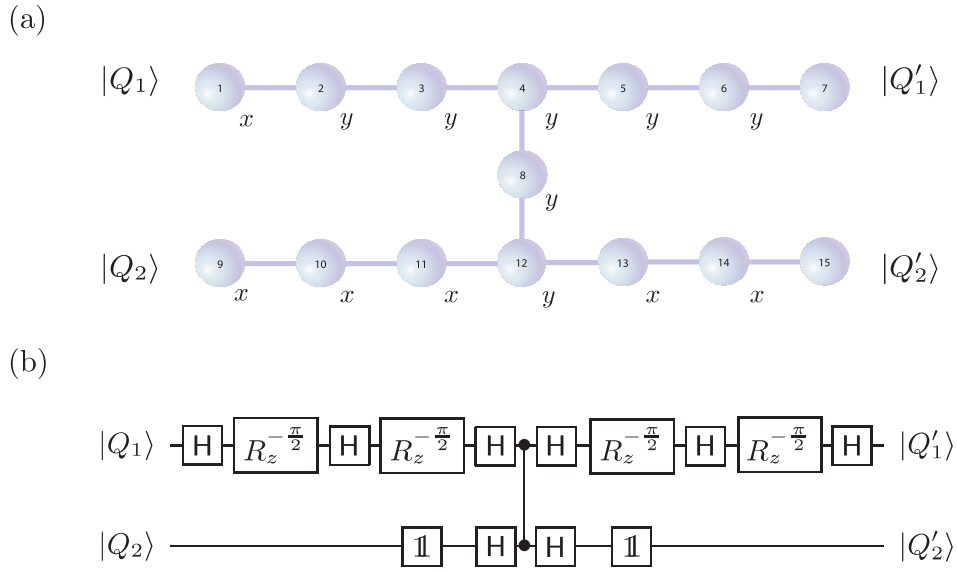

Figure 3.6: **(a)**: *Squashed*-I configuration for a CNOT simulation. The input (output) control and target logical qubit are qubits 1 (7) and 9 (15) respectively, with qubit 8 as a bridging qubit. **(b)**: The equivalent quantum circuit as a concatenation of BBB's and EBB's.

here. The byproduct operator can be evaluated starting from this equivalent decomposition and explicitly found to be $\tilde{U}_\Sigma = \otimes_{j=7,15} \sigma_z^{(j)\gamma_z^{(j)}} \sigma_x^{(j)\gamma_x^{(j)}}$ with

$$\begin{aligned} \gamma_x^{(7)} &= s_2^y + s_3^y + s_5^y + s_6^y, \\ \gamma_x^{(15)} &= s_2^y + s_3^y + s_8^y + s_{10}^x + s_{12}^y + s_{14}^x, \\ \gamma_z^{(7)} &= s_1^x + s_3^y + s_4^y + s_5^y + s_8^y + s_9^y + s_{11}^x + 1, \\ \gamma_z^{(15)} &= s_9^x + s_{11}^x + s_{13}^x, \end{aligned} \tag{3.10}$$

where $s_i^y = s_i^{xy(\pi/2)}$ and $s_i^x = s_i^{xy(0)}$ irrespective of i. We can now consider the simulation of a CNOT with a noisy squashed-I cluster. The technique already exploited in Section 3.4.1 in order to write an implicit (but manageable) expression for the global state of a cluster in a given configuration is used again and the starting point for the calculation is the state

$$|\varphi\rangle^D_{1\to4} \otimes |\varphi\rangle^D_{5\to7} \otimes |+\rangle_8 \otimes |\varphi\rangle^D_{9\to12} \otimes |\varphi\rangle^D_{13\to15}\,. \tag{3.11}$$

Here $|\varphi\rangle^D = |\psi\rangle^D + |\chi\rangle^D = |\eta\rangle^D + |\mu\rangle^D$, where $|\psi\rangle^D$ is the part of $|\varphi\rangle^D$ which has the last qubit in $|0\rangle$, while $|\chi\rangle^D$ is the part with the last qubit in $|1\rangle$. The

State	Explicit form in the computational basis
$\|\psi\rangle^D_{1\to4}$	$(a\|0\rangle + b\|1\rangle)_1(\|000\rangle + \|010\rangle)_{2\to4}$ $+(a\|0\rangle - e^{i\theta_1}b\|1\rangle)_1(\|100\rangle - e^{i\theta_2}\|110\rangle)_{2\to4}$
$\|\chi\rangle^D_{1\to4}$	$(a\|0\rangle + b\|1\rangle)_1(\|001\rangle - e^{i\theta_3}\|011\rangle)_{2\to4}+$ $(a\|0\rangle - e^{i\theta_1}b\|1\rangle)_1(\|101\rangle + e^{i(\theta_2+\theta_3)}\|111\rangle)_{2\to4}$
$\|\eta\rangle^D_{5\to7}$	$(\|000\rangle + \|010\rangle + \|001\rangle - e^{i\theta_6}\|011\rangle)_{5\to7}$
$\|\mu\rangle^D_{5\to7}$	$(\|100\rangle + \|101\rangle - e^{i\theta_5}\|110\rangle + e^{i(\theta_6+\theta_5)}\|111\rangle)_{5\to7}$
$\|\psi\rangle^D_{9\to12}$	$(c\|0\rangle + d\|1\rangle)_9(\|000\rangle + \|010\rangle)_{10\to12}+$ $(c\|0\rangle - e^{i\theta_9}d\|1\rangle)_9(\|100\rangle - e^{i\theta_{10}}\|110\rangle)_{10\to12}$
$\|\chi\rangle^D_{9\to12}$	$(c\|0\rangle + d\|1\rangle)_9(\|001\rangle - e^{i\theta_{11}}\|011\rangle)_{10\to12}+$ $(c\|0\rangle - e^{i\theta_9}d\|1\rangle)_9(\|101\rangle + e^{i(\theta_{10}+\theta_{11})}\|111\rangle)_{10\to12}$
$\|\eta\rangle^D_{13\to15}$	$(\|000\rangle + \|010\rangle + \|001\rangle - e^{i\theta_{14}}\|011\rangle)_{13\to15}$
$\|\mu\rangle^D_{13\to15}$	$(\|100\rangle + \|101\rangle - e^{i\theta_{13}}\|110\rangle + e^{i(\theta_{13}+\theta_{14})}\|111\rangle)_{13\to15}$

Table 3.1: The notation used in Eq. (3.12) for the noisy squashed-I cluster state used to simulate a CNOT.

explicit form of $|\psi\rangle^D$, $|\chi\rangle^D$, $|\eta\rangle^D$ and $|\mu\rangle^D$ is given in Table 3.1. In Eq. (3.11) the encoded logical input state of the control and target qubits, as well as the state of the bridging qubit 8, have been properly singled out. The $1 \to 4$ ($9 \to 12$) symbol means that qubits $1, 2, 3, 4$ ($9, 10, 11, 12$) are involved. By applying the entangling operations $S_D^{4,8}$, $S_D^{8,12}$, $S_D^{4,5}$ and $S_D^{12,13}$, the state of the cluster becomes

$$\begin{aligned}
&\left[|\psi\rangle^D_{1\to4}|\varphi\rangle^D_{5\to7} + |\chi\rangle^D_{1\to4}\left(|\eta\rangle^D - e^{i\theta_4^R}|\mu\rangle^D\right)_{5\to7}\right]|0\rangle_8 \otimes \\
&\left[|\psi\rangle^D_{9\to12}|\varphi\rangle^D_{13\to15} + |\chi\rangle^D_{9\to12}\left(|\eta\rangle^D - e^{i\theta_{12}}|\mu\rangle^D\right)_{13\to15}\right] + \\
&\left[|\psi\rangle^D_{1\to4}|\varphi\rangle^D_{5\to7} - e^{i\theta_4^C}|\chi\rangle^D_{1\to4}\left(|\eta\rangle^D - e^{i\theta_4^R}|\mu\rangle^D\right)_{5\to7}\right]|1\rangle_8 \otimes \\
&\left[|\psi\rangle^D_{9\to12}|\varphi\rangle^D_{13\to15} - e^{i\theta_8}|\chi\rangle^D_{9\to12}\left(|\eta\rangle^D - e^{i\theta_{12}}|\mu\rangle^D\right)_{13\to15}\right].
\end{aligned} \tag{3.12}$$

Here, θ_4^R (θ_4^C) denotes the unwanted phase introduced when the entanglement between qubits 4 and 5 (qubits 4 and 8) is considered. Using this notation, the entangling operation which glues together two subclusters is considerably simplified. For instance, gluing $|\varphi\rangle^D_{1\to4}$ and $|\varphi\rangle^D_{5\to7}$ leads to

$$\begin{aligned}
&S_D^{4,5}|\varphi\rangle^D_{1\to4} \otimes |\varphi\rangle^D_{5\to7} = S_D^{4,5}(|\psi\rangle^D + |\chi\rangle^D)_{1\to4} \otimes \\
&(|\eta\rangle^D + |\mu\rangle^D)_{5\to7} = |\psi\rangle^D_{1\to4}|\varphi\rangle^D_{5\to7} + |\chi\rangle^D_{1\to4}|\eta\rangle^D_{5\to7} \\
&-e^{i\theta_4}|\chi\rangle^D_{1\to4}|\mu\rangle^D_{5\to7},
\end{aligned} \tag{3.13}$$

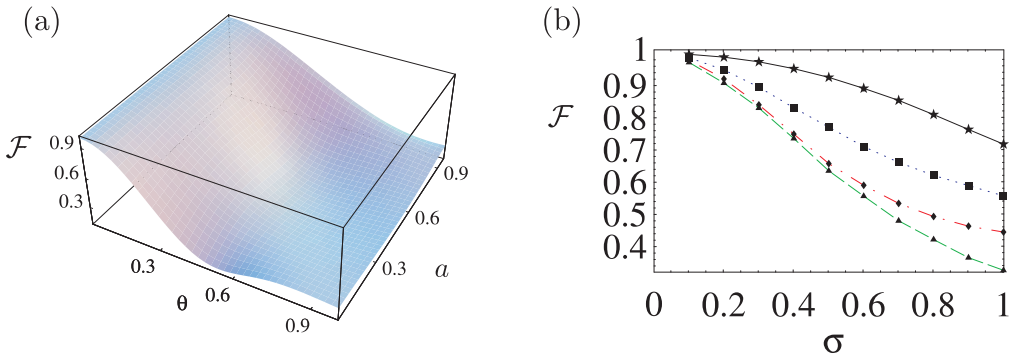

Figure 3.7: **(a)**: Fidelity for a squashed-I CNOT plotted against the unwanted phase θ and the input control-state coefficient a (set as real for convenience). In this plot $a = c$. **(b)**: Gate fidelities for different simulations of a CNOT. From top to bottom curve, we show the fidelity of the four-qubit CNOT of Fig. 3.9, the helix configuration of figure Fig. 3.8, the squashed-I of Fig. 3.6 and the squashed-I with an additional bridging qubit.

which is a seven-qubit linear cluster state. It should be noted that this expression has been obtained without actually writing the subcluster states in the computational basis. This method is therefore space-saving and computationally useful. On the other hand, by dealing each time with small subcluster states, it is handy to find out the explicit form of the state of the output logical qubits after the application of the appropriate measurement pattern. It is easy to build up a table for the transformations occurring after the completed measurements. Following these lines, the gate fidelity $\mathcal{F}_{\mathsf{CNOT}}$ can be explicitly evaluated by hand. A plot is given in Fig. 3.7 **(a)** against both $\theta_j = \theta$ ($\forall j$ involved in Eq. (3.12)) and $a = c$ (for convenience) with the normalisation conditions $b = \sqrt{1-a^2}$, $d = \sqrt{1-c^2}$. As in the case of single-qubit rotations, the post-selection of the event corresponding to $s_i^y = s_j^x = 0$ among the set of outcomes resulting from the measurements is considered. In this case, the decoding operator is $\tilde{U}_\Sigma^\dagger(\{0\}) = \sigma_z^{(7)} \otimes \mathbb{1}^{(15)}$. Behaviours qualitatively similar to Fig. 3.7 **(a)** can be observed for any other choice of the relation between a and c with this plot having the merit of showing an almost uniform behaviour of $\mathcal{F}_{\mathsf{CNOT}}$ against a, for a fixed θ and a fast decay of the gate fidelity is found for non-zero values of the unwanted phases. Near $\theta = 0.6$ and $a = c = 0.5$, $\mathcal{F}_{\mathsf{CNOT}} \simeq 0.2$ is found and is never exceeded for fixed a, whatever the choice for the relation between a and c. By showing the fidelity behaviour in Fig. 3.7 **(a)**, a significant example is given of the performances of the squashed-I CNOT simulation in the presence of

the model for noise, showing that the one-way model has to face a considerable decay in the two-qubit gate fidelity. These conclusions are strengthened by the calculation of the average fidelity over Gaussian distributions for the unwanted phases shown as the dot-dashed line (♦ symbol) in Fig. 3.7 **(b)**. Although a more complete analysis requires an average over all the outcome configurations[4], this example provides sufficient physical insight.

One can study the way in which the noise inheritance attacks the CNOT fidelity by analyzing the simple but interesting example of a modified squashed-I where the bridging zone between the control and target subclusters includes an additional redundant qubit. This qubit can be removed from the cluster (via a measurement in the σ_x-eigenbasis) retrieving the fifteen-qubit cluster state through appropriate local operations on qubit 12. Following the lines depicted above, *i.e.* attaching Gaussian distributions of standard deviation σ to the unwanted phases appearing in the noisy cluster state, it can be verified that the average gate fidelity is spoiled, as shown in Fig. 3.7 **(b)** (▲, dashed line), by the expected spread of additional phases relative to the removed qubit.

3.4.3 Alternative routes to CNOT

The discussion about noise inheritance in the last Section reinforces the view introduced previously concerning the importance of keeping the number of qubits in a cluster as low as possible. The analysis of the squashed-I layout revealed it to be rather prone to the effects of the intrinsic noise model considered. This can be ascribed to the *expensive* nature of the configuration in terms of the number of qubits in the cluster. Thus, there is a necessity for looking at different ways in which an entangling two-qubit gate can be simulated through cluster states. Here, examples of alternative cluster configurations are provided, which are able to simulate a CNOT gate involving less qubits than the squashed-I.

First, the qubit layout and measurement pattern sketched in Fig. 3.8 **(a)** simu-

[4] A calculation of the complete set of outcomes is prohibitive. Indeed, $N = 10$ represents a sort of limiting value on the dimension of a cluster, beyond which the computational time becomes exceedingly large.

lates a CNOT using ten qubits. This configuration will be referred to as the *helix* configuration. The scheme is based on the simulation of a CZ gate [128] (within the dashed box) and realises the transformation $(\mathbb{1}\otimes \mathsf{H})\ \mathsf{CZ}\ (\mathbb{1}\otimes \mathsf{H}) \equiv \mathsf{CNOT}$. A more detailed analysis of the gate simulation, using the concatenation technique is given in Fig. 3.8 **(b)**, where a relabeling of the logical output qubits (effectively equivalent to a SWAP gate) is required. The crucial feature is the use of a box cluster from Fig. 2.9 in Chapter 2.

It is possible to carry out an analytic calculation of the dynamics of a noisy helix cluster state using the same technique highlighted previously. The resulting average gate fidelity is shown in Fig. 3.7 **(b)** (■, dotted line). As before, a post-selection of the event corresponding to the set of outcomes $s_i^x = 0$ is assumed (*i.e.* all the measured qubits are found in $|+\rangle$). This results in no decoding operator at the end of the procedure, an advantage with respect to the squashed-I CNOT. The usual individual Gaussian functions have been considered, with σ as their standard deviation and a noticeable improvement in the gate fidelity is observed, compared to the squashed-I configuration.

The situation can be further improved by looking at the squashed-I cluster configuration and examining more closely the simulation performed there. It is easy to recognise that the non-local nature of the CNOT gate in Fig. 3.6 **(b)** is entirely in the CZ gate sandwiched by the Hadamards on the $|Q_2\rangle - |Q_2'\rangle$ target line. The remainder of the circuit realises local operations on the control qubit, which are unnecessary for the CNOT simulation. Thus, there is a considerable *redundancy* in this cluster configuration. Stripping the squashed-I cluster bare to eliminate the unnecessary local parts, leads directly to the EBB already introduced in Fig. 2.11 (see Chapter 2) at its very core. But even this is unnecessary as we already know that it is possible to obtain a better configuration which provides an even more economical configuration for a CNOT simulation. This is the four-qubit EBB discussed in Chapter 2 and shown in Fig. 3.9 again for convenience, which naturally simulates a CNOT (with output states in the σ_x-eigenbasis). The aim is therefore confronting the performance of the noisy version of this simple configuration with the other simulations treated so far. The results are shown in Fig. 3.7 **(b)** (★ and solid line). Evidently the gate fidelity corresponding to this linear layout is vastly superior to any other case treated so far. This four-qubit

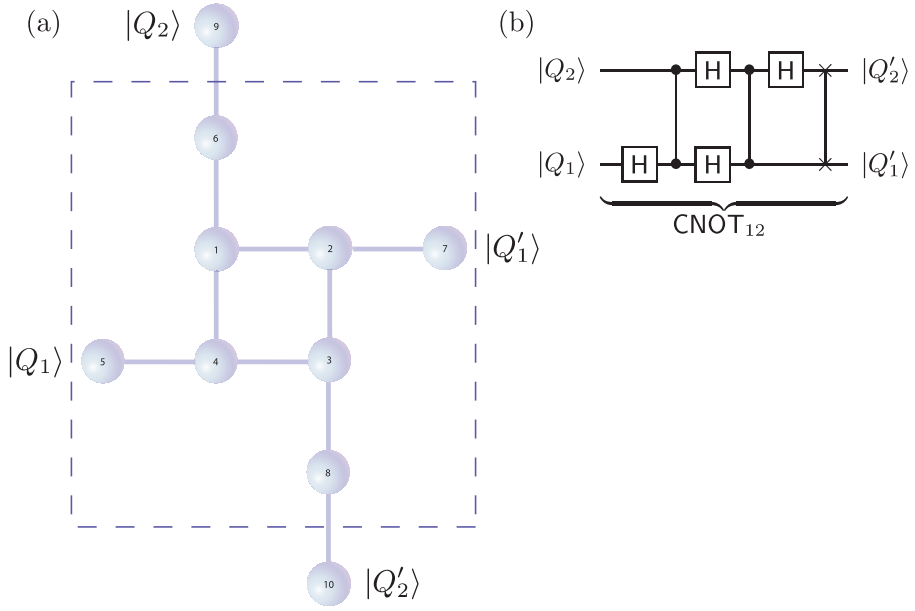

Figure 3.8: **(a)**: *Helix* layout and measurement pattern for a CNOT simulated through a CZ gate (within the dashed square) and two Hadamard gates involving qubits 6 & 9 and 8 & 10. **(b)**: Equivalent quantum circuit drawn by exploiting the concatenation of six BBB_1's and one box-shaped EBB involving qubits $1, 2, 3, 4$ (see Fig. 2.9 in Chapter 2).

EBB CNOT is important for two essential reasons: First, it can be seen as a final confirmation that in a noisy scenario, those features which the ideal one-way model takes for granted, *i.e.* the management of an arbitrarily large cluster and the innocuousness of the measurements performed in order to process the encoded information, sensibly affect a computational task when imperfections are embedded in the cluster state. Second, it is evident that more economical configurations for gate simulation are required if reliable computation is to be performed. The four-qubit linear EBB provides an economical CNOT simulation in which the number of parameters involved corresponds to the number of qubits in the cluster resource.

3.4.4 Experimental proposal

As a proof-of-principle experiment, the four-qubit CNOT could be realised in an all-optical setup, requiring two pure entangled states (encoded in photonic

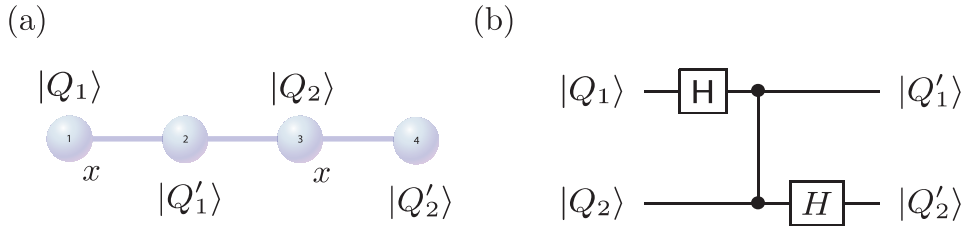

Figure 3.9: The concatenation of two BBB_1's and one BBB_2 with measurements in the $B_1(0)$ and $B_3(0)$ basis.

polarisations) and an entangling gate. A pure state of arbitrary entanglement can be produced using the entanglement between two photon modes generated by concatenating two Type-I parametric-down-conversion (PDC) processes [41, 42] as shown in Fig. 3.10 **(a)**. In this scheme, the polarisation of the pump field sets the entanglement at the output of the PDC process and encodes arbitrary target and control input states in pairs of output modes (*i.e.* pairs $1+2$ and $3+4$) without postselection. By adapting the scheme [156], modes 2 and 3 can be entangled through an effective CZ gate as shown in Fig. 3.10 **(b)**. This method would result in the encoded four-qubit linear cluster state addressed here. Alternative *gluing* schemes for modes 2 and 3 such as those proposed in Ref. [131] and realised in Ref. [74] could also be employed.

3.5 Remarks

The construction of cluster configurations suitable for the simulation of desired quantum circuits can be simplified by introducing a class of elementary BBB's and concatenating them together as we saw in Chapter 2. By properly designing the cluster state resource, it is possible to minimise the number of redundant qubits in a circuit simulation. This point is related to the main task accomplished in this Chapter, namely the detailed analysis of MB QIP using intrinsic imperfections in the generation of cluster configurations. It has been shown that uncontrollable randomness in the qubit-qubit interactions which create a cluster state, affect both communication and computation protocols based on the MB one-way model. A direct consequence of the analysis is that in the processing of information encoded in a cluster state, both the number of qubits involved and

the measurements to be performed must be carefully managed. In this context, an experimentally realisable four-qubit CNOT has been proposed, which uses a minimal number of qubits for a cluster state based CNOT. This study paves the way towards research of gate simulations and protocols performed using only small clusters of just a few qubits.

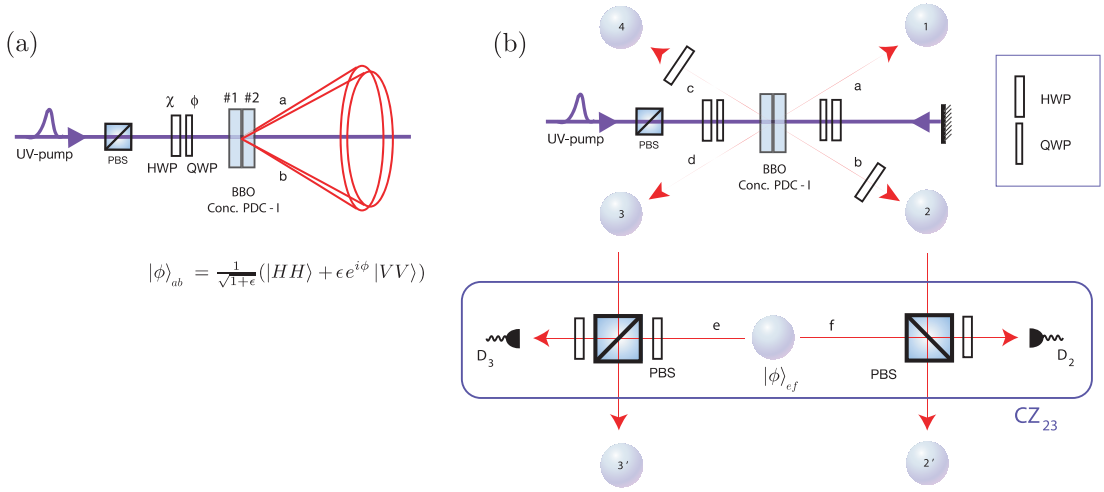

Figure 3.10: Experimental setup for a 4-qubit encoded linear cluster state that simulates the CNOT gate shown in Fig. 3.9. **(a)**: Parametric down-conversion type-I (PDC-I) phase matching process. Here a laser pumps two concatenated Beta-Barium-Borate (BBO) crystals, where the optic axis of crystal 1 (2) is in the vertical (horizontal) plane at an angle of $55^\circ \rightarrow 65^\circ$ to the direction of the pump beam. Crystal 1 (2) will produce a correlated pair $|HH\rangle_{ab}$ ($|VV\rangle_{ab}$) from a V (H) polarised pump beam. By setting the angles χ and ϕ in a half-wave plate (HWP) and quarter-wave plate (QWP) respectively, one can produce the state $|\phi\rangle_{ab} = \frac{1}{\sqrt{1+\epsilon}}(|HH\rangle + \epsilon e^{i\phi}|VV\rangle)$, where $\epsilon = \tan\chi$. This is due to the polarisation of the pump beam affecting the likelihood of down-converting in either crystal [41, 42]. **(b)**: A double-pass scheme with modified CZ gate [156] applied so as to generate the desired entangled 4-qubit cluster. The HWP-QWP pair on the left (right) hand side of the BBO crystals sets the input logical qubits $|Q_1\rangle$ ($|Q_2\rangle$) encoded in the state $|\phi\rangle_{ab}$ ($|\phi\rangle_{cd}$). The HWP's on modes b and c are set at -22.5^0 to implement a Hadamard operation on the photonic polarisation giving the state $\frac{1}{\sqrt{1+\epsilon}}(|H+\rangle + \epsilon e^{i\phi}|V-\rangle)_{12} \otimes \frac{1}{\sqrt{1+\epsilon'}}(|H+\rangle + \epsilon' e^{i\phi}|V-\rangle)_{34}$ prior to the CZ. A state $|\phi\rangle_{ef} = \frac{1}{\sqrt{2}}(|HH\rangle + |VV\rangle)$ is produced from an additional PDC-I process. When a single photon in $|H\rangle$ is detected at both D_2 and D_3 (after HWP's at -25.5^0) the CZ is implemented. For other combinations of polarisation detection, feed-forward is necessary. This means that operations on the output qubits are needed which depend on detected polarisation. The CZ_{23} has a success of $p = 1/4$ [156].

Chapter 4

Minimal resource algorithms

The increasing interest in topics of QIP and QC has stimulated considerable effort in the realisation of *quantum hardware* based on various experimental settings. It has resulted in the realisation of one and two-qubit logical gates [128], even though the combining of these basic building blocks in the standard network model is still far from being practical. Nevertheless, investigations in this direction, both at the experimental and theoretical level are vital for the advancement of QIP. The ultimate aim is the realisation of multi-qubit quantum algorithms able to outperform their classical analogues [23–25, 128, 157, 158]. In this context, the implementation of few-qubit quantum algorithms represents a step forward in the construction of working processors based on quantum technology [35, 36, 159, 160]. In this Chapter, two quantum algorithms are introduced that can be implemented using the MB one-way model with cluster states containing small numbers of qubits. In Section 4.1 it will be shown how Deutsch's algorithm can be performed using a state-of-the-art all-optical setup [71, 76], together with the subsequent experimental results. In Section 4.2 a cluster state implementation of a quantum game is proposed, where the role of classical and quantum correlations in the dynamics of the game are discussed in detail.

4.1 Deutsch's Algorithm

In this Section, the first experimental demonstration of an all-optical one-way implementation of Deutsch's quantum algorithm on a four-qubit cluster state is described. All the possible configurations of a balanced or constant function acting on a two-qubit register can be realised using MB QIP, as will be shown. The experimental results obtained are in excellent agreement with the theoretical model and demonstrate a successful performance of the algorithm.

4.1.1 Introduction

Deutsch's algorithm [23] represents a simple but yet interesting instance of the role that the inherent parallelism of QC plays in the speed-up characterizing

quantum versions of classical problems. An all-optical setup is used for its demonstration, where the construction of cluster states has been successfully established [71, 76]. Negligible decoherence affecting qubits embodied by photonic degrees of freedom ensure the performance of the protocol in a virtually noise-free setting. Although Deutsch's algorithm has been implemented in a linear optical setup before [161], the protocol presented here represents its first realisation in the context of one-way QC. It is based on the use of an entangled resource locally equivalent to the cluster state used recently for performing a two-qubit search algorithm [71, 76] and reinforces the idea of the high flexibility of cluster resources. It will be shown that four qubits in a linear cluster configuration are sufficient to realise all the possible functions acting on a logical two-qubit register. Two of these result from the application of an entangling gate to the elements of the register. In principle, this gate could be realised by inducing an interaction between photonic qubits. In the cluster state approach described next, the required entangling operations are realised by using the entanglement in the photonic cluster resource and the nonlinearity induced by detection. There is no need for *engineering* it on a case-by-case basis [161], which is an important advantage. In Section 4.1.3, the density matrix of the logical output qubits for the functions will be seen to show excellent performance of the algorithm in the optical setup.

4.1.2 The model

The generalised version of Deutsch's two-bit algorithm, also known as the Deutsch-Josza algorithm [158], takes an N-bit binary input string $x \in \{0,1\}^N$ and allows one to distinguish two different types of function $f(x)$ that apply the decimal transformation $f(x) : \{0, ..., 2^N - 1\} \mapsto \{0, 1\}$ implemented by an oracle[1]. A function is *constant* if it returns the same value (either 0 or 1) for all possible inputs of x and *balanced* if it returns 0 for half of the inputs and 1 for the other half. Classically one needs to query this oracle as many as $(2^N/2)+1$ times in the worst case scenario, as $2^N/2$ 0's could be output before finally a 1 is obtained.

[1]An oracle (also known as a black box) is an unknown computational process where one cannot obtain knowledge about its operation by any means other than evaluating it on points of its domain.

However the quantum version requires only one query in all cases [158]. To start with, in Deutsch's two-qubit version [23, 162], the algorithm implements the oracle as a function f on a *single* query bit x (N=1) using an input ancilla bit[2] y. The applied unitary operation is given by $|x\rangle|y\rangle \mapsto |x\rangle|y \oplus f(x)\rangle$. Preparing the input state as $(1/\sqrt{2})\sum_{x\in\{0,1\}}|x\rangle|y\rangle = |+\rangle|-\rangle$, where $|\pm\rangle = (|0\rangle \pm |1\rangle)/\sqrt{2}$ and $\{|0\rangle, |1\rangle\}$ is the single-qubit computational basis, the oracle maps the state to $(1/\sqrt{2})[(-1)^{f(0)}|0\rangle + (-1)^{f(1)}|1\rangle]|-\rangle$. By measuring the query qubit in the $\{|\pm\rangle\}$ basis, one can determine which type of function $f(x)$ corresponds to. If $f(x)$ is balanced (constant), the query qubit is always $|-\rangle$ ($|+\rangle$). Thus, only one query of the oracle is necessary, compared to two in the classical version[3].

The generalised Deutsch-Josza N-qubit version begins similarly, with the preparation of the state $(1/\sqrt{2^N})\sum_{x\in\{0,1\}^N}|x\rangle|y\rangle = |+\rangle^{\otimes N}|-\rangle$. The oracle transformation $|x\rangle|y\rangle \mapsto |x\rangle|y \oplus f(x)\rangle$ is then applied, producing the state

$$\left[(1/\sqrt{2^N})\sum_{x\in\{0,1\}^N}(-1)^{f(x)}|x\rangle\right]|-\rangle\,. \tag{4.1}$$

Next, Hadamard gates are applied to all the query qubits[4] which results in the state $|\psi_{out}\rangle = (1/2^N)\sum_z\sum_x(-1)^{x\cdot z+f(x)}|z\rangle|-\rangle$. The amplitude for the state of the query qubits as $|0\rangle^{\otimes N}$ is $\sum_x[(-1)^{f(x)}/2^N]$. There are now two cases: First, if $f(x)$ is *constant* then the amplitude for $|0\rangle^{\otimes N}$ is +1 or -1 depending on the constant value that $f(x)$ takes. As $|\psi_{out}\rangle$ is of unit length, all other amplitudes go to zero. Second, if $f(x)$ is *balanced*, then the positive and negative contributions to $|0\rangle^{\otimes N}$ cancel, leaving an amplitude of zero. Therefore if $|\psi_{out}\rangle = |0\rangle^{\otimes N}$ is measured, then $f(x)$ is constant and if $|\psi_{out}\rangle$ is found to be equal to any other computational basis states, $f(x)$ is balanced. As a Hadamard operation followed by a measurement in the computational basis is equivalent to a measurement in the $\{|\pm\rangle\}$ basis for a single qubit, all query qubits can be measured in the $\{|\pm\rangle\}$

[2]The ancilla bit is necessary so that the operation of the function f is reversible [163–165] and therefore the corresponding QC will be unitary (as described next).

[3]Informally this problem can be put into the context of determining whether a given coin is genuine (with a head on one side and a tail on the other) or fake (both sides are the same). Classically one needs to look at the coin twice.

[4]For a single qubit $\mathsf{H}|x\rangle = (1/\sqrt{2})\sum_z(-1)^{xz}|z\rangle$ and for N qubits $\mathsf{H}|x_1,...,x_N\rangle = (1/\sqrt{2^N})\sum_{z_1,...,z_N}(-1)^{x_1z_1+...+x_Nz_N}|z_1,...,z_N\rangle \equiv (1/\sqrt{2^N})\sum_z(-1)^{x\cdot z}|z\rangle$, where $x\cdot z$ is the bitwise scalar product of x and z using *modulo*-2 arithmetic.

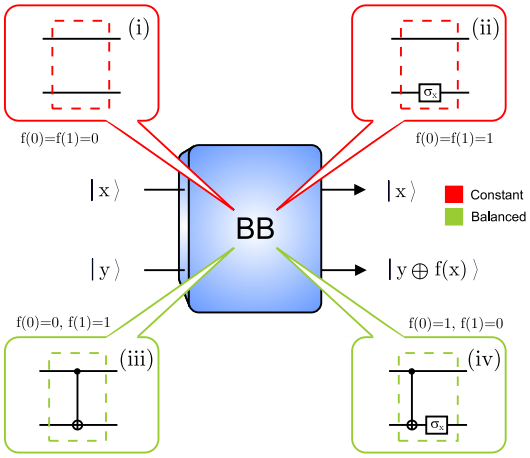

Figure 4.1: Network diagrams for the black boxes in Deutsch's algorithm. We have BB(i)=$\mathbb{1} \otimes \mathbb{1}$, BB(ii)=$\mathbb{1} \otimes \sigma_x$, BB(iii)=CNOT and BB(iv)=($\mathbb{1} \otimes \sigma_x$)CNOT (CNOT denotes a Control-NOT gate).

basis straight after the oracle's action (see Eq. (4.1)). In this case, the query qubits' state $|+\rangle^{\otimes N}$ will be measured for a constant function and otherwise for a balanced function. This coincides naturally with the two-qubit version.

The action of the above oracle is either preset or dictated by the outcome of another algorithm. In order to implement all possible configurations that it might take in a two-qubit version, we must be able to construct them using a combination of quantum gates. In Fig. 4.1 all possible oracles are shown in terms of their quantum network. By describing each as a "black box", one can see that all four black boxes (BB(i)-(iv)) implement their respective oracle operation. In order to implement the algorithm using these quantum gates, a cluster state is used to carry out one-way QC by performing a correct program of measurements (measurement pattern). No adjustment to the experimental set-up is necessary.

4.1.3 Experimental implementation

For the entangled resource, in an ideal case, the following four-photon state is produced by means of the set-up shown in Fig. 4.3 **(a)**

$$|\Phi_c\rangle = \frac{1}{2}(|0000\rangle + |0011\rangle + |1100\rangle - |1111\rangle)_{1234} \tag{4.2}$$

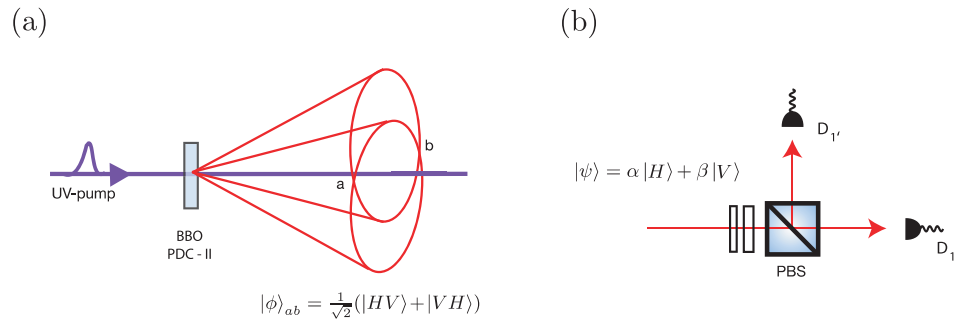

Figure 4.2: **(a)**: Parametric down-conversion type-II (PDC-II) phase matching process [40]. A horizontally polarised laser pumps a BBO crystal with optic axis in the horizontal plane at an angle $\sim 49.5°$ to the direction of the pump beam. Two cones of photon spatial modes correlated in H and V polarisation respectively are produced due to phase matching conditions. At the points a and b which define two chosen photon modes, the cones overlap. If a photon at point a is $|H\rangle$ then its counterpart at point b will be $|V\rangle$ and vice-versa. Due to the indistinguishability of which polarisation cone a photon in a given spatial mode originates from, the state $|\phi\rangle_{ab} = (1/\sqrt{2})(|HV\rangle + |VH\rangle)$ in modes a and b is produced. **(b)**: Single qubit linear tomography using projective measurements. When no HWP and QWP are present, the PBS acts as a σ_z-eigenbasis measurement. By incorporating a HWP and QWP, then setting them at various angles, one can implement any single qubit projective measurement. Using the basis sets $\{|H\rangle, |V\rangle\}$, $\{|+\rangle, |-\rangle\}$ and $\{|R\rangle, |L\rangle\}$ (corresponding to ($\text{QWP}^{0°}$, $\text{HWP}^{0°}$), ($\text{QWP}^{45°}$, $\text{HWP}^{22.5°}$) and ($\text{QWP}^{45°}$, $\text{HWP}^{0°}$) respectively) and using many copies of the photonic qubit state $|\psi\rangle = \alpha|H\rangle + \beta|V\rangle$, one can fully determine the coefficients α and β [41, 166]. One way to see how this is possible is that *any* qubit state ρ can be expanded as $\rho = \mathbb{1} + \text{Tr}(\sigma_x\rho)\sigma_x + \text{Tr}(\sigma_y\rho)\sigma_y + \text{Tr}(\sigma_z\rho)\sigma_z$, where $\text{Tr}(\sigma_i\rho)$ is the expectation value of the Pauli operator σ_i (see Chapter 2). These expectation values can be accurately determined from a large number of σ_i projective measurements. Therefore, this linear expansion can be obtained from the count statistics at detectors D_1 and D_1'. However, due to freedom in the choice of basis for linearly reconstructing ρ, one need only find the count rates from the minimal set of states $\{|H\rangle, |V\rangle, |+\rangle, |R\rangle\}$ (or any other appropriate choice) [41, 166].

with $|0\rangle_j$ ($|1\rangle_j$) embodied by the horizontal (vertical) polarisation state of one photon populating a spatial mode $j = 1, .., 4$. The preparation of the resource relies on postselection: a four-photon coincidence event at the detectors facing each spatial mode witnesses the preparation of the state. In order to understand how the state in Eq. (4.2) can be produced, consider the parametric down-conversion process type-II described in Fig. 4.2 **(a)** and used in the double pass scheme of

Fig. 4.3 **(a)**. In this setup, Compensators and HWP's are aligned in order to produce the Bell state $|\phi^-\rangle = (1/\sqrt{2})(|HH\rangle - |VV\rangle)_{ab}$ into the forward modes a and b, with $|\phi^+\rangle = (1/\sqrt{2})(|HH\rangle + |VV\rangle)_{cd}$ into the backward modes c and d. If a pair of photons is emitted into modes a and b together with a pair into modes c and d on the return passage of the laser pulse, the state $|HHHH\rangle_{1234} - |VVVV\rangle_{1234}$ is produced in the case all four photons emerge in different output modes after the PBS's (which transmit (reflect) horizontally (vertically) polarised light). With approximately the same probability, two pairs of photons are emitted into either the forward or backward (on the return passage) directions. This results in the state $-|HHVV\rangle_{1234}$ on the forward or $|VVHH\rangle_{1234}$ on the backward passage. As each of these processes is indistinguishable and considering that their relative phases are kept fixed by careful calibration, the final state in the case all four photons emerge in different output modes is a coherent superposition of the four terms $|\Phi\rangle = (1/2)(|HHHH\rangle - |HHVV\rangle + |VVHH\rangle - |VVVV\rangle)_{1234}$. By inserting a HWP in mode a, which rotates the polarisation by an angle θ, the amplitudes of the first, second and fourth states are modified to become $\cos\theta\,|HHHH\rangle$, $-\cos 2\theta\,|HHVV\rangle$ and $-\cos\theta\,|VVVV\rangle$ respectively. Note that the third term originates from modes c and d, hence no modification is made to this state. For $\theta > 45^0$ we have that $\cos 2\theta$ becomes negative, whereas $\cos\theta$ remains positive. By taking into account the relative emission rates of the forward and backward photon pairs, the angle θ can be adjusted in order to equalise the amplitudes in the state $|\Phi\rangle$ to give the state $|\Phi_c\rangle$ in Eq. (4.2). This state is locally equivalent to a four-qubit linear cluster state $|\Phi_{lin}\rangle$ (the local operation being $\mathsf{H}_1 \otimes \mathbb{1}_2 \otimes \mathbb{1}_3 \otimes \mathsf{H}_4$). The experimentally produced state ϱ (with a rate of generation of 1 Hz) is verified by means of a maximum-likelihood technique for tomographic reconstruction [41, 166] performed over a set of 1296 local measurements using 81 detection settings [71, 76], each implemented within a time-window of 500 seconds. This provides information about the overall quality of the experimental state on which the algorithm is performed. All the possible combinations of the elements of the mutually unbiased basis $\{|0\rangle, |1\rangle, |+\rangle, |-\rangle, |R\rangle, |L\rangle\}_j$ have been used with $|\pm\rangle_j$ embodied by the polarisation state at $\pm 45^\circ$ and $|L/R\rangle_j = (|0\rangle \pm i\,|1\rangle)_j/\sqrt{2}$ corresponding to left and right-circularly polarised photons. The tomography process for a single qubit is outlined in Fig. 4.2 **(b)** and extending this technique to four-qubit systems is straightforward [166]. The over-complete state tomography used has the advantage of providing a more precise state estimation and

significantly smaller error bars [71, 76]. The reconstructed density matrix ϱ is shown in Fig. 4.3 **(c)** & **(d)** and has a fidelity with the ideal state $|\Phi_c\rangle$ of $F = \langle\Phi_c|\varrho|\Phi_c\rangle = 0.62 \pm 0.01$. The error bar was estimated by performing a 100 run Monte Carlo simulation of the whole state tomography analysis, with Poissonian noise added to the count statistics in each run [41, 166]. Obtaining a higher fidelity is limited by phase instability during the lengthy process of state tomography and non-ideal optical elements. However, it is well-above the limit $F = 0.5$ for any biseparable four-qubit state[5] and demonstrates the presence of genuine four particle entanglement.

In order to perform Deutsch's algorithm on the cluster resource $|\Phi_c\rangle$, a specific set of measurement bases for the qubits is used in each black box case. In Table 4.1 these basis sets (BB_c) are provided together with feed-forward (FF) operations used to carry out the black boxes on $|\Phi_c\rangle$ and also $|\Phi_{lin}\rangle$ (BB basis sets). As BB(ii) and BB(iv) are obtained from BB(i) and BB(iii) by using alternative FF operations (corresponding to adaptive measurements on the output qubits), in what follows BB(i) and BB(iii) will be explicitly described. Fig. 4.3 **(b)** shows the in-out logical states of the algorithm, where the logical input state corresponding to $|x\rangle = |+\rangle$ is encoded on qubit 1. The state $|y\rangle = |-\rangle$ will be encoded on qubit 3 by measuring qubit 4 in the $B_4(\pi)$ basis during the implementation of the algorithm (described next). This gives $|x\rangle\,|y\rangle \equiv (\mathbb{1}\otimes R_z^{\pi})\,|+\rangle\,|+\rangle$.

Qubit 2 in $|\Phi_{lin}\rangle$ plays the pivotal role of the oracle as it performs a two-qubit gate on the logical input states $|x\rangle$ and $|y\rangle$. For BB(i), measuring qubit 2 in the computational basis disentangles it from the cluster and $|\Phi_{lin}\rangle$ is transformed into $|\pm\rangle_1\,(1/\sqrt{2})(|0\rangle\,|+\rangle \pm |1\rangle\,|-\rangle)_{34}$ (+ (−) for outcome $|0\rangle_2$ ($|1\rangle_2$)). The effective logical operation performed by this choice of the oracle's measurement basis is $\mathbb{1}\otimes\mathbb{1}$. By including the H operation applied to the input state $|y\rangle$ from the measurement of qubit 4, the overall computation results in $(\mathbb{1}\otimes\mathbb{1})(\mathbb{1}\otimes \mathsf{H}R_z^{\pi})\,|+\rangle\,|+\rangle$ which is equivalent to $|x\rangle\,|y\oplus f(x)\rangle = (\mathbb{1}\otimes\mathbb{1})\,|+\rangle\,|-\rangle$ up to a local rotation H on physical qubit 3, which is applied at the FF stage. Qubits 1 and 3 can now be taken as the output $|x\rangle\,|y\oplus f(x)\rangle$. For BB(iii), upon measuring qubit 2 in the $B_2(\pi/2)$ basis, the oracle applies the gate $(R_z^{\pi/2}\otimes R_z^{\pi/2})\mathsf{CZ}$ on

[5] For a formal proof of this statement and the definition of biseparable states in multipartite systems, see Ref. [167].

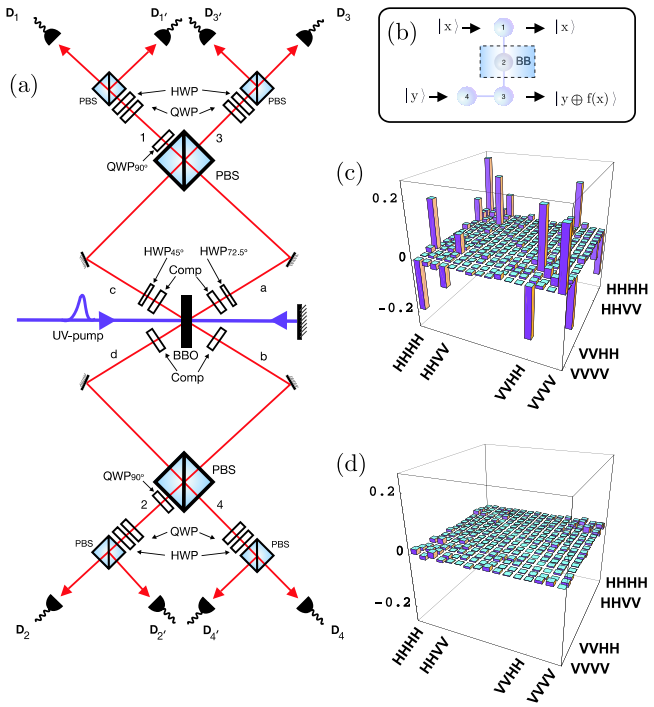

Figure 4.3: **(a)**: Experimental setup. An ultraviolet pump-laser performs two passages through a nonlinear BBO aligned to produce entangled photon pairs of the form $(|00\rangle - |11\rangle)_{ab}/\sqrt{2}$ and $(|00\rangle + |11\rangle)_{cd}/\sqrt{2}$. Compensators (Comp) are HWP's and BBO crystals used in order to counteract walk-off effects at the BBO. By considering the possibility of obtaining a double-pair emission into the same pair of modes and the action of the PBS's, the four terms entering $|\Phi_c\rangle$ are obtained and their amplitudes and respective signs adjusted [71, 76] with an additional HWP in mode a, as discussed in the text. The algorithm is executed by using QWP's, HWP's, PBS's and photocounter pairs $\{\mathrm{D}_j, \mathrm{D}_{j'}\}$ for the performance of polarisation measurements in arbitrary bases of the photons in mode j (see also Fig. 4.2 **(b)**). **(b)**: Sketch of the cluster-state configuration. Qubit 1 embodies the logical input for $|x\rangle$ and its output. Qubit 4 (3) is the logical input (output) for $|y\rangle$, which is always found to be $|-\rangle_3$. **(c)** & **(d)**: Real and Imaginary plots respectively of the reconstructed experimental density matrix ϱ.

$|x\rangle$ and $|y\rangle$ (see BBB_3 in Chapter 2), where CZ shifts the relative phase of the state $|1\rangle|1\rangle$ by π. This gives the computation $|x\rangle|y \oplus f(x)\rangle = \mathsf{CNOT}|+\rangle|-\rangle \equiv (R_z^{\pi/2} \otimes R_z^{\pi/2})\mathsf{CZ}(\mathbb{1} \otimes \mathsf{H} R_z^{\pi})|+\rangle|+\rangle$ up to local rotations $R_z^{-\pi/2} \otimes \mathsf{H}\, R_z^{-\pi/2}$ on qubits 1 and 3, applied at the FF stage. The measurements and outcomes of qubits 1, 3 and 4 constitute the algorithm. The additions to the FF stages described above, together with the measurement of qubit 2 should be viewed as being carried out

	Measurement basis
BB(i)	$\{B_1(0), \{\|0\rangle_2, \|1\rangle_2\}, \{\|0\rangle_3, \|1\rangle_3\}, B_4(\pi)\}$
BB_c(i)	$\{\{\|0\rangle_1, \|1\rangle_1\}, \{\|0\rangle_2, \|1\rangle_2\}, \{\|0\rangle_3, \|1\rangle_3\}, \{\|1\rangle_4, \|0\rangle_4\}\}$
BB(iii)	$\{B_1(\pi/2), B_2(\pi/2), \{\|0\rangle_3, \|1\rangle_3\}, B_4(\pi)\}$
BB_c(iii)	$\{B_1(3\pi/2), B_2(\pi/2), \{\|0\rangle_3, \|1\rangle_3\}, \{\|1\rangle_4, \|0\rangle_4\}\}$

Table 4.1: Measurement bases for the black boxes. The FF operations are $(\sigma_x^{s_2})_1(\sigma_x^{s_4})_3$ for BB_c(i) and $(\sigma_z^{s_2 \oplus s_4})_1(\sigma_x^{s_4})_3$ for BB_c(iii). Here, s_j is 0 (1) if the outcome is $|\alpha_+\rangle_j$ ($|\alpha_-\rangle_j$) on qubit j.

entirely by the oracle.

The results of the experiment are shown in Fig. 4.4, where a full characterisation of the output states of the quantum computer is achieved by repeating the algorithm a large number of times. A single run of the algorithm (measuring the output qubit 1 in a specific basis only once) is sufficient in the setup to carry out the QC with success rates as large as 90% (78%) for BB(i) (BB(iii)). However, repeating it several times allows one to verify the density matrix for the quantum state of qubits 1 and 3 reconstructed through a maximum likelihood technique [41, 166]. Although only the logical state residing on qubit 1 provides the outcome of the algorithm, it is useful for the characterisation of the quantum computer's performance to also determine the state residing on qubit 3. Ideally, the joint state of qubits 1 and 3 should be the product state $|x\rangle\,|y \oplus f(x)\rangle$. By obtaining both correct logical output states, it confirms that the algorithm will run correctly if included in a larger protocol. Fig. 4.4 shows the output density matrices for BB(i) and BB(iii). Both the no-feed-forward (no-FF) and FF situations are shown. In the latter case, the state of the output qubits is corrected from the randomness of the measurements performed on the physical qubits 2 and 4. From the previous analysis in Section 4.1.2, we know that the expected outcome from a single run, when a constant (balanced) function is applied is $|+,-\rangle_{13}$ ($|-,-\rangle_{13}$). Evidently, the reconstructed density matrices, both in the FF and no-FF cases, show a very good performance of the algorithm when compared with the theoretical expectations. The real parts are dominated by the correct matrix elements and no significant imaginary parts are found. Quantitatively, the fidelity with the desired state in the case of a constant (balanced) function is found to be as large as 0.90 ± 0.01 (0.78 ± 0.01) for the FF

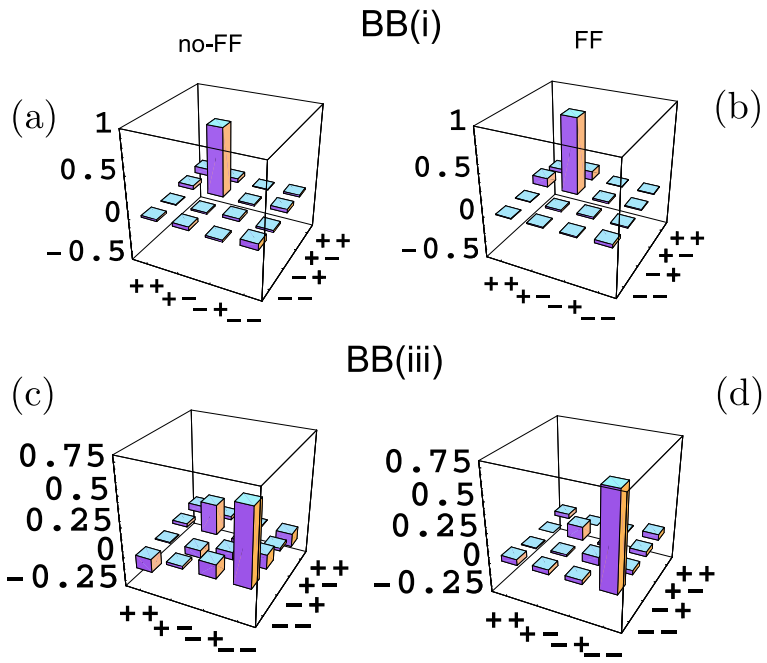

Figure 4.4: The output density matrices for cluster qubits 1 and 3 when BB(i) and BB(iii) are implemented. Panels (**a**) and (**c**) show the real parts of the two-qubit density matrix elements as obtained from a maximum likelihood reconstruction for the no-FF cases of BB(i) and BB(iii) respectively. Panels (**b**) and (**d**) show the corresponding plots for a FF case, due to the randomness of measurement outcomes for qubits 2 and 4. In all four cases the imaginary parts are zero in theory and negligible in the experiment (average values < 0.02).

case and 0.82 ± 0.01 (0.63 ± 0.01) for the no-FF one. The discrepancies in the values of these fidelities are due to errors originating from the generation and measurement stages being redistributed within the smaller Hilbert space of the remaining cluster state qubits. One can expect that mutual cancellations and amplifications of these errors occur depending on the measurement basis of the measurement pattern being used (see chapter 3). This is an intrinsic feature of the $\mathrm{QC}_{\mathcal{C}}$ model. In addition to the fidelities, no entanglement is found in any of the joint output states, as witnessed by the NPT criterion [100, 101]. The small admixture of the undesired $|+,-\rangle_{13}$ to the expected $|-,-\rangle_{13}$ state when a balanced function is applied (Fig. 4.4 **(c)**) is due to the non-ideal fidelity of the experimental cluster state with $|\Phi_c\rangle$ in Eq. (4.2). This is more pronounced for BB(iii) than for BB(i), where the measurement basis of qubit 2 breaks the channel between $|x\rangle$ and $|y\rangle$ resulting in a protocol-dependent *noise-inheritance* effect for imperfect cluster states (see Chapter 3).

4.2 The Prisoners' Dilemma

In this Section an experimental implementation of a quantum game algorithm is proposed using a hybrid scheme combining the quantum circuit approach and the cluster state model. An economical cluster configuration is suggested to embody a quantum version of the Prisoners' Dilemma [168]. This proposal is shown to be within the experimental state-of-art, with the basic features being realised recently with existing all-optical technology [81]. The effects of relevant experimental imperfections are carefully examined in Section 4.2.3.

4.2.1 Introduction

The proposal outlined here in order to implement a quantum version of the two-player Prisoners' Dilemma, is based on the use of small multipartite entangled cluster states, recently realised in all-optical setups [71–78, 80]. The choice of an optical scenario for the implementation of the proposal is incomparable in its suitability for studying the influences of quantum entanglement in the game. Indeed, even though the quantum game in [169] has been implemented in a nuclear magnetic resonance (NMR) system [170], the density matrices of the highly mixed states involved in NMR can always be described as disentangled [171]: the use of ensemble-averaged pseudopure states renders the observation of the effects of the entanglement ambiguous [171]. An all-optical implementation is not affected by this ambiguity. The multipartite entangled resource used in the proposal is given by a cluster state [55, 56, 129, 130] constructed through a double-pass scheme generating a four-photon entangled state via parametric down-conversion [71, 76, 77], with the information encoded in orthogonal photonic polarisations (See Section 4.1 for more details). Cluster states naturally and economically simulate several operations which are central to the scheme [134, 136]. It will be discussed how the proposal combines the standard quantum circuit model and MB QIP, enhancing the one-way model. This *hybrid* model has put the scheme for a quantum game within the current state-of-the-art and allowed for its recent experimental demonstration [81]. It constitutes one of the first immediately realisable protocols for quantum algorithms designed for

small cluster configurations [71, 76, 77, 80].

4.2.2 The model

Consider two players Alice (A) and Bob (B) involved in the classical Prisoners' Dilemma, which is a non-zero sum game. Informally, one can understand the 'game' as follows:

> *"Alice and Bob are arrested by the police at the scene of the gruesome murder of Charlie. Both are immediately taken away to separate interview rooms and questioned, before they have a chance to communicate with each other. They played a joint role in the murder, but the police have insufficient evidence for a conviction. The police visit each of them to offer the same deal: if one defects and testifies for the prosecution against the other and the other cooperates by remaining silent, the defector goes free and the silent accomplice receives the full 5-year sentence. If both cooperate and stay silent, the police can sentence both prisoners to only 2 years in prison for a minor charge. If each betrays the other and defects, they will share the murder charge and both receive a 4-year sentence. Each prisoner must make the choice of whether to defect and betray the other or to cooperate and remain silent. However, neither prisoner knows for sure what choice the other will make. So the question this dilemma poses is: How will the prisoners act?"*

In a mathematical formalism of the game, the strategy space of each player is denoted $S_j = \{c_j, d_j\}$ ($j = A, B$), where c (d) corresponds to a cooperate (defect) strategy [169]. The game is non-cooperative and selfish, as the players aim to maximise their own payoff $\$_j(s)$, where s is the strategy profile $s = (s_A, s_B)$ and $s_j \in S_j$ is the strategy chosen by player $j = A, B$ [172]. We have $\$_A(s) = 0$ with $\$_B(s) = 5$ (vice-versa) if the chosen profile is $s = (c_A, d_B)$ ($s = (d_A, c_B)$), as shown in Fig. 4.5. When both players carry out the same strategy, the payoff is equally shared. They obtain the *cooperative payoff* (CP) $\$_{A,B}(s) = 3$

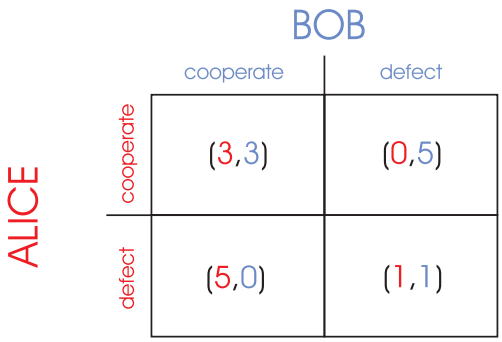

Figure 4.5: A *Payoff Table* for the game, with numbers appearing in the brackets (a, b) denoting the amount of time taken off Alice's prison sentence (a years) and Bob's prison sentence (b years), with a maximum of a 5-year prison sentence for the murder.

if $s = (c_A, c_B)$, whereas they obtain the *equilibrium payoff* (EP) $\$_{A,B}(s) = 1$ if $s = (d_A, d_B)$. A posteriori, (d_A, d_B) is found to be a *dominant profile*[6]. In fact, choosing d_j and regardless of the strategy adopted by the adversary, player j maximises their payoff. The profile (d_A, d_B) has the property that neither player can improve their payoff by a unilateral change of strategy, making it a *Nash equilibrium*[7] [173]. The rationality of the players and the non-cooperative nature of the game prevents A and B playing (c_A, c_B) which is the *Pareto optimum* [173]: no player can increase their payoff (which is the CP), by changing strategy, without reducing the payoff of the adversary. The Dilemma is in the dichotomy between the best choice for both and the highest payoff available individually.

This Dilemma cannot be solved without some degree of cooperativity between the players. This is introduced in the quantum version of the game in Ref. [169], where the strategies which the players can use are embodied by a qubit: $|c\rangle = (1\ 0)^T, |d\rangle = (0\ 1)^T$, where T denotes the transpose. Entangling stages $\mathcal{P}$ and $\mathcal{M}$ are introduced before and after the players perform their strategies. The

[6]This is an equilibrium in dominant strategies *i.e.* both players' dominant strategies match up. Alice's dominant strategy is s_A if $\$_A(s_A, s'_B) \geq \$_A(s'_A, s'_B),\ \forall s'_A \in S_A,\ s'_B \in S_B$ and similarly for Bob.

[7]Neither player can improve their payoff by a unilateral change of strategy. The profile (s_A, s_B) is a Nash equilibrium if $\$_A(s_A, s_B) \geq \$_A(s'_A, s_B)$ and $\$_B(s_A, s_B) \geq \$_B(s_A, s'_B),\ \forall s'_A \in S_A,\ s'_B \in S_B$. One can find it (or them) easily by elimination.

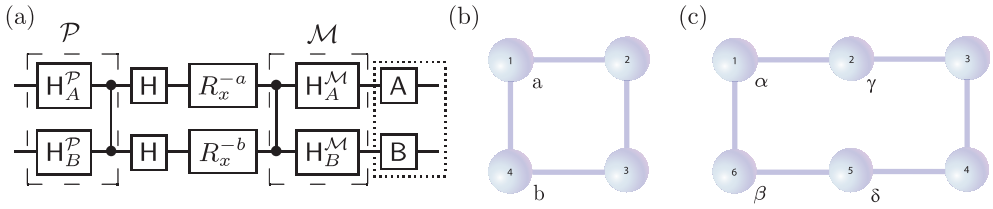

Figure 4.6: **(a)**: Scheme of the quantum game. The input state is $|c,c\rangle_{AB}$, which evolves through $\mathcal{P}$ and $\mathcal{M}$ and the players' local strategies. Vertical lines denote (CZ's), H's Hadamard gates and $R_x^{-(a,b)}$ single-qubit rotations around the x-axis. The dotted box is a utility stage. **(b)** & **(c)**: *Box* and *wafer* configuration for the sampling of the payoff. α, β, γ and δ are measurement angles.

strategy space is now $S_j = \{U_j(\theta_j,\phi_j)|\theta_j \in [0,\pi], \phi_j \in [0,\pi/2]\}$, where

$$U_j(\theta_j,\phi_j) = \begin{pmatrix} e^{-i\phi_j}\cos(\theta_j/2) & -\sin(\theta_j/2) \\ \sin(\theta_j/2) & e^{i\phi_j}\cos(\theta_j/2) \end{pmatrix} \tag{4.3}$$

with $c_j = U_j(0,0)$ and $d_j = U_j(\pi,0)$. In Refs. [169, 172], the choice of $U_{A,B}$ and its consequences on the performances of the game are discussed in more detail. The entanglement provides A and B with a degree of cooperativity. If their strategy profile $s = (U_A, U_B)$ is such that this cooperativity is preserved, a reconciliation between CP and EP can occur[8]. It is important to note that the procedure in Ref. [169] is just one of the ways in which the game can be extended to the quantum realm. The choice in Ref. [169] stresses that the payoffs associated with c_j and d_j should be the classical values and new equilibrium features are sought from the additional strategies provided by the quantum strategic space. In general, the constraint imposed on the quantum version of a protocol is that it reproduces the classical process, in the proper limiting case. Here, this means that the description of the Prisoners' Dilemma when $\mathcal{P}$ and $\mathcal{M}$ are removed and only c_j and d_j strategies are allowed must match the classical one.

The structure of the entangling steps is dictated by the interaction naturally realised by the setup considered. In this case, $\mathcal{P}$ and $\mathcal{M}$ must be related to the two-qubit gates simulated by a particular cluster configuration. In this respect, it is important to notice that a simple two-qubit cluster state results in the effective

[8]Issues related to the fact that the players are provided with the aid of an entangled state are not considered here [see S. J. van Enk and R. Pike, *Phys. Rev. A* **66**, 024306 (2002)] as this does not imply the possibility for them to coordinate their strategies.

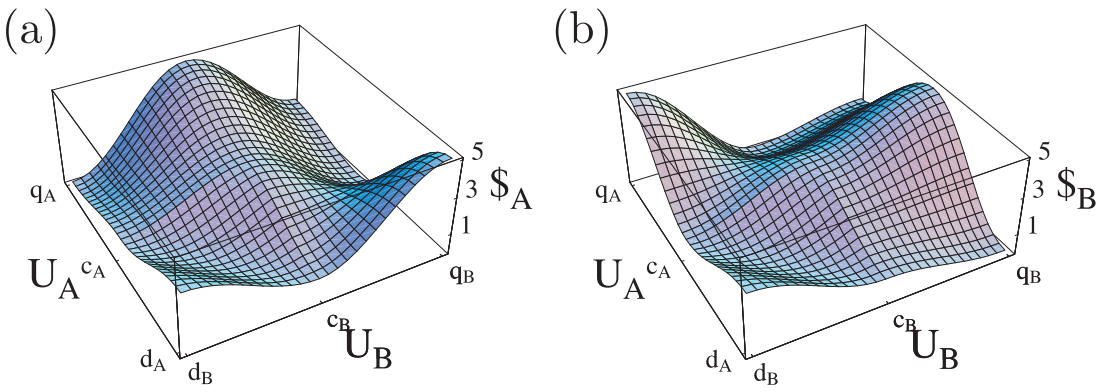

Figure 4.7: **(a)**: $\$_A$ vs. the strategies $U_{A,B}$. **(b)**: $\$_B$ vs. $U_{A,B}$. In both the panels, the parameterisation is $U_j = U_j(p\pi, 0)$ for $p \in [0, 1]$ and $U_j = U_j(0, -p\pi/2)$ for $p \in [-1, 0)$ $(j = A, B)$. Here, d_j corresponds to $p = 1$, c_j to $p = 0$ and q_j to $p = -1$.

simulation of a CZ gate (see BBB_2 in Chapter 2). This is a key advantage with respect to non-cluster based standard quantum circuit schemes. A cluster state can be constructed to naturally embody nearly the entire quantum steps $\mathcal{P}$ and $\mathcal{M}$, which otherwise, have to be implemented by two independent two-qubit operations. This is because networking these operations to obtain the scheme in Fig. 4.6 **(a)** is in general a difficult task. The use of a cluster state in this proposal, represents a major advantage in this respect. In addition, in the same two-qubit cluster, the measurement of a qubit in the basis $B(\alpha)$ simulates the application of $R_x^{-a}\mathsf{H} \equiv \mathsf{H}R_z^{-a}$ on a logical qubit, where R_x^{-a} is a rotation by an angle $-a$ around the x-axis of the Bloch sphere and H is the Hadamard gate. The full quantum circuit proposed is shown in Fig. 4.6 **(a)**, with the part prior to the dotted box being simulated by the cluster in Fig. 4.6 **(b)**. The state corresponding to this box cluster [71, 76, 78, 80], can be put into the form $|box\rangle = (1/4)[|0\rangle_1 + |1\rangle_1 (\sigma_{z,2} \otimes \sigma_{z,4})](\mathsf{H}_2 \otimes \mathsf{H}_4) |ghz\rangle_{234}$, where $|ghz\rangle = (1/\sqrt{2})(|000\rangle + |111\rangle)$ is a GHZ state [148]. One can now exploit the naturally simulated CZ gate and $\mathsf{H}_j^{\mathcal{P}}$'s (implicit in the preparation of a cluster state [55, 56]) to obtain $\mathcal{P} = \mathsf{CZ}(\mathsf{H}_A^{\mathcal{P}} \otimes \mathsf{H}_B^{\mathcal{P}})$. The $\mathsf{H}_j^{\mathcal{P}}$'s allow one to generate a maximally entangled strategic state and to combine superpositions of orthogonal strategies and entanglement [174]. Despite the conceptual equivalence of $\mathcal{P}^\dagger$ and $\mathcal{M} = (\mathsf{H}_A^{\mathcal{M}} \otimes \mathsf{H}_B^{\mathcal{M}})\mathsf{CZ}$, it is worth differentiating them as the $\mathsf{H}_j^{\mathcal{M}}$'s are simulated in the box cluster by measuring qubits 2 and 3 in the σ_x eigenbasis.

Strategy		$-a$	$-b$	A	B	Strategy		$-a$	$-b$	A	B
c_A	c_B	0	0	$\mathbb{1}$	$\mathbb{1}$	q_A	d_B	0	π	$i\sigma_x$	$i\sigma_x$
c_A	q_B	0	0	$\mathbb{1}$	$i\sigma_x$	d_A	c_B	π	0	$i\sigma_x$	$\mathbb{1}$
c_A	d_B	0	π	$\mathbb{1}$	$i\sigma_x$	d_A	q_B	π	0	$i\sigma_x$	$i\sigma_x$
q_A	c_B	0	0	$i\sigma_x$	$\mathbb{1}$	d_A	d_B	π	π	$i\sigma_x$	$i\sigma_x$
q_A	q_B	0	0	$i\sigma_x$	$i\sigma_x$	m_A	m_B	π	π	$\mathbb{1}$	$\mathbb{1}$

Table 4.2: Rotation angles and imported operations for the strategies in the quantum game with $m_{A,B} = \frac{1}{\sqrt{2}}(\mathbb{1} + i\sigma_y^{(A,B)})$.

Quantitatively, the following expression needs to be calculated

$$P_{\xi\chi} = |_{AB}\langle \xi, \chi | \mathcal{M}(U_A \otimes U_B)\mathcal{P} \, |c, c\rangle_{AB}|^2 \;\; (\xi, \chi = c, d), \tag{4.4}$$

which gives the probability that the evolved strategy profile, after the operations by the players, is $s = (\xi_A, \chi_B)$. With Eq. (4.4) it is easy to evaluate $\$_A(U_A, U_B) = 3P_{cc} + P_{dd} + 5P_{dc}$ and $\$_B(U_A, U_B) = 3P_{cc} + P_{dd} + 5P_{cd}$. The results are shown in Figs. 4.7 **(a)** and **(b)**. The strategic sector $[c_j, d_j]$ ($[q_j, c_j]$) corresponds to $\phi_j = 0$ ($\theta_j = 0$) with $\theta_j \in [0, \pi]$ ($\phi_j \in [0, \pi/2]$). This parameterisation reveals the relevant features of the game.

From Fig. 4.7 **(a)**, one can see that for B choosing d_B or q_B, the best strategy by A is d_A with payoffs $\$_A(d_A, d_B) = 3$ or $\$_A(d_A, q_B) = 5$ respectively. Analogous considerations can be made *mutatis mutandis* about $\$_B(U_A, U_B)$ (Fig. 4.7 **(b)**). It can be seen that the profile (d_A, d_B) is the only Nash equilibrium. The players' payoff for this profile is exactly the CP and (d_A, d_B) is found to be Pareto optimal. This result is quantum mechanical, as the payoff corresponding to (d_A, d_B), in a game without $\mathcal{P}$ and $\mathcal{M}$, is EP. Indeed, in the separable quantum game resulting from the removal of the CZ's in $\mathcal{P}$ and $\mathcal{M}$ (keeping $\mathsf{H}_{A,B}^{\mathcal{P},\mathcal{M}}$), no reconciliation is achieved. Moreover, it will be shown in the next section that the Pareto optimality cannot be attained by using classical correlations shared between the players of the game, suggesting that the entanglement the players are provided with favours the reconciliation of the Dilemma. While the procedure in Ref. [169] introduces a *new strategy profile* which is a Nash equilibrium and achieves CP, in this scheme the equilibrium strategy is the same as in the non-entangled game. The entanglement renders (d_A, d_B) the profile that *preserves* the cooperativity introduced by $\mathcal{P}$.

Parts of the game can be naturally implemented by a box cluster, but the strategies $U_{A,B}$ must be simulated by an appropriate measurement pattern. As shown in Figs. 4.6 **(a)** and **(b)**, by measuring qubits 1 and 4 one can simulate just a rotation around the x axis of the single-qubit Bloch sphere. Thus, more freedom is required for the players to perform their strategies. For this task, we can exploit the fact that $\mathsf{H}^{\mathcal{M}}_{A,B}$ and CZ belong to the Clifford group. The operations $\mathsf{A},\mathsf{B} \in \{\sigma_{x,y,z}, R^{\mu}_{x}\}$ in the dotted box of Fig. 4.6 **(a)**, can therefore be *imported* to the dashed section of the circuit. They are seen as operations on the qubits $2,3$ of the box cluster applied before their final measurement. Together with $R^{-a,-b}_{x}$ simulated by the measurement of 1 and 4, these enlarge the strategy space of the players. In Table 4.2, the measurement angles a and b are shown together with the corresponding A and B for various strategies. Only two measurement bases are needed and $\mathbb{1}$ or σ_x must be imported before the measurements are performed.

Note that the use of local operations on the logical output qubits of a cluster is inherent to the $\mathrm{QC}_{\mathcal{C}}$ model [129, 130]. The randomness of the measurement outcomes affects a gate simulation which has to be corrected by local decoding operators. Here, the postselection of those events corresponding to the projection of qubits 1 and 4 onto $|+\rangle^{a,b}_{1,4}$ is implicitly assumed. In this case, the decoding operators are $\mathbb{1}_{2,3}$. A and B may be seen as decoding operators selected not by the measurement outcomes but by the task to perform. The hybrid nature of this approach should be clear: one cannot rely just on the MB gate simulations because additional rotations of the logical output qubits are needed. Here, A and B can easily be realised in the all-optical setups in Refs. [71, 76, 80]. Indeed, by exploiting the relation $\mathsf{H}^{\mathcal{M}}_{j}\sigma_{x,j} = \sigma_{z,j}\mathsf{H}^{\mathcal{M}}_{j}$, the players only need to apply σ_z to the output qubits, which is possible via phase shifters, before they are measured in the σ_x eigenbasis. In this way, all the strategies in Table 4.2 can be achieved, which is *sufficient* to experimentally study the Pareto-optimality of the Nash equilibrium point (Fig. 4.8 **(a)** graphically shows these strategies). However, this does not exhaust all the possibilities. For instance, the entire quadrant $[q_A, c_A]\times[q_B, c_B]$ can be sampled simply by taking $a = b = 0$, importing $\mathsf{A} = R^{\mu}_{x}$ and $\mathsf{B} = R^{\nu}_{x}$ then scanning the angles μ, ν. Single-qubit manipulations through linear-optical elements just prior to the detection stage make this scheme feasible [71, 76, 80].

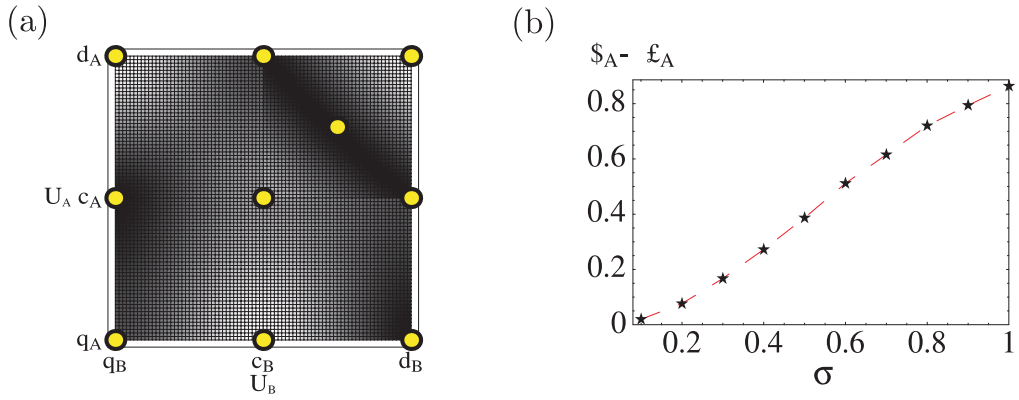

Figure 4.8: **(a)**: Density plot of $\$_A$ (see Fig. 4.7 **(a)**). The brighter the plot, the higher the payoff. Each bright dot shows a strategy in Table 4.2. The central dot in the top-right quadrant corresponds to the profile (m_A, m_B). **(b)**: Differences between $\$_A(d_A, d_B)$, the ideal payoff, and $£_A(d_A, d_B)$, the average with imperfections, plotted against the standard deviation σ of the normal distributions attached to the rotation angles.

However, it is not possible to sample the entire payoff $\$_{A,B}$ with the box cluster because it is not possible to obtain $R_y^{\theta_j} = R_x^{-\pi/2} R_z^{\theta_j} R_x^{\pi/2} \equiv U_j(\theta_j, 0)$. For a complete tomography of $\$_{A,B}$, the price to pay is the use of a larger number of qubits. Indeed, using the concatenation technique as described in Chapter 2 and an analysis similar to the one relative to the box cluster, one finds that the *wafer* configuration in Fig. 4.6 **(c)** can fully embody this quantum game. The rotation R_y^θ can be realised by choosing $\alpha = \beta = \pi/2$, $\gamma = \theta_A$, $\delta = \theta_B$ and importing $\mathsf{A} = \mathsf{B} = R_x^{\pi/2}$, which correspond to a phase shift $R_z^{\pi/2}$ applied to 3 and 4 before measuring in the σ_x eigenbasis. This wafer configuration could be realised by gluing two four-photon entangled linear cluster states [71–73, 76, 77, 80] using the technique suggested in Ref. [131] and realised in Ref. [74].

4.2.3 Effects of imperfections

The effects of realistic imperfections in the game are now addressed. There are two main sources of error that need to be considered. First, non-idealities can originate from errors introduced in the measurements. The waveplates in front of the photodetectors used to measure the state of the photonic cluster qubits may introduce unwanted rotations of a polarisation state, leading to inaccurate

measurement bases. In addition, imperfections at the down-conversion stage in generating a box cluster provide mixed entangled states to the players[9]. Both these sources of error can be formally addressed by the replacement $\theta_j \rightarrow \theta_j + \epsilon_j$ in Eq. (4.3) (analogously for ϕ_j) and averaging the payoffs over appropriate probability distributions, with standard deviation σ_j attached to the ϵ_j's. This randomness results in a corrupted mixed entangled resource [175, 176] whose degree of entanglement diminishes if σ is increased. In Fig. 4.8 **(b)** the differences are shown between the ideal (Pareto optimal) $\$_A(d_A, d_B)$ and the average payoff $£_A(d_A, d_B)$ obtained when the ϵ_j's are normally distributed around 0. The result is not affected by fluctuations in ϕ_j as d_j does not depend on this parameter. At $\sigma \simeq 0.9$ the degree of entanglement (quantified by the measure introduced in Chapter 2, based on the NPT criterion [100–103]) is $\lesssim 0.01$. The larger the fluctuations allowed for ϵ_j, the larger the deviation of the corresponding payoff from the behaviours in Fig. 4.7. The effect of classical correlations can also be studied by considering the mixed initial state $\otimes_{j=A}^{B}[(1-x)\,|c\rangle_j\langle c| + x\,|d\rangle_j\langle d|]$ ($x \in [0, 0.5]$) to enter $\mathcal{P}$, resulting in a non-ideal entangled mixed resource which A and B use to play the game. For $x \geq 0.29$, this mixed state is separable so that A and B only share classical correlations. In this case, it is easy to find that CP$>$ $\$_{A,B}^{x\geq 0.29}(d_A, d_B)$ $>$EP. Furthermore, no other Pareto optimal points arise as a result of different strategy profiles. The method outlined here provides an operative way in which to study how the Pareto optimality is lost when corrupted resources and imperfect measurements are present in an experimental realisation of the protocol. It represents a useful tool in studying the performance of the quantum game.

[9]With respect to the influences of photon-loss, it is important to note that this is effectively overcome in retrospective one-way experiments (such as the setup described in Section 4.1) by the use of post-selection. This allows one to discard the events associated with photon-losses by tracking the detection outcomes, therefore enabling reliable computation in this context. In addition, the inefficiency of single-photon detectors can be mapped into equivalent photon-loss events and therefore treated on the same footage as described above.

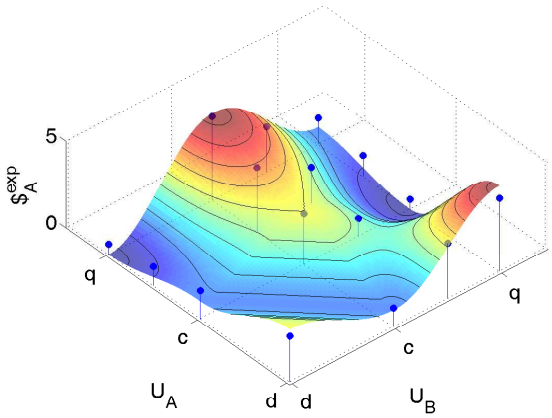

Figure 4.9: Experimental plot from an all-optical setup resulting in $\$_A$ pay-off points corresponding to Fig. 4.7 **(a)** (Courtesy of R. Prevedel [81]).

4.3 Remarks

In Section 4.1, the design, demonstration and characterisation of the performance of the first experimental realisation of Deutsch's algorithm on a cluster state was provided and discussed. The experiment is one of the few quantum algorithms entirely implemented utilizing the MB one-way model [71, 76, 77, 80]. The agreement between the experimental data and theory was found to be excellent and only limited by the overall quality of the entangled resource in the experiment. In Section 4.2, an implementation of the quantum Prisoners' Dilemma was proposed using an economical and experimentally realisable cluster state configuration. At the same time, it was shown that the cluster model can be complemented by simple rotations of the logical output qubits to add freedom to the gate simulation. This enabled the building of a hybrid model that has subsequently been realised recently with existing all-optical technology [81]. This has allowed for an immediate experimental investigation of the role of entanglement in the search for a Pareto optimal Nash equilibrium point in a system exhibiting quantum correlations. Fig. 4.9 shows the experimental points from the linear optical experiment.

Chapter 5

Resources using natural three-body interactions

For the entangled resource on which an MB one-way protocol is realised, a benefit of using more sophisticated entanglement structures should be the ability to construct compact and economical simulations of quantum algorithms with limited resources. In this Chapter, the effects of natural three-qubit interactions on the computational power of one-way QC will be studied. It will be shown that the features of this study can be embodied by suitably prepared optical lattices, where effective three-spin interactions have been theoretically demonstrated. The setup is then used to provide a more compact construction for a three-qubit Toffoli gate (control-control-NOT, or $\mathsf{C^2NOT}$) than in the standard $\mathrm{QC}_{\mathcal{C}}$ model. This is an important gate for performing quantum algorithms on registers larger than just two qubits (*e.g.* those in chapter 4). The reason for this is because not only is it a universal gate (together with single qubit arbitrary rotations one can perform any unitary operation, just like the CNOT), but one can build n-time controlled-NOT ($\mathsf{C^nNOT}$) gates from it polynomially [177] (a factor of six better than from CNOT's [62]). $\mathsf{C^nNOT}$ gates are crucial in various n-qubit quantum algorithms, most notably Grover's search algorithm [25]. Therefore finding compact constructions of Toffoli gates allows for a more compact algorithm design than using CNOT's and thus lessens the effects of noise (as seen in Chapter 3). Information flow and two-qubit gates (CNOT's) are also outlined using this new entangled resource to highlight the potential of the model, together with an analysis of relevant sources of imperfection.

5.1 Introduction

The realisation of MB cluster state quantum algorithms is often expensive in terms of qubit resources, an aspect quite detrimental to the efficiency of the QC, as highlighted in Chapter 3. An illuminating example is provided by the n-qubit generalisation of the simple two-qubit *searching for a marked entry* algorithm realised in [71, 76, 80]. In the standard network model for QC [60–62] this consists of $\mathcal{O}(\sqrt{2^n})$ oracle-inversion steps [25] each requiring two n-time controlled-NOT gates. For $n > 3$, these can be made from $4(n-3)$ three-qubit Toffoli gates [62], which in a cluster-state based implementation require 65 qubits [130]. A three-qubit version of the algorithm would require ~ 245 cluster

qubits[1], a number which makes the protocol susceptible to even small amounts of noise affecting the cluster resource as we have seen in Chapter 3. A way to counteract this difficulty is the use of more compact cluster configurations which simulate three-qubit gates. If the universal three-qubit Toffoli gate is realised in a compact way, the number of qubits and manipulations needed to perform a given task will be dramatically reduced. Unfortunately any attempt in this direction in a cluster state-based scenario seems to be destined to failure. The reason is due to the underlying two-qubit structure imposed by the effective CZ gates used in the construction of cluster states [55, 56]: a constraint preventing any further compacting of a natural three-qubit gate is set. On the other hand, if one considers using generalised graph states as the initial entanglement resource [178], the number of physical qubits required can be reduced. However, this kind of resource generation involves a complex web of specially arranged entanglement, with no naturally accessible physical systems for their realisation. They are a result of consecutive active entanglement generation. It is therefore interesting to investigate whether other entanglement structures are possible for the multipartite entangled resource, providing economical configurations which scale better in the presence of noise and can be generated in a system-wide fashion physically. In this Chapter, one such possibility is described, based on recently demonstrated three-spin interactions in optical lattices [179]. The proposal allows the construction of compact configurations for the simulation of Toffoli gates in the $\mathrm{QC}_{\mathcal{C}}$ model and opens up new possibilities in the search for conducting economical and robust-to-noise quantum algorithms.

The Chapter is structured as follows: In Section 5.2, the entanglement structure of the resource is introduced and simulations of QIP protocols via measurements are discussed. Next, in Section 5.3 a physically realisable setup for the proposal is provided, in the form of a *bowtie* shaped optical superlattice. In Section 5.4, imperfections within the model at the entanglement stages are then addressed. Finally, in Section 5.5 a summary of the results, together with some interesting and relevant comments concerning the outlook of this model are given.

[1] A concatenation of Toffoli gates rather than stabiliser formalism is assumed, where we have (2 iterations $\times$ 2 Toffoli's $\times$ 65 qubits) - (18 overlap qubits) + (local rotations).

5.2 The model

Consider a lattice of qubits with the *bowtie* structure depicted in Fig. 5.1 **(a)**, where each qubit with logical basis $\{|0\rangle, |1\rangle\}$ is initially prepared in the state $|+\rangle = (1/\sqrt{2})(|0\rangle + |1\rangle)$. For every closed triangle, an entangling operation is applied between qubits i, j and k at the vertices equivalent to a control-control-σ_z gate ($\mathsf{C}^2\mathsf{Z}$),

$$S^{ijk} = \mathbb{1}^{(ijk)} - 2|111\rangle_{ijk}\langle 111|. \tag{5.1}$$

For convenience this operation will be denoted by $\circlearrowleft$ and $\sigma_{l,i}\,(l = x, y, z)$ will be used as the l-Pauli matrix applied to the i-th qubit. This particular lattice of qubits can be described as a graph state, where the coincidence/adjacency matrix [180] becomes a generalised tensor. The physical mechanism which realises this configuration is addressed later. First, a way to achieve information-flow across the lattice is described.

In order to create a path for information to be propagated along via measurements, it is necessary to remove the influence of particular lattice qubits depending on the protocol being performed. It is straightforward to check that due to the three-body nature of the entanglement, a measurement in the single-qubit σ_z eigenbasis with outcome $|0\rangle$ ($|1\rangle$) destroys (sustains) entanglement between the remaining two qubits. On the other hand, by setting the qubit to be removed in $|0\rangle$ or $|1\rangle$ before entanglement is generated across the entire lattice, a path can be formed, the choice being dependent on the required shape of the path itself. Setting a qubit to $|1\rangle$ generates the well-known Ising-type interaction between the other two, while setting it to $|0\rangle$ prevents any interaction from being generated. Paths of linear cluster states may then be embedded within the lattice and used to propagate information using techniques borrowed from the cluster-state model [129, 130], as shown in Fig. 5.1 **(a)** and **(b)**. This technique, which initialises the qubits not involved in a specific protocol before introducing the entanglement across the lattice, puts the *removed* qubits in an eigenstate of σ_z. This vastly reduces the effects of spreading measurement or environment-induced noise created at the entangling stage (see Chapter 3). Two-qubit gates can also be realised in a similar way to the cluster state model. An example is given in Fig. 5.1 **(b)**, where measuring the *bridging qubit* (*b.q*) in the σ_y eigen-

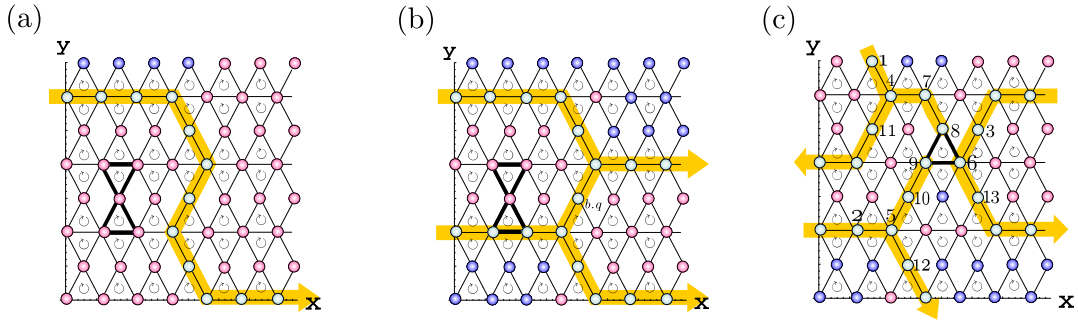

Figure 5.1: **(a)** & **(b)**: The lattice structure and propagation of quantum information. Red (blue) dots represent qubits in $|1\rangle$ ($|0\rangle$) and ⟳ denotes the three-spin interaction. The dark arrow shows the path of information, which is propagated via σ_x measurements. A two qubit interaction is also shown in **(b)**, where the *bridging* qubit ($b.q$) should be measured in the σ_y eigenbasis (see BBB_3 in Chapter 2). **(c)**: A three-qubit interaction and the paths to bring information in/out of the interaction region.

basis simulates the gate $U = \mathsf{CNOT}(\mathbb{1} \otimes R_z^{\pi/2})\mathsf{CNOT}$ (see BBB_3 of Chapter 2), with $R_z^{\pi/2}$ a single-qubit rotation about $\hat{\mathbf{z}}$ on the Bloch sphere by $\pi/2$.

In addition to the embedded standard cluster-state based manipulation of information, the three-spin entanglement structure can be exploited to construct compact three-qubit controlled gates using a small number of qubits. One example is shown in Fig. 5.1 **(c)**, where we require the logical qubits to propagate away after the interaction via ⟳ at the central triangle. It is easy to see that an enlargement of the basic three-spin triangle is necessary. In order to give a better insight into this, the core entangled resource involved in simulating a Toffoli gate has been extracted from Fig. 5.1 **(c)** into Fig. 5.2 **(a)**. The enlargement can be achieved by measuring qubits 7 to 10 in the σ_x eigenbasis, a method similar to that used in the standard cluster state model to remove pairs of adjacent qubits. The byproduct operation needed to retrieve the original $\mathsf{C}^2\mathsf{Z}$ of the central triangle between qubits $4, 5$ and 6 after enlargement $\mathscr{E}$ is given by

$$\tilde{U}_{\Sigma_{\mathscr{E}}} = (\sigma_{z,4}^{s_8^x} \otimes \sigma_{z,5}^{s_9^x} \otimes \sigma_{z,6}^{s_7^x s_{10}^x})(\mathbb{1}_5 \otimes \mathsf{CZ}_{4,6}^{s_{10}^x})(\mathbb{1}_4 \otimes \mathsf{CZ}_{5,6}^{s_7^x}). \tag{5.2}$$

Here s_i^x is the outcome of the measurement of qubit i in the σ_x eigenbasis with $s_i^x = 0$ ($s_i^x = 1$) corresponding to $|+\rangle_i$ ($|-\rangle_i$). The CZ's in $\tilde{U}_{\Sigma_{\mathscr{E}}}$ result from the $\mathsf{C}^2\mathsf{Z}$ operation not being in the Clifford group [130]. In order to show that

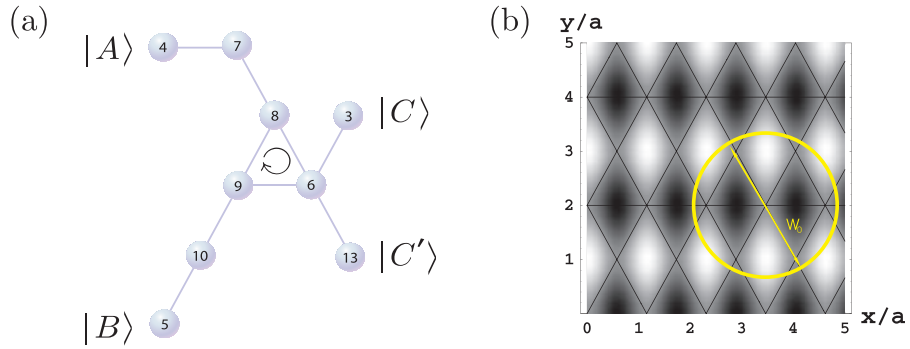

Figure 5.2: **(a)**: A $\mathsf{C^2NOT}$ extracted from Fig. 5.1 **(b)**. Qubit $|C\rangle$ is the target and $\circlearrowleft$ naturally realises a $\mathsf{C^2P}$. σ_x-measurements of qubits 3 and 6 realise Hadamard gates before and after $\circlearrowleft$. **(b)**: The *bowtie* lattice structure created by V_{off}, where the x and y axes are scaled by $a = \lambda/2$. Dark (light) regions correspond to small (large) positive valued potential shifts, with the vertices of the superimposed grid representing lattice sites. The width $w_0 \sim 2.8\,a$ of a Gaussian beam (used for register initialisation) is shown.

the enlarged three-spin triangle can be concatenated with the paths propagating the logical qubits toward and away from it, we can write the CZ operator as $S^{ij} = \mathbb{1}^{(ij)} - 2\,|11\rangle_{ij}\langle 11|$, which is applied to qubits i and j in a triangle when the third qubit k is in $|1\rangle$. Let qubits 1, 2 and 3 in Fig. 5.1 **(c)** encode the states $|A\rangle$, $|B\rangle$ and $|C\rangle$ respectively. Then, we can entangle and measure the qubits as follows: $(\otimes_{i=1}^{3} P_X^i)(\otimes_1^3 S^{i,i+3})\,|A\rangle_1\,|B\rangle_2\,|C\rangle_3\,|+\rangle_{\mathcal{T}}$, where $|+\rangle_{\mathcal{T}} = \otimes_{i=4}^{13}|+\rangle_i$ and P_X^i represents the projector for a measurement in the $\sigma_{x,i}$ eigenbasis. This procedure realises a two-site cluster-state based propagation of the logical qubits, with qubits $7 \rightarrow 13$ left unaffected. Now, consider the triangle enlargement described previously and a subsequent information-flow away from it. The entire process is written as

$$(\otimes_{i=1}^{10} P_X^i)S^{6,13}S^{5,12}S^{4,11}(S^{6,9,8})S^{5,10}S^{9,10}S^{7,8}S^{4,7} \times (\otimes_{i=1}^{3} S^{i,i+3})\,|A\rangle_1\,|B\rangle_2\,|C\rangle_3\,|+\rangle_{\mathcal{T}}\,. \tag{5.3}$$

As $[S^{ijk}, \mathbb{1}^l \otimes S^{mn}] = 0$ $(\forall i,j,k,l,m,n)$ using the concatenation rules of propagation from Chapter 2, one can see that the entire lattice can be entangled and then measurements performed. To complete this analysis, it is now shown how an arbitrary byproduct operator changes on propagation through the $\mathsf{C^2Z}$. Let $\otimes_{j=1}^{3}(\sigma_{x,\alpha_j}^{s_{\alpha_j}^x}\sigma_{z,\alpha_j}^{s_{\alpha_j}^z})$ denote the byproduct operator for any measurement pattern $\mathcal{M}$

carried out before the gate, where α_j is the site-label of the logical qubits, with values $s^x_{\alpha_j}$ and $s^z_{\alpha_j}$ dependent on the outcomes of $\mathcal{M}$ before α_j. Upon propagation through, we obtain

$$\tilde{U}_{\Sigma_{\mathcal{M}}} = \prod_{j=1}^{3}(\mathcal{P}_j \mathsf{CZ}_{\alpha_2,\alpha_3}^{s^x_{\alpha_1}}) \times \prod_{j=1}^{3}(\mathcal{P}_j \sigma_{x,\alpha_1}^{s^x_{\alpha_1}} \sigma_{z,\alpha_1}^{s^x_{\alpha_2} s^x_{\alpha_3} + s^z_{\alpha_1}}), \tag{5.4}$$

where $\mathcal{P}_j$ is an operator that exchanges label 1 with j. A two-qubit byproduct operator is again produced. For both $\tilde{U}_{\Sigma_{\mathcal{M}}}$ and $\tilde{U}_{\Sigma_{\mathscr{E}}}$, any CZ cannot be propagated trivially and it is necessary to remove it straight after the gate. This can be achieved by applying two-qubit gates analogous to the one in Fig. 5.1 **(b)** to logical qubits that underwent the $\mathsf{C^2Z}$. In this case, we can measure the $b.q$'s in the σ_y (σ_z) eigenbasis, resulting in a CZ (breaking the link) between the logical qubits up to local rotations, thus reducing $\tilde{U}_{\Sigma_{\mathcal{M},\mathscr{E}}}$ to local forms again. The simulation then proceeds as in the cluster-state model until the next three-qubit gate occurs.

5.3 Physical Realisation

To realise the model outlined in the previous Section, the trapping of alkali-metal atoms such as ^{87}Rb in triangular two-dimensional optical lattices is considered. The trapping of atoms can be achieved using three pairs of counter-propagating laser beams (L, $L^{\pm}$), tuned between the $D1$ and $D2$ line with $\lambda = 785$ nm and slightly detuned from each other. The pairs are in a lin||lin configuration [146], which means that the lasers are linearly polarised with the angle between the polarisations of each laser beam set at $\theta = 0$, as shown in Fig. 5.3 **(a)** and described in the caption. The pairs L, $L^{\pm}$ propagate along $\hat{\mathbf{y}}$ and $(\hat{\mathbf{y}} \pm \sqrt{3}\hat{\mathbf{x}})/2$ respectively. This provides lattice sites with periodicity $\lambda/\sqrt{3}$ as depicted in Fig. 5.3 **(b)**. An appropriate external trapping field is applied in the $\hat{\mathbf{z}}$ direction to confine the atoms to the $x-y$ plane. Each logical qubit can be embodied by the single-atom hyperfine states[2] $|a\rangle = |0\rangle \equiv |F = 1, m_f = 1\rangle$ and $|b\rangle = |1\rangle \equiv |F = 2, m_f = 2\rangle$, as shown in Fig. 5.3 **(c)**, with F and m_f the total angular

[2]The atomic weight of atoms such as ^{87}Rb leads to relativistic effects of the electronic orbitals which induce hyperfine splittings [181].

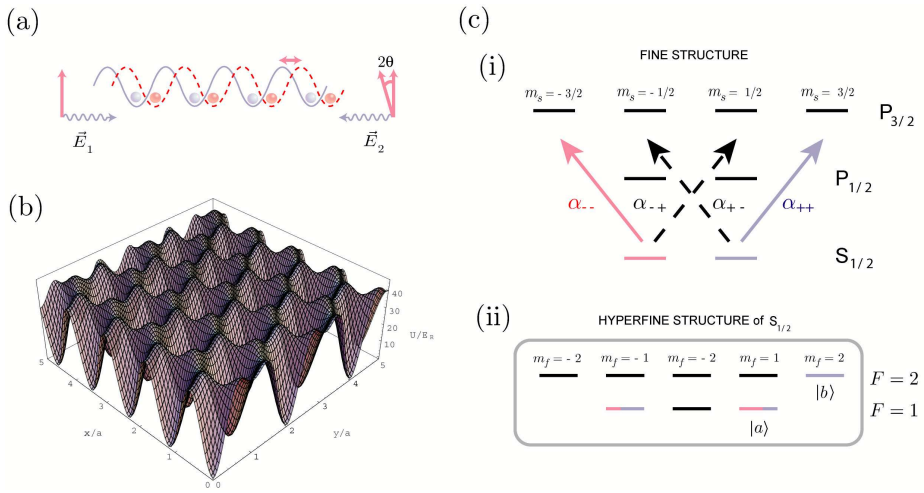

Figure 5.3: **(a)**: Trapping of atoms such as ^{87}Rb in a periodic potential. Two counter-propagating *linearly* polarised plane waves of same intensity E_0 form a total electric field $E^T = E_0 e^{-i\omega t}(\vec{\epsilon}_1 e^{ikz} + \vec{\epsilon}_2 e^{-ikz})$, where ω is the frequency of the lasers, k is the wave vector and $\vec{\epsilon}_1$ and $\vec{\epsilon}_2$ represent the polarisations of the two lasers. E^T can be described as a superposition of left and right circularly polarised waves by denoting the angle between $\vec{\epsilon}_1$ and $\vec{\epsilon}_2$ as 2θ and transforming to the basis $\vec{\epsilon}_\pm = (1/\sqrt{2})(\vec{\epsilon}_x \pm i\vec{\epsilon}_y)$. We can then write $E^T = \sqrt{2}E_0 e^{-i\omega t}(\vec{\epsilon}_+ \sin(kz+\theta) + \vec{\epsilon}_- \sin(kz-\theta))$, where $\vec{\epsilon}_\pm$ denote unit right and left circular polarisation vectors. The optical potentials experienced by the hyperfine states $|a\rangle$ and $|b\rangle$ shown in **(c) (ii)** are related to those of the $S_{1/2}$ fine structure states $m_s = \pm 1/2$ shown in **(c) (i)**, given by $V_{m_s=\pm 1/2}(z,\theta) = \alpha |E_0|^2 \sin^2(kz \pm \theta)$. Here $\alpha = \alpha_{++} = \alpha{--}$, where α_{++} and $\alpha{--}$ are the dynamical polarisabilities due to the $\epsilon_\pm$ standing polarised waves ($\Delta m_s = 0\ (\pm 1)$ for linear (circularly) polarised light). By tuning the lasers between the $D1$ ($S_{1/2} \leftrightarrow P_{1/2}$) and $D2$ ($S_{1/2} \leftrightarrow P_{3/2}$) line, the α_{+-} and $\alpha{-+}$ dynamical polarisabilities due to the laser polarisation $\epsilon_\mp$ can be made to vanish. The relation between the fine and hyperfine state potentials can then be found using the Clebsch-Gordon coefficients and we may write the trapping potentials for $|a\rangle$ and $|b\rangle$ as $V^a(z,\theta) = [V_{m_s=+1/2}(z,\theta) + 3V_{m_s=-1/2}(z,\theta)]/4$ and $V^b(z,\theta) = V_{m_s=+1/2}(z,\theta)$ respectively. A lin||lin configuration means $\theta = 0$, thus both the states experience the same periodic optical potential. **(b)**: Plot of the trapping potential in the x-y plane (see also Fig. 5.2 **(b)**, where an off-set potential has been applied).

momentum of the atom and its projection along $\hat{\mathbf{z}}$ respectively. These states can then be coupled via a Raman transition [182], using an excited state $|e\rangle$ embodied by another hyperfine state, as outlined in Fig. 5.4. The lattice is assumed to be initially loaded with one atom per site, which can be achieved by making a Bose-Einstein condensate undergo a superfluid to Mott insulator (MI)

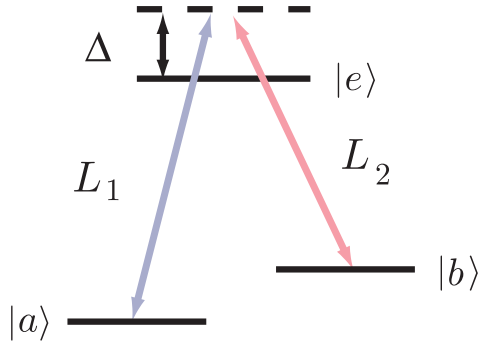

Figure 5.4: A Raman transition, where the effective Hamiltonian describing the effect of two detuned laser fields L_1 and L_2 on the states of a three-level system (Λ configuration) is given by $H_{eff} = g(t)|a\rangle\langle b| + g^*(t)|b\rangle\langle a|$. The coupling parameter $g(t) = -\frac{\tilde{\Omega}}{2}e^{-i\delta t}$, with $\tilde{\Omega} = \frac{\Omega_1^*\Omega_2}{2\Delta}$ and $\delta = \frac{|\Omega_1|^2 - |\Omega_2|^2}{4\Delta}$. Ω_1 and Ω_2 are the complex Rabi frequencies associated with the coupling of field modes of frequencies ω_{L_1} and ω_{L_2} to the atomic transitions $|a\rangle \leftrightarrow |e\rangle$ and $|b\rangle \leftrightarrow |e\rangle$ respectively. Δ is the two-photon Raman detuning. If $g(t)$ is real we have $\mathcal{U} = e^{-i\int_0^T g(t)dt(|a\rangle\langle b| + |b\rangle\langle a|)}$ and an initial atomic state $|\psi(0)\rangle = |a\rangle$ is rotated into the state $|\psi(t)\rangle = \mathcal{U}|a\rangle = \cos\Lambda|a\rangle - i\sin\Lambda|b\rangle$, where $\Lambda = \int_0^T g(t)dt$.

phase transition [70, 182, 183]. In a second-quantisation picture, the two-species Bose-Hubbard Hamiltonian

$$H = -\sum_{\alpha=a,b}(J^\alpha \sum_{\langle i,j\rangle} \alpha_i^\dagger \alpha_j - \frac{1}{2}U^{\alpha\alpha}\sum_i \alpha_i^{\dagger 2}\alpha_i^2) + U^{ab}\sum_i a_i^\dagger b_i^\dagger a_i b_i \qquad (5.5)$$

describes the dynamics of the cold gas of interacting bosons in the periodic trapping potential considered (as outlined earlier in Chapter 3). Here, α_i ($\alpha_i^\dagger$) [$\alpha = a, b$] are the annihilation (creation) operators for atomic species α at site i and the summations are taken over nearest-neighbor (NN) sites, indicated by $\langle i, j\rangle$. $U^{\alpha\alpha}$ ($U^{ab} = U^{ba}$) represents the strength of the homo-species (hetero-species) on-site repulsive force experienced by the atoms. J^α is the homo-species tunneling strength between sites i and j. For both U and J, effects from atoms in NN and next-NN sites respectively are assumed to be negligible [182]. For a triangular periodic potential, the Hamiltonian can be confined to a unit-cell of three sites in an equilateral triangular configuration [179] obtaining $H =$

$H^{(0)} + V$, where

$$H^{(0)} = \frac{1}{2}\sum_{i\,\alpha\,\beta} U^{\alpha\beta}\alpha_i^\dagger\beta_i^\dagger\beta_i\alpha_i \tag{5.6}$$

$$V = -\sum_{i\,\alpha} J_i^\alpha(\alpha_i^\dagger\alpha_{i+1} + \alpha_{i+1}^\dagger\alpha_i). \tag{5.7}$$

For $J_j^\alpha \ll U^{\alpha\,\beta}\,(\forall j)$, $\alpha, \beta \in \{a, b\}$, V can be treated as a perturbation. In these conditions, leaving the subspace M corresponding to the prepared MI (with unit filling-fraction) is energetically unfavourable for the system: its spectrum is gapped and states with higher filling-fractions can be adiabatically eliminated using standard techniques [184]. An effective Hamiltonian is obtained with only virtual transitions to higher population subspaces [179]. By switching to a *pseudo-spin* basis: $|\uparrow\rangle = \left|n_i^a = 1,\, n_i^b = 0\right\rangle$ and $|\downarrow\rangle = \left|n_i^a = 0,\, n_i^b = 1\right\rangle$, this Hamiltonian can be written as [184]

$$\begin{aligned} H_{eff} = \sum_{j=1}^{3}[&A_j\mathbb{1} + \lambda_j^{(0)}\sigma_j^z + \lambda_j^{(1)}H_{j,j+1}^I + \lambda_j^{(2)}H_{j,j+1}^{XY} \\ &+\lambda^{(3)}H_{j,j+1,j+2}^T + \lambda_j^{(4)}H_{j,j+1,j+2}^{XYZ}], \end{aligned} \tag{5.8}$$

where $H_{j,j+1}^I = \sigma_j^z\sigma_{j+1}^z$, $H_{j,j+1}^{XY} = \sum_{l=x,y}\sigma_j^l\sigma_{j+1}^l$, $H_{j,j+1,j+2}^T = \sigma_j^z\sigma_{j+1}^z\sigma_{j+2}^z$ and $H_{j,j+1,j+2}^{XYZ} = \sum_{l=x,y}\sigma_j^l\sigma_{j+1}^z\sigma_{j+2}^l$. Here A and the $\lambda^{(i)}$'s depend on J_j^α and $U^{\alpha\beta}$. By varying the laser parameters these coefficients can be modified and specific parts of H_{eff} can dominate over the remainder [185]. In particular, we are interested in the terms containing $\lambda_j^{(0)}$, $\lambda_j^{(1)}$ and $\lambda^{(3)}$. A suitable choice for the physical parameters in H_{eff} will be addressed later. To realise a $\mathsf{C^2Z}$ from H_{eff}, $\Lambda_0 = \Lambda_3 = -\Lambda_1 = \pi/8$ is required, where $\Lambda_i = \int_0^T \lambda^{(i)}dt$. This is possible by correctly tuning J^α, $U^{\alpha\beta}$ and T. However a restriction is imposed by the condition $U/(zJ) \gtrsim 5.8$, which guarantees the MI regime with one atom per site [147], where z is the number of NN seen by a given site. H_{eff} can be generalised to the triangular lattice, with each site having 6 NN, so that the model is valid for $J/U \lesssim 0.03$.

In order to produce the bowtie pattern used in Section 5.2, one can create an optical potential of period $> \lambda/2$ [186]. Here, two laser-beams, at angles $\pm\theta/2$ to a given direction $\vec{v}$ on the $x-y$ plane produce a two-dimensional standing-wave in

the direction perpendicular to $\vec{v}$ on the $x-y$ plane with period $d = \lambda/[2\sin(\theta/2)]$. Using two pairs of lasers, one can produce the periodic pattern

$$V_{off} = V_0 - V_1 \cos(|\vec{k}|\hat{\mathbf{y}}) + V_2 \cos(|\vec{k}|\sqrt{3}\hat{\mathbf{x}}) \tag{5.9}$$

that offsets the original triangular lattice as shown in Fig. 5.2 **(b)**. Here V_1 (V_2) is a potential produced by the first (second) pair of lasers, $V_0 = V_1 + V_2$ and $|\vec{k}| = 2\pi/\lambda$. V_{off} suppresses tunneling between specific sites on the lattice according to the pattern in Fig. 5.2 **(b)**. During the time evolution, a $\mathsf{C^2Z}$ is realised between the sites of closed triangles only.

The initialisation of the register prior to the entanglement is achieved by applying Raman transitions to all lattice sites. These can be activated by standing-waves of period a from two pairs of lasers L_1 and L_2, far blue-detuned by Δ from the transition $|\{a,b\}\rangle \leftrightarrow |e\rangle$ (see Fig. 5.4) and orientated along the $\hat{\mathbf{y}}$-axis. All the sites will be located at the maximum-intensity peaks [187] and with the atoms initially in $|a\rangle$, a rotation of the qubits into the state $|+\rangle$ can be achieved. In order to perform information-flow as described above, individual qubits along the edges of a path must be set to $|\{0,1\}\rangle$. It is experimentally feasible to apply a Raman transition to a bunch of qubits by addressing them with two lasers of cross-section $\sigma \simeq 10^{-12}m^2$. With a Gaussian radial intensity-profile, positioning the beams' centre between the atoms to be addressed, as shown in Fig. 5.2 **(b)**, applies the same transition to all the closest surrounding atoms. Thus the qubits may be rotated from $|+\rangle$ to $|0\rangle$ or $|1\rangle$ as needed using a sort of *blurred removal* [3]. The state of the center qubit is irrelevant, as it will be disentangled from the rest of the lattice. This allows the overlapping of blurred removals and the creation of entangled-state subspaces separated from the rest of the lattice. Other techniques, such as using a diffraction limited lens system [188], would be suitable for this task. Such methods can also be used in preparing cluster states in square lattice configurations, although single-atom addressing would obviously allow more compact gate constructions in both models.

[3] Alternatively, a far-off-resonant laser can be focused to a fraction of the lattice spacing, Stark shifting $|a\rangle$ and $|b\rangle$ differently. A global addressing microwave pulse then only rotates states of atoms that are exactly in resonance.

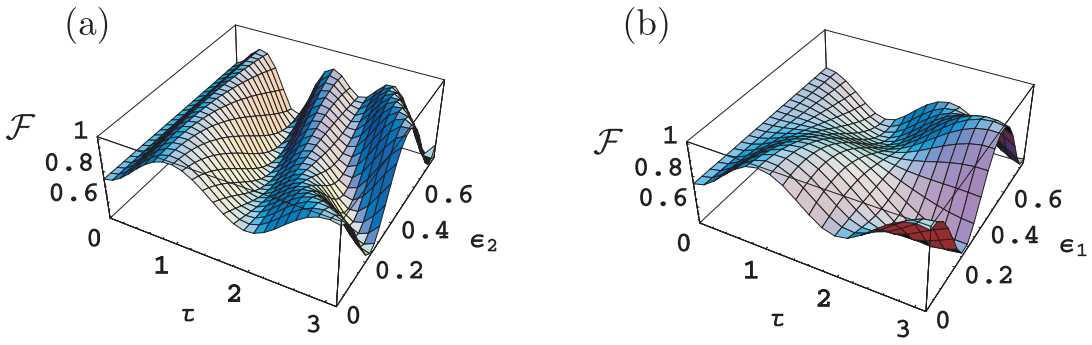

Figure 5.5: **(a)**: The fidelity $\mathcal{F}$ of the entanglement generation against the rescaled time τ and the coupling ϵ_2. **(b)**: Similar to **(a)** but with the replacement $\epsilon_2 \to \epsilon_1$, to study imperfectness in the H^I coupling.

5.4 Imperfect Operation

The realisation of a single lattice-wide $\mathsf{C}^2\mathsf{Z}$ should be carried out within the system's coherence time. Both $\lambda^{(1)}$ and $\lambda^{(3)}$ roughly scale as J^3/U^2 ($J_i^\alpha = J^\alpha,\ \forall i$), with variability upper-bounded by $J/U \sim 0.03$. One can set J and U so that $|\lambda^{(0,1,3)}| \sim 0.3$ Hz and $\lambda^{(2,4)} = 0$ ($\lambda^{(0)}$ can be adjusted by an appropriate Zeeman term [185]). Here $J^b \simeq 0$, $J^a = 2$ kHz and $U^{\alpha\alpha} = 2U^{\alpha\beta} = 120$ kHz are taken, possible using Feshbach resonances [189], which correspond to interaction-times within the coherence time of this far-detuned configuration [190]. Couplings one order of magnitude larger are possible, thus lowering the operation time, with the requirement that J and U increase by an order of magnitude. Small deviations from the desired values of J and U imply slight variations of the $\lambda^{(i)}$'s, with $\lambda^{(2,4)}$ becoming nonzero and affecting the system. In general, as $\lambda^{(2)} \simeq 10\lambda^{(4)}$ for the parameter choices above, we can neglect its effect. Thus, the replacements $\lambda^{(j)} \to \lambda^{(j)} + \epsilon_j\,(j = 0, .., 3)$, in H_{eff} allow for the formal study of imperfect entanglement-generation. The imperfect Hamiltonian evolves the initial state $|\psi(0)\rangle = \sum_{\beta,\gamma,\delta=0}^{1} \alpha_{\beta\gamma\delta}(0)\,|\beta,\gamma,\delta\rangle$ of qubits within a triangle into the state $|\psi(t)\rangle = e^{-i\int_0^T H_{eff}(t)dt}\,|\psi(0)\rangle$. To determine the quality of the dynamics, $|\psi(t)\rangle$ can be compared with $|\psi^I\rangle = \mathsf{C}^2\mathsf{Z}\,|\psi(0)\rangle$ using the fidelity $\mathcal{F} = |\langle\psi^I|\psi(t)\rangle|^2$. Fig. 5.5 **(a)** shows the result for $\alpha_{\beta\gamma\delta}(0) = 1/(2\sqrt{2}), \forall\alpha,\beta,\gamma$. Here ϵ_2 has been allowed to vary with $\epsilon_{0,1,3} = 0$. For convenience $|\Lambda_{0,1,3}| = (\pi/8)\tau$ has been set. For $\tau = 1$, corresponding to an application of $\mathsf{C}^2\mathsf{Z}$ (if $\epsilon_2 = 0$), there is a noticeable fidelity decay against ϵ_2. Moreover, for $\epsilon_2 > 0$, $\mathcal{F} = 1$ at $\tau < 1$, which may

allow a compensation for the fidelity decay by using a shorter interaction-time. However this procedure is ineffective if ϵ_2 is unknown. Fig. 5.5 **(b)** shows another example of the effect of imperfect couplings, where ϵ_1 has been allowed to vary, keeping $\epsilon_{0,2,3} = 0$, a choice due to $\lambda^{(1)}$ changing more rapidly than $\lambda^{(3)}$ in the chosen parameter regime. It is clear from this analysis that the parameters in H_{eff} should be accurately tuned if the correct entanglement is to be realised.

5.5 Remarks

In this Chapter, it has been shown that the MB QIP model can be performed on a three-body type entangled resource. Using concatenation methods from Chapter 2, an economical Toffoli gate simulation can be constructed, which is fundamental to compact algorithm realisations and robust-to-noise QIP. The feasibility of an optical lattice-based implementation of the model has been analysed in detail. The theoretical model discussed here could even be adapted to the case of more sophisticated types of multi-qubit interactions permitted within the physical setup (see Eq. (5.8) and Refs. [179, 184, 185]). If the model is developed along these lines, the study could be advantageous to the standard $\mathrm{QC}_{\mathcal{C}}$ model for the purposes of realizing compact and economical algorithm simulations.

Chapter 6

Measurement-based QIP using d-dimensional Hilbert spaces

In the search for compact gate constructions and minimal resource algorithm design in order to reduce the effects of imperfections, so far only modifications to the entanglement structure of the resources has been considered. However, one can also consider the possibility of using higher-dimensional elementary units instead of qubits at each lattice site in the cluster state. In order to understand motivations for the extension of the MB one-way model to higher dimensions [191–193], in this Chapter the effects of amplitude and phase damping decoherence in d-dimensional one-way QC are analysed. Attention is focused on low dimensions and elementary one-dimensional spatial cluster state resources. The investigation shows how information transfer and entangling gate simulations are affected for $d \geq 2$. A description is also provided of how basic *qudit* cluster states deteriorate under environmental noise of experimental interest. In order to protect quantum information from the damaging effects of the environment, encoding logical qubits into qudits is considered. A comparison is also made between entangled pairs of linear qubit-cluster states with single linear qudit-clusters of equal length (in terms of their elementary units) and total Hilbert space dimension. A significant reduction in the performance of cluster state resources for $d > 2$ is found when Markovian-type decoherence models are present.

6.1 Introduction

The standard MB one-way model considered up until this Chapter, relies on the use of entangled qubits and adaptive single-qubit measurements to propagate information and simulate quantum gates. Recently, this model was extended to d-dimensional *qudit* systems [191–193]. Many physical setups exist that could be tailored to embody systems with the correct entanglement structure for qudit cluster states. These include ion-traps [194], cavity quantum electrodynamic (cavity-QED) settings [195] and linear optical setups [196–198]. Compared to qubits, d-dimensional systems ($d \geq 3$) provide improvements in channel capacities for quantum communication [199], better levels of security in quantum bit-commitment and coin-flipping protocols [200] and violations of local realism are stronger for two maximally entangled qudits [201, 202]. Three-dimensional systems (qutrits) are also known to optimise the Hilbert space dimensionality

for QC power [203]. However, it is not clear if the use of d-dimensional information carriers provides any substantial advantage in one-way QC. It is therefore interesting to investigate the use of d-dimensional systems in this context to see if advantages can be given by accessing a larger Hilbert space. The accuracy of MB QIP protocols using qubit cluster states is known to be affected significantly by sources of environmental decoherence and imperfections (as we saw in Chapter 3) and removing all but only the most essential qubits in the cluster state is key to effective simulations. The central aim of this Chapter is the study of the behaviour of QIP carried out when an environment affects single-mode d-dimensional systems that comprise the qudit cluster states. It is found that disadvantages appear, in terms of robustness of QIP protocols, when moving to higher dimensions; the accuracy of simulations decreases as the dimension increases. In addition, entangled pairs of qubit linear clusters appear to be more resilient to environmental effects in comparison with qudit clusters. This study questions the worthiness of efforts made toward the extension of one-way QC to higher-dimensional systems, where global properties of the entangled resources are crucial for the performance of a given MB QIP protocol.

In Section 6.2 an overview of d-dimensional one-way QC is provided. In Section 6.3, the decoherence models used in the analysis are introduced and their overall effect on qudit cluster states is determined using the state fidelity. Entanglement decay is also studied using techniques for deducing concurrence in bipartite mixed states of arbitrary dimension [204]. However, it is not straightforward to compare properties such as the strength of entanglement or fidelity for states from different dimensions. Thus, in Section 6.4 an operational point-of-view is taken and attention is focused on the performance of information transfer, gate simulations and encoding techniques. Section 6.5 summarises the Chapter's main results.

6.2 Background

6.2.1 General properties of qudit cluster states

A qudit cluster state $|\phi\rangle_{\mathcal{C}}$ is a pure multipartite entangled state of qudits positioned at specific sites of a lattice structure known as the cluster $\mathcal{C}$. It is defined as the eigenstate of the set of operators $K^{(a)} = X_a^{\dagger} \bigotimes_b Z_b$ [129, 130, 191–193], where X and Z are generalised Pauli operators [205] given by $Z = \sum_{k=0}^{d-1} \omega^k |k\rangle\langle k|$ and $X = \sum_{k=0}^{d-1} |k-1\rangle\langle k|$. Modulo-$d$ arithmetic is used for k, $\omega = e^{2\pi i/d}$ is the d-th root of unity and $\{|k\rangle\}_{k=0}^{d-1}$ is a basis of eigenstates of Z with eigenvalues ω^k. Each $K^{(a)}$ acts on the qudit occupying site $a \in \mathcal{C}$ and all others occupying a neighbouring lattice site b. The cluster state $|\phi\rangle_{\mathcal{C}}$ can be generated by first preparing a product state $|+\rangle_{\mathcal{C}} = \bigotimes_{a\in\mathcal{C}} |+\rangle_a$ of the qudits at all sites a, where the Fourier transform basis $|+_j\rangle = 1/\sqrt{d} \sum_{k=0}^{d-1} \omega^{jk} |k\rangle$ is used with $|+\rangle := |+_0\rangle$. The set $\{|+_j\rangle\}_{j=0}^{d-1}$ contains the eigenstates of the operator X with eigenvalues ω^j respectively. A unitary transformation $S^{(\mathcal{C})} = \prod_{\langle a,b\rangle} S^{ab}$ is then applied to the initial state $|+\rangle_{\mathcal{C}}$, where $\langle a,b\rangle := \{a,b \in \mathcal{C} | b-a \in \gamma_D\}$ and $\gamma_1 = \{1\}$, $\gamma_2 = \{(1,0)^T, (0,1)^T\}$, $\gamma_3 = \{(1,0,0)^T, (0,1,0)^T, (0,0,1)^T\}$ for the respective spatial dimension D of the cluster being used. Each S^{ab} can be described by the entangling operator [191–193]

$$S^{ab} = \sum_{k=0}^{d-1} |k\rangle_a\langle k| \otimes Z_b^k = \sum_{k,l=0}^{d-1} \omega^{kl} |k,l\rangle_{a,b}\langle k,l|. \tag{6.1}$$

The state generated by the action of $S^{(\mathcal{C})}$ on $|+\rangle_{\mathcal{C}}$ is found to be $S^{(\mathcal{C})}|+\rangle_{\mathcal{C}} \equiv \prod_{\langle a,b\rangle} S^{ab} \bigotimes_{a\in\mathcal{C}} |+\rangle_a = |\phi\rangle_{\mathcal{C}}$, where the cluster state $|\phi\rangle_{\mathcal{C}}$ satisfies the eigenvalue equations $K^{(a)}|\phi\rangle_{\mathcal{C}} = |\phi\rangle_{\mathcal{C}},\ \forall a \in \mathcal{C}$.

6.2.2 Qudit basic building blocks

In order to carry out quantum simulations, a cluster of qudits in a particular physical configuration $\mathcal{C}(g)$ is used. To understand how to design correct configurations for carrying out specific protocols, it is convenient to start from the

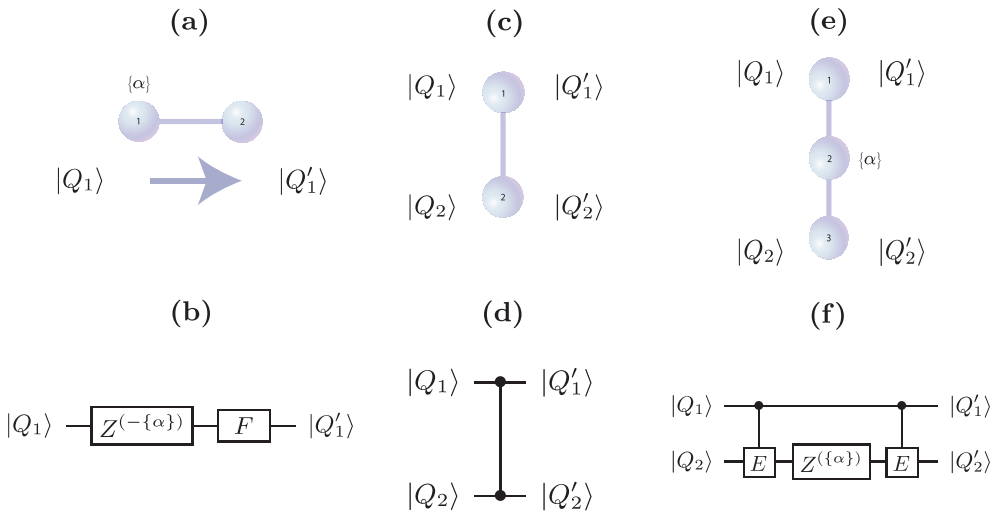

Figure 6.1: **(a)**, **(c)** and **(e)** show the layouts of BBB_1, BBB_2 and BBB_3. **(b)**: The operation simulated on logical qudit $|Q_1\rangle$, when physical qudit 1 is measured in the $B_1(\{\alpha\})$ basis and $s_1 = 0$ is obtained. **(d)**: The S^{12} gate simulated by BBB_2 on two logical qudits $|Q_1\rangle$ and $|Q_2\rangle$. **(f)**: The quantum circuit corresponding to the operation BBB_3 with $\{\alpha\}$ satisfying the conditions in the text, when $s_2 = 0$. Here, the controlled-E operation is equivalent to $F_2 S^{12} F_2$.

concept of qudit BBB's and their equivalent network circuits. Simple concatenation rules can then be used to build up more complicated protocols, in a similar way to the qubit case described in Chapter 2.

The diagrammatic notation that will be used is such that each physical qudit is represented by a circle. The angle set $\{\alpha\}$ next to the ith qudit symbol identifies the basis $B_i(\{\alpha\}) = \{Z^{(\{\alpha\})}|+_j\rangle\}_{j=0}^{d-1}$ in which that qudit is measured. Here, $Z^{(\{\alpha\})} = \sum_{k=0}^{d-1} e^{i\alpha_k}|k\rangle\langle k|$ is completely defined by the set of angles $\{\alpha\} = \{\alpha_k \in [0, 2\pi)\}$ and $s_i \in \{0, .., d\}$ is the corresponding measurement outcome. The smallest cluster state consists of two qudits and can be used to simulate a unitary operation on one logical qudit encoded onto a physical cluster qudit [191–193], as shown in Fig. 6.1 **(a)**. This configuration is denoted as BBB_1. The operation simulated by BBB_1 when a measurement on qudit 1 gives outcome $s_1 = 0$ is shown in Fig. 6.1 **(b)**. There, $Z^{(-\{\alpha\})}$ represents the rotation carried out on the logical qudit and F is the quantum Fourier transform in d-dimensions, given by $F = d^{-1/2} \sum_{j,k=0}^{d-1} \omega^{jk}|j\rangle\langle k|$. Due to the probabilistic nature of the simulation, it is necessary to apply a decoding operator $\mathcal{D}(s_1) \equiv \tilde{U}_\Sigma^\dagger = X^{s_1}$ to qudit 2, found via the relations $XZ = \omega ZX$, $FZ = XF$ and $FX = Z^\dagger F$ [191–193].

Using the same layout, with two encoded qudits $|Q_{1,2}\rangle$, the operation S^{12} in Eq. (6.1) is simulated as shown in Fig. 6.1 **(d)**. This configuration is denoted as BBB_2. Finally, in Fig. 6.1 **(e)** qudits 1 and 3 embody the input logical qudits and a measurement is performed on qudit 2 in the $B_2(\{\alpha\})$ basis. This pattern simulates the operation $T_{13}(s_2) = d^{-1/2}\sum_{k,l,j=0}^{d-1}\omega^{j(k+l-s_2)}e^{-i\alpha_j}|k,l\rangle_{1,3}\langle k,l|$. This is unitary only when the set $\{\alpha\}$ satisfies $|\sum_{j=0}^{d-1}\omega^{j(k+l)}e^{-i\alpha_j}|^2 = d$. The index j of α_j follows a modulo-d arithmetic. Additionally when $d^{-1}\sum_{j=0}^{d-1}\omega^{j(k+l)}e^{-i\alpha_j} = e^{i\alpha_{-(k+l)}}, \forall l,k \in \{0,..,d-1\}$, we have for $s_2 = 0$ the unitary transformation $U_{13} = d^{-1/2}\sum_{k,l=0}^{d-1}e^{i\alpha_{-(k+l)}}|k,l\rangle_{1,3}\langle k,l|$. This corresponds to the operation in Fig. 6.1 **(f)**.

Using this set of BBB's, one can construct more complicated configurations using the simple concatenation technique of Chapter 2, which holds true for any d-dimensional qudit cluster state. To find the form of the decoding operators $\mathcal{D}$ to apply to the output logical qubit of a particular concatenated cluster configuration, one can use the relations $Z^{(\{\alpha\})}Z = ZZ^{(\{\alpha\})}$, $Z^{(\{\alpha\})}X = XZ^{(\{\alpha'\})}$ $[\alpha'_j = \alpha_{j-1}]$, $FZ = XF$, $FX = ZF$ and $S^{12}(X^{x_1}Z^{z_1})_1(X^{x_2}Z^{z_2})_2 = (X^{x_1}Z^{z_1-x_2})_1(X^{x_2}Z^{z_2-x_1})_2S^{12}$ [191–193]. The second relation implies the use of adaptive measurements in the simulations, similar to the qubit case [129, 130]. For prime dimensions, universal QC can be achieved with the set of $d+1$ single qudit rotations $\{Z^{(\{\alpha\})}, X^{(\{\alpha\})}, Z(X^{(\{\alpha\})})^k\}$, $k = 1,..,d-1$ and the two-qudit gate S^{12}, where $X^{(\{\alpha\})} = FZ^{(\{\alpha\})}F^\dagger$. Finding the corresponding universal sets in the case of any dimension is more involved [191–193].

6.3 Decoherence models and general properties

In the analysis presented here, each physical qudit in the cluster state is considered to be interacting independently with a local environment as shown in Fig. 6.2 **(a)**. The evolution of the state of a single qudit can be given in terms of the master equation $\frac{\mathrm{d}\rho}{\mathrm{d}t} = \mathcal{L}_D[\rho]$, where ρ is the density matrix of the qudit and $\mathcal{L}_D$ represents the Lindblad superoperator describing the particular decoherence model (as introduced in Chapter 2). Here, each qudit will be treated as a bosonic mode (where $a^\dagger$ (a) denotes the creation (annihilation) operator for an

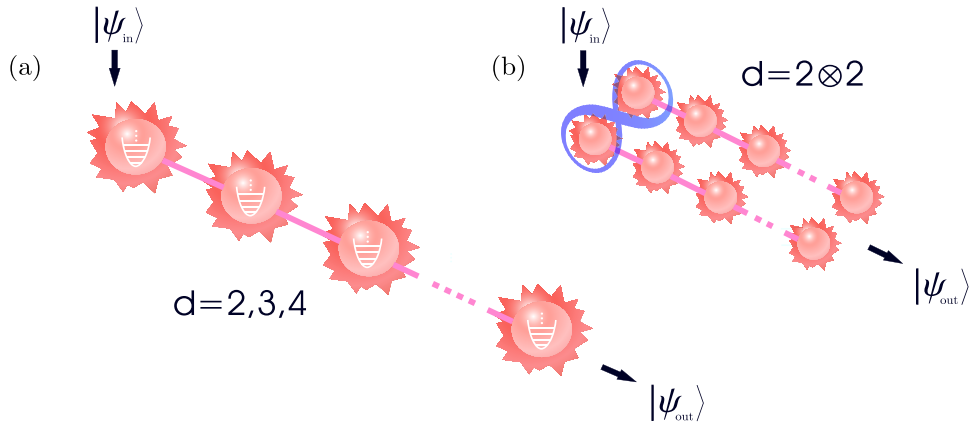

Figure 6.2: The linear qudit-clusters studied in this work. Each physical qudit is affected by its local environment (jagged surroundings) by AD and PD decoherence. **(a)**: Linear qudit clusters. **(b)**: Entangled pair of linear qubit-clusters.

excitation within the qudit mode) with a truncated basis of length d. Taking the local environment as a thermal bath[1], one may write the Lindblad superoperator acting on the qudit in the *interaction picture*[2] as

$$\begin{aligned}\mathcal{L}_A[\varrho] &= \frac{\Gamma_A(\bar{n}+1)}{2}\left(2a\varrho a^\dagger - a^\dagger a\varrho - \varrho a^\dagger a\right) + \frac{\Gamma_A\bar{n}}{2}\left(2a^\dagger\varrho a - aa^\dagger\varrho - \varrho aa^\dagger\right) \\ &\equiv g_A^1(a\varrho a^\dagger - a^\dagger a\varrho) + g_A^0(a^\dagger\varrho a - aa^\dagger\varrho) + h.c\ , \end{aligned} \tag{6.2}$$

where $g_A^k = (\Gamma_A/2)(\bar{n}+k)$, Γ_A is the strength of the qudit-environment coupling and $\bar{n}$ parameterises a non-zero temperature environment. This model is usually referred to as amplitude damping (AD) and characterises the energy dissipation of a system to its environment. If on the other hand the local environment acts to destroy the phase-coherence in the qudit state via random scattering processes[3],

[1]The interaction Hamiltonian is given by $H' = \sum_i \lambda_i(ab_i^\dagger + a^\dagger b_i)$, where $b_i^\dagger$ (b_i) denotes the creation (annihilation) operator for bath mode i.

[2]Here the term $-i[H,\rho]$, where $H = \omega a^\dagger a$ is the free Hamiltonian of the system, is removed by making a transformation into the interaction picture: $\rho(t) = e^{-iHt}\varrho(t)e^{iHt}$ and $L_\mu(t) = e^{-iHt}L_\mu^I(t)e^{iHt}$. The Lindblad operators are given by $L_1^I(t) = \sqrt{\Gamma_A(\bar{n}+1)}a_I(t)$ and $L_2^I(t) = \sqrt{\Gamma_A\bar{n}}a_I(t)$, where $a_I(t) = e^{iHt}a(t)e^{-iHt} = ae^{-i\omega t}$. They are obtained by making a Markov and weak coupling approximation in the system-environment dynamics, as outlined in Chapter 2 (see also [96, 125–127]).

[3]The interaction Hamiltonian is given by $H' = \sum_i \lambda_i(b_i + b_i^\dagger)a^\dagger a$. Note that this Hamiltonian commutes with the free Hamiltonian H of the system and hence no energy is actually transferred–only a change of phase in the system occurs.

the Lindblad superoperator can be written as

$$\begin{aligned}\mathcal{L}_P[\varrho] &= \frac{\Gamma_P}{2}\left(2\,a^\dagger a\varrho a^\dagger a-(a^\dagger a)^2\varrho-\varrho(a^\dagger a)^2\right)\\ &\equiv \frac{\Gamma_P}{2}\left(2\,a^\dagger a\varrho a^\dagger a-\{(a^\dagger a)^2,\varrho\}\right).\end{aligned}\tag{6.3}$$

Here the rate Γ_P represents the strength of the scattering process. This decoherence is usually referred to as phase damping (PD).

The master equations corresponding to the Lindblad superoperators in Eqs. (6.2) and (6.3) can be solved by expressing them in the single-qudit computational basis. However, in order to solve the dynamics of environment-affected many-qudit cluster states, it is convenient to rely on the Kraus operator formalism [115]. In this context, the evolution of a single qudit density matrix ϱ can be written as $\varrho(t)=\sum_\mu K_\mu^i(t)\varrho(0)K_\mu^{i\,\dagger}(t)$, where $\{K_\mu^i(t)\}$ is the set of Kraus operators for qudit i satisfying the completeness relation $\sum_\mu K_\mu^{i\,\dagger}(t)K_\mu^i(t)=\mathbb{1},(K=A,P)$. The AD Kraus operators are given by

$$A_\mu^i(t)=\sum_{n=\mu}^{\infty}[C(n,\mu)\gamma(t)^{n-\mu}(1-\gamma(t))^\mu]^{\frac{1}{2}}|n-\mu\rangle_i\langle n|,\tag{6.4}$$

where $(1-\gamma(t))^{\frac{\mu}{2}}$ is the probability that the qudit system loses μ particles[4] up to time t [206, 207][5]. The parameter $\gamma(t)=e^{-\Gamma_A t}$ is set for the solution $\varrho(t)$ to be consistent with Eq. (6.2) in the limit $\bar{n}=0$. The PD Kraus operators are given by [208, 211]

$$P_\mu^i(t)=\sum_{n=0}^{\infty}e^{-\frac{1}{2}n^2\tau}\left[\frac{(n^2\tau)^\mu}{\mu!}\right]^{\frac{1}{2}}|n\rangle_i\langle n|\tag{6.5}$$

where $\tau=\Gamma_P t$ is chosen as a rescaled interaction time and $(1-e^{-n^2\tau})^{1/2}$ can be interpreted as the probability that n particles from the qudit system are scattered by the environment up to time t. For an n-qudit cluster state initially described

[4]The nth excitation state $|n\rangle$ of the bosonic mode (describing the qudit system) can be interpreted as a state of n non-interacting particles, each with the same probability of decay $\sqrt{1-\gamma(t)}$ up to time t. Therefore $\sqrt{1-\gamma(t)}$ is the probability that the system loses *one* particle up to time t.

[5]Alternatively $[\gamma(t)]^{\frac{(n-\mu)}{2}}$ can be seen as the probability the state $|n\rangle$ is undecayed for μ particle decay processes up until time t.

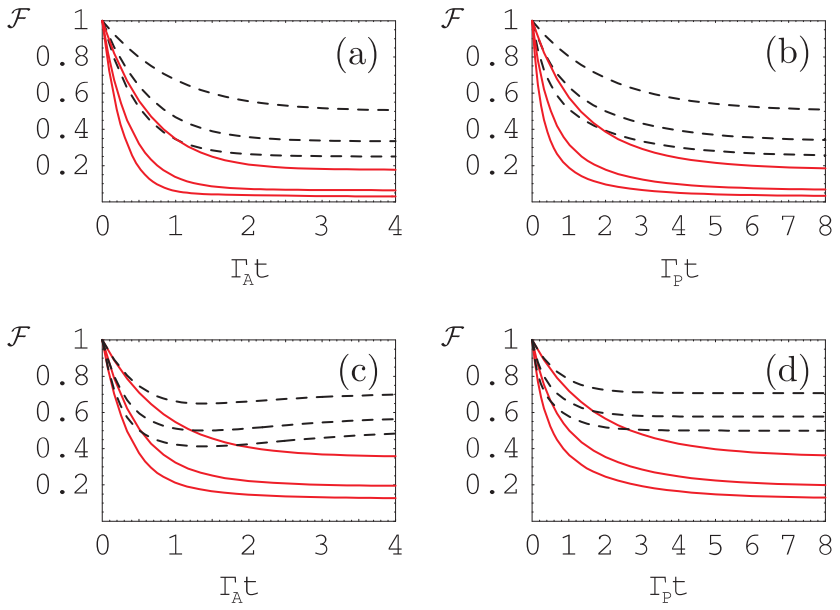

Figure 6.3: Fidelities of decoherence-affected linear qudit-clusters. In **(a)** and **(b)** the dashed (solid) lines correspond to $n = 2$ ($n = 5$) with dimension $d = 2 \rightarrow 4$ from top to bottom in each line-style. In **(c)** and **(d)** we compare $n = 3$ qudit cluster states (solid lines) with 3-qudit GHZ states (dashed lines) for $d = 2 \rightarrow 4$ from top to bottom in each line-style. We consider AD (**(a)** & **(c)**) and PD channels (**(b)** & **(d)**).

by the density matrix $\varrho(0)$ and each qudit interacting with its own local environment, we then have an evolution described by $\varrho(t) = \sum_{\mu_i} \tilde{K}_{\{\mu_i\}}(t)\varrho(t)\tilde{K}^{\dagger}_{\{\mu_i\}}(t)$, where $\tilde{K}_{\{\mu_i\}}(t) = \otimes_{i=1}^{n} K^i_{\mu_i}(t)$ and each $K^i_{\mu_i}(t)$ acts separately on qudit i in the cluster. By truncating the basis at dimension d, we can remove the infinity limit in the definition of $\{A^i_\mu(t)\}$ as number states outside the d-dimensional Hilbert space do not play a role in the decoherence mechanism. The index μ is also restricted and results in a finite number of AD Kraus operators. For $\{P^i_\mu(t)\}$, the index μ is not restricted, resulting in an infinite number of operators. This is because the system can be scattered by any number of particles in the environment. However, the index n is restricted by the truncation of the basis at dimension d and therefore one can redefine $\{P^i_\mu(t)\}$ into a finite sum of PD Kraus operators [208]. In order to give a general idea of how qudit cluster states are affected by both these decoherence models, the state fidelity $\mathcal{F}(|\psi\rangle, \varrho)$ for a pure cluster state $|\psi\rangle$ and environment exposed mixed cluster state ϱ is used. In Fig. 6.3 the fidelities are shown for linear qudit cluster states of length $n = 2$ and 5 for dimensions $d = 2,\ 3$ and 4. In Fig. 6.3 **(a)** and **(b)**, AD and PD behaviour

is shown for lengths $n = 2$ and 5. Here one can see that the higher the dimension of the qudits, the stronger the decay becomes with increased exposure time for both decoherence models. In general one must be careful when comparing the fidelity decays for cluster states of different dimension (at fixed n). While the fidelity decay is stronger the higher the dimension of the cluster state, this does not provide any information about how other properties are behaving, such as entanglement decay. However, as the task here is the evaluation of the global quality of the entangled resource to be used for computation, the state fidelity embodies an informative operative quantity and provides insight into the way linear qudit clusters of various lengths are affected by environmental noise. In Fig. 6.3 **(c)** and **(d)**, $n = 3$ qudit cluster states are compared with their local unitary (LU) equivalent $n = 3$ qudit GHZ states [148]. Due to the effect of the environment on the basis the cluster states are expressed in (spread out across the eigenstate basis of the Z operator), their fidelities decay more strongly than the GHZ states.

The information gathered by means of the state fidelity is complemented and completed in this investigation by the study of the entanglement decay under environmental action. An analysis of how decay in entanglement is affected as the dimension of the cluster increases is now considered. For the moment the analysis will be limited to $n = 2$ qudit cluster states, which are locally equivalent to the maximally entangled bipartite states $|\Psi_d\rangle = (1/\sqrt{d}) \sum_{i=0}^{d-1} |ii\rangle$ for a given dimension d. Later, bipartite entanglement decay in $n = 3$ qudit cluster states will be considered, where one of the qudits has been measured. For d-dimensional bipartite *pure* states $\varrho = |\Psi\rangle \langle\Psi|$, the concurrence $C(\varrho)$ [93, 98, 99] provides a good measure of entanglement[6]. In general though, for d-dimensional bipartite *mixed* states the calculation of $C(\varrho)$ is a formidable task (unlike the simple qubit case). However, it is possible to obtain approximations providing tight upper and lower bounds to $C(\varrho)$ [93]. In this case, a good entanglement measure known as the *quasi-pure* concurrence $C_{qp}(\varrho)$ can be used. It is defined

[6]For a pure d-dimensional bipartite state $\varrho = |\Psi\rangle\langle\Psi|$, where $|\Psi\rangle \in \mathcal{H}_1 \otimes \mathcal{H}_2$, the concurrence $C(\varrho)$ can be defined as $C(\varrho) = (\mathrm{Tr}(|\Psi\rangle \langle\Psi|)^2 - \mathrm{Tr}_1 \varrho_1^2 - \mathrm{Tr}_2 \varrho_2^2 + (\mathrm{Tr}\, |\Psi\rangle \langle\Psi|)^2)^{1/2}$ [209], where $\varrho_1 = \mathrm{Tr}_2 |\Psi\rangle \langle\Psi|$, $\varrho_2 = \mathrm{Tr}_1 |\Psi\rangle \langle\Psi|$ and the trace over both subsystems is denoted by Tr. This can be written in a more compact way as $C(\varrho) = \sqrt{2(\langle\Psi|\Psi\rangle^2 - \mathrm{Tr}\varrho_r^2)}$ [210], with $\varrho_r = \varrho_1$ or ϱ_2. For $\mathcal{H}_1,\ \mathcal{H}_2 \in \mathbb{C}^2$ this can be reduced further into the original form $C(\varrho) = |\langle\Psi| \sigma_y \otimes \sigma_y |\Psi^*\rangle|$ [98, 99, 209], where $|\Psi^*\rangle$ is the complex conjugate of $|\Psi\rangle$. $C(\varrho)$ ranges from $0 \to 1$ in the qubit case only.

as $C_{qp}(\varrho) = \max(\lambda_1 - \sum_{i>1}\lambda_i, 0)$ [204], with λ_i's the eigenvalues of the matrix $\sqrt{\tau\tau^\dagger}$ (decreasingly ordered) and $\tau_{jk} = \mathcal{A}^{11}_{jk}/\sqrt{\mathcal{A}^{11}_{11}}$, where

$$\begin{aligned}\mathcal{A}^{11}_{jk} &= \mu_1\sqrt{\mu_j\mu_k}[\mathrm{Tr}(|\Phi_j\rangle\langle\Phi_1|\Phi_k\rangle\langle\Phi_1|) - \sum_{l\neq m=1}^{2}\mathrm{Tr}_l(\mathrm{Tr}_m(|\Phi_j\rangle\langle\Phi_1|)\mathrm{Tr}_m(|\Phi_k\rangle\langle\Phi_1|) \\ &\quad -\mathrm{Tr}(|\Phi_j\rangle\langle\Phi_1|)\mathrm{Tr}(|\Phi_k\rangle\langle\Phi_1|)]. \qquad (6.6)\end{aligned}$$

The set $\{\mu_i, |\Phi_i\rangle\}$ in Eq. (6.6) corresponds to the eigensystem of ϱ. This entanglement measure is ideal for describing the entanglement decay in a system where the environment acts to destroy its purity slowly: under these conditions $C_{qp}(\varrho)$ represents a value very close to the actual concurrence $C(\varrho)$ (obtained via numerical optimisation [93]), with the approximation valid for $\mu_1 \gg \mu_{i>1}$ (the μ_i being non-increasingly ordered). When the approximation is no longer valid $C_{qp}(\varrho)$ nevertheless represents a lower bound to $C(\rho)$. In Fig. 6.4 the effect of AD and PD on entanglement decay is shown in the form of the concurrence $C(\varrho)$ for $d = 2$ and normalised quasi-concurrence[7] (NQC) $\tilde{C}_{qp}(\varrho) = C_{qp}(\varrho)/C(\Psi_d)$ for $d = 3$ and 4, where $C(\Psi_d) = \sqrt{2(1-1/d)}$. This normalisation is used so that we have $0 \geq C(\rho) \geq 1$. In Figs. 6.4 **(a)** and **(b)** qubits are compared with $d = 3$ and $d = 4$ systems respectively. In both decoherence models considered, one finds that the NQC decay is faster for larger dimensions. However, it cannot be infered that the total amount of entanglement decreases faster at higher dimensions. Only the fraction of the maximal value $C(\Psi_d)$ decays faster. The validity of the quasi-pure approximation (*i.e.* $\mu_1 \gg \mu_{i>1}$ for the eigenvalues of ϱ) for the parameter range shown in Fig. 6.4 has been checked by inspecting the largest μ_1 and second largest μ_2 eigenvalues of the eigensystem decomposition of the decayed state ϱ.

[7] For larger Hilbert spaces, $\mathcal{H}_1,\ \mathcal{H}_2 \in \mathbb{C}^d$ the maximum concurrence C_d is given by the concurrence of the corresponding maximally entangled state given by $|\Psi_d\rangle = 1/\sqrt{d}(\sum_{i=0}^{d}|ii\rangle)$. We then have $C_d \equiv C(\varrho_d) = \sqrt{2(1-1/d)}$. This provides a normalisation factor for scaling purposes so that $C(\varrho)$ never exceeds unity for a particular dimension d.

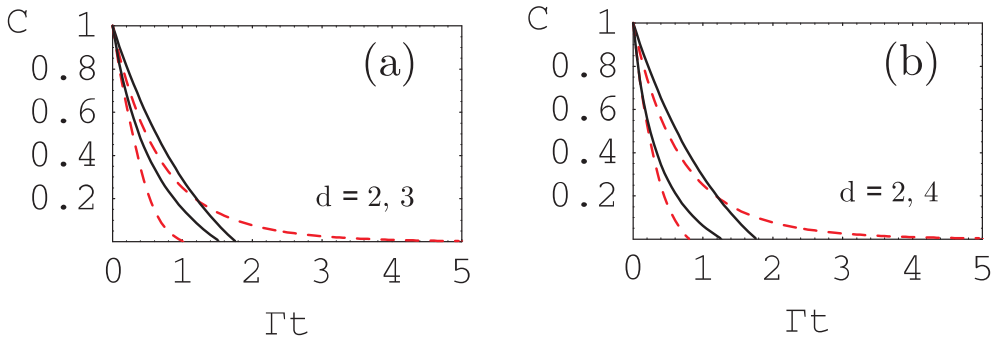

Figure 6.4: Bipartite entanglement decay in two-qudit cluster states when decoherence affects the individual qudits. The concurrence of qubit cluster states affected by PD and AD (top solid and dashed lines respectively) is compared with the normalised quasi-concurrence for $d = 3$ **(a)** and $d = 4$ qudit cluster states **(b)**. PD and AD correspond to the lower solid and dashed lines in each panel respectively.

6.4 Manipulating Information

6.4.1 Information transfer

In this Section, linear qudit cluster states of length $n = 2 \rightarrow 5$ are considered to be subject to the AD and PD decoherence models introduced in the last Section. Individual qudits in the clusters are exposed to a local environment for a rescaled interaction time $\Gamma_i t$, $i = \mathrm{A}, \mathrm{P}$. A logical state is encoded on the first physical qudit and measurements are performed in order to propagate the state across the cluster: see Fig. 6.2 **(a)**. This simple model gives an idea of how information flow is affected in general and the range of lengths of clusters considered allows one to see the effects on logical states rotated (spread) across the Hilbert space. Indeed, in a cluster of length n, the rotation applied to the logical qudit is given by F^{n-1}, where F denotes the quantum Fourier transform operation for the respective dimension (see Section 6.2). The identity operation is therefore only applied to clusters whose lengths are multiples of 4 (plus output qudit), as $F^4 = \mathbb{1}$. For qubits however, the identity operation is applied to all odd length clusters, as $F^2 \equiv \mathsf{H}^2 = \mathbb{1}$, where H is the Hadamard operation. For convenience, measurement outcomes corresponding to the state $|+\rangle$ being obtained are considered.

A logical state $|\psi\rangle_d$ in a Hilbert space of d dimensions can be parameterised by the *Hurwitz parameterisation* [212]: Using angles $\theta_k \in [0, \pi/2]$ and $\phi_k \in [0, 2\pi)$ for $k = 1, .., d-1$ we can write $|\psi\rangle_d = \sum_{i=0}^{d-1} c_i |i\rangle$, where the coefficients c_i are given by $c_0 = \cos\theta_1$, $c_j = (\Pi_{k=1}^{j} \sin\theta_k)\cos\theta_{j+1} e^{i\phi_j}$ $(0 < j < d-1)$ and $c_{d-1} = (\Pi_{k=1}^{d-1} \sin\theta_k) e^{i\phi_{d-1}}$ [8]. A pure state $|\psi\rangle_d$ representing the logical input qudit will loose purity as it propagates across a linear cluster state under the influence of AD and PD. The rescaled interaction times $\Gamma_i t$ determine how fast purity is lost. In general, the fidelity between the output logical qudit in the ideal and environment affected cases is given by $\mathcal{F} = \mathcal{F}(\{\theta_k\}_{k=1}^{d-1}, \{\phi_k\}_{k=1}^{d-1}, \Gamma_i t)$. In order to determine the behaviour of the fidelity for an arbitrary state $|\psi\rangle$, one must average it over all angle sets $\{\theta_k\}$ and $\{\phi_k\}$ representing the configuration space Ω at each instant of time $\Gamma_i t$. This allows one to find the mean fidelity $\bar{\mathcal{F}}(\Gamma_i t)$ by using the multi-dimensional integral $\int_\Omega \mathrm{d}\nu$ with $\mathrm{d}\nu = (1/\mathrm{V}(\Omega)) \prod_{k=1}^{d-1} \cos\theta_k (\sin\theta_k)^{2k-1} \mathrm{d}\theta_k \mathrm{d}\phi_k$ as a natural measure corresponding to a uniform distribution with respect to the Haar measure[9] [212]. The total volume for the manifold of pure states is given by $\mathrm{V}(\Omega) = [\pi^{d-1}/(d-1)!]$. This gives the mean fidelity $\bar{\mathcal{F}}(\Gamma_i t) = \int_\Omega \mathcal{F}(\{\theta_k\}_{k=1}^{d-1}, \{\phi_k\}_{k=1}^{d-1}, \Gamma_i t)\mathrm{d}\nu$, at each instant of time $\Gamma_i t$. Before considering information transfer across linear clusters, in Fig. 6.5 **(a)** and **(b)** the effect of AD and PD respectively is shown for arbitrary *single* logical qudits encoded onto *single* physical qudits for $d = 2$, 3 and 4. The average fidelity decays faster as the dimension increases. A $d = 4$ qudit encoded onto an entangled pair of qubits $|\psi\rangle_{2\otimes 2}$ is also considered, where each qubit is individually affected by AD and PD as shown in Fig. 6.2 **(b)**. The definition $|\psi\rangle_{2\otimes 2} = \sum_{i=0}^{3} c_i \left|\tilde{i}\right\rangle_{12}$ is used, where $\tilde{i}$ is the binary expression for the integer i, the subscripts 1 and 2 label the qubits and $\{c_i\}$ is that of a $d = 4$ qudit. In this case as the dimensionality of the $d = 4$ qudit and $d = 2 \otimes 2$ qubit systems is equal we may directly compare the fidelity behaviours. Evidently the entangled

[8] For example, $|\psi\rangle_2 = \cos\theta_1 |0\rangle + \sin\theta_1 e^{i\phi_1} |1\rangle$ and $|\psi\rangle_3 = \cos\theta_1 |0\rangle + \sin\theta_1 \cos\theta_2 e^{i\phi_1} |1\rangle + \sin\theta_1 \sin\theta_2 e^{i\phi_2} |2\rangle$

[9] The Haar measure corresponds to a distribution which assigns equal probability to each element of a group. For example, the Haar measure μ for $U(N)$ satisfies $\int_{U(N)} d\mu = 1$, where μ is a variable (dependent on the parameterisation of $U(N)$) such that each matrix $U \in U(N)$ has equal probability of being chosen at random. This allows one to integrate functions of randomly chosen matrices $U \in U(N)$ as $\int_{U(N)} f(U) d\mu$. A randomly chosen state $|\psi\rangle \in \Omega$ can be written as $U|\psi_0\rangle$ for a fixed state $|\psi_0\rangle$ $(e.g.\ |0\rangle)$ and randomly chosen U, thus one can write $\int_\Omega d\nu \Leftrightarrow \int_{U(N)} d\mu$ if ν corresponds to a uniform probability distribution of pure states $|\psi\rangle$. Therefore $\int_\Omega f(|\psi\rangle) d\nu = \int_{U(N)} f(U|\psi_0\rangle) d\mu$.

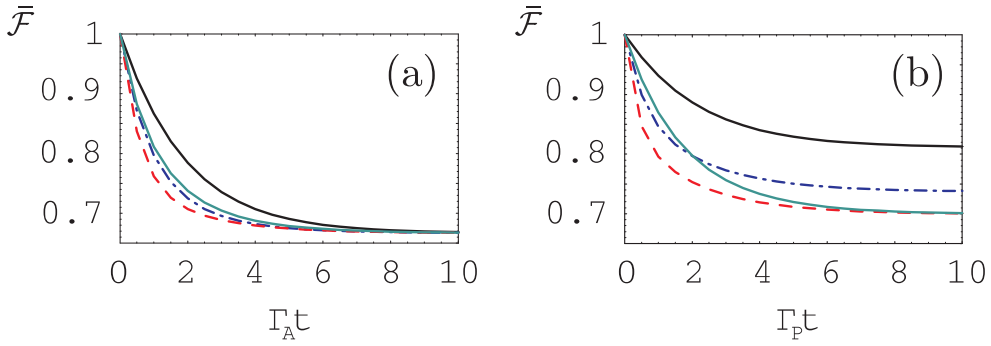

Figure 6.5: Fidelity decay for arbitrary single qudits with $d = 2,\ 3,\ 4$ and $2 \otimes 2$ when affected by AD **(a)** and PD **(b)**. In both panels the upper solid, lower solid, dash-dotted and dashed lines correspond to $d = 2,\ 2 \otimes 2,\ 3$ and 4 respectively.

pair has a slower decay than that of the $d = 4$ qudit in both decoherence models.

To find out if the fidelity behaviours discussed above carry over to information transfer, in Fig. 6.6 the average fidelities of arbitrary encoded logical qudits are considered when propagated along qudit cluster states of lengths $n = 2 \rightarrow 5$ with AD individually affecting the physical qudits. Comparing Fig. 6.6 **(a)**, **(b)** and **(c)** corresponding to dimensions $d = 2,\ 3$ and 4 respectively, it becomes clear that there is a splitting effect seen only for dimensions $d > 2$, where clusters of even length suffer a more pronounced fidelity decay than those of odd length. In addition to this, for even lengths there is a noticeable drop in the fidelities as $\Gamma_A t \rightarrow \infty$ for increasing dimension. In Fig. 6.6 **(d)** the final even and odd fidelity values are shown for increasing dimension. In Fig. 6.6 **(c)**, regardless of the splitting effects, one can see that a $d = 2 \otimes 2$ linear cluster always outperforms a $d = 4$ one.

The reason for the above mentioned splitting in odd and even lengths is the following: the state of a logical qudit propagated across a cluster of length $n \geq 2$ in the limit $\Gamma_A t \rightarrow \infty$ becomes equal to that of the final physical qudit in the same limit, *i.e.* it becomes $|0\rangle\langle 0|$. When the fidelity is taken and averaged over the configuration space, one obtains $\bar{\mathcal{F}}(\Gamma_A t \rightarrow \infty) = \int_\Omega |\langle 0| F^{n-1} |\psi\rangle_d| d\nu$. For odd-length clusters (even powers of F) we have $(F^\dagger)^{n-1}|0\rangle = |0\rangle$ because $F^2 = \sum_{k=0}^{d-1} |-k\rangle\langle k|$ and for even-length clusters (odd powers of F) we have $(F^\dagger)^{n-1}|0\rangle = |+\rangle$. Therefore for odd lengths, only the $|0\rangle$ entry of the logical qudit state $|\psi\rangle$ takes part in the overlap. When the average is performed over

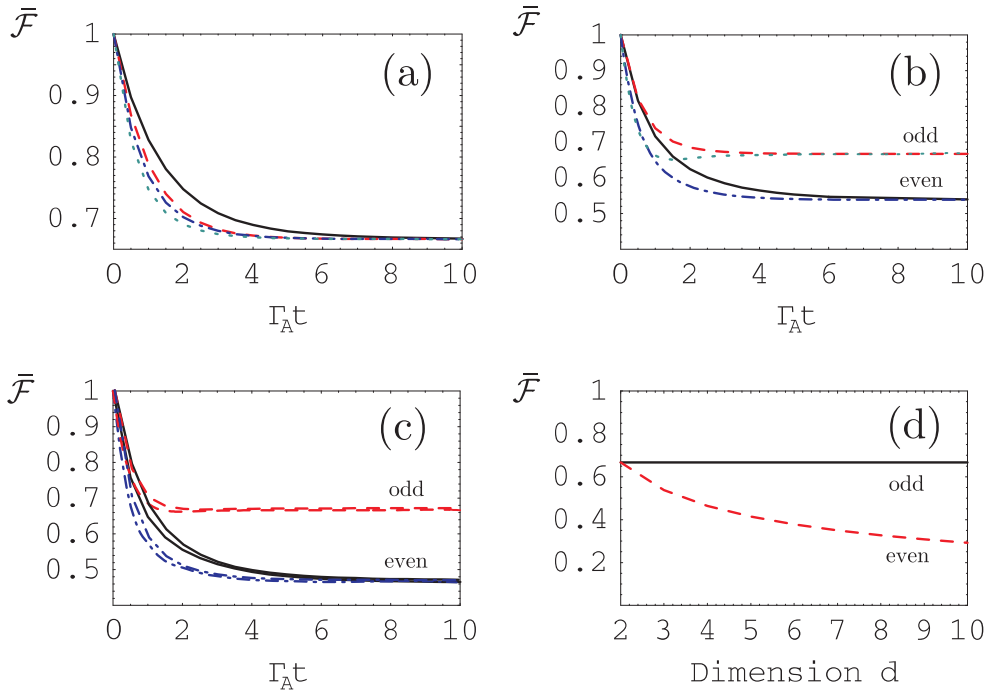

Figure 6.6: Average fidelities of AD-affected qudits propagated along qudit cluster states of lengths $n = 2 \rightarrow 5$. In **(a)**, **(b)** and **(c)** the solid, dashed, dash-dotted and dotted lines correspond to $n = 2,\ 3,\ 4$ and 5 length clusters respectively. **(a)**: AD for $d = 2$. **(b)**: AD for $d = 3$. **(c)**: AD for $d = 4$ compared with $2 \otimes 2$ (top lines at each n). **(d)**: Even and odd length average fidelity as $\Gamma_A t \rightarrow \infty$. The solid (dashed) line corresponds to odd (even) lengths.

the configuration space only θ_1 is averaged. In the even length case we have the integral $\bar{\mathcal{F}}(\Gamma_A t \rightarrow \infty) = (1/\sqrt{d}) \int_\Omega |\sum_{i=0}^{d-1} c_i| \mathrm{d}\nu$. For qubits this gives 2/3, which matches the odd length integral.

For PD, no splitting effects arise because as $\Gamma_P t \rightarrow \infty$ the final logical qudit state becomes $(1/d)\mathbb{1}$, giving a fidelity of $\bar{\mathcal{F}}(\Gamma_P t \rightarrow \infty) = 1/\sqrt{d}$ for all lengths $n \geq 2$. For $n = 1$, the final state of the qudit (entangled pair) as $\Gamma_P t \rightarrow \infty$ becomes $\varrho = \sum_{i=0}^{d-1} |c_i|^2 |i\rangle \langle i| \ (\sum_{i=0}^{3} |c_i|^2 |\tilde{i}\rangle \langle \tilde{i}|)$ leading to higher final fidelity values than in the case of arbitrary n, as can be seen by comparing Fig. 6.5 **(b)** with Fig. 6.7. Here Fig. 6.7 shows the average fidelity decay for arbitrary qudits propagated along linear clusters of length $n = 2 \rightarrow 5$ for dimensions $d = 2, 3$ and 4. It is evident that as the dimension increases, the fidelity decay becomes faster for each cluster length. For clarity, the $d = 2 \otimes 2$ case has been separated and compared with the $d = 4$ case in Fig. 6.8. For each n the $d = 2 \otimes 2$ cluster

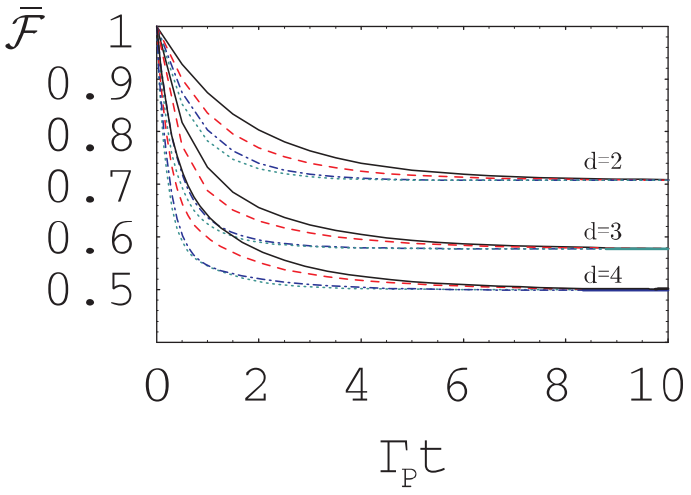

Figure 6.7: Average fidelities of PD-affected qudits propagated along qudit cluster states of lengths $n = 2 \rightarrow 5$. The solid, dashed, dash-dotted and dotted lines correspond to $n = 2,\ 3,\ 4$ and 5 respectively. The top, middle and bottom four lines correspond to dimensions $d = 2, 3, 4$.

outperforms the $d = 4$ qudit cluster.

To explain the robustness of the entangled qubit pair one needs to consider how the environment acts on each physical cluster qudit. Due to the nature of the PD environment which scatters off each qudit system in the cluster, the terms $\varrho_{nm}(t)|n\rangle\langle m|$ $(n \neq m)$ of the density matrix decay faster for larger values of $|n - m|$. One can see this from the time dependence of these terms by using Eq. (6.5) in the Kraus operator evolution to obtain the relation $\varrho_{nm}(t)|n\rangle\langle m| = \varrho_{nm}(0)e^{-\frac{1}{2}\Gamma_P t(n-m)^2}|n\rangle\langle m|$. The behaviours shown above suggest that it is best to restrict logical qudit simulations to lower levels in smaller dimensional physical qudits that are entangled, rather than using the same dimension for the physical qudits in the cluster. In this way one can exclude faster decay terms due to larger differences in the levels between low and high number states. Thus, when PD is considered, $d = 2 \otimes 2$ will always outperform $d = 4$.

For AD the elements of ϱ decay in favour of $\varrho_{00}(t)|0\rangle\langle 0|$ ($\varrho_{00}(t) \rightarrow 1$ as $\Gamma_A t \rightarrow \infty$). In these dynamics, the slowly decaying elements for $d = 4$ are $\varrho_{00}(t)|0\rangle\langle 0|$, $\varrho_{01}(t)|0\rangle\langle 1|$, $\varrho_{10}(t)|1\rangle\langle 0|$. For $d = 2 \otimes 2$, $\varrho_{00}(t)|\tilde{0}\rangle\langle\tilde{0}|$, $\varrho_{01}(t)|\tilde{0}\rangle\langle\tilde{1}|$, $\varrho_{10}(t)|\tilde{1}\rangle\langle\tilde{0}|$, $\varrho_{02}(t)|\tilde{0}\rangle\langle\tilde{2}|$ and $\varrho_{20}(t)|\tilde{2}\rangle\langle\tilde{0}|$ are the slowly-decaying ones. The last two elements give an additional contribution to the fidelity with respect to the $d = 4$ case.

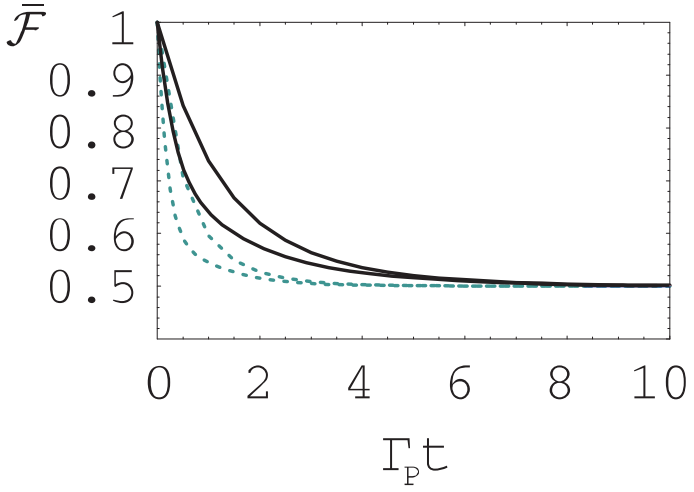

Figure 6.8: Average fidelities of PD-affected qudits propagated along qudit cluster states of lengths $n = 2$ and 5. The solid and dotted lines correspond to $n = 2$ and 5 respectively. Comparison between $d = 4$ and $d = 2 \otimes 2$. The top lines always correspond to an entangled pair for each n.

Their presence is understood by inspecting ϱ in the qubit basis where one can see that the last two terms have the same total energy as the second and third terms and are identically affected by the AD environment, which cannot distinguish between them. For higher dimensions, similar considerations can be made for PD and AD. It can be conjectured that, based on the arguments described above, $d = 2 \otimes ... \otimes 2$ systems will have slower average fidelity decay than their d-dimensional equivalents.

6.4.2 Encoded information transfer

From the analysis of information flow it appears that moving to higher dimensions decreases the transfer quality, characterised by the state fidelity, when decoherence is present. Even though the analysis focuses on the use of state fidelity, as the one-way model is based on the ability of transferring information across linear subclusters comprising the entangled resource, this suggests the use of higher-dimensional systems might not provide advantages for MB QIP when the decoherence models considered act on the system. However, the previous analysis did not exhaust the possibilities offered by the employment

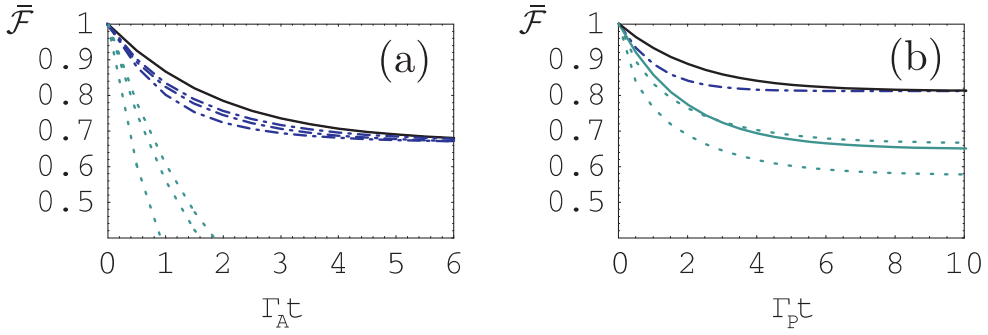

Figure 6.9: Average fidelities of qubits encoded into decoherence-affected single qudits. The upper solid lines correspond to $d = 2$ and G encodings for $d = 3$ and 4 in both **(a)** and **(b)**. In **(a)** we consider AD. The dash-dotted lines correspond to an L-encoded qubit for $d = 2 \otimes 2$, 3 and 4 (from top to bottom). The dotted lines correspond to M encoding for $d = 2 \otimes 2$, T encoding for $d = 3$ and 4 from top to bottom respectively. In **(b)** we consider PD. The G and T encodings for $d = 3$ and 4 match the $d = 2$ case. The dash-dotted line is for an O/M-encoded qubit in $d = 2 \otimes 2$. The dotted lines correspond to E encoding for $d = 3$ and 4 (from top to bottom). The lower solid line is for L encoding in $d = 2 \otimes 2$.

of d-dimensional elements. For instance it is known that protocols such as entanglement purification can be carried out, using the additional dimensions to improve error thresholds [213]. Another interesting possibility is encoding a logical qubit within the logical qudit being propagated. The average fidelity decays shown so far cover the entire Hilbert space for a particular d. Qubits encoded in these spaces do not necessarily have to make use of the full space and some advantage could be obtained by (in some sense) *hiding* the information from the environment.

In order to introduce the encoding techniques, we need to look back at the Hurwitz parameterisation [212]. A qubit state $|\psi\rangle_2 \in \mathcal{H}_2$ can be described simply as a state within the subspace of a $d = 3$ dimensional Hilbert space $\mathcal{H}_3$ where $\theta_2 = 0$. In general, any d'-dimensional state $|\psi\rangle_{d'}$ $(d' < d)$ can be described as a state within a particular subspace of a d-dimensional Hilbert space $\mathcal{H}_d$. We can thus take a state $|\psi\rangle_{d'} \in \mathcal{H}_d$ and use a unitary transformation Λ_d to encode the state into the entire Hilbert space. To apply an operation $\chi_{d'} \in \mathcal{H}_{d'}$ to a state encoded in a larger Hilbert space, we can use the transformation

$$\chi_d = \Lambda_d \; \tilde{\chi}_{d'} \Lambda_d^\dagger, \quad \chi_d \in \mathcal{H}_d \tag{6.7}$$

Encoding	State
G-Ground	$\|\psi_G\rangle_3 = \|\psi_G\rangle_4 = a\|0\rangle + b\|1\rangle$.
T-Top	$\|\psi_T\rangle_3 = a\|1\rangle + b\|2\rangle$, $\|\psi_T\rangle_4 = a\|2\rangle + b\|3\rangle$.
L-Lopsided	$\|\psi_L\rangle_d = a\|0\rangle + \frac{b}{\sqrt{d-1}}\sum_{j=1}^{d-1}\|j\rangle$ (d=3,4), $\|\psi_L\rangle_{2\otimes 2} = a\|\tilde{0}\rangle + \frac{b}{\sqrt{3}}(\|\tilde{1}\rangle + \|\tilde{2}\rangle + \|\tilde{3}\rangle)$.
O-Outside	$\|\psi_O\rangle_{2\otimes 2} = a\|\tilde{0}\rangle + b\|\tilde{3}\rangle$.
M-Middle	$\|\psi_M\rangle_{2\otimes 2} = a\|\tilde{1}\rangle + b\|\tilde{2}\rangle$.
E-Equal	$\|\psi_E\rangle_d = \frac{1}{\sqrt{d}}\sum_{n=0}^{d-1}(a+\omega^n b)\|n\rangle$ (d=3,4), $\|\psi_E\rangle_{2\otimes 2} = \frac{1}{2}\sum_{n=0}^{3}(a+\omega^n b)\|\tilde{n}\rangle$.

Table 6.1: Encodings used in the analysis.

with $\tilde{\chi}_{d'} = \chi_{d'} \oplus R$. Here R is a $(d-d') \times (d-d')$ matrix with arbitrary phase factors along its diagonal. These phases can be used to simplify the encoded operation χ_d. If we would like to encode qubits ($d' = 2$) into higher dimensions ($d \geq 3$) and manipulate them using d-dimensional one-way QC, we should consider encoded states $|\psi_{\mathcal{E}}\rangle_d$ given by

$$|\psi_{\mathcal{E}}\rangle_d = \Lambda_d(a|0\rangle + b|1\rangle), \quad |\psi_{\mathcal{E}}\rangle_d, \Lambda_d \in \mathcal{H}_d, \tag{6.8}$$

where $a = \cos\theta_1$ and $b = \sin\theta_1 e^{i\phi_1}$ [10]. Although many types of encodings have been considered, for clarity the performances of only the best and worst encodings found for each dimension will be shown under AD and PD decoherence. In Fig. 6.9 the effect of encoding logical qubits into *single* physical qudits is depicted. For notational reasons, $\mathcal{E}$ denotes the encoding type and d gives the dimension for which the encoding is used. The encodings are given in Table 6.1. One can see in Fig. 6.9 **(a)** that for AD, G encoding is the best for encoding qubits into single qudits as the fidelity-decays match exactly that of a single qubit. The worst encoding for AD is given by T. This is because in the limit $\Gamma_A t \to \infty$ the final state of the qudit becomes $|0\rangle\langle 0|$ for all dimensions and

[10] One could encode the qubit state across a qutrit, using $\Lambda_3 = 1 \oplus H$ to obtain $|\psi_{\mathcal{E}}\rangle_3 = a|0\rangle + b(|1\rangle + |2\rangle)/\sqrt{2}$. A rotation on this encoded qubit given by $\chi_2 = R_z^\gamma \equiv |0\rangle\langle 0| + e^{i\gamma}|1\rangle\langle 1|$ uses $\tilde{\chi}_2 = |0\rangle\langle 0| + e^{i\gamma}|1\rangle\langle 1| + e^{i\delta}|2\rangle\langle 2|$ setting $\delta = \gamma$ to give $\chi_3 = |0\rangle\langle 0| + e^{i\gamma}|1\rangle\langle 1| + e^{i\gamma}|2\rangle\langle 2|$. For $\chi_2 = H$ we get $\chi_3 = \cos^2(\pi/8)\mathbb{1} + \cos^2(3\pi/8)|0\rangle\langle 0| + [|0\rangle\langle 1| + |0\rangle\langle 2| - 2\cos^2(3\pi/8)|1\rangle\langle 2| + h.c.]/2$, by setting $\delta = 0$. This can be applied to any $d \geq 3$ and Λ_d to find equivalent operations for R_z^γ and H. These are sufficient to carry out any qubit rotation [128–130]. We can simulate any rotation on a d-dimensional logical qudit using d-dimensional cluster states [191]. Thus, arbitrary rotations can be simulated on qubits encoded within logical qudits.

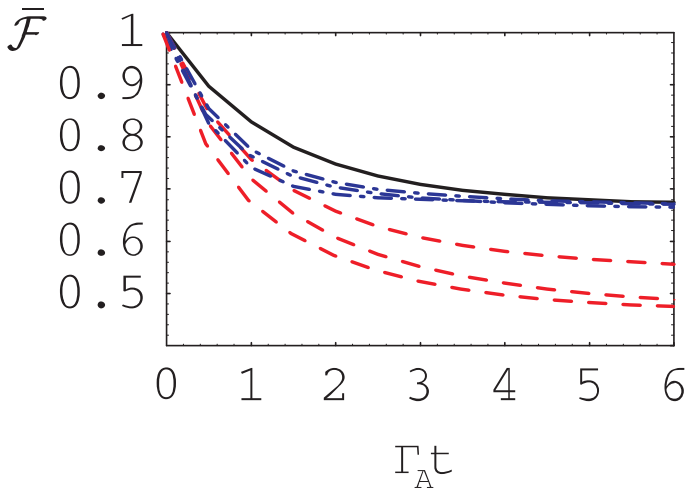

Figure 6.10: Average fidelities of AD-affected encoded qubits propagated along qudit cluster states of length $n = 2$. The solid line corresponds to $d = 2$, the dash-dotted lines represent L encoding for $d = 2 \otimes 2$, 3 and 4 (from top to bottom) and finally dashed lines represent G encoding for $d = 3$ and 4, and O/M encoding for $d = 2 \otimes 2$ (from top to bottom).

therefore the average fidelity $\bar{\mathcal{F}}(\Gamma_A t \to \infty) = 0$. The next best encoding is given by L, for any dimension. In Fig. 6.9 **(b)** the PD case is shown, where one can see that G and T represent the best encoding for qubits into single qudits. The next best encodings are L, for both $d = 3$ and 4, and O/M for $d = 2 \otimes 2$, the latter performing significantly better than that for $d = 3$ and 4. Moreover, it is known that to transmit qubits through qudit channels in presence of the AD and PD models considered here, the best encoding is given by using the two lowest and two contiguous states respectively [211]. The results shown here agree with this finding. Now we can investigate to see whether this feature holds true also for information transfer along cluster states.

In Figs. 6.10 and 6.11 average fidelities of encoded qubits propagated across AD-affected qudit clusters of lengths $n = 2$ and 3 are shown. The case of $n = 4$ ($n = 5$) has also been checked and has similar behaviour to $n = 2$ ($n = 3$). No encoding surpasses the qubit cluster state propagation, regardless of n. The next best encodings come from $d = 2 \otimes 2$, where L encoding is the best. The worst encodings are G (O/M) for even-length clusters and T (M) for odd-length ones with $d = 3$ and 4 ($2 \otimes 2$). In Figs. 6.12 and 6.13 average fidelities of encoded qubits propagated across PD-affected qudit clusters of lengths $n = 2$ and 3 are

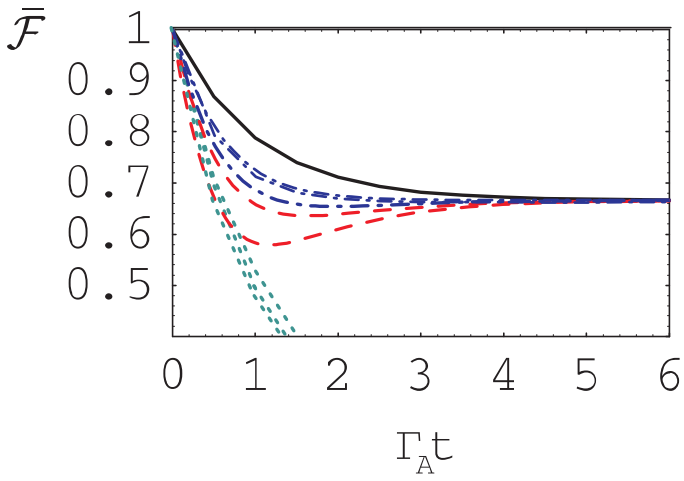

Figure 6.11: Average fidelities of AD-affected encoded qubits propagated along qudit cluster states of length $n = 3$. The solid line represents $d = 2$, dash-dotted lines represent L encoding for $d = 2 \otimes 2, 3$ and 4 (from top to bottom), dashed lines represent G encoding for $d = 3$ and 4 (from top to bottom) and dotted lines represent T encoding for $d = 3$ and 4, and M encoding for $d = 2 \otimes 2$ (from top to bottom).

shown. Evidently, no encoding surpasses propagation through qubit clusters. The next best encoding for $d = 3$ and 4 is T ($\forall n > 2$), while L is always the worst.

6.4.3 Encoded gate simulation

In this Section, gate operations on qudits and qubits encoded within the logical qudits in d-dimensional cluster states are studied. To understand how the entangling capabilities of BBB_2 and BBB_3 are affected by decoherence, the case when both logical input qudits are in $|+\rangle$ can be taken. Under ideal conditions, both BBB_2 and BBB_3 will create bipartite states LU equivalent to maximally entangled states. Entanglement decay for BBB_2 in higher dimensions has already been investigated in Section 6.3. Indeed, the entanglement generated between two logical qudits in the state $|+\rangle$ through BBB_2 is the same as that for a 2-qudit cluster state. We are therefore interested in the amount of entanglement generated by BBB_3 under decoherence. This will provide an indication of the effects of measuring *bridging* qubits in the interaction regions of gates in one-way QC. It

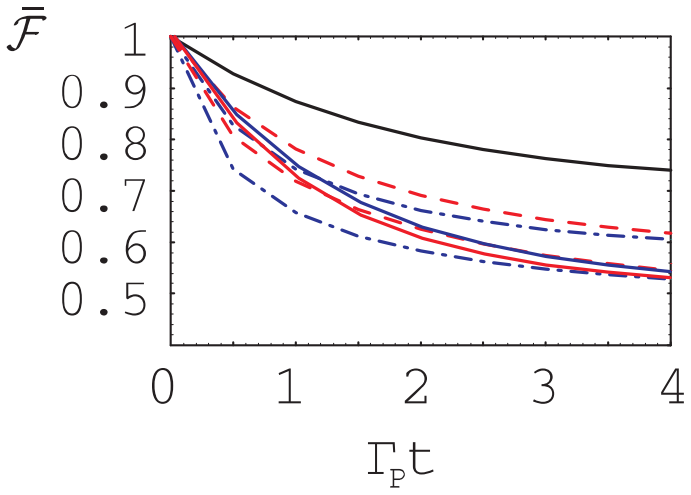

Figure 6.12: Average fidelities of PD-affected encoded qubits propagated along qudit cluster states of length $n = 2$. The top solid line corresponds to $d = 2$, the dashed lines to T and G encodings for $d = 3$ and 4 (from top to bottom), the dash-dotted lines to L encoding for $d = 3$ and 4 (from top to bottom). For $d = 2 \otimes 2$, the middle (bottom) solid line corresponds to L (O/M) encoding.

is also interesting to study how decoherence effects the entanglement generated by BBB_3 between two qubits in $|+\rangle$ encoded in the two lowest states of logical qudits. Consider the entangling gate BBB_3 (see Fig. 6.1 **(e)** in Section 6.2) with two qubits labeled $|q_{1,2}\rangle$ encoded in two logical qudits, labeled $|Q_{1,2}\rangle$ respectively. Assume the two qubits are decoded just before this entangling gate is simulated on the logical qudits. Such a decoding can be achieved with appropriate rotations applied from a chain of concatenated BBB_1's, using measurement bases dependent on the encoding used. BBB_3 is concatenated with these and with the rest of the entangled resource[11]. However, in order to gain an insight into its performance under the noise models considered here, it is separated so that no measurements are performed. Let $|q_1\rangle = a\,|0\rangle + b\,|1\rangle$ and $|q_2\rangle = c\,|0\rangle + d\,|1\rangle$. Within the un-encoded subspace of $\mathcal{H}_3$, for example, we have an application of the entangling gate $E^{12} = |0\rangle_1\langle 0| \otimes \mathbb{1}_2 + |1\rangle_1\langle 1| \otimes (|0\rangle_2\langle 0| + e^{i2\pi/3}|1\rangle_2\langle 1|)$. Two applications of E^{12} (and local rotations) are required to implement S^{12} for $d = 2$ (see Eq. (6.1)) [128, 214]. However, together with Hadamard and R_z^γ rotations, it is sufficient for universality. In the ideal case just described, now for $d = 4$, an $n = 2$ qubit state LU equivalent to a maximally entangled state is generated. It

[11]The physical qudits in BBB_3 will be measured in specific bases in the complete measurement pattern.

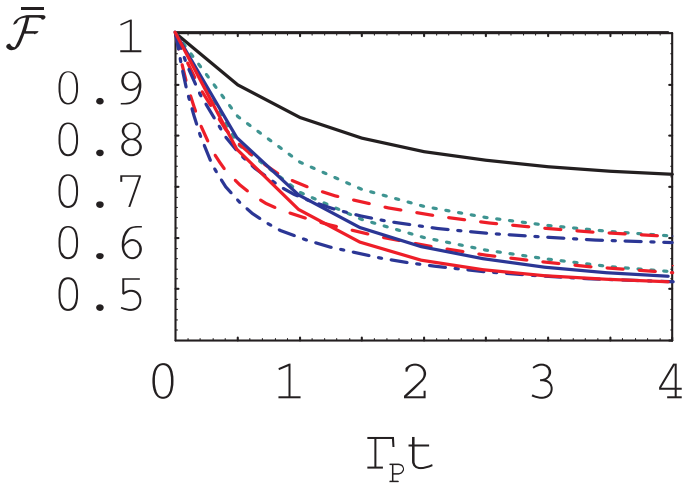

Figure 6.13: Average fidelities of PD-affected encoded qubits propagated along qudit cluster states of length $n = 3$. The top solid line corresponds to $d = 2$, the dashed lines to G encoding for $d = 3$ and 4 (from top to bottom), the dash-dotted lines to L encoding for $d = 3$ and 4 (from top to bottom), and the dotted lines to T encoding for $d = 3$ and 4 (from top to bottom). For $d = 2 \otimes 2$, the middle (bottom) solid line corresponds to L/M (E) encoding.

is interesting to see if any advantage can be found by using higher dimensions for gate simulations on qubits when noise is present.

In Fig. 6.14 the concurrence decay is shown for BBB_3 when $d = 2$ and normalised quasi-concurrence when $d = 4$. As the dimension increases, the proportion of the maximum achievable entanglement decays faster for both AD and PD. Also shown in Fig. 6.14 is the case when two qubits are encoded into the two lowest states and sent through BBB_3 for $d = 4$. In this case one can see that entanglement generated by the BBB_3 gate, in terms of concurrence, decays much faster than in the qubit case.

6.5 Remarks

In this Chapter an extension of the MB one-way model to d-dimensional systems was investigated. This was achieved by providing an analysis of entanglement properties, information transfer and gate simulation when specific types of environmental noise affects individual qudits in the cluster state resource. Such

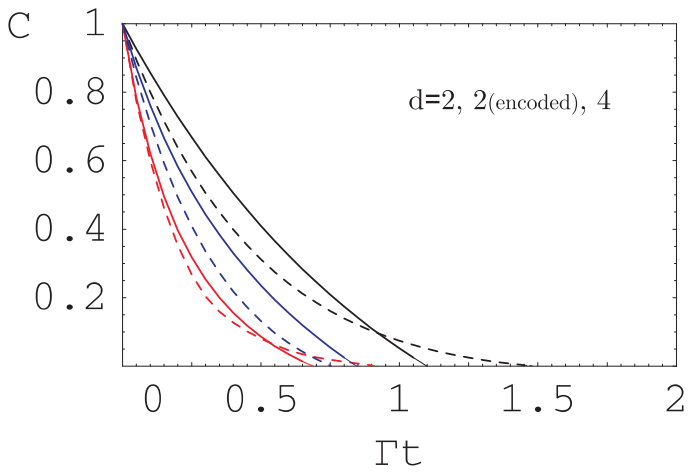

Figure 6.14: Entanglement in decohered BBB_3-produced cluster states. In all graphs the solid (dashed) lines correspond to PD (AD). We show $C(\varrho)$ for $d = 2$ (top two curves), $C_{qp}(\varrho)$ for $d = 4$ (bottom two curves) and $C(\varrho)$ for 2 qubits encoded in the lowest levels of $d = 4$ logical qudits and propagated through BBB_3 (middle two curves).

an extension appears not to provide any significant advantages with respect to the *standard* qubit MB one-way model when global properties of the entanglement resource are used in order to quantify the performances of a given QC protocol. Indeed, this study also reveals the previously overlooked superiority of a resource built out of pairs of entangled two-level systems with respect to higher-dimensional elementary systems. The analysis here covers several physically relevant situations of which there is much experimental interest. By raising the question of the quantification of advantages in d-dimensional MB QIP, this study paves the way toward further exploration of the problem using more sophisticated methods and other decoherence models. Specialised measures for the evaluation of the quality of the decoherence processes are the focus of further studies in this context. In addition, analysing the performance of one-way QC protocols in two and three dimensions (spatially) would also be of direct interest.

Chapter 7

Decoherence-free subspace resources

Decoherence is known to be the main obstacle in the grounding of quantum technology as a realistic scenario for ultra-fast and massively parallel information processing. We have seen already in some detail throughout the previous Chapters that the accuracy of protocols using cluster states is affected greatly by environment-induced decoherence and imperfections in the supporting quantum system. The design and experimental testing of fault-tolerant protocols for the $QC_{\mathcal{C}}$ model, capable of counteracting the damaging effects of decoherence is therefore important, as they will allow us to achieve accurate and efficient MB QIP. It is also highly desirable from an experimental point-of-view to design these protocols in such a way that they use a small amount of resources. In this Chapter a novel fault-tolerant scheme for the $QC_{\mathcal{C}}$ model is introduced. It is based on the use of encoded qubits in an effective cluster state resource and allows one to protect the quality of the entangled resources and the encoded information within from practically relevant sources of decoherence. In Section 7.1, the theory behind this scheme is provided along with an analysis of its performance compared with the standard $QC_{\mathcal{C}}$ model. A proposal for a physically realisable setup is also outlined. Then, in Section 7.2, an experimental test of the scheme using an all-optical setup is described in detail.

7.1 The $QC_{\mathcal{C}}$ model using decoherence-free subspaces: Theory

In this section, it will be shown that it is possible to protect an entangled cluster state resource from symmetric phase damping decoherence. The effective protected cluster state can be described as residing in a decoherence-free subspace (DFS) of its supporting quantum system. One-way QC then requires either single or two-qubit adaptive measurements. As an example where this proposal could be realised, an optical lattice setup is described, where the scheme provides robust QIP. An outline of how one could adapt the model to provide protection from other types of decoherence is also given.

7.1.1 Introduction

Quantum error-correction (QEC) [52–54] and the use of DFS's [215–218] are two well-known methods that offer protection against the loss of information from a supporting quantum system to its environment. The former requires a considerable overhead in system resources largely due to redundancy of the encoded information, while the latter requires a careful understanding of symmetries in the system-environment dynamics. The role of QEC in one-way QC has been studied previously [219–226], therefore in this Chapter the perspective is changed and the application of DFS is discussed as a novel method for protecting quantum information during the performance of one-way QC. The approach requires significantly less physical qubits and adaptive measurements than a scheme based on QEC and puts the proposal closer to experimental implementation in far simpler physical setups.

In Section 7.1.2, a model is introduced for a quantum system that supports a multipartite entangled resource constituting an effective cluster state. This specially constructed cluster is invariant under random phase errors induced from scattering type decoherence in the system-environment dynamics. It is then shown how one-way QC can be carried out on this entangled resource with single or two-qubit adaptive measurements. In order to give an operative way to evaluate the resilience to noise provided by the protection of the register by using a DFS, a *quantum process tomography* technique is outlined that can easily be adapted to various experimental setups [227–232]. A quantitative analysis is performed in the case of information transfer across a linear cluster state whose physical qubits are affected by phase damping decoherence and the superiority of the DFS encoding is shown. In Section 7.1.3, a description is provided of an optical lattice setup, where the required resource can be generated with cold controlled collisions and the measurements performed via Raman transitions and fluorescence techniques. Finally, Section 7.1.4 summarises the results and includes a brief outline of how the scheme can be adapted to provide protection from other forms of collective decoherence.

7.1.2 The Model

Consider a set of qubits occupying the sites of a lattice structure $\mathcal{C}$ as shown in Fig. 7.1 **(a)**. Each pair of qubits is prepared in the singlet state

$$\left|\psi^{-}\right\rangle_{ab} = \frac{1}{\sqrt{2}}(|01\rangle - |10\rangle)_{ab} \tag{7.1}$$

with $\{|0\rangle, |1\rangle\}$ the single-qubit basis. In what follows, each first (second) *pedex* labels a qubit belonging to the top (bottom) qubit-layer with respect to the positive z-axis (see Fig. 7.1 **(a)**). The top qubits a and c of two neighbouring pairs are connected via the controlled-σ_z operation

$$S^{ac} = |0\rangle_a\langle 0| \otimes \mathbb{1}_c + |1\rangle_a\langle 1| \otimes \sigma_{z,c} \tag{7.2}$$

with $\sigma_{l,i}$ $(l = x, y, z)$ the l-Pauli matrix applied to qubit i. In order to generate this entanglement structure, one initially sets the top and bottom qubits a, b to the state $|-\rangle$, resulting in the total state $\otimes_{a,b\in\mathcal{C}} |-,-\rangle_{ab}$. The transformation

$$\mathcal{S}^{\mathcal{C}}_{\parallel} = \prod_{a,b\in\mathcal{C}|a,b\in\gamma_{\parallel}} S^{ab} \tag{7.3}$$

is then applied to the qubits along the z-axis, where $\gamma_{\parallel} = (0,0,1)^T$. This is followed by the operation $\prod_{a,b\in\mathcal{C}|a,b\in\gamma_{\parallel}} \mathbb{1}_a \otimes \mathsf{H}_b$, where H_i is the Hadamard gate applied to qubit i, resulting in the state

$$\bigotimes_{a,b\in\mathcal{C}|a,b\in\gamma_{\parallel}} \left|\psi^{-}\right\rangle_{ab}. \tag{7.4}$$

The next step is the application of the transformation $\mathcal{S}^{\mathcal{C}}_{=} = \prod_{a,c\in\mathcal{C}|a,c\in\gamma_{=}} S^{ac}$ to qubits belonging to the top layer of the lattice, where $\gamma_{=} = \{(1,0,0)^T, (0,1,0)^T\}$. The encoding $\{|0_E\rangle_{a'} := |01\rangle_{ab}, |1_E\rangle_{a'} := -|10\rangle_{ab}\}$ is now used, where each pair of physical qubits embodies an *effective* qubit a' in a single-layer lattice $\mathcal{C}'$. The state generated in this way corresponds to a standard cluster state $\left|\phi_{\{\kappa\}}\right\rangle_{\mathcal{C}'}$ with eigenvalue set $\{\kappa\}$ containing $\kappa_{a'} = 0$, $(\forall a' \in \mathcal{C}')$ (see Chapter 2), which is denoted, for ease of notation, as $|\phi\rangle_{\mathcal{C}'}$. From now on, the top and bottom physical qubits encompassed in a' will be labeled as a'_1 and a'_2 respectively.

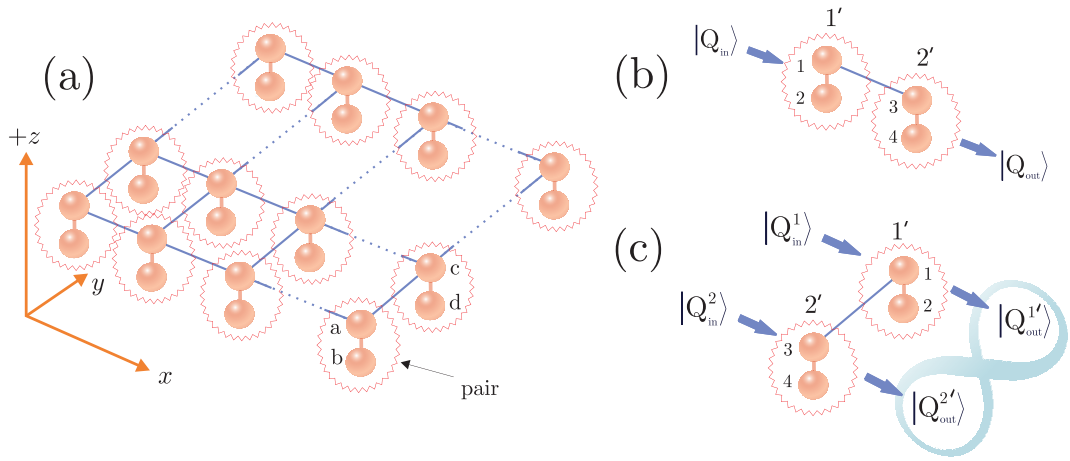

Figure 7.1: **(a)**: The effective two-dimensional cluster state layout with each pair of physical qubits representing an encoded effective qubit. The qubits belonging to each pair couple to the environment in the same way, as described by Eq. (7.5). **(b)**: Schematics for information propagation of a logical qubit $|Q_{\rm in}\rangle$. **(c)**: The simulation of a gate operation on two logical qubits $|Q^1_{\rm in}\rangle$ and $|Q^2_{\rm in}\rangle$. A detailed account of the procedures to follow in **(b)** and **(c)** is provided in the body of the text.

The physical assumption made here concerning the noise affecting the prepared entangled resource is that while qubits in the x-y plane across the lattice structure are at a fixed distance from each other, the qubits along the z-axis are closer together (see Fig. 7.1 **(a)**) such that each qubit in a pair couples to the environment in the same way. This means that the environment cannot distinguish the qubits and one can write the Hamiltonian for the paired-qubit system and the environment as [215–218]

$$H = E_0 \otimes \mathbb{1} + E_x \otimes J_x + E_y \otimes J_y + E_z \otimes J_z, \tag{7.5}$$

where E_0, E_x, E_y and E_z are the operators of the environment together with $J_x = (1/2)\sum_{i=1}^{2} \sigma_{a_i',x}$, $J_y = (1/2)\sum_{i=1}^{2} \sigma_{a_i',y}$ and $J_z = (1/2)\sum_{i=1}^{2} \sigma_{a_i',z}$. The Hamiltonian in Eq. (7.5) describes well the physical situation when both qubits are very close together when compared to the environment's coherence length [215–218], where a Markov approximation is implicit in the description. This is a reasonable assumption in many physical situations, one of which will be treated in detail in Section 7.1.3. The qubits affected by the collective type of noise described in Eq. (7.5) are depicted by jagged surroundings in Fig. 7.1. The en-

coded qubit state $|+\rangle_{a'}$ (equivalent to $|\psi^{-}\rangle_{a'_1 a'_2}$), before entanglement generation on the top layer, is invariant under environment-induced phase shifts (associated with the final term in Eq. (7.5)) on the physical qubits $|j\rangle \rightarrow e^{i\phi_j}|j\rangle$ $(j = 0, 1)$. As any random phase shifts of this form commute with the operations S^{ac} on the top layer producing the encoded cluster state, the final state $|\phi\rangle_{\mathcal{C}'}$ is unaffected by such an environment also. The *dual-rail* encoding used here is well-known in providing robust protection against phase damping decoherence [215–218]. The combination of this encoding and the entangling operations described, put the encoded cluster state $|\phi\rangle_{\mathcal{C}'}$ in a DFS for the phase damping class of noise considered here, *i.e.* to describe the dynamics $E_x = E_y = 0$ is set in Eq. (7.5). The possibility of encoding within such a DFS is important in many physical setups where random phase fluctuations are the dominant source of decoherence. For example, in optical lattices and ion traps this decoherence mechanism is caused by an environment at non-zero temperature exciting the motional states of the atoms that embody the physical qubits [233–236].

In order to understand how information can be propagated across the effective single layer lattice shown in Fig. 7.1 **(a)**, consider the prototypical configuration shown in Fig. 7.1 **(b)**. Here a normalised logical qubit $|Q_{\mathrm{in}}\rangle = \mu|0_E\rangle_{1'} + \nu|1_E\rangle_{1'}$ is encoded on the effective qubit $1'$ embodied by the physical qubits 1 and 2. After the entangled resource is prepared, the total state of the effective qubits $1'$ and $2'$ is written as

$$|\Phi\rangle_{\mathrm{DFS}} = \mu|0_E, +_E\rangle_{1'2'} + \nu|1_E, -_E\rangle_{1'2'} \tag{7.6}$$

with $|\pm_E\rangle = (1/\sqrt{2})(|0_E\rangle \pm |1_E\rangle)$. There are two ways to propagate information across effective sub-clusters such as the one considered here. Depending on the physical setup, one strategy may be preferable to the other. The first is to perform a joint measurement on a pair of qubits comprising an effective qubit i' in the basis $B_{i'}(\alpha) = \{|\psi^{+\alpha}\rangle_{i'}, |\psi^{-\alpha}\rangle_{i'}\}$ with outcomes $s^{\alpha}_{i'} = \{0, 1\}$ and $|\psi^{\pm\alpha}\rangle_{i'} = (1/\sqrt{2})(|01\rangle \pm e^{i\alpha}|10\rangle)_{i'_1 i'_2}$. In the case of $i' = 1'$ in Eq. (7.6) this strategy simulates the transformation $\sigma_x^{s^{\alpha}_{1'}\oplus 1}\mathsf{H}R_z^{-\alpha}$ on the logical qubit $|Q_{in}\rangle$.

The second method is to perform single-qubit measurements on i'_1 and i'_2 in the bases $B_{i'_1}(\alpha) = \{|+\alpha\rangle_{i'_1}, |-\alpha\rangle_{i'_1}\}$ and $B_{i'_2}(0) = \{|+\rangle_{i'_2}, |-\rangle_{i'_2}\}$ with outcomes

$s^{\alpha}_{i'_{1,2}} = \{0,1\}$ and $|\pm\alpha\rangle_{i'_j} = (1/\sqrt{2})(|0\rangle \pm e^{i\alpha}|1\rangle)_{i'_j}$ $(j = 1, 2)$. For $i' = 1'$, $i'_j = j$, this simulates the transformation $\sigma_x^{s^{\alpha}_{i'_1} \oplus s^{0}_{i'_2} \oplus 1} \mathsf{H} R_z^{-\alpha}$ on the logical qubit.

Consider now the situation depicted in Fig. 7.1 **(c)** with input logical qubits $|Q^1_{\rm in}\rangle$ and $|Q^2_{\rm in}\rangle$. If no measurements take place on the qubit pairs and the two-qubit gate S^{13} is applied to the top-layer physical qubits 1 and 3, we obtain a state that simulates the outcome of the effective gate CZ being applied to the logical qubits $1'$ and $2'$. These two examples represent the DFS-encoded version of the basic building blocks BBB$_1$ and BBB$_2$ described in Chapter 2. From the above discussions, one can clearly see how similar the simulations on encoded cluster states are to the original MB one-way model [55, 56, 129, 130]. In fact with the addition of a third building block, BBB$_3$, acting on an effective three-qubit cluster structure (whose construction and demonstration in a DFS-encoded scenario goes simply along the lines depicted above for BBB$_1$ and BBB$_2$), the same concatenation rules described in Chapter 2 can be applied here. Therefore the concatenation of the three BBB's is sufficient to simulate any computational process.

A stabiliser-based approach is also possible in this model by using the correlation relations $G^{(a')}|\phi\rangle_{\mathcal{C}'} = (-1)^{\kappa_{a'}}|\phi\rangle_{\mathcal{C}'}$ where

$$\begin{aligned} G^{(a')} &= X_{a'} \bigotimes_{c' \in \mathrm{nghb(a')} \cap \mathcal{C}'} Z_{c'}, \\ X_{a'} &= (\sigma_z\sigma_x)_{a'_1} \otimes (\sigma_z\sigma_x)_{a'_2}, \\ Z_{c'} &= \sigma_{z,c'_1} \otimes \mathbb{1}_{c'_2}. \end{aligned} \tag{7.7}$$

With these tools, one can manipulate the relevant eigenvalue equations defining the cluster resource and design the correct measurement pattern for any unitary simulation [129, 130].

All the computational steps can be performed within the DFS and at no point during the computation is the effective cluster state exposed to phase damping type decoherence. In the case of an ideal cluster-resource being produced, this allows the noise effects to be canceled exactly. However in a real experiment, due to imperfections at the cluster generation stages, a state having non-unit

overlap with the ideal resource $|\phi\rangle_{\mathcal{C}'}$ is obtained. This results in an effective resource that is partially residing outside the DFS and it is only this fraction that is prone to environmental effects. The benefits of this proposal should now be clear: encoding in a protected DFS provides a method of reducing greatly decoherence processes (ideally, their complete cancellation) in such a way that avoids the use of *a posteriori* procedures for correcting the resulting errors as in QEC.

Noise-resilience characterisation

Here a general operative way is presented for determining the effectiveness of the noise protection provided by the realisation of one-way QC within a DFS. This can be efficiently done by means of a characterisation of the effective map the logical state of a register undergoes in the presence of a noisy computational process. This characterisation requires the use of *quantum process tomography* [128], whose main features are outlined next.

A dynamical map $\mathcal{E}$, also called a "channel", acting on the density matrix of a quantum system ϱ is fully identified by the set of Kraus operators $\{\hat{K}_i\}$ such that

$$\varrho \to \mathcal{E}(\varrho) = \sum_i \hat{K}_i \varrho \hat{K}_i^\dagger, \tag{7.8}$$

with $\sum_i \hat{K}_i^\dagger \hat{K}_i = \mathbb{1}$. Channel characterisation then reduces to the determination of the $\hat{K}_i$'s. By choosing a complete set of orthogonal operators $\{\hat{\mathcal{K}}_m\}$ over which the expansion $\hat{K}_i = \sum_m e_{im} \hat{\mathcal{K}}_m$ is made, one finds

$$\mathcal{E}(\varrho) = \sum_{m,n} \chi_{mn} \hat{\mathcal{K}}_m \varrho \hat{\mathcal{K}}_n^\dagger \tag{7.9}$$

with the *channel matrix* $\chi_{mn} = \sum_i e_{im} e_{in}^*$. This is a pragmatically very useful result as it shows that it is sufficient to consider a fixed set of operators $\{\hat{\mathcal{K}}_m\}$, whose knowledge is enough to characterise a channel through the matrix χ. Thus, its matrix elements must be found. In order to provide them, it is important to notice that the action of the channel over a generic element $|n\rangle\langle m|$ of a basis in the space of the $d \times d$ matrices (and thus $n, m = 0, .., d^2 - 1$), given by

$\mathcal{E}(|n\rangle\langle m|)$, can be determined from a knowledge of the map $\mathcal{E}$ on the fixed set of states $|n\rangle$, $|m\rangle$, $|\tilde{+}\rangle = (1/\sqrt{2})(|n\rangle + |m\rangle)$ and $|\tilde{+}_y\rangle = (1/\sqrt{2})(|n\rangle + i\,|m\rangle)$ as follows

$$\begin{aligned}\mathcal{E}(|n\rangle\langle m|) = \mathcal{E}(|\tilde{+}\rangle\langle\tilde{+}|) + i\mathcal{E}(|\tilde{+}_y\rangle\langle\tilde{+}_y|) \\ - \frac{i+1}{2}[\mathcal{E}(|n\rangle\langle n|) + \mathcal{E}(|m\rangle\langle m|)].\end{aligned} \tag{7.10}$$

Therefore, the effect of the channel $\mathcal{E}$ on each $\varrho_j = |n\rangle\langle m|$ (with $j = 1, .., d^2$) can be found completely via state tomography of just four fixed states. It is clear that $\mathcal{E}(\varrho_j) = \sum_k \lambda_{jk}\varrho_k$ as $\{\varrho_k\}$ form a basis, therefore from the above discussion

$$\begin{aligned}\mathcal{E}(\varrho_j) = \sum_{m,n} \hat{\mathcal{K}}_m \varrho_j \hat{\mathcal{K}}_n^\dagger \chi_{mn} = \sum_{m,n,k} \beta_{jk}^{mn} \varrho_k \chi_{mn} \\ \equiv \sum_k \lambda_{jk}\varrho_k,\end{aligned} \tag{7.11}$$

where $\hat{\mathcal{K}}_m \varrho_j \hat{\mathcal{K}}_n^\dagger = \sum_k \beta_{jk}^{mn}\varrho_k$ has been defined. Therefore we can write

$$\lambda_{jk} = \sum_{m,n} \beta_{jk}^{mn}\chi_{mn}. \tag{7.12}$$

The complex tensor β_{jk}^{mn} is set once a choice is made for $\{\hat{\mathcal{K}}_i\}$ and the λ_{jk}'s are determined from a knowledge of $\mathcal{E}(\varrho_j)$. By inverting Eq. (7.12), one can determine the channel matrix χ completely and characterise the map. Let $\hat{U}^\dagger$ be the operator diagonalising the channel matrix (which is always possible for a generic complex matrix that is not a null set with respect to the Lebesgue measure [238]). Then it is straightforward to prove that if D_i are the elements of the diagonal matrix $\hat{U}^\dagger\chi\hat{U}$, then $e_{im} = \sqrt{D_i}\hat{U}_{mi}$ so that

$$\hat{K}_i = \sqrt{D_i}\sum_j \hat{U}_{ji}\hat{\mathcal{K}}_j. \tag{7.13}$$

Important information can be extracted from this characterisation for the case of a channel describing a logical qubit transferred across a linear cluster subjected to environment-induced noise. In particular, we can infer how close a logical output state $\mathcal{E}(\varrho)$ will be on average to a logical output qubit ρ when no noise is present. The Schmidt-decomposed bipartite Bell state $|\phi^+\rangle$ can be written as $|b\rangle = (1/\sqrt{d})\sum_i |i\rangle\,|i\rangle$ and the *entanglement fidelity* of the characterised

channel [237] becomes

$$F_e(\mathcal{E}) = \langle b| \left(\mathbb{1} \otimes \mathcal{E}\right)(|b\rangle \langle b|) |b\rangle . \tag{7.14}$$

This quantifies the resilience of a maximally entangled state to a unilateral action of the channel. $F_e(\mathcal{E})$ can easily be determined from the knowledge of the set $\{\hat{K}_i\}$. By using the channel entanglement fidelity, the average state fidelity resulting from the application of $\mathcal{E}$ can be determined as [154, 239]

$$\bar{F} = \frac{1}{3}(2F_e(\mathcal{E}) + 1). \tag{7.15}$$

The theory of quantum process tomography can be applied to the specific experimental setup used for the implementation of DFS encoded one-way QC. The setup dependence is the method used for the state tomography required in order to find the set of output states $\mathcal{E}(|n\rangle\langle n|)$, $\mathcal{E}(|m\rangle\langle m|)$, $\mathcal{E}(|\tilde{+}\rangle\langle\tilde{+}|)$, $\mathcal{E}(|\tilde{+}_y\rangle\langle\tilde{+}_y|)$ [227–232]. Here, a realisation in a condensed-matter system is concentrated on, where these four state tomographies can be determined through photon-scattering out of an optical lattice embodying the physical support for the entangled resource. However, the technique is easily adapted to any other choice.

An application: Information transfer through a linear cluster state

An example application of quantum process tomography is now provided to a case of interest for the discussion. Information flow across both a DFS and standard encoded linear cluster state of three effective qubits is considered, as shown in Fig. 7.2. Here, in the standard encoded case (Fig. 7.2 **(b)**), the effective qubits correspond to the physical ones. It is assumed that each qubit (pair of qubits) in the standard (DFS-encoded) cluster is affected by a phase damping (collective phase damping) decoherence channel characterised by a strength Γ that, for the sake of simplicity, is also assumed to be same for the entire qubit register. The parameter Γ can be thought of physically as the rate of damping, or random scattering per unit time of the environment with the qubit systems (as described in Chapters 2, 3 and 6). This is related to the coupling strength of the environment to the qubit-pair system in the final term of Eq. (7.5).

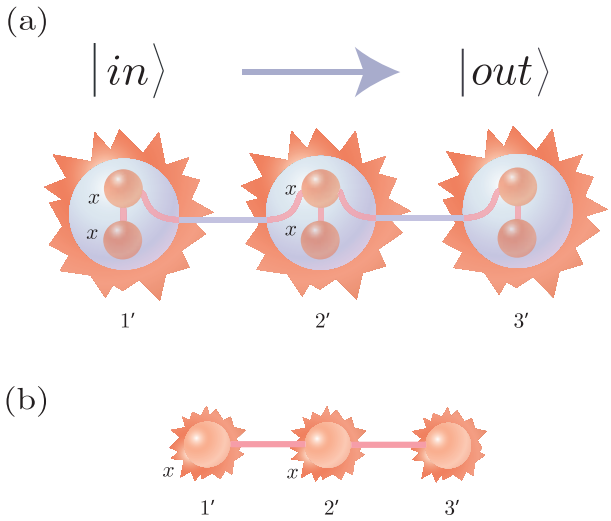

Figure 7.2: Quantum information transfer across a three-element cluster. All measurements are in the σ_x eigenbasis. **(a)**: DFS encoded cluster state. **(b)**: Standard cluster state.

A quantum state is transferred from the first to the last effective qubit in a chain of three elements (as shown in Fig. 7.2), which from now on are labelled $j = 1', 2', 3'$. In the standard one-way model, this implies the measurement of qubits $1'$ and $2'$ in the $B_{1'}(0)$ and $B_{2'}(0)$ bases. In order to fix the ideas, in what follows, the case where the measurements have outcomes $s^0_{1'} = s^0_{2'} = 0$ are considered for definiteness. This corresponds to the identity operation being carried out on a logical input state. From the discussion in Section 7.1.2, it is clear that the DFS encoding leaves the input state $|in\rangle = \cos\theta\,|0\rangle + e^{i\phi}\cos\theta\,|1\rangle$ unaffected by the noise during the transfer across the chain. On the other hand, a calculation using the Kraus operators for phase damping described in Chapters 2 and 6 reveals that in the standard encoded case, the state of the logical output qubit residing on qubit $3'$, *i.e.* after the performance of the protocol, in the presence of the phase damping environment characterised by the strength Γ, is written as

$$\begin{aligned}\rho_{3'} = &\frac{e^{-\frac{3\Gamma t}{2}-i\phi}}{2}(e^{\Gamma t/2}\cos\phi - i\sin\phi)\sin(2\theta)\,|0\rangle_{3'}\langle 1| + h.c. \\ &+ \frac{1}{2}\mathbb{1}_{3'} + \frac{e^{-\Gamma t/2}\cos(2\theta)}{2}\sigma_{z,3'}.\end{aligned} \tag{7.16}$$

Having this output state of the effective map undergone by the input logi-

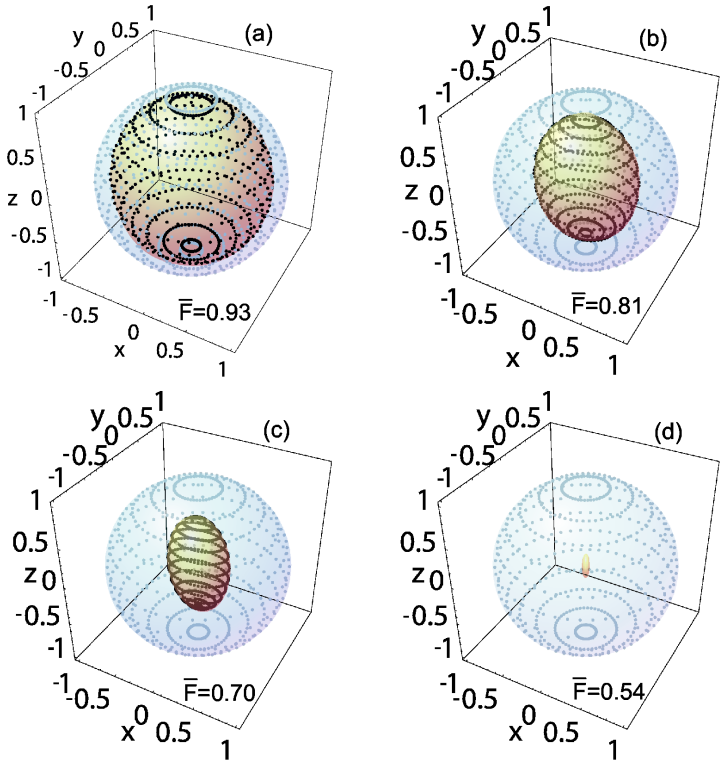

Figure 7.3: Comparison between the DFS and standard evolution of a pure input state transferred across a three-element (effective) cluster state with phase damping affecting the individual physical qubits. From (**a**) to (**d**), Γt is taken to be 0.15, 0.5, 1 and 5 respectively. The outer blue ball shows the Bloch sphere of output logical qubits in the DFS case. The states are kept pure all along the evolution. The inner ball corresponds to the standard case. An anisotropic shrinking of the Bloch sphere, increasing with Γt, occurs in a way that quickly decoheres the output states into a totally mixed state. Each dot on a sphere represents a physical density matrix associated with a chosen set (θ, ϕ) for the input state. One can see that the effect of the logical channel is a mixture of depolarising and phase damping mechanisms (see Chapter 2, Fig. 2.3). The phase damping squeezes states along the x-y plane, while the depolarising causes a general shrinking into the centre.

cal state $|in\rangle$ [1] and using quantum process tomography, it is possible to compute the corresponding Kraus operators for the logical channel using $|in\rangle \in$

[1]Note that for $\Gamma t = 0$, $\rho_{3'} = |in\rangle\langle in|$ in Eq. (7.16).

$\{|0\rangle, |1\rangle, |+\rangle, |+_y\rangle\}$, giving

$$\begin{aligned}
\hat{K}_1 &= e^{-3\tau/8}\sqrt{\sinh\frac{\tau}{4}\cosh\frac{\tau}{2}}\sigma_x, \\
\hat{K}_2 &= e^{-3\tau/8}\sqrt{\cosh\frac{\tau}{4}\cosh\frac{\tau}{2}}\mathbb{1}, \\
\hat{K}_3 &= e^{-3\tau/8}\cosh\frac{\tau}{4}\sqrt{2\sinh\frac{\tau}{4}}\sigma_z, \\
\hat{K}_4 &= -ie^{-3\tau/8}\sinh\frac{\tau}{4}\sqrt{2\cosh\frac{\tau}{4}}\sigma_y.
\end{aligned} \tag{7.17}$$

In these equations $\tau = \Gamma t$ is set as a rescaled interaction time. It is straightforward to check that $\sum_i \hat{K}_i^\dagger \hat{K}_i = \mathbb{1}$ and that $\sum_i \hat{K}_i |in\rangle\langle in| \hat{K}_i^\dagger = \rho_{3'}$. The evolutions induced by the Kraus operators associated with the channel in the DFS and standard case are pictorially shown in Fig. 7.3. A striking shielding of the quantum information from the action of the environment is revealed. While in the standard case the evolution quickly collapses the state of the output qubit into a maximally mixed state $(1/2)\mathbb{1}$, the DFS encoded state is kept pure throughout the dynamics and for any value of the decoherence parameter Γt. In order to provide a full characterisation of the channel, in panels (**a**) to (**d**) the average state fidelity associated with each instance of the non-DFS channel is given.

7.1.3 Realisation in optical lattices

The effective two-dimensional cluster state shown in Fig. 7.1 **(a)** can be realised by using alkali-metal atoms such as ^{87}Rb trapped in a cubic three-dimensional optical lattice. The lattice configuration is achieved with three slightly detuned pairs of counter-propagating laser beams L^X, L^Y and L^Z, tuned between the $D1$ and $D2$ line with wavelength $\lambda = 785$ nm (see Fig 5.3 of Chapter 5 for more details). The pairs propagate along $\hat{\mathbf{x}}$, $\hat{\mathbf{y}}$ and $\hat{\mathbf{z}}$ respectively and are in a lin$\angle$lin configuration: linearly polarised with electric fields forming an angle $2\theta_i,\ i \in \{x, y, z\}$ [146], providing lattice sites with periodicity $\lambda/2$ for $\theta_i = 0,\ \forall i$. It is assumed that the lattice is initially loaded with one atom per site, which can be achieved by making a Bose-Einstein condensate undergo a superfluid to

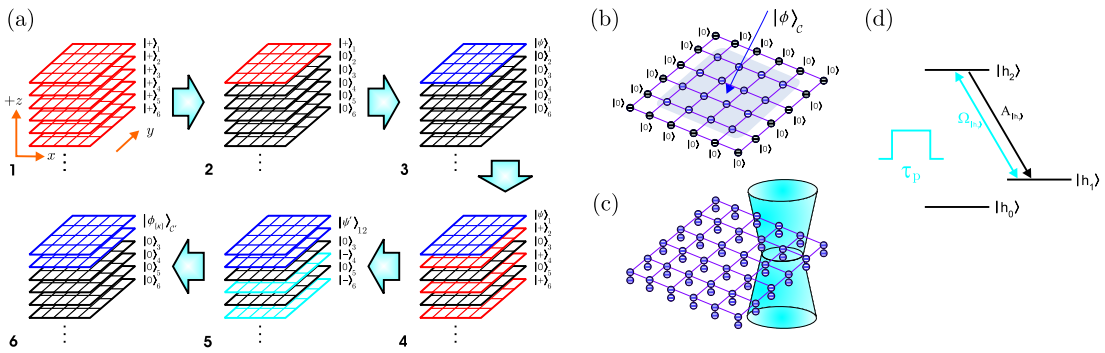

Figure 7.4: **(a)**: Steps taken to create the effective cluster state in an optical lattice setup. **(b)**: A barrier technique (see footnote 2) to create a cluster state $|\phi\rangle_{\mathcal{C}'}$ with the set $\kappa_a = 0,\ \forall a$ in the central region. **(c)**: Tightly focused laser beam with Gaussian profile used for measurements of the atomic states via fluorescence. **(d)**: Level structure for projective measurements via fluorescence.

Mott insulator (MI) phase transition [70, 141, 182, 183]. Each physical qubit at a lattice site can then be embodied by the single-atom hyperfine states $|h_0\rangle = |0\rangle \equiv |F = 2, m_f = 2\rangle$ and $|h_1\rangle = |1\rangle \equiv |F = 1, m_f = 1\rangle$ with F and m_f the total angular momentum of the atom and its projection along $\hat{\mathbf{z}}$ respectively. These states can be coupled via a Raman transition [182] (see also Fig. 5.4 in Chapter 5), using an excited state $|h_e\rangle$ embodied by an additional hyperfine state. Cold controlled collisions using moving trapping potentials between adjacent atoms along the three spatial dimensions can be achieved by individually changing the angles θ_i [70, 233]. The controlled collisions result in a dynamically induced phase shift applied to only one of the joint states of adjacent atoms, $|0\rangle_a |1\rangle_{a+1} \rightarrow -|0\rangle_a |1\rangle_{a+1}$. The entangling operation $\tilde{S}^{ac} = |0\rangle_a\langle 0| \otimes \sigma_{z,c} + |1\rangle_a\langle 1| \otimes \mathbb{1}_c$ is therefore produced and describes a conditional phase shift equivalent to S^{ac} in Eq. (7.2) with a σ_z operation on qubit $c = (a + 1)$.

The initialisation of the qubit register prior to any entanglement generation can be achieved by applying Raman transitions to all lattice sites. These can be activated by standing-waves of period $\lambda/2$ from two pairs of lasers L_1 and L_2, far blue-detuned by an amount Δ from the transition $|\{h_0, h_1\}\rangle \leftrightarrow |h_e\rangle$ and oriented along $\hat{\mathbf{z}}$. All the sites will be located at the maximum-intensity peaks [187] and with the atoms initially in $|h_0\rangle$, a rotation of the qubits into the state $|+\rangle$ can be achieved as shown in Fig. 7.4 **(a)**, step 1. Next, a one-off setting of atoms on all layers (apart from the the top layer) to the state

$|0\rangle$ can be achieved by either a blurred addressing technique (see Chapter 5), interference methods [240, 241] or microwave addressing [242], see Fig. 7.4 **(a)**, step 2. To generate entanglement on the top layer only, angles θ_x and θ_y are varied so as to apply the operation $\tilde{\mathcal{S}}^{\mathcal{C}}_{=} = \prod_{a,c\in\mathcal{C}|a,c\in\gamma_=} \tilde{S}^{ac}$. This creates a cluster state with a particular set of eigenvalues $\{\kappa\}$. The non-zero values in this set can be accommodated by modifying the measurement pattern later, as they will determine corresponding values in the final effective lattice[2]. The resulting cluster state on the top layer is denoted as $|\psi\rangle$ as shown in Fig. 7.4 **(a)**, step 3. It is possible to form standing waves of period larger than $\lambda/2$ with the two pairs of lasers $L_{1,2}$ used for the Raman transitions [243]. Here, the two lasers in each pair are set at angles $\pm\theta/2$ to a given direction $\vec{v}$ on the x-z plane. This produces an intensity pattern in the direction perpendicular to $\vec{v}$ on the x-z plane with period $d = \lambda/[2\sin(\theta/2)]$. Thus one can rotate states on the even labelled layers to $|+\rangle$ via a Hadamard rotation H, as shown in Fig. 7.4 **(a)**, step 4. Next, controlled collisions can be initiated along $\hat{\mathbf{z}}$ by varying the angle θ_z. This applies the operation $\tilde{\mathcal{S}}^{\mathcal{C}}_{\parallel} = \prod_{a,b\in\mathcal{C}|a,b\in\gamma_\parallel} \tilde{S}^{ab}$ creating an entangled state $|\psi'\rangle$ on the top two layers. Due to the transformation $|0\rangle_a |+\rangle_b \rightarrow |0\rangle_a |-\rangle_b$ from the controlled collisions of the atoms on odd layers a with those on even layers b, one produces the structure shown in Fig. 7.4 **(a)**, step 5. In step 6, the rotation $\tilde{\mathsf{H}} := \mathsf{H}\sigma_x$ is applied to all even labeled layers using Raman transitions. Finally, the x-y lattice spacing is increased from $\lambda/2$ by adiabatically turning on a periodic potential with a larger lattice spacing [243], while turning off the original laser pairs L^X and L^Y [3].

In order to understand how the DFS encoded cluster state $|\phi\rangle_{\mathcal{C}'}$ is generated by the previous steps on the top two layers of the lattice, one needs to consider the operations performed in each step. First, we start with the state $\otimes_{a,b\in\mathcal{C}} |+,0\rangle_{ab}$ in step 2. Then $\tilde{\mathcal{S}}^{\mathcal{C}}_{=}$ is applied on the top layer, followed by H to the bottom layer. Finally $\tilde{\mathcal{S}}^{\mathcal{C}}_{\parallel}$ is applied between the top and bottom layers and $\tilde{\mathsf{H}}$ to the

[2] *Barrier technique*: In step 3, a barrier of atoms in the state $|0\rangle$ could be created and a transformation $|0\rangle_a |+\rangle_c \rightarrow |0\rangle_a |-\rangle_c$ from the controlled collisions of the barrier atoms with those within the barrier would produce a cluster state $|\phi\rangle_{\mathcal{C}}$ as shown in Fig. 7.4 **(b)**.

[3] The new enlarged lattice spacing will be restricted by the validity of the Mott Insulator regime [182].

bottom layer. The entire process is

$$\prod_{a,b\in\mathcal{C}|a,b\in\gamma_{\|}} (\mathbb{1}_a \otimes \tilde{\mathsf{H}}_b)\tilde{S}^{ab}(\mathbb{1}_a \otimes \mathsf{H}_b) \prod_{a,c\in\mathcal{C}|a,c\in\gamma_{=}} \tilde{S}^{ac} \bigotimes_{a,b\in\mathcal{C}|a,b\in\gamma_{\|}} |+,0\rangle_{ab} \tag{7.18}$$

which can be reordered to give

$$\prod_{a,c\in\mathcal{C}|a,c\in\gamma_{=}} \tilde{S}^{ac} \left[\prod_{a,b\in\mathcal{C}|a,b\in\gamma_{\|}} (\mathbb{1}_a \otimes \tilde{\mathsf{H}}_b)\tilde{S}^{ab} \bigotimes_{a,b\in\mathcal{C}} |+,+\rangle_{ab} \right]. \tag{7.19}$$

The square bracketed part is equivalent to $\otimes_{a,b\in\mathcal{C}|a,b\in\gamma_{\|}} |\psi^{-}\rangle_{ab}$. Using a barrier technique (see footnote 2) on the top layer allows $\prod_{a,c\in\mathcal{C}|a,c\in\gamma_{=}} \tilde{S}^{ac}$ to be formally equivalent to $\prod_{a,c\in\mathcal{C}|a,c\in\gamma_{=}} S^{ac}$ for the central section of atoms. If this method is not used, then a different set $\{\kappa\}$ must be taken into account for the effective cluster state in the measurement pattern design. Comparing the above steps with those described in Section 7.1.2, one can easily see that they create the required effective cluster state $|\phi\rangle_{\mathcal{C}'}$. An alternative method for setting up the required effective lattice could be the use of a pattern-formation technique [244] to separate two layers of a three-dimensional lattice from the rest by a gap of at least two layers. As the entanglement is generated via controlled collisions, only the two separated layers will take part in the effective cluster state generation. The benefit of the method outlined here is that all other layers are in the state $|0\rangle$, which is important for the measurement stage discussed next.

In order to perform the measurements, the expansion of the x-y plane is taken into account such that a single two-qubit pair can be addressed individually in a top-down fashion by a tightly focused laser beam with a Gaussian profile, as schematically shown in Fig. 7.4 **(c)** [4]. This laser is tuned to a hyperfine transition $|h_1\rangle \rightarrow |h_2\rangle$ and applied for a pulse-time τ_p (see Fig. 7.4 **(d)**). The state $|h_2\rangle$ is taken to have a large spontaneous-emission rate A_{h_2} such that, within the time τ_p, many cycles of absorption-emission will occur (i.e. $A_{h_2}^{-1} \ll \tau_p$). Let $N_{|h_1\rangle}$ be the number of photons emitted by a single atom during τ_p when it is in the state $|h_1\rangle$ and η' be the ratio of the number of detected photons to emitted photons, due to non-ideal quantum efficiency of the detectors that collect the scattered photons.

[4] Position dependent energy shifts from focused lasers and an addressing microwave laser is also an option [242].

Pair $1'$	Pair $2'$	Logical	U_Σ
$\|00\rangle_{12}$	$\frac{1}{\sqrt{2}}[(\mu-\nu)\|01\rangle-(\mu+\nu)\|10\rangle]_{34}$	$\sigma_x H\|\psi\rangle$	σ_x
$\|01\rangle_{12}$	$-\frac{1}{\sqrt{2}}[(\mu+\nu)\|01\rangle-(\mu-\nu)\|10\rangle]_{34}$	$H\|\psi\rangle$	$\mathbb{1}$
$\|10\rangle_{12}$	$\frac{1}{\sqrt{2}}[(\mu+\nu)\|01\rangle-(\mu-\nu)\|10\rangle]_{34}$	$H\|\psi\rangle$	$\mathbb{1}$
$\|11\rangle_{12}$	$-\frac{1}{\sqrt{2}}[(\mu-\nu)\|01\rangle-(\mu+\nu)\|10\rangle]_{34}$	$\sigma_x H\|\psi\rangle$	σ_x

Table 7.1: Outcomes from a laser measurement of qubits 1 and 2 in Fig. 7.1 **(b)**.

Starting with the atom in the state $|\psi\rangle = \mu|h_0\rangle + \nu|h_1\rangle$, if one or more photons are detected, the state of the atom is inferred to be $|h_1\rangle$. On the other hand if no photons are detected, the state of the atom is $|\mu|^2|h_0\rangle\langle h_0| + |\nu|^2 P_0^d |h_1\rangle\langle h_1|$, where $e^{-(1+\eta'/2)\eta' N_{|h_1\rangle}} \leq P_0^d \leq (1+2\eta'/3)e^{-\eta' N_{|h_1\rangle}}$ [245]. Taking $|h_2\rangle$ from the $\mathrm{P}_{3/2}$ fine manifold with $A_{h_2}^{-1} = 2.62 \times 10^{-8}$ [246] and a pulse time $\tau_p = 2.62 \times 10^{-6}$, with $\eta' = 0.89$ [247], we can effectively set $P_0^d = 0$.

Consider the measurement laser addressing the two atoms embodying qubits 1 and 2 (effective qubit $1'$) as shown in Fig. 7.1 **(b)** in the top-down fashion described above. Before the laser is applied, an encoded state $|\psi\rangle = \mu|0\rangle + \nu|1\rangle$ is taken as being prepared on the first effective qubit and a pair of tightly focused lasers L_1 and L_2 with Gaussian profiles address the lattice along the x and y axes respectively between the top two layers. This causes the states of qubits 1 and 2 to be subject to the Hadamard gate H via a Raman transition. More formally, the operation $\mathsf{H}_1 \otimes \mathsf{H}_2 \otimes \mathbb{1}_3 \otimes \mathbb{1}_4$ is applied to the qubits. This produces the state

$$\begin{aligned} |\phi\rangle_{1'2'} = (&\mu|+\rangle|-\rangle|01\rangle - \mu|+\rangle|-\rangle|10\rangle \\ &- \nu|-\rangle|+\rangle|01\rangle - \nu|-\rangle|+\rangle|10\rangle)_{1234}. \end{aligned} \tag{7.20}$$

The measurement laser is then applied to qubits 1 and 2 projecting the atomic states into the σ_z eigenbasis via the fluorescence technique described above. Together with the Hadamard rotations, this carries out a σ_x projective measurement. A degeneracy in the outcomes exists because both the states $|01\rangle$ and $|10\rangle$ will produce the same statistics of detected photons. However as it can be seen in Table 7.1, they apply the same rotations to the logical state upon propagation across to effective qubit $2'$. The byproduct operator U_Σ which is used to cancel the probabilistic nature of state transfer in one-way QC can therefore be found from a photon-number-resolving detector [247].

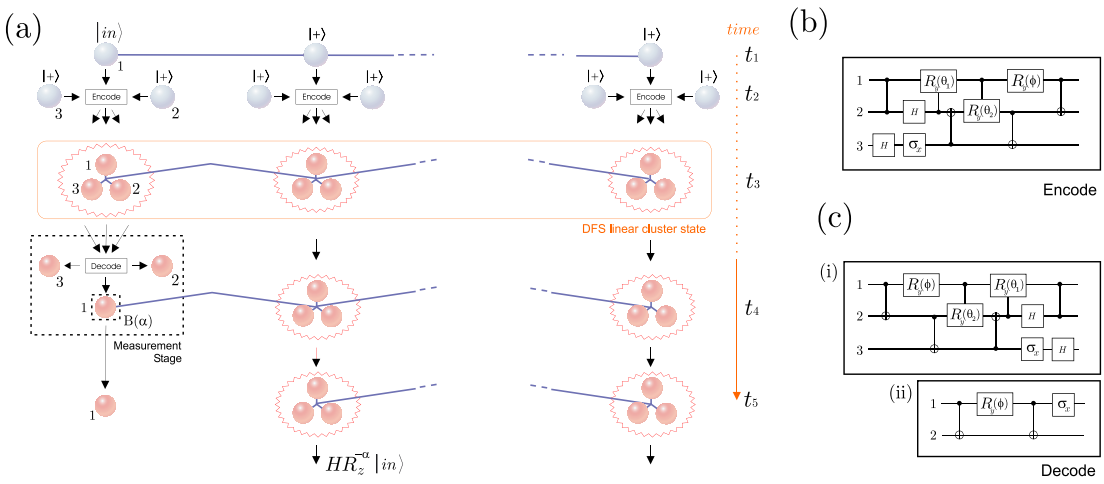

Figure 7.5: DFS linear cluster state protected from all system-environment coupling terms of the form given in Eq. (7.5). **(a)**: Sequence of operations for transferring an arbitrary qubit input state $|in\rangle$. First, the standard cluster state is prepared, then the qubits are encoded (see **(b)**). The only time at which the cluster state is not protected is when the measurements are performed. However, if the measurement stages (which include the decoding stage **(c)**) are carried out in negligible time (with respect to the rate of decoherence), then the remaining cluster after each measurement is never exposed to the environment. **(b):** Encoding Stage, where $\phi = 3\pi/4$, $\theta_1 = -\cos^{-1}(\sqrt{2/3})$ and $\theta_2 = -\pi/4$. **(c):** Decoding Stage, where $\phi = -3\pi/4$, $\theta_1 = \cos^{-1}(\sqrt{2/3})$ and $\theta_2 = \pi/4$. In (i), output qubit 3 is measured in the $\{|0\rangle, |1\rangle\}$ basis and if $|0\rangle_3$ is obtained, then the circuit (ii) must be performed. Qubits 2 and 3 can be discarded after the decoding stage.

In order to carry out an arbitrary measurement along the equatorial plane of the Bloch sphere, one must implement an additional Raman transition prior to the Hadamard rotations. This transition uses a tightly focused laser beam L_1 in a top-down fashion along the z axes addressing qubits 1 and 2 and all the qubits below them in that column. This laser together with a paired laser field L_2, which has intensity maxima on every odd layer, rotates qubit 1 and all qubits below it on odd layers by R_z^α. However, qubits on odd layers below qubit 1 are unaffected as they are in the state $|0\rangle$. Alternative methods for the above processes could be given by an interference approach [240] or microwave addressing [242].

7.1.4 Full protection

So far, only phase damping errors have been considered in the DFS scheme. However it is possible to extend the approach to the construction of a DFS offering protection from all types of environmental error resulting from the terms in Eq. (7.5). In Fig. 7.5 a sketch of the steps for the achievement of full protection is given. The scheme is inspired by recent work [248–251]. The encoding is given by $\{|0_E\rangle_{1'} := (1/\sqrt{2})(|10\rangle - |01\rangle)_{12}\,|0\rangle_3\,, |1_E\rangle_{1'} := (2/\sqrt{6})\,|0\rangle_1\,(|10\rangle - |01\rangle)_{23} + (1/\sqrt{6})(|10\rangle - |01\rangle)_{12}\,|0\rangle_3\}$, where now three entangled physical qubits (instead of two) embody a single effective cluster qubit. An important difference here with respect to the phase damping DFS is that now encoding (see Fig. 7.5 **(b)**) and decoding stages (see Fig. 7.5 **(c)**) are essential for providing the protection and recovery of the cluster state.

7.2 The $QC_{\mathcal{C}}$ model using decoherence-free subspaces: Experiment

In this Section, the first experimental demonstration of a one-way quantum processor that can reliably operate in the presence of environment-induced decoherence is described. The fragile quantum information being processed is protected by a specially designed DFS in which a cluster state resource resides (as introduced in Section 7.1). An all-optical setup has been used and the information was encoded into the entangled polarisation states of four photons. A one-way information transfer protocol was performed while the photons were exposed to severe environmental symmetric phase noise. Remarkable protection of the information is accomplished, delivering outcomes extremely close to the ideal ones.

7.2.1 Introduction

Experimentally, DFS's have been tested previously in setups of linear optics [252–254], trapped ions [234–236] and nuclear magnetic resonance [249, 255] (NMR). Here, in contrast to most of these earlier implementations (which focused on the generation and verification of a DFS), and in line with the work of Refs. [252, 255], DFS states are utilised in a scheme to successfully process quantum information in a controlled all-optical system explicitly subject to noise.

Despite the existence of a threshold for fault-tolerance [137, 138, 140] and its quantitative estimate for the case of linear optics implementations [219, 220], there has so far been no experimental realisation of noise-resilient MB QIP. This constitutes a vital step toward the upgrading of the model as a viable route for scalable QC. In this Section, such an important step is performed by designing and experimentally demonstrating the encoding of a four-qubit photonic entangled resource into a DFS cluster state. It is shown that the combination of MB QIP and passive protection from noise is effective in manipulating information, shielded from the action of an undesired symmetric phase-damping mechanism [128]. The model, which is complementary to the proposed use of QEC in a one-way scenario [219–226], has the potential to be scaled to larger cluster states, as shown in Section 7.1. In the successful experimental demonstration described here, an encoded version of the key building block on which the one-way model is built is carried out - *i.e.* genuine teleportation [55, 130] in the form of a one-way information transfer protocol - across a photonic cluster state protected from multi-qubit symmetric phase damping noise. The experimental linear optics realisation employed in order to verify the theoretical predictions of Section 7.1 demonstrates processing outcomes strikingly close to the ideal situation where decoherence is not present. Linear optics is at the forefront of experimental implementations of the one-way model, therefore representing the most appropriate and accessible test-bed for the DFS one-way model. The inherent manipulability of a linear optics setup guarantees the successful controlled engineering of the decoherence mechanism that needs to be tested.

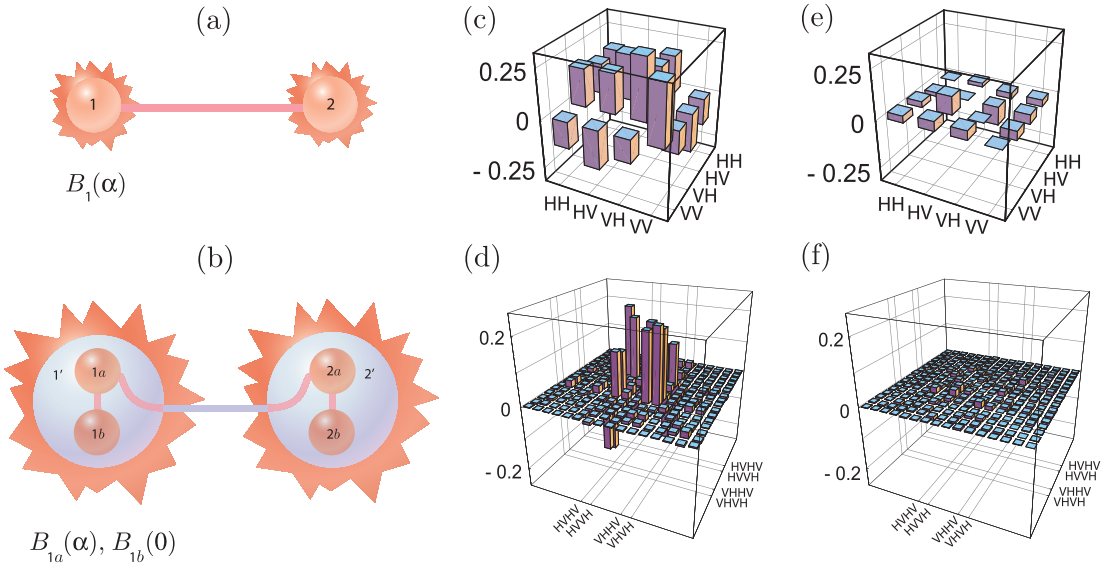

Figure 7.6: Cluster state configurations and photonic tomographic plots: In **(a)**, a two-qubit standard cluster state is shown, while in **(b)** the DFS-encoded cluster state is depicted. Each effective qubit (blue sphere) is represented by two physical qubits prepared in $|\psi^-\rangle$. Since $|\psi^-\rangle$ is locally equivalent to a standard 2-qubit cluster state (the local rotations being $\mathbb{1}_1 \otimes (\sigma_x\sigma_z H)_2$), the pairwise entanglement operations that build up larger clusters commute with each other (as discussed in Section 7.1). Therefore, an arbitrary sized DFS-encoded cluster state can be created [55, 130]. **(c)** & **(e):** Tomographic plots showing the real (**(c)**) and imaginary (**(e)**) parts of the experimentally produced density matrices corresponding to a 2-qubit standard cluster state. **(d)** & **(f):** Tomographic plots showing the real (**(d)**) and imaginary (**(f)**) parts of the experimentally produced density matrices corresponding to a 4-qubit DFS encoded cluster state.

7.2.2 Experimental Implementation

The DFS protocol experimentally demonstrated - quantum information transfer - has the setup shown in Fig. 7.6 **(b)** and can be understood as follows: A logical qubit $|Q_{in}\rangle = \mu|0\rangle + \nu|1\rangle$ (with $|\mu|^2 + |\nu|^2 = 1$) is encoded on the effective qubit $1'$ embodied by the physical qubits $1a$ and $1b$. After the entangled resource is prepared, the effective qubits $1'$ and $2'$ are in the DFS-encoded state $|\Phi_{DFS}\rangle = \mu|0_E, +_E\rangle_{1'2'} + \nu|1_E, -_E\rangle_{1'2'}$ (see Eq. (7.6) in Section 7.1). Information is then transferred across the encoded cluster by measuring the state of the qubits in the bases $B_{1a}(\alpha)$ and $B_{1b}(0)$, where α determines the rotation $\mathsf{H}R_z^{-\alpha}$ on $|Q_{in}\rangle$. This can be compared to the case of a standard cluster being used, as shown in

Fig. 7.6 **(a)**, where $B_1(\alpha)$ is used.

To test the DFS protection, phase damping noise is applied to the physical qubits (*i.e.* photons) during information transfer in both the standard and DFS-encoded cases. For the DFS-encoded cluster, symmetric noise is applied to qubit pairs $1' = (1a, 1b)$ and $2' = (2a, 2b)$, while for the standard cluster, noise is applied to qubits 1 and 2. For phase damping acting on a single qubit, the non-zero Kraus operators are given by $\hat{K}_1 = (1/\sqrt{2})(1 + e^{-\Gamma t})^{1/2}\mathbb{1}$ and $\hat{K}_2 = (1/\sqrt{2})(1 - e^{-\Gamma t})^{1/2}\sigma_z$ with Γ the strength of the system-environment coupling and t the corresponding interaction time (see Chapter 2). In the experiment, symmetric phase damping noise is simulated for the worst case scenario, *i.e.* for the limit $\Gamma t \to \infty$. This corresponds to $\hat{K}_1 = (1/\sqrt{2})\mathbb{1}$ and $\hat{K}_2 = (1/\sqrt{2})\sigma_z$ which completely destroy the coherences in a single-qubit state. In the DFS-encoded case, the action of symmetric noise on the state of the entire system $\rho_{\rm DFS} = |\Phi_{\rm DFS}\rangle\langle\Phi_{\rm DFS}|$ is described by the output state

$$\begin{aligned}\mathcal{E}(\rho_{\rm DFS}) &= \frac{1}{4}[\rho_{\rm DFS} + \sigma_z^{1a}\otimes\sigma_z^{1b}\otimes\mathbb{1}^{2a,2b}\rho_{\rm DFS}\sigma_z^{1a}\otimes\sigma_z^{1b}\otimes\mathbb{1}^{2a,2b} \\ &\quad +\mathbb{1}^{1a,1b}\otimes\sigma_z^{2a}\otimes\sigma_z^{2b}\rho_{\rm DFS}\mathbb{1}^{1a,1b}\otimes\sigma_z^{2a}\otimes\sigma_z^{2b} \\ &\quad +\sigma_z^{1a}\otimes\sigma_z^{1b}\otimes\sigma_z^{2a}\otimes\sigma_z^{2b}\rho_{\rm DFS}\sigma_z^{1a}\otimes\sigma_z^{1b}\otimes\sigma_z^{2a}\otimes\sigma_z^{2b}], \quad (7.21)\end{aligned}$$

and in the standard cluster state scenario, for the density matrix $\rho_C = |\Phi_C\rangle\langle\Phi_C|$ of a two-qubit cluster $|\Phi_C\rangle = (1/\sqrt{2})(|0,+\rangle + |1,-\rangle)_{12}$, by

$$\mathcal{E}(\rho_C) = \frac{1}{4}[\rho_C + \sigma_z^1\otimes\mathbb{1}^2\rho_C\sigma_z^1\otimes\mathbb{1}^2 + \mathbb{1}^1\otimes\sigma_z^2\rho_C\mathbb{1}^1\otimes\sigma_z^2 + \sigma_z^1\otimes\sigma_z^2\rho_C\sigma_z^1\otimes\sigma_z^2]. \quad (7.22)$$

A logical state $|Q_{in}\rangle$ encoded into ρ_C and transferred across the cluster under the action of the channel described by $\mathcal{E}(\rho_C)$ in Eq. (7.22) will result in the maximally mixed output state $(1/2)\mathbb{1}$. On the other hand, $\mathcal{E}(\rho_{DFS})$ in Eq. (7.21) will perfectly preserve the coherences during the transfer of the state $|Q_{in}\rangle$ encoded into $\rho_{\rm DFS}$. An experimental determination of the *logical* transfer channels $\mathcal{E}_{\rm L}(\rho_{in})$ is required during exposure of the qubits to noise, where $\rho_{in} = |Q_{in}\rangle\langle Q_{in}|$. To achieve this task, the QPT technique discussed in Section 7.1 is used. In order to understand the way the protocol has been implemented, it should be stressed that the experimental reconstruction of the effect of $\mathcal{E}_{\rm L}$

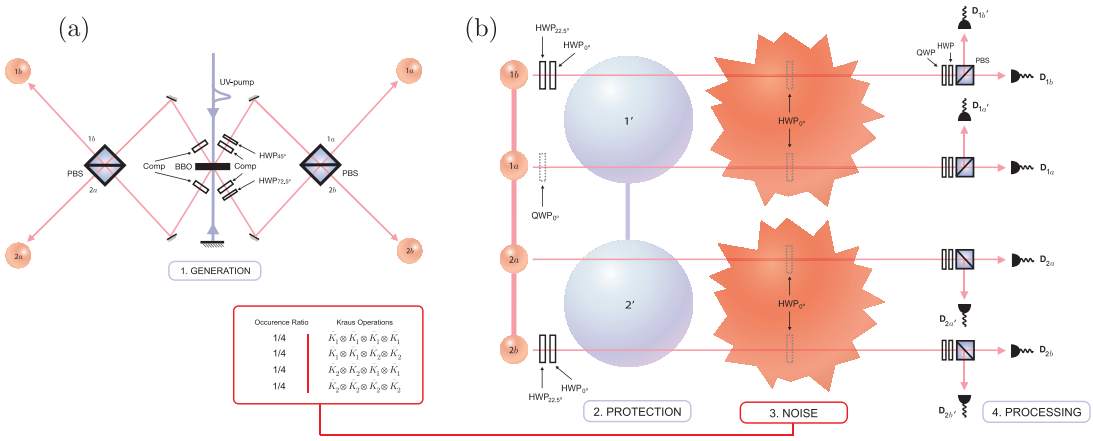

Figure 7.7: Experimental scheme: The optical *generation* stage is shown in **(a)**, while **(b)** depicts the *protection* and *processing* steps that create and manipulate the protected DFS cluster state and also the *noise* stage. A femto-second laser pulse with 1 W of cw-power pumps a non-linear crystal (BBO) in a double-pass configuration. Compensation of walk-off effects in the crystal leads to the emission of highly entangled Bell states ($|\Phi^-\rangle$ and $|\Phi^+\rangle$ in the forward and backward direction, respectively, as discussed in Chapter 4). Coherent combination of these states on polarizing beam-splitters (PBS) and postselection yields the generation of a cluster state with a rate of approximately 1Hz in output modes $1a$, $1b$, $2a$ and $2b$. To effectively rotate this cluster into a DFS, the single-qubit rotations $\sigma_x\sigma_z$ on qubits $1b$ and $2b$ are realised with half-wave plates (HWP) and the logical state $|L\rangle$ can be encoded with an additional quarter-wave plate (QWP) in mode $1a$. Phase damping is implemented using the occurrence of σ_z operations, *i.e.* by inserting HWPs at 0° between the *protection* and *processing* stages. Polarisation measurements are performed using analyzers consisting of a PBS, preceded by a HWP and QWP.

on the set of logical input states (the *probe states*) $\{|0\rangle, |1\rangle, |+\rangle, |L\rangle\}$ is enough for a full characterisation of the physical process encompassed by such a logical channel [257, 258]. For this reason, the DFS protocol has been experimentally implemented by encoding the probe states onto photons 1a and 1b of the 4-photon DFS cluster. To perform the DFS one-way protocol, a photonic linear cluster state $|\Phi_{lin}\rangle$ of the form reported in [71, 76, 77] and given in Eq. (4.2) of Chapter 4 is created post-selectively by using the setup illustrated in Fig. 7.7 **(a)**. This technique has now established itself as a standard tool for the efficient generation of four-photon clusters, and ensures that photon loss and photo-detector inefficiency do not affect the experimental results. The cluster

state $|\Phi_{lin}\rangle$ is rotated into a DFS-encoded cluster of the form

$$\begin{aligned} |\Phi_{DFS}\rangle &= \frac{1}{2}(|0\rangle_{1a}|1\rangle_{1b}|0\rangle_{2a}|1\rangle_{2b} - |0\rangle_{1a}|1\rangle_{1b}|1\rangle_{2a}|0\rangle_{2b} \\ &\quad -|1\rangle_{1a}|0\rangle_{1b}|0\rangle_{2a}|1\rangle_{2b} - |1\rangle_{1a}|0\rangle_{1b}|1\rangle_{2a}|0\rangle_{2b}) \end{aligned} \tag{7.23}$$

by applying the single-qubit rotations $\sigma_x\sigma_z$ to qubits $1b$ and $2b$ (the subscripts label the photon modes), as shown in Fig. 7.7 **(b)**. Here, $\{|0\rangle, |1\rangle\}$ is experimentally embodied by the horizontal and vertical polarisation states of a photon respectively (as in Chapter 4). The DFS state creation is verified by performing an over-complete state tomography [166]. This allows a reconstruction of the density matrix of the DFS-encoded cluster using a maximum-likelihood technique performed by taking a set of 1296 local measurements, using 81 detection settings [71, 76], each implemented within a time window of 350 seconds. All combinations of polarisation projections on the individual qubits are used, *i.e.* $\{|0\rangle, |1\rangle; |+\rangle, |-\rangle; |R\rangle, |L\rangle\}$. The experimentally obtained density matrix ρ has state fidelity $F_{DFS} = \langle\Phi_{DFS}|\rho|\Phi_{DFS}\rangle = (0.70 \pm 0.01)$ with the ideal DFS-cluster. Tomographic plots of both the standard two-qubit cluster state $|\Phi_C\rangle$ (generated out of the four-photon resource) and DFS generated resources are given in Fig. 7.6 **(c)** & **(e)** and **(d)** & **(f)** respectively, where $F_C = \langle\Phi_C|\rho|\Phi_C\rangle = (0.74 \pm 0.02)$. The uncertainty of the state fidelities F_C and F_{DFS} have been estimated by performing a 100 run Monte Carlo simulation of the state tomography analysis, with Poissonian noise added to the count statistics in each run.

By measuring photon $1b$ in $|1\rangle$, the probe state $|0\rangle$ is encoded on the effective qubit $1'$. Then measuring photon $1a$ in $|+\rangle$ transfers the logical state across the cluster to effective qubit $2'$ (embodied by photons $2a$ and $2b$). Analogously the other probe states are encoded and transferred by the measurement patterns $B_{1a}(0), |0\rangle_{1b}$ for $|1\rangle$, $B_{1a}(0), B_{1b}(0)$ for $|+\rangle$ and $B_{1a}(0), B_{1b}(0)$ for $|L\rangle$. Note that for the logical $|L\rangle$ input, a quarter-wave plate (QWP) at 0° has been placed in mode $1a$, effectively realizing the rotation $R_z^{\pi/2}$. For each of these input states, an over-complete two-qubit state tomography is performed [166] for the output qubits $2a$ and $2b$. This is then repeated with phase damping noise added to the system, *i.e.* by applying half-wave plates (HWP's) at 0° (σ_z operation) to the photons, with the occurrence ratio of the specific noise for each term appearing in $\mathcal{E}(\rho_{DFS})$ implemented during the tomographic process. This full realisation

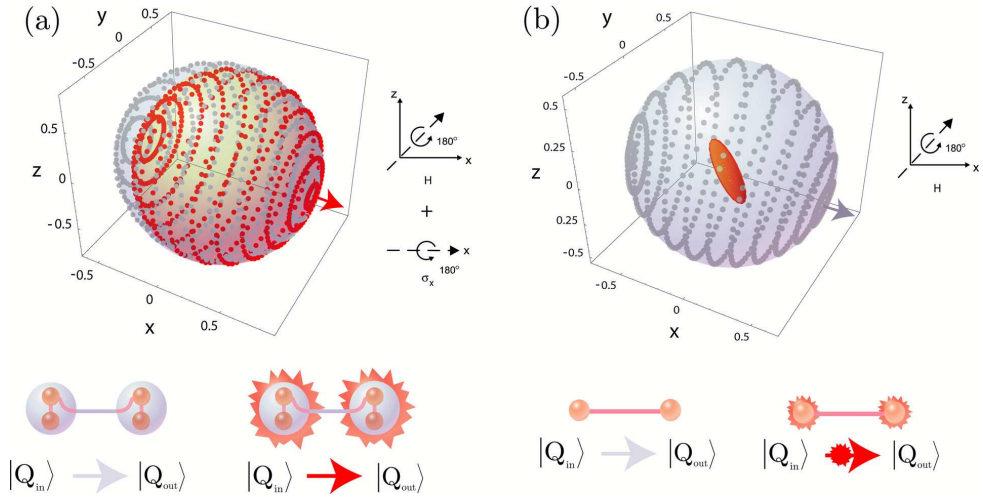

Figure 7.8: Quantum process tomographic plots of the information channel: In **(a)** (**(b)**) the QPT-reconstructed Bloch spheres are shown, corresponding to the use of a DFS-encoded (standard) cluster state. Underneath shows the information transfer protocol experimentally realised for measurement outcomes $|+\rangle_{1a}\,|+\rangle_{1b}$ ($|+\rangle_1$). The light-blue sphere shows the case of no noise being applied to the system, while the inner red one is for an environment-exposed channel. While the comparison in **(a)** reveals striking protection of the processed quantum information (the average state fidelity is larger than 99%), **(b)** shows that in a non-protected scenario the information is almost completely lost, as discussed in the main text. The shape of the inner spheroid in **(a)** is due to the existence of relatively small coherences in the corresponding reconstructed density matrix. This stems from quantum noise affecting the encoding of the probe state $|L\rangle$ and leads to non-zero x and y components of the Bloch vectors. It can be checked that by using a better encoding of $|L\rangle$, the evident distortion of the inner spheroid for negative values of x is reduced. A better quality cluster state would therefore help in obtaining an increased overlap of the two experimental Bloch spheres. The orientation of the pole of the Bloch sphere corresponding to the $|0\rangle$ logical input state, shown by an arrow in **(a)** (**(b)**), is in agreement with the expected transformation $\sigma_x\mathsf{H}$ (H) being applied during the computation of the protocol (see insets). The dots represent output states corresponding to the action of the channel on pure input states $|Q_{in}\rangle$ for various choices of μ.

of complete symmetric phase-damping noise is in striking contrast with simpler phase-flip mechanisms frequently adopted in previous experimental characterisations of photonic DFS's. From this set of data for the probe states (1728 measurements in total), a reconstruction of the complete effect of the transfer channel $\mathcal{E}_{\mathrm{L}}$ on an arbitrary logical input state is possible using the derived logical Kraus operators for the channel from QPT. The action of $\mathcal{E}_{\mathrm{L}}$ can then

be visualised by considering the correspondence between a single-qubit density matrix and its Bloch vector. Taking $|Q_{in}\rangle$ from a large set of values for μ and representing their output states from the QPT-reconstructed transfer channel in a three-dimensional space, allows a depiction of the deformation of the single-qubit Bloch sphere induced by the experimental logical channel. The results of this visualisation process are shown in Fig. 7.8 **(a)** for the case of a DFS-encoded channel with and without noise. The protection from phase damping effects is striking: the Bloch sphere for the noise-affected DFS-encoded state is almost identical to the case without phase-damping noise. An informative way to quantify the closeness of two experimental channels is to consider the output state fidelity averaged over μ. An average state fidelity of 0.991 ± 0.003 is found. In addition, the process fidelity $F(\chi_1, \chi_2) = \mathrm{Tr}(\sqrt{\sqrt{\chi_1}\chi_2\sqrt{\chi_1}})^2$ [259], between the DFS transfer channel matrices $\chi^{DFS}_{\mathrm{noise}}$ and $\chi^{DFS}_{\mathrm{no-noise}}$ corresponding to with and without noise respectively is found to be 0.95 ± 0.02. The uncertainties in the above results were estimated by performing a 50 run Monte Carlo simulation of the QPT analysis, with Poissonian noise added to the count statistics in each run.

The benefit of the DFS-protocol should of course be evaluated with respect to the standard case. Therefore, an experiment has been performed where a two-qubit cluster state is used for the information transfer protocol. Here, the input state is transferred across the cluster with and without phase-damping noise being applied as before. The measurement patterns chosen are $B_{1a}(0), |0\rangle_{1b}, |+\rangle_{2a}$ for the probe state $|0\rangle$, $B_{1a}(0), |1\rangle_{1b}, |+\rangle_{2a}$ for $|1\rangle$, $|+\rangle_{1a}, B_{1b}(0), |+\rangle_{2b}$ for $|+\rangle$ and $|+\rangle_{1a}, B_{1b}(0), |+\rangle_{2b}$ for $|L\rangle$, with an additional HWP as in the DFS case. This time, the single-qubit operations $\sigma_x\sigma_z$ that rotate the cluster into the DFS are not present. The output state - that is the remaining photon - is analyzed using single-qubit state tomography while the channels with and without noise being applied are analysed using QPT. The resulting deformation of the Bloch sphere is shown in Fig. 7.8 **(b)**. By comparison with Fig. 7.8 **(a)**, it is evident that the standard noise-free channel is very close to the analogous DFS-encoded situation. However, one can now see that if the information is not shielded by a DFS encoding, the induced environment is affecting the quantum information in a severe way. The output states in the presence of noise suffer strong decoherence effects, resulting in a significant shrinking of the Bloch sphere and an almost

complete loss of coherence. This is even more evident by closely analysing the output density matrix resulting from an input state $|Q_{in}\rangle$, whose average state fidelity with the maximally mixed state $(1/2)\mathbb{1}$ (resulting from an ideal full phase-damping process) is 0.994 ± 0.002. Clearly, the information initially encoded in the standard cluster resource has almost entirely been 'washed away' by the noise.

7.3 Remarks

In this Chapter the design, analysis and experimental demonstration of a strategy to protect MB QIP from symmetric, multi-qubit phase-damping noise was provided. In Section 7.1, a possible optical lattice setup was proposed as an example to show how the scheme could be achieved in a physically realisable setting. Then in Section 7.2, the effectiveness of the DFS one-way model was established in a proof-of-principle experiment conducted in a linear optics setting. Excellent shielding of information processed in a genuine quantum mechanical way was found. The successful experimental verification and the setup-independent nature of this DFS protection for the $\mathrm{QC}_{\mathcal{C}}$ model guarantee its applicability to any physical situation where symmetric phase-damping noise is a dominant source of error. Conceptually, the model also holds the promise of a generalisation to any form of symmetric noise. In Section 7.1 it was shown that by encoding an effective qubit into the state of three physical ones, protection from general multi-qubit noise is possible [248–251]. The associated resource overheads could be bypassed by using additional degrees of freedom within the same physical information carrier or hyper-entangled states [78, 80, 262–264]. An extension to more general forms of environment will require the integration of DFS's with other tools for environmental protection [260, 261]. This is most certainly a stimulating challenge.

Chapter 8

Conclusion

In this Thesis, measurement-based (MB) quantum information processing (QIP) in the presence of operational imperfections was investigated. The imperfections studied were in the context of intrinsic systematic noise, natural limitations in the structure of the quantum resources and environment-induced decoherence. The main task of the work presented here was to identify whether useful and reliable protocols could be performed using this newly introduced model for QIP under realistic experimental conditions.

It was shown that uncontrollable randomness in the qubit-qubit interactions which generate the cluster state resources, reduces the performance of both communication and computational protocols using MB QIP. A direct consequence of this analysis is that in the processing of information encoded in a cluster state, both the number of qubits involved and the measurements to be performed must be carefully managed. This has led to the important observation that by properly designing the cluster state resource using elementary basic building blocks and concatenation, it is possible to minimise the number of redundant qubits for various key circuit simulations. Thus an economical strategy was found for reducing the effects of intrinsic imperfections in the cluster state generation stage on the performance of given protocols. Using this strategy, an experimentally realisable four-qubit CNOT gate was then proposed. This study, along with several others [71, 132, 133], has paved the way towards the search for gate simulations and protocols performed using only small clusters of just a few qubits.

The design, demonstration and characterisation of the performance of the first experimental realisation of Deutsch's algorithm on a cluster state was also provided and discussed. The experiment is one of the few quantum algorithms entirely implemented utilising the MB model [71, 76, 77, 80]. The agreement between the experimental data and theory was found to be excellent and only limited by the overall quality of the entangled resource in the experiment. In addition, an implementation of the quantum Prisoners' Dilemma was proposed using an economical and experimentally realisable cluster state configuration. At the same time, it was shown that the MB model can be easily complemented by simple rotations of the logical output qubits to add freedom to gate simulations, building a hybrid model that has subsequently been realised with existing all-optical technology [81]. This has allowed for an immediate experimental in-

vestigation of the fascinating role entanglement plays in the search for a Pareto optimal Nash equilibrium point in a system exhibiting true multiparticle quantum correlations.

It was also shown that MB QIP can be performed on a three-body type entangled resource. Using concatenation methods, an economical Toffoli gate simulation was constructed, which is known to be fundamental to compact algorithm realisations and therefore robust-to-noise QIP. The feasibility of an optical lattice-based implementation of the model was analysed in detail. It was suggested that the theoretical model could be adapted to the case of more sophisticated types of multi-qubit interactions permitted within the physical setup [179, 184, 185]. If the proposed model is developed along these lines using techniques from recent work by other researchers [135, 265], the study could be considerably advantageous for the standard MB one-way model with regards to realising compact and economical algorithm simulations.

An extension of the MB one-way model to d-dimensional systems (qudits) was also investigated. This was achieved by providing an analysis of entanglement properties, information transfer and gate simulation when specific types of environmental noise affect individual qudits in the cluster state resource. The extension to higher-dimensional elements, performed so far without reasonable justification, appears not to provide any significant advantages with respect to the *standard* two-level system (qubit) MB model when global properties of the entanglement resource are used in order to quantify the performances of a given quantum computation (QC) protocol. This study has also revealed the previously overlooked superiority of a resource built out of pairs of entangled two-level systems with respect to many-level elementary systems. By raising the question of the quantification of advantages in d-dimensional MB QIP, the analysis opens up a way toward further exploration of the model using more sophisticated methods, such as those recently used in Ref. [265] and other physically relevant decoherence models.

Finally, the design, analysis and experimental demonstration of a strategy to protect MB QIP from physically relevant symmetric multi-qubit phase-damping noise was provided. A possible optical lattice setup was proposed as an exam-

ple to show how the scheme could be achieved in a physically realisable setting. The effectiveness of the decoherence-free subspace (DFS) MB one-way model was then established in a proof-of-principle experiment conducted in a linear optical setup. Excellent shielding of information processed in a genuine quantum mechanical way was found. The successful experimental verification and the setup-independent nature of the DFS protection for the MB one-way model guarantee its applicability to any physical situation where symmetric phase-damping noise is a dominant source of error. Conceptually, the model also holds the promise of a minimal resource generalisation to any form of symmetric noise: it was shown that by encoding an effective qubit into the state of three physical ones, protection from general multi-qubit noise is possible, using techniques inspired by the work in Refs. [248–251]. However, extending this model to more general forms of environment will require the integration of DFS's with other tools for environmental protection [260, 261]. This is a stimulating challenge for the future.

MB QIP is an exciting new topic in the field of quantum information and has generated great interest from numerous research groups around the world. Theoreticians are proposing many novel and interesting ideas for implementations in various physical setups, such as semiconducting and superconducting charge/flux settings [65], continuous variables [66], cavity quantum electrodynamical setups [67], nitrogen-vacancy centers in diamond [68], electron spins in quantum dots [68, 69] and many more. Experimentalists are beginning to implement MB QIP with remarkable success, most notably work on the realisation of algorithms in linear optics setups [71, 76, 77, 80, 81]. These experiments have shown that minimal resource MB QIP can be efficiently and reliably achieved. The work presented in this Thesis has contributed to these demonstrations and to the identification of useful and reliable protocols that can be performed using MB QIP under realistic experimental conditions. Despite the great initial success in linear optical setups and theoretical work on its scalability [266–269], it remains to be seen whether the model can be demonstrated in more suitable and scalable settings such as optical lattices [70]. Many experimental setups like optical lattices are only able to achieve a limited set of the prerequisites needed to carry out MB QIP. They also suffer from the many sources of noise described and analysed in this Thesis. It is therefore clear that pragmatic studies such as those

carried out here must continue. This will enable researchers to make significant advances in closing the gap between what is possible in theory and what can realistically be implemented in the laboratory.

Bibliography

[1] A. L. Schawlow and C. H. Townes *Phys. Rev.* **112**, 1940 (1958).

[2] L. S. Brown and G. Gabrielse, *Rev. Mod. Phys.* **58**, 233 (1986).

[3] S. Chu, *Rev. Mod. Phys.* **70**, 685 (1998).

[4] W. D. Phillips, *Rev. Mod. Phys.* **70**, 707 (1998).

[5] C. N. Cohen-Tannoudji, *Rev. Mod. Phys.* **70**, 707 (1998).

[6] C. E. Wieman, D. E. Pritchard and D. J. Wineland, *Rev. Mod. Phys.* **71**, 253 (1999).

[7] H. J. Metcalf and P. van der Straten, *Laser Cooling and Trapping*, (Springer, Berlin, 2001).

[8] W. Ketterle, *Rev. Mod. Phys.* **74**, 1131 (2002).

[9] M. A. Kastner, *Rev. Mod. Phys.* **64**, 849 (1992).

[10] Y. Makhlin, G. Schön and A. Shnirman, *Rev. Mod. Phys.* **73**, 357 (2001).

[11] A. Zeilinger, G. Weihs, T. Jennewien and M. Aspelmeyer, *Nature* **433**, 230 (2005).

[12] T. H. Cormen, C. E. Leiserson and R. L. Rivest, *Introduction to Algorithms*, (MIT Press, Cambridge, MA, 1990).

[13] G. E. Moore, *Electronics*, April **19** (1965).

[14] Press release available at: ⟨*http://domino.research.ibm.com/comm/pr.nsf/pages/news.20060220_nemorelease.html*⟩ (2006).

[15] Press release available at: ⟨*http://domino.research.ibm.com/comm/pr.nsf/pages/news.20070412_3dchip.html*⟩ (2007).

[16] P. A. Benioff, *J. Stat. Phys.* **22**, 563 (1980).

[17] P. A. Benioff, *Int. J. Theor. Phys* **21**, 177 (1982).

[18] P. A. Benioff, *Phys. Rev. Lett.* **48**, 1581 (1982).

[19] R. P. Feynman, *Int. J. Theor. Phys.* **21** 467 (1982).

[20] A. Church, *Am. J. Math.* **58**, 345 (1936).

[21] A. M. Turing, *Proc. Lond. Math. Soc.* **2**, 42, 230-265 (1936).

[22] S. C. Kleene, *Mathematical Logic* (Wiley, New York, 1967) p232.

[23] D. Deutsch, *Proc. Roy. Soc. Lond.* **A 400**, 97 (1985).

[24] P. Shor, *SIAM J. Comput.* **26**, 1484 (1997).

[25] L. K. Grover, *Phys. Rev. Lett.* **79**, 325 (1997).

[26] S. Wiesner, *SIGNAT News* **15** 1 78 (1983).

[27] C. H. Bennett and G. Brassard, *Proceedings of IEEE International Conference on Computers, System and Signal Processing* **175**, (December, 1984).

[28] G. S. Vernam, *U. S. Patent 1310719* (1919).

[29] C. E. Shannon, *Bell System Tech.* 28 657 (1949).

[30] N. Gisin, G. Ribordy, W. Tittel and H. Zbinden, *Rev. Mod. Phys.* **74**, 145 (2002).

[31] A. Ekert, *Phys. Rev. Lett.* **67**, 661 (1991).

[32] M. Hillery, V. Bužek and A. Berthiaume *Phys. Rev. A* **59**, 1829 (1999).

[33] H. Buhrman, R. Cleve, J. Watrous and R. de Wolf, *Phys. Rev. Lett.* **87**, 167902 (2001).

[34] Quantum Computing Roadmap Overview, Quantum Information Science and Technology Roadmap Project, Quantum Information Science Technology Experts Panel, Los Alamos National Lab, available at: ⟨*http://qist.lanl.gov*⟩ (2004).

[35] I. L. Chuang, L. M. K. Vandersypen, X. Zhou, D. W. Leung and S. Lloyd, *Nature* **393**, 143 (1998).

[36] J. Jones and M. Mosca, *J. Chem. Phys.* **109**, 1 (1998); J. Jones, M. Mosca and R. H. Hansen, *Nature* **393**, 344 (1998).

[37] L. M. K. Vandersypen, M. Steffen, G. Breyta, C. S. Yannoni, M. H. Sherwood and I. L. Chuang, *Nature* **414**, 883 (2001).

[38] S. L. Braunstein and P. van Loock, *Rev. Mod. Phys.* **77**, 513 (2005).

[39] P. Kok, W. J. Munro, K. Nemoto, T. C. Ralph, J. P. Dowling and G. J. Milburn, *Rev. Mod. Phys.* **79**, 135 (2007).

[40] P. G. Kwiat, K. Mattle, H. Weinfurter, A. Zeilinger, A. V. Sergienko and Y. Shih, *Phys. Rev. Lett.* **75**, 4337 (1995).

[41] A. G. White, D. F. V. James, P. H. Eberhard and P. G. Kwiat, *Phys. Rev. Lett.* **83**, 3103 (1999).

[42] P. G. Kwiat, E. Waks, A. G. White, I. Appelbaum and P. H. Eberhard, *Phys. Rev. A* **60**, R773 (1999).

[43] P. R. Tapster, J. G. Rarity and P. C. M. Owens, *Phys. Rev. Lett.* **73**, 1923 (1994).

[44] W. Tittel, J. Brendel, H. Zbinden and N. Gisin, *Phys. Rev. Lett.* **81**, 3563 (1998).

[45] G. Weihs, T. Jennewein, C. Simon, H. Weinfurter and A. Zeilinger, *Phys. Rev. Lett.* **81**, 5039 (1998).

[46] D. Stucki, N. Gisin, O. Guinnard, G. Ribordy and H. Zbinden, *New. J. Phys.* **4**, 41 (2002).

[47] H. Kosaka, A. Tomita, Y. Nambu, T. Kimura and K. Nakamura, *Electron. Lett.* **39**, 16, 1199 (2003).

[48] A. Shields *et al.* , *Conference on Lasers and Electro-Optics (CLEO)*, in Baltimore, Maryland, US (2003).

[49] M. Aspelmeyer, H. R. Böhm, T. Gyatso, T. Jennewein, R. Kaltenbaek, M. Lindenthal, G. Molina-Terriza, A. Poppe, K. Resch, M. Taraba, R. Ursin, P. Walther and A. Zeilinger, *Science* **301** 621 (2003).

[50] R. Ursin, F. Tiefenbacher, T. Schmitt-Manderbach, H. Weier, T. Scheidl, M. Lindenthal, B. Blauensteiner, T. Jennewein, J. Perdigues, P. Trojek, B. Ömer, M. Fürst, M. Meyenburg, J. Rarity, Z. Sodnik, C. Barbieri, H. Weinfurter and A. Zeilinger, Nature Physics **3**, 629 (2007).

[51] D. P. DiVincenzo, *Topics in Quantum Computers*, in Mesoscopic Electron Transport, (ed. L. Kowenhoven, G. Schön and L. Sohn), NATO ASI Series E, (Kluwer Ac. Publ., Dordrecht, 1997).

[52] P. W. Shor, Phys. Rev. A. **52**, R2493 (1995).

[53] A. M. Steane, Phys. Rev. Lett. **77**, 793 (1996).

[54] A. M. Steane, in *Quantum Error Correction*, H. K. Lo, S. Popescu and T. P. Spiller (Eds.), pp. 184 (World Scientific, Singapore, 1999).

[55] R. Raussendorf and H. J. Briegel, *Phys. Rev. Lett.* **86**, 910 (2001).

[56] R. Raussendorf and H. J. Briegel, *Phys. Rev. Lett.* **86**, 5188 (2001).

[57] D. Gottesman and I. Chuang, *Nature* **402**, 390 (1999).

[58] M. A. Nielsen, *Phys. Lett. A* **308**, 96 (2003).

[59] D. Leung, *Int. J. Quant. Info.* **2** (1), 33 (2004).

[60] R. P. Feynman, *Optics News*, Feb., 11, p. 11 (1985).

[61] D. Deutsch, *Proc. Roy. Soc. Lond. A* **425**, 73 (1989).

[62] A. Barenco, C. H. Bennett, R. Cleve, D. P. DiVincenzo, N. Margolus, P. Shor, T. Sleator, J. Smolin and H. Weinfurter, *Phys. Rev. A* **52**, 3457 (1995).

[63] M. Van den Nest, W. Dür, A. Miyake, H. J. Briegel, Preprint at ⟨*http://www.arxiv.org/abs/quant-ph/0702116*⟩ (2007).

[64] M. Hein, W. Dür, J. Eisert, R. Raussendorf, M. Van Den Nest and H. J. Briegel, in *Proceedings of the International School of Physics Enrico Fermi on "Quantum Computers, Algorithms and Chaos", Varenna, Italy, July, 2005.*

[65] T. Tanamoto, Y.-X. Liu, S. Fujita, X. Hu, and F. Nori, *Phys. Rev. Lett.* **97**, 230501 (2006).

[66] N. C. Menicucci, P. van Loock, M. Gu, C. Weedbrook, T. C. Ralph and M. A. Nielsen, *Phys. Rev. Lett.* **97**, 110501 (2006).

[67] J. Cho and H.-W. Lee, *Phys. Rev. Lett.* **95**, 160501 (2005).

[68] S. D. Barrett and P. Kok, *Phys. Rev. A* **71**, 060310(R) (2005).

[69] M. Borhani and D. Loss, *Phys. Rev. A* **71**, 034308 (2005).

[70] O. Mandel, M. Greiner, A. Widera, T. Rom, T. W. Hänch and I. Bloch, *Nature* (London) **425**, 937 (2003).

[71] P. Walther , K. J. Resch, T. Rudolph, E. Schenck, H. Weinfurter, V. Vedral, M. Aspelmeyer and A. Zeilinger, *Nature* **434**, 196 (2005).

[72] P. Walther, M. Aspelmeyer, K. J. Resch and A. Zeilinger, *Phys. Rev. Lett.* **95**, 020403 (2005).

[73] N. Kiesel, C. Schmid, U. Weber, O. Gühne, G. Toth, R. Ursin and H. Weinfurter, *Phys. Rev. Lett.* **95**, 210502 (2005).

[74] A.-N. Zhang, C.-Y. Lu, X.-Q. Zhou, Y.-A. Chen, Z. Zhao, T. Yang and J.-W. Pan, *Phys. Rev. A* **73**, 022330 (2006).

[75] C.-Y. Lu, X.-Q. Zhou, O. Guhne, W.-B. Gao, J. Zhang, Z.-S. Yuan, A. Goebel, T. Yang and J.-W. Pan, *Nature Physics* **3**, 91 (2007).

[76] R. Prevedel, P. Walther, F. Tiefenbacher, P. Böhi, R. Kaltenbaek, T. Jennewein and A. Zeilinger, *Nature* **445**, 65 (2007).

[77] M. S. Tame, R. Prevedel, M. Paternostro, P. Böhi, M. S. Kim and A. Zeilinger, *Phys. Rev. Lett.* **98**, 140501 (2007).

[78] G. Vallone E. Pomarico, P. Mataloni, F. De Martini and V. Berardi, *Phys. Rev. Lett.* **98**, 180502 (2007).

[79] X. Su, A. Tan, X. Jia, J. Zhang, C. Xie and K. Peng, *Phys. Rev. Lett.* **98**, 070502 (2007).

[80] K. Chen, C.-M. Li, Q. Zhang, Y.-A. Chen, A. Goebel, S. Chen, A. Mair and J.-W. Pan, Preprint at ⟨*http://www.arxiv.org/abs/0705.0174*⟩ (2007).

[81] R. Prevedel, P. Walther, A. Stefanov and A. Zeilinger, *New J. Phys.* (in press, 2007).

[82] C. E. Shannon, *Bell System Tech.* F.. 27 329, 623 (1948).

[83] B. Schumacher, *Phys. Rev. A* **51**, 2738 (1995).

[84] W. Son, C. Brukner and M. S. Kim, *Phys. Rev. Lett.* **97**, 110401 (2006).

[85] P. A. M. Dirac, *The Principles of Quantum Mechanics* (The international series on monographs on physics; 27) - Fourth Edition (Oxford University Press, Oxford, 1999) - first published (1930).

[86] W. K. Wootters and W. H. Zurek, *Nature* 299, 802 (1982).

[87] E. Schrödinger, Proceedings of the Cambridge Philosophical Society **31** (1935); 555-563; **32** (1936): 446-451.

[88] A. Doherty, P. A. Parrilo and F. M. Spedalieri, *Phys. Rev. Lett.* **88**, 187904 (2002).

[89] L. Gurvits, Preprint at ⟨*http://www.arxiv.org/abs/quant-ph/0201022*⟩ (2002).

[90] C. H. Bennett, D. P. DiVincenzo, J. Smolin and W. K. Wootters, *Phys. Rev. A* **54** 3824 (1996).

[91] G. Vidal, *J. Mod. Opt.* **47** 355 (2000).

[92] V. Vedral and M. B. Plenio, *Phys. Rev. A* **57**, 1619 (1998).

[93] F. Mintert, A. R. R. Carvalho, M. Kuś and A. Buchleitner, *Phys. Rep.* **415**, 207 (2005) (Errata, **419**,143).

[94] R. Horodecki, P. Horodecki, M. Horodecki and K. Horodecki, *quant-ph/0702225* (2007).

[95] C. H. Bennett, H. J. Bernstein, S. Popescu and B. Schumacher, *Phys. Rev. A* **53** 2046 (1996);

[96] J. Preskill, *Lecture Notes for Physics 229: Quantum Information and Computation*, California Institute of Technology (1998), e-print: www.theory.caltech.edu/∼preskill/ph229.

[97] M. Horodecki, P. Horodecki and R. Horodecki, *Phys. Rev. Lett.* **84**, 2014 (2000).

[98] S. Hill and W. K. Wootters, *Phys. Rev. Lett.* **78**, 5022 (1997).

[99] W. K. Wootters, *Phys. Rev. Lett.* **80**, 2245 (1998).

[100] A. Peres, *Phys. Rev. Lett.* **1996**, 1413 (1996).

[101] M. Horodecki, P. Horodecki and R. Horodecki, *Phys. Lett. A* **223**, 1 (1996).

[102] J. Lee and M. S. Kim, *Phys. Rev. Lett.* **84**, 4236 (2000).

[103] J. Lee, M. S. Kim, Y.-J. Park and S. Lee, *J. Mod. Opt.* **47**, 2151 (2000).

[104] E. Schrödinger, *Ann. Physik* **79**, 361 & 489 (1925); **80**, 437 (1926); **81**, 109 (1926).

[105] C. A. Fuchs and A. Peres, *Physics Today* **53** (3), 70 (2000).

[106] J. von Neumann, *Mathematische Grundlagen der Quantenmechanik* (Springer, Berlin, 1932) p236; J. von Neumann, *Mathematical Foundations of Quantum Mechanics*, translated by R. T. Beyer (Princeton University Press, Princeton, NJ, 1955) p418;

[107] *Quantum Theory and Measurement*, edited by J. A. Wheeler and W. H. Zurek (Princeton University Press, Princeton, 1983).

[108] A. Peres, *Phys. Rev. A.* **61**, 022116 (2000).

[109] A. Peres, *Phys. Rev. D.* **22**, 879 (1980).

[110] J. S. Bell, *Speakable and Unspeakable in Quantum Mechanics* (Cambridge University Press, Cambridge, 1987).

[111] W. H. Zurek, *Physics Today* **44**, (10) 36 (1991).

[112] W. H. Zurek, *Physics Today* **46**, (4) 13 (1993).

[113] W. H. Zurek, *Los Alamos Sci.* **27**, 2 (2002).

[114] W. H. Zurek, *Rev. Mod. Phys.* **75**, 715 (2003).

[115] K. Kraus, *States, Effects and Operations: Fundamental Notions of Quantum Theory* (Springer, Berlin, 1983).

[116] E. B. Davies, *Quantum Dynamics of Open Systems* (Academic, New York, 1976).

[117] A. S. Holevo, *Probabilistic and Statistical Aspects of Quantum Theory* (North Holland, Amsterdam, 1982).

[118] P. Busch, M. Grabowski and P. J. Lahti, *Operational Quantum Physics* (Springer, Berlin, 1995).

[119] W. F. Stinespring, *Proc. Am. Math. Soc.* **6**, 211 (1955).

[120] M. A. Neumark, *C. R. (Dokl.) Acad. Sci. USSR* **41**, 359 (1943).

[121] A. Peres, *Found. Phys.* **20**, 1441 (1990).

[122] A. A. Markov, *Extension of the limit theorems of probability theory to a sum of variables connected in a chain*, reprinted in Appendix B of: R. Howard, *Dynamic Probabilistic Systems, volume 1: Markov Chains* (John Wiley and Sons, 1971).

[123] H.-P. Breuer and F. Petruccione, *The theory of open quantum systems* (Oxford University Press, Oxford, 2002).

[124] G. Lindblad, *Comm. Math. Phys.* **48**, 119 (1976).

[125] D. F. Walls and G. J. Milburn, *Quantum Optics* (Springer-Verlag, Berlin, 1994).

[126] M. O. Scully and M. S. Zubairy, *Quantum Optics* (Cambridge University Press, Cambridge, 1997).

[127] C. W. Gardiner and P. Zoller, *Quantum Noise, 2nd Edition* (Springer, Berlin, 2000)

[128] M. A. Nielsen and I. L. Chuang, *Quantum computation and quantum information* (Cambridge University Press, Cambridge, 2000).

[129] R. Raussendorf, D. E. Browne and H. J. Briegel, *J. Mod. Opt.* **49**, 1299 (2002).

[130] R. Raussendorf, D. E. Browne and H. J. Briegel, *Phys. Rev. A* **68**, 022312 (2003).

[131] D. E. Browne and T. Rudolph, *Phys. Rev. Lett.* **95**, 010501 (2005).

[132] M. Nielsen, *Journal club notes on the cluster-state model of quantum computation*, Available at ⟨*http://www.qinfo.org/qc-by-measurement/cluster-state.pdf*⟩(2003).

[133] V. Danos, E. Kashefi and P. Panangaden, Preprint at ⟨*http://www.arxiv.org/abs/quant-ph/0412135*⟩ (2004).

[134] M. S. Tame, M. Paternostro, M. S. Kim and V. Vedral, *Phys. Rev. A* **72**, 012319 (2005).

[135] D. Gross and J. Eisert, *Phys. Rev. Lett.* **98**, 220503 (2007).

[136] M. S. Tame, M. Paternostro, M. S. Kim and V. Vedral, *Int. J. Quant. Inf.* **4**, 4 689 (2006).

[137] R. Raussendorf, Ph.D. thesis, Ludwig-Maximillians Universität München, ⟨*http://edoc.ub.unimuenchen.de/archive/00001367*⟩ (2003).

[138] M. A. Nielsen and C. M. Dawson, *Phys. Rev. A* **71**, 042323 (2005).

[139] B. M. Terhal and G. Burkard, *Phys. Rev. A* **71**, 012336 (2005).

[140] P. Aliferis and D. W. Leung, *Phys. Rev. A* **73**, 032308 (2006).

[141] M. Greiner, O. Mandel, T. Esslinger, Th. W. Hänsch and I. Bloch, *Nature* **415**, 39 (2002).

[142] M. Greiner, O. Mandel, Th. W. Hänsch and I. Bloch, *Nature* **419**, 51 (2002).

[143] S. R. Clark, C. Moura Alves and D. Jaksch, *New J. Phys.* **7**, 124 (2005).

[144] J. García-Ripoll and J. I. Cirac, *New J. Phys.* **5**, 76 (2003).

[145] T. Calarco, E. A. Hinds, D. Jaksch, J. Schmiedmayer, J. I. Cirac and P. Zoller *Phys. Rev. A* **61** 22304 (2000).

[146] T. Calarco, H.-J. Briegel, D. Jaksch, J. I. Cirac, P. Zoller *J. Mod. Opt.* **47** 12, 2137 (2000).

[147] M. P. A. Fisher, P. B. Weichman, G. Grinstein and D. S. Fisher, *Phys. Rev. B* **40**, 546 (1989).

[148] D. Greenberger, M. A. Horne and A. Zeilinger, in *Bells Theorem, Quantum Theory and Conceptions of the Universe*, edited by M. Kafatos (Kluwer Academic, Dordrecht, 1989) p. 69.

[149] M. S. Tame, Code available at: ⟨*http://library.wolfram.com/infocenter/MathSource/5571/*⟩ (2004).

[150] S. Bose, *Phys. Rev. Lett.* **91**, 207901 (2003);

[151] M. Christandl, N. Datta, A. Ekert and A. J. Landahl, *Phys. Rev. Lett.* **92**, 187902 (2004).

[152] M. Paternostro, G. M. Palma, M. S. Kim and G. Falci, *Phys. Rev. A* **71**, 042311 (2005).

[153] M. Christandl, N. Datta, T. C. Dorlas, A. Ekert, A. Kay and A. J. Landahl, *Phys. Rev. A* **71**, 032312 (2005).

[154] M. Horodecki, P. Horodecki and R. Horodecki, *Phys. Rev. A* **60**, 1888 (1999).

[155] S. L. Braunstein, C. A. Fuchs and H. J. Kimble, *J. Mod. Opt.* **47** 267 (2000).

[156] S. Gasparoni, J.-W. Pan, P. Walther, T. Rudolph and A. Zeilinger, *Phys. Rev. Lett.* **92**, 020504 (2004).

[157] E. Bernstein and U. Vazirani, *Proceedings of the 25th Annual ACM Symposium on the Theory of Computing*, San Diego, CA, May 1993 (New York: ACM 1993).

[158] D. Deutsch and R. Jozsa, *Proc. R. Soc. Lond.* **A 439**, 553 (1992).

[159] N. A. Gershenfeld and I. L. Chuang, *Science* **275**, 350 (1997).

[160] D. G. Cory, A. F. Fahmy and T. F. Havel, *Proc. Nat. Acad. Sci. USA* **94**, 1634 (1997).

[161] M. Mohseni, J. S. Lundeen, K. J. Resch and A. M. Steinberg, *Phys. Rev. Lett.* **91**, 187903 (2003).

[162] R. Cleve, A. K. Ekert, C. Macchiavello and M. Mosca, *Proceedings of the Royal Society London, A* **454** 339 (1998).

[163] C. H. Bennett, *IBM Journal of Research and Development* **17**, 525 (1973).

[164] T. Toffoli, *Proc. of ICALP'80*, p. 632-644 (LNCS 84, Springer-Verlag, 1980); T. Toffoli, *Math. Sys. Theor.* **14**, 13 (1981).

[165] E. Fredkin and T. Toffoli, *Int. J. Theor. Phys.* **21** 219 (1982).

[166] D. F. V. James, P. G. Kwiat, W. J. Munro and A. G. White, *Phys. Rev. A* **64**, 052312 (2001).

[167] G. Tóth and O. Gühne, *Phys. Rev. Lett.* **94**, 060501 (2005).

[168] M. Dresher, *Research Rep.* **R-216**, RAND Corporation, Santa Monica, CA (1951); M. M. Flood, *Management Science* **5**, 1 (1958), also available as *Research Mem.* **RM-789-1-RR**, RAND Corporation, Santa Monica, CA (1952); A. W. Tucker, *UMAP J.* **1**, 101; W. Poundstone, *Prisoners' Dilemma: John von Neumann, Game Theory and the puzzle of the bomb* (Oxford University Press, Oxford, 1993).

[169] J. Eisert, M. Wilkens and M. Lewenstein, *Phys. Rev. Lett.* **83**, 3077 (1999); (Comment and Reply, **87**, 069802).

[170] J. Du, H. Li, X. Xu, M. Shi, J. Wu, X. Zhou and R. Han, *Phys. Rev. Lett.* **88**, 137902 (2002).

[171] S. L. Braunstein, C. M. Caves, R. Jozsa, N. Linden, S. Popescu and R. Schack, *Phys. Rev. Lett.* **83**, 1054 (1999).

[172] S. C. Benjamin and P. M. Hayden, *Phys. Rev. A* **64**, 030301 (2001); (Comment and Reply, **87**, 069801).

[173] C. F. Lee and N. F. Johnson, *Phys. World*, **15**, 25 (2002).

[174] D. A. Meyer, *Phys. Rev. Lett.* **82**, 1052 (1999).

[175] N. F. Johnson, *Phys. Rev. A* **63**(R), 020302 (2001).

[176] S. K. Ozdemir, J. Shimamura and N. Imoto, Preprint at ⟨*http://www.arxiv.org/abs/quant-ph/0402038*⟩ (2004).

[177] T. Toffoli *Reversible Computing*, in Automata, Languages and Programming, eds. J. W. de Bakker and J. van Leeuwen, p. 632 (Springer, New York, 1980).

[178] S. C. Benjamin, J. Eisert and T. M. Stace, *New J. Phys.* **7**, 194 (2005).

[179] J. K. Pachos and M. B. Plenio, *Phys. Rev. Lett.* **93**, 056402 (2004).

[180] D. Schlingemann and R. F. Werner, *Phys. Rev. A* **65**, 012308 (2001).

[181] E. Fermi, *Z. Phys.* **60**, 320 (1930).

[182] D. Jaksch, C. Bruder, J. I. Cirac, C. W. Gardiner and P. Zoller, *Phys. Rev. Lett.* **81**, 3108 (1998).

[183] Inhomogeneities in the atomic distribution can be fixed as in P. Rabl, A. J. Daley, P. O. Fedichev, J. I. Cirac and P. Zoller, *Phys. Rev. Lett.* **91**, 110403 (2003); D. S. Weiss, J. Vala, A. V. Thapliyal, S. Myrgren, U. Vazirani and K. B. Whaley, *Phys. Rev. A* **70**, 040302(R) (2004).

[184] J. K. Pachos and E. Rico, *Phys. Rev. A* **70**, 053620 (2004).

[185] A. Kay, D. K. K. Lee, J. K. Pachos, M. B. Plenio, M. E. Reuter and E. Rico, *Opt. Spectrosc.* **99**, 355 (2005).

[186] S. Peil, J. V. Porto, B. Laburthe Tolra, J. M. Obrecht, B. E. King, M. Subbotin, S. L. Rolston and W. D. Phillips, *Phys. Rev. A* **67**, 051603 (2003).

[187] A. Kay and J. K. Pachos, *New J. Phys.* **6**, 126 (2004).

[188] P. Baranowski, J. Zacks, G. Hechenblaikner and C. J. Foot, Preprint at ⟨*http://www.arxiv.org/abs/physics/0412126*⟩ (2004).

[189] J. M. Vogels, C. C. Tsai, R. S. Freeland, S. J. J. M. F. Kokkelmans, B. J. Verhaar and D. J. Heinzen, *Phys. Rev. A.* **56**, R1067 (1997).

[190] Q. Thommen, J. C. Garreau and V. Zehnlé, *Am. J. Phys.* **72**, 1017 (2004).

[191] D. L. Zhou, B. Zeng, Z. Xu and C. P. Sun, *Phys. Rev. A.* **68**, 062303 (2003).

[192] S. Clark, *J. Phys. A: Math. Gen.* **39**, 2701-2721 (2006).

[193] W. Hall, *Quant. Inf. and Comp.* **7**, 3, 184 (2007).

[194] A. B. Klimov, R. Guzmán, J. C. Retamal and C. Saavedra, *Phys. Rev. A* **67**, 062313 (2003).

[195] S. B. Zheng, *Phys. Rev. A* **68**, 035801 (2003).

[196] A. Vaziri, G. Weihs and A. Zeilinger, *Phys. Rev. Lett.* **89**, 240401 (2002);

[197] R. Thew, A. Acín, H. Zbinden and N. Gisin, *Quant. Inf. Proc.* **4**, 2 (2004);

[198] N. K. Langford, R. B. Dalton, M. D. Harvey, J. L. OBrien, G. J. Pryde, A. Gilchrist, S. D. Bartlett and A. G. White, *Phys. Rev. Lett.* **93**, 053601 (2004).

[199] M. Fujiwara, M. Takeoka, J. Mizuno and M. Sasaki, *Phys. Rev. Lett.* **90**, 167906 (2003).

[200] R. W. Spekkens and T. Rudolph, *Phys. Rev. A.* **65**, 012310 (2001).

[201] D. Kaszlikowski, P. Gnaciński, M. Żukowski, W. Miklaszewski and A. Zeilinger, *Phys. Rev. Lett.* **85**, 4418 (2000);

[202] W. Son, J. Lee and M. S. Kim, *Phys. Rev. Lett.* **96**, 060406 (2006).

[203] A. D. Greentree, S. G. Schirmer, F. Green, L. C. Hollenberg, A. R. Hamilton and R. G. Clark, *Phys. Rev. Lett.* **92**, 097901 (2004).

[204] F. Mintert and A. Buchleitner, *Phys. Rev. A.* **72**, 012336 (2005).

[205] E. Knill, Preprint at ⟨*http://www.arxiv.org/abs/quant-ph/9608048*⟩ (1996).

[206] G. J. Milburn, *Proceedings of the Fifth Physics Summer School, 435-465, Atomic and Molecular Physics and Quantum Optics*, edited by H-A. Bachor, *et al.* (World Scientific, Singapore, 1992).

[207] D. Vitali, P. Tombesi and G. J. Milburn, Phys. Rev. A **57**, 4930 (1998).

[208] Y. Liu, S. K. Özdemir, A. Miranowicz and N. Imoto, *Phys. Rev. A* **70**, 042308 (2004).

[209] K. Audenaert, F. Verstraete and B. De Moor, *Phys. Rev. A.* **64**, 052304 (2001).

[210] P. Rungta, V. Buzek, C. M. Caves, M. Hillery, G. J. Milburn and W. K. Wooters, *Phys. Rev. A.* **64**, 042315 (2001).

[211] G. G. Amosov, S. Mancini and V. I. Manko, *J. Phys. A: Math. Gen.* **39**, 3375-3380 (2006).

[212] K. Zyczkowski and H.-J. Sommers, *J. Phys. A: Math. Gen.* **34**, 7111 (2001).

[213] W. Dür and H. J. Briegel, *Phys. Rev. Lett.* **90**, 067901 (2003)

[214] K. Hammerer, G. Vidal, and J. I. Cirac, *Phys. Rev. A* **66**, 062321 (2002).

[215] I. L. Chuang and Y. Yamamoto, Phys. Rev. Lett. **76**, 4281 (1996).

[216] G. M. Palma, K. A. Suominen and A. K. Ekert, Proc. R. Soc. London A **452**, 567 (1996).

[217] L. M. Duan and G. C. Guo, Phys. Rev. Lett. **79**, 1953 (1997).

[218] D. A. Lidar and K. B. Whaley, in *Irreversible Quantum Dynamics*, F. Benatti and R. Floreanini (Eds.), pp. 83-120 (Springer Lecture Notes in Physics vol. 622, Berlin, 2003).

[219] C. M. Dawson, H. L. Haselgrove and M. A. Nielsen, *Phys. Rev. A* **73**, 052306 (2006).

[220] C. M. Dawson, H. L. Haselgrove and M. A. Nielsen, *Phys. Rev. Lett.* **96**, 020501 (2006).

[221] T. C. Ralph, A. J. F. Hayes and A. Gilchrist, *Phys. Rev. Lett.* **95**, 100501 (2006).

[222] M. Varnava, D. E. Browne and T. Rudolph, *Phys. Rev. Lett.* **97**, 120501 (2006).

[223] R. Raussendorf, J. Harrington and K. Goyal, *Ann. Phys.* **321**, 2242 (2006).

[224] R. Raussendorf and J. Harrington, *Phys. Rev. Lett.* **98**, 190504 (2007).

[225] M. Silva, V. Danos, E. Kashefi, H. Ollivier, Preprint at ⟨*http://www.arxiv.org/abs/quant-ph/0611273*⟩ (2006).

[226] K. Fujii and K. Yamamoto, Preprint at ⟨*http://www.arxiv.org/abs/quant-ph/0611160*⟩ (2006).

[227] M. A. Nielsen, E. Knill and R. Laflamme, *Nature* (London) **396**, 52 (1998).

[228] J. B. Altepeter, D. Branning, E. Jeffrey, T. C. Wei, P. G. Kwiat, R. T. Thew, J. L. O'Brien, M. A. Nielsen and A. G. White, *Phys. Rev. Lett.* **90**, 193601 (2003).

[229] J. L. O'Brien, G. J. Pryde, A. Gilchrist, D. F. V. James, N. K. Langford, T. C. Ralph and A. G. White, *Phys. Rev. Lett.* **93**, 080502 (2004).

[230] N. K. Langford, T. J. Weinhold, R. Prevedel, K. J. Resch, A. Gilchrist, J. L. OBrien, G. J. Pryde and A. G. White, *Phys. Rev. Lett.* **95**, 210504 (2005).

[231] Y. Nambu and K. Nakamura, *Phys. Rev. Lett.* **94**, 010404 (2005).

[232] T. Yamamoto, R. Nagase, J. Shimamura, S. K. Özdemir, M. Koashi, and N. Imoto, Preprint at ⟨ *http://www.arxiv.org/abs/quant-ph/0607159*⟩ (2006).

[233] D. Jaksch, H.-J. Briegel, J. I. Cirac, C. W. Gardiner, and P. Zoller, *Phys. Rev. Lett.* **82**, 1975 (1999).

[234] D. Kielpinski, V. Meyer, M. A. Rowe, C. A. Sackett, W. M. Itano, C. Monroe and D. J. Wineland, *Science* **291**, 1013-1015 (2001).

[235] C. F. Roos, G. P. T. Lancaster, M. Riebe, H. Häffner, W. Hänsel, S. Gulde, C. Becher, J. Eschner, F. Schmidt-Kaler and R. Blatt, *Phys. Rev. Lett.* **92** 220402 (2004).

[236] C. Langer, R. Ozeri, J. D. Lost, J. Chiaverini, B. DiMarco, A. Ben-Kish, R. B. Blakestad, J. Britton, D. B. Hume, W. M. Itano, D. Liebfried, R. Riechle, T. Rosenband, T. Schaetz, P. O. Schmidt and D. Wineland, *Phys. Rev. Lett.* **95** 060502 (2005).

[237] B. Schumacher, *Phys. Rev. A* **54**, 2614 (1996).

[238] G. B. Arfken and H. J. Weber *Mathematical Methods For Physicists* (Elsevier, London, 2005).

[239] M. A. Nielsen, *Phys. Lett. A* **303**, 249 (2002).

[240] J. Joo, Y. L. Lim, A. Beige, P. L. Knight, *Phys. Rev. A* **74**, 042344 (2006).

[241] J. Cho, Preprint at ⟨*http://www.arxiv.org/abs/quant-ph/0703185*⟩ (2007).

[242] C. Zhang, S. L. Rolston, and S. D. Sarma, *Phys. Rev. A.* **74**, 042316 (2006).

[243] S. Peil, J. V. Porto, B. Laburthe Tolra, J. M. Obrecht, B. E. King, M. Subbotin, S. L. Rolston, and W. D. Phillips, *Phys. Rev. A* **67**, 051603 (2003).

[244] J. Vala, A. V. Thapliyal, S. Myrgren, U. Vazirani, D. S. Weiss, and K. B. Whaley, *Phys. Rev. A* **71**, 032324 (2005).

[245] A. Beige and G. C. Hegerfeldt, *J. Mod. Opt.* **44**, 345-357 (1997);

[246] U. Volz and H. Schmoranzer, *Physica Sripta*, **T65**, 48 (1996).

[247] D. Rosenberg, A. E. Lita, A. J. Miller and S. W. Nam, *Phys. Rev. A* **71**, R061803 (2005).

[248] E. Knill, R. Laflamme and L. Viola, *Phys. Rev. Lett.* **84**, 2525 (2000).

[249] L. Viola, E. M. Fortunato, M. A. Pravia, E. Knill, R. Laflamme and D. G. Cory, *Science* **293** 2059 (2001).

[250] J. Kempe, D. Bacon, D. A. Lidar and K. Birgitta-Whaley, *Phys. Rev. A* **63**, 042307 (2001).

[251] C-P. Yang and J. Gea-Banacloche, *Phys. Rev. A.* **63**, 022311 (2001).

[252] P. G. Kwiat, A. J. Berglund, J. B. Altepeter and A. G. White, *Science* **290**, 498-501 (2000).

[253] M. Mohseni, J. S. Lundeen, K. J. Resch and A. M. Steinberg, *Phys. Rev. Lett.* **91**, 187903 (2003).

[254] M. Bourennane, M. Eibl, S. Gaertner, C. Kurtsiefer, A. Cabello and H. Weinfurter, *Phys. Rev. Lett.* **92**, 107901 (2004).

[255] J. E. Ollerenshaw, D. A. Lidar and L. E. Kay, *Phys. Rev. Lett.* **91**, 217904 (2003).

[256] C. M. Dawson, H. L. Haselgrove and M. A. Nielsen, *Phys. Rev. Lett.* **96**, 020501 (2006).

[257] I. L. Chuang and M. A. Nielsen, *J. Mod. Opt.* **44**, 2455-2467 (1997).

[258] J. L. O'Brien, G. J. Pryde, A. Gilchrist, D. F. V. James, N. K. Langford, T. C. Ralph and A. G. White, *Phys. Rev. Lett.* **93**, 080502 (2004).

[259] P. P. Rohde, G. J. Pryde, J. L. O'Brien and T. C. Ralph, *Phys. Rev. A* **72**, 032306 (2005).

[260] D. A. Lidar, D. Bacon and K. B. Whaley, *Phys. Rev. Lett.* **82**, 4556 -4559 (1999).

[261] L.-A. Wu and D. A. Lidar, *Phys. Rev. Lett.* **88**, 207902 (2002).

[262] C. Cinelli, M. Barbieri, R. Perris, P. Mataloni and F. De Martini, *Phys. Rev. Lett.* **95**, 240405 (2005).

[263] T. Yang, Q. Zhang, J. Zhang, J. Yin, Z. Zhao, M. Zukowski, Z.-B. Chen, J.-W. Pan, *Phys. Rev. Lett.* **95**, 240406 (2005).

[264] J. T. Barreiro, N. K. Langford, N. A. Peters and P. G. Kwiat, *Phys. Rev. Lett.* **95**, 260501 (2005).

[265] W. Dür, M. J. Bremner and H. J. Briegel, Preprint at ⟨*http://www.arxiv.org/abs/quant-ph/0706.0154*⟩ (2007).

[266] K. Kieling, D. Gross and J. Eisert, *J. Opt. Soc. Am. B* **24** (2), 184 (2007).

[267] D. Gross, K. Kieling and J. Eisert, *Phys. Rev. A* **74**, 042343 (2006).

[268] K. Kieling, D. Gross, J. Eisert *New J. Phys.* (in press, 2007).

[269] K. Kieling, T. Rudolph and J. Eisert, Preprint at ⟨*http://www.arxiv.org/abs/quant-ph/0611140*⟩ (2007).